UNIVERSITY OF CALIFORNIA

Santa Barbara

MEMS-tunable vertical-cavity SOAs

A Dissertation submitted in partial satisfaction of the

requirements for the degree Doctor of Philosophy

in Materials

by

Garrett D. Cole

Committee in charge:

Professor Noel C. MacDonald, Co-Chair

Professor John E. Bowers, Co-Chair

Professor Kimberly L. Turner

Professor Evelyn L. Hu

Professor Arthur C. Gossard

December 2005

The dissertation of Garrett D. Cole is approved.

Kimberly L. Turner

Evelyn L. Hu

Arthur C. Gossard

John E. Bowers, Committee Co-Chair

Noel C. MacDonald, Committee Co-Chair

October 2005

MEMS-tunable vertical-cavity SOAs

Copyright © 2005

by

Garrett D. Cole

ACKNOWLEDGEMENTS

"…to educate graduate students in advanced materials and to introduce them to novel ways of doing research in a collaborative, multidisciplinary environment."
–from the Graduate Student Manual, Department of Materials, UCSB

The research presented in this dissertation is just one of many examples of the open and collaborative research environment fostered at UCSB. It is always interesting to explain that, yes, I am a materials student, although I am advised by professors in Electrical and Mechanical Engineering. While, any work in MEMS is interdisciplinary by its very nature, optical MEMS devices in particular require a diverse set of backgrounds ranging from solid mechanics to quantum mechanics, and it is here that my diverse advisorship comes in handy. Thus, I would like to begin by thanking Professors John Bowers and Noel MacDonald for the guidance they have given me over the past few years. Professor Bowers has always been there to provide insight into a diverse range of topics including fabrication, device design, and characterization; as well as an introduction to the finer things in life, including sailing and wine tasting. I would like to thank Professor MacDonald for his invaluable insight into all things MEMS, and for giving me the freedom to be the one black sheep of the group working on compound-semiconductor-based devices. Being the sixth member of the UCSB MEMS group allowed me to better understand the trials and tribulations of getting a research group up and running. Further appreciation goes out to Professor Kim Turner for her indispensable lessons on the linear and non-linear dynamics of microsystems, and to Professors Evelyn Hu and Art Gossard for their unique perspectives and for reviewing this dissertation.

To the few, the proud—those that dare not exceed threshold—I express unflinching loyalty to the VCSOA cause. Much gratitude goes to my friend, mentor, and fellow skateboarder Staffan Björlin, who taught me everything I know regarding VCSOAs, theoretical modeling, and optical testing; and who I respect more for his skateboarding ability than anything else. Further love goes out to my original partner in crime, and the other half responsible for the first demonstration of a MEMS-tunable VCSOA, Qi Chen. Special thanks are reserved for VCSOA visiting researcher Toshio Kimura, and the world's greatest summer intern, Cavan Chan. Without the availability of world class epi-material none of this would be possible. The excellent DBRs produced by Chad Wang and Shaomin Wu contributed to the success of this work, as did the exquisite 25 and 28 MQW active regions provided by Tec-Well. Chad especially deserves praise for his selfless contributions, including weekend mirror growths requiring thick non-digital AlGaAs sacrificial layers.

I am indebted to the members of the MacMEMS group for their camaraderie and support-group-like environment. Special thanks go out to Dave Bothman for his Herculean efforts including management of the Engineering Science Building, support of countless ME research groups, working with the COE machine shop, etc.,

while at the same time keeping the MacMEMS test equipment up and running. To our esteemed post-doc Masa Rao for originally introducing me to Staffan and starting me down this path of research, to you I give a high five. To Marco Aimi for general processing discussions, vibrometer upkeep, and for making a mean loaf of French bread. To Seth Boeshore for keeping it real in the office and leaving me with a few bruised ribs in the process. To office mates Emily Parker, Yanting Zhang, and Adam Monkowski, I would like to acknowledge your unwavering support. To the Generation 1 MacMEMS group members: Lori Callaghan, Dave Follman, Alok Paranjpye, and Adam Pyzyna, who braved the rough road of a new research group at UCSB. I would also like to thank the remaining members of MacMEMS support center: Justin Bellante, Changsong Ding, Trent Huang, Zuruzi Abu Samah, Marcus Ward, Geoffrey Bennes, and Anton Riley. Finally, credit is due to ME computer support staff members Jeff Oakes and Simon Ibsen for general technical assistance and help with the MEMS web server.

Having worked with two research groups really helped to broaden my horizons. Much love goes out to the Femtonians for allowing me into their hearts and for letting me mooch off of their water supply. I would like to thank Jon Geske for giving me the reigns of the optical pump palace and for his amazing ability to simultaneously provide insults as well as technical assistance. If I could, I would create a separate disacknowledgements section for Manish Mehta, but unfortunately his boyish good looks and suave personality have captured my heart. Special thanks are reserved for Raja Jindal who helped motivate me to start attending the Bowers group meetings and become a part of this esteemed organization. To Alex Fang, Hyundai Park, and Brian Koch for proving that you can always take an uncomfortable and outright inappropriate situation one step further. I would like to apologize to Emily Burmeister for the constant barrage of lame comments each time I visited her office. My thanks go out to the Femto sailing crew: Kian-Giap Gan, Hsu-Feng (Hubert) Chou, Je-Hyeong Bahk, Gehong Zeng, and Jasmine Young. Jasmine must be singled out as the world’s greatest assistant, Nor-Cal homie, and much appreciated supplier of free chocolate. Finally, a hearty thanks is reserved for the former Bowers group assistants Kate Ferrian and Hillary Greenlee, visiting researcher Satoshi Kodama, former students Yae Okuno and Maura Raburn, and the newbies Shane Todd and Anand Ramaswamy.

To the 20% of the Cal Poly Materials Engineering class of 2001 that continued on to the Materials Department at UCSB for graduate school, I thank you for the long hours of prelim studying and for the debates over the satanic nature of my liberal hippy beliefs. Matt and James, I hope that we all continue to make our slow progression southward along the western coast of North America. Additional praise is reserved for Cannon Green roommate Nick Stoltz for proving that a human can indeed survive on a diet consisting solely of frozen pizza and beer.

The most intensive portion of this research was device fabrication, utilizing the state-of-the-art facilities under the umbrella of the UCSB nanofab and microscopy staff. Thus I owe much to the steadfast support of Jack Whaley, Brian Thibeault, Martin Vandenbroek, Don Freeborn, Bob Hill, Tom Reynolds, Ning Cao, Luis Zuzunaga and Jan Lofvander. Another important part of work is actually getting

there, so special thanks are given to the Santa Barbara Metropolitan Transit District for the free rides to campus each day. A special place in my heart is reserved for my 24X bus buddies Amanda Hoagland and Mike Requa. And for those days when it was pouring rain, or I just didn't feel like taking the bus, I would like to thank my 1972 Ford Galaxie 500 for getting me down the 101 in style.

To conclude, I need to thank the most important contribution to this work, that being the loving home environment provided by my faux family at 1632 ½ De La Vina, consisting of my common-law wife (and girlfriend of 8 years) Laura Gibb and our practice kids Cosmo and Newman. Finally, nothing that I have done would be possible without the endless love and support of my family including my mom and step-dad: Cindy and David, my dad and step-mom: David and Cindy, my brother James and sister Jenni, and finally, I can't forget the help of my extended family including the Coles (also Ruddles and Painters), the Thompsons, and the Gibbs.

The tunable VCSOA project at UCSB has been supported by a number of sources including: the NSF IGERT Advanced Optical Materials program, award number DGE-9987618; E2O Communications Inc. (now JDS Uniphase) through a UC Discovery Grant; DARPA via the Center for Chips with Heterogeneously Integrated Photonics (CHIPS); and finally Furukawa Electric Co., LTD—who generously donated a number of 980-nm pump lasers and visiting researcher Toshio Kimura.

CURRICULUM VITAE

GARRETT DAVID COLE

PERSONAL
Born May 31, 1979, San Jose, California

EDUCATION
Doctor of Philosophy, Materials Science and Engineering
University of California, Santa Barbara, October 2005

Bachelor of Science, Materials Engineering
California Polytechnic State University, SLO, June 2001 (magna cum laude)

PROFESSIONAL EMPLOYMENT
Mechanical Engineering Intern, Flight and Guidance Simulation Laboratory, NASA Ames Research Center, Moffett Field, CA, June–September 2000

Machinist Apprentice, Design Machining, Campbell, CA, May–September 1997

AWARDS
Fellowship: NSF IGERT, Advanced Optical Materials

PUBLICATIONS
Journal Papers
G.D. Cole, E.S. Bjorlin, C.S. Wang, N.C. MacDonald, J.E. Bowers, "Widely tunable bottom-emitting vertical cavity SOAs," *IEEE Photonics Technology Letters*, to be published in vol. 17, no. 12, December 2005.

G.D. Cole, E.S. Bjorlin, Q. Chen, C.-Y. Chan, S. Wu, C.S. Wang, N.C. MacDonald, J.E. Bowers, "MEMS-tunable vertical-cavity SOAs," *IEEE Journal of Quantum Electronics*, vol. 41, no. 3, March 2005, pp. 390–407.

Q. Chen, G.D. Cole, E.S. Bjorlin, T. Kimura, S. Wu, C.S. Wang, N.C. MacDonald, J.E. Bowers, "First demonstration of a MEMS tunable vertical-cavity SOA," *IEEE Photonics Technology Letters*, vol.16, no. 6, June 2004, pp.1438–1440.

Conference Presentations
G.D. Cole, "Tunable Vertical-Cavity SOAs: a unique combination of tunable filtering and optical gain," *SPIE Optics East, IT103 Optoelectronic Devices: Physics, Fabrication, and Application II*, Boston, MA, 23–26 Oct. 2005. (invited)

G.D. Cole, J.E. Bowers, K.L. Turner, N.C. MacDonald, "Dynamic characterization of MEMS-tunable vertical-cavity SOAs," *IEEE/LEOS International Conference on Optical MEMS and Their Applications*, Oulu, Finland, 1–4 Aug. 2005, Paper F4.

G.D. Cole, E.S. Björlin, Q. Chen, C.-Y. Chan, S. Wu, C.S. Wang, J.E. Bowers, N.C. MacDonald, "Design and analysis of MEMS tunable vertical-cavity semiconductor optical amplifiers," in *Proceedings of the 17th International Conference on InP and Related Materials*, Glasgow, Scotland, UK, 8–12 May 2005, Paper TuB-1-4.

G.D. Cole, Q. Chen, E.S. Björlin, T. Kimura, S. Wu, C.S. Wang, J.E. Bowers, and N.C. Macdonald, "Wavelength selection in MEMS tunable vertical-cavity SOAs," in *15th International Conference on Optical Amplifiers and their Applications Technical Digest*, OSA Topical Meeting and Exhibit, San Francisco, CA, USA, 27–29 June 2004, Paper OMB3.

T. Kimura, S. Bjorlin, G.D. Cole, H.F. Chou, J. Bowers, "1550-nm vertical-cavity SOAs for optically preamplified high bit rate receivers," in *Proceedings of 30th European Conference on Optical Communications*, Stockholm, Sweden, 5–9 September 2004, Paper We4.P.070.

G.D. Cole, Q. Chen, E.S. Björlin, T. Kimura, S. Wu, C.S. Wang, J.E. Bowers, N.C. MacDonald, "Microelectromechanical tunable long-wavelength vertical-cavity semiconductor optical amplifiers,", in *Proceedings of 16th International Conference on InP and Related Materials*, Kagoshima, Japan, 31 May–4 June 2004, Paper FA2-4, pp. 708–711.

FEATURED PRESS

"R&D Highlights: MEMS enhance SOA tuning range," by Tami Freeman, *FibreSystems Europe/LIGHTWAVE Europe*, December 2004, pp. 5.

"Light Booster," by Larry Hardesty, *Technology Review*, September 2004, pp. 19.

"MEMS make SOAs tune farther and faster," by Tami Freeman, *FibreSystems Europe/LIGHTWAVE Europe*, August 2004, pp. 7.

PATENTS

Provisional filing, UC Case 2005-623, "Tunable Optical Amplifying Filter Array"

ABSTRACT

MEMS-tunable vertical-cavity SOAs
Garrett D. Cole

Vertical-cavity semiconductor optical amplifiers (VCSOAs) are attractive as a low-cost alternative to existing amplifier technologies for use in fiber-optic communication systems such as metro and access networks. In contrast with in-plane SOAs, the surface-normal operation of vertical-cavity SOAs gives rise to a number of advantages including a high coupling efficiency to optical fiber, polarization insensitive gain, the potential to fabricate high fill-factor two-dimensional arrays, and the ability to test devices on wafer.

Due to their narrow gain bandwidth, VCSOAs function as amplifying filters. In these devices the inherent spectral filtering of the high-finesse Fabry-Pérot cavity leads to the elimination of out-of-band noise and results in channel-selective amplification. For multi-wavelength communications systems, it is of great interest to develop widely tunable VCSOAs that can be dynamically adjusted to match the signal wavelength. A promising approach to achieve wide wavelength tuning in VCSOAs is micromechanical, or MEMS-based tuning. Here, mechanical alteration of the effective cavity length gives rise to tuning ranges greater than those that can be achieved via refractive index modulation.

This dissertation outlines the development of three generations of MEMS-tunable VCSOAs (MT-VCSOAs), with the initial generation of devices being noteworthy as the first demonstration of a micromechanically-tunable VCSOA. In

contrast with temperature tuning, the AlGaAs-based electrostatic actuator used in these devices allows for rapid, low power, and wide wavelength tuning. In the final generation, the MT-VCSOA utilizes a bottom-emitting configuration in which the MEMS-tuning element serves as the high-reflectivity back mirror. By suppressing the variation in reflectance with tuning, this configuration exhibits a two-fold increase in the effective tuning range as compared with the initial generation of devices—with a minimum of 5 dB fiber-to-fiber gain (12 dB on-chip gain) over a wavelength span of 21 nm, from 1557.4 nm to 1536.4 nm, while requiring a maximum tuning bias of 10.5 V (a five-fold reduction when compared with the first generation of MT-VCSOAs). Furthermore, these devices exhibit properties comparable to state-of-the-art fixed-wavelength VCSOAs, with a maximum fiber-coupled saturation output power of -1.4 dBm and an average gain bandwidth and noise figure of 65.2 GHz and 7.5 dB respectively.

CONTENTS

1 Introduction

1.1 Fixed Wavelength VCSOAs 1
1.1.1 History of the VCSOA 2
1.1.2 Advantages Over Existing Amplifier Technologies 4
1.2 MEMS-tunable Vertical-Cavity Devices 6
1.3 Scope of this Dissertation 12
References 16

2 Device Design

2.1 Tunable VCSOA Principle of Operation 22
2.2 Fixed-Wavelength VCSOA Theoretical Model 24
2.2.1 General Design Principles 25
2.2.2 Signal Gain and Gain Bandwidth 28
2.2.3 Saturation and Noise Figure 31
2.3 Tunable Cavity Design Options 34
2.3.1 Semiconductor Coupled Cavity Design 36
2.3.2 Extended Cavity Design 37
2.4 Tunable VCSOA Theoretical Model 38
2.4.1 Wavelength Tuning 38
2.4.2 Peak Gain Response of MEMS-Tunable VCSOAs 42
2.5 MEMS Actuator Design 44
2.5.1 Electrostatic Actuation 44
2.5.2 Static Response of the Deformable Membrane Structure 46
2.5.3 Dynamic Mechanical Response 50
2.6 Summary 54
References 55

3 Tunable VCSOA Processing

3.1 MEMS in AlGaAs 60
3.2 Tunable VCSOAs Fabricated in this Dissertation 62
3.3 GaAs to InP Direct Wafer Bonding 64
3.3.1 Pre-Bond Wafer Characterization 67
3.3.2 Wafer Bonding Process 74
3.4 Basic Fabrication Sequence Following Bonding 78
3.4.1 General Processing Procedure 78
3.5 Additional Processing Notes 83
3.6 Summary 85
References 86

4 Generation 1: Initial Device Demonstration

4.1 Top Emitting MEMS-Tunable VCSOAs 89
4.1.1 Material Structure 90
4.2 Tunable VCSOA Characterization 94
4.2.1 Optical Test Setup 95
4.2.2 Vertical Scanning Interferometer 97
4.2.3 Laser Doppler Vibrometer 99
4.3 Generation 1 Results 101
4.3.1 Wavelength Tuning Response 101
4.3.2 Signal Gain and Gain Bandwidth 103
4.3.3 Saturation Properties 107
4.4 Limitations of the Initial Device Design 109
4.4.1 Control of Air-Gap Thickness 109
4.4.2 Device Reliability 112
4.5 Summary 114
References 115

5 Generation 2: Revised Mechanical Structure

5.1 Updated Lithographic Mask Set 120
5.1.1 Modified Actuator Design 120
5.1.2 Updated Process Flow 122
5.2 Generation 2 Results 124
5.2.1 Improved Wavelength Tuning Response 124
5.2.2 Dynamic Characterization 129
5.3 Limitations of the Current Optical Cavity Design 134
5.3.1 Variation in Mirror Reflectance 134
5.4 Investigation of Alternative Optical Cavity Designs 139
5.4.1 Determination of the Materials Gain Spectrum 139
5.4.2 Peak Gain Response: SCC-design MT-VCSOAs 143
5.4.3 Peak Gain Response: EC-design MT-VCSOAs 149
5.4.4 Saturation Properties 151
5.4.5 Noise Characteristics 154
5.5 Summary 158
References 161

6 Generation 3: Revised Optical Cavity Design

6.1 Bottom-Emitting Tunable VCSOAs 167
6.1.1 Material Structure 167
6.1.2 Active Region Design 168
6.1.3 Resonant Cavity Design 170
6.1.4 Process Modifications 172

6.2 Revised Optical Test Setup 174
6.3 Generation 3 Results 176
6.3.1 Enhanced Effective Tuning Range 176
6.3.2 Improved Amplifier Properties 178
6.4 Variation in Amplifier Properties with Tuning 181
6.4.1 Comparison with Initial Optical Cavity Design 182
6.4.2 Effective Reflectance 183
6.4.3 Material Gain Spectrum 183
6.5 Summary 186
References 187

7 Conclusions
7.1 Summary 189
7.2 Future Directions 191
7.2.1 Alternative Optical Cavity Designs 192
7.2.2 Electrically Pumped VCSOAs 192
7.2.3 Novel Actuator Designs and Processing Procedures 193
7.2.4 Monolithic Integration 195
References 196

A Mask Layout and Device Geometry
A.1 Generation 1 MT-VCSOAs 199
A.2 Generations 2 & 3 MT-VCSOAs 199

B Material Structures
B.1 Generations 1 & 2 Detailed Materials Structure 200
B.2 Generation 3 Detailed Materials Structure 202

C Wafer Bonding Procedure
C.1 MT-VCSOA Wafer Bonding Process 204

D Process Travelers
D.1 Generation 1: Fabrication Procedure 207
D.2 Generation 2: Fabrication Procedure 210
D.3 Generation 3: Fabrication Procedure 214

CHAPTER 1

Introduction

This dissertation outlines all aspects of the development of widely tunable vertical-cavity semiconductor optical amplifiers (VCSOAs), including the theoretical design, microfabrication, and mechanical and optical characterization. In these devices, wide wavelength tuning is realized through the integration of a microelectromechanical (MEMS) actuator. The MEMS-tunable VCSOAs (MT-VCSOAs) outlined in this work represent the first widely tunable VCSOAs—with the initial generation of devices being noteworthy as the first ever demonstration of a micromechanically-tunable VCSOA. Because of the significant differences in optical design when compared with existing devices, MT-VCSOAs allow for further exploration of the design space of tunable vertical-cavity structures and help to shed light on some of the fundamental limitations of coupled-cavity tuning designs.

1.1 Fixed-Wavelength VCSOAs

Compared with the extensive research completed on vertical-cavity surface-emitting lasers (VCSELs), relatively little work has focused specifically on the development of VCSOAs. Recently a number of investigations into these unique

devices have been undertaken, resulting in the demonstration of multifunctional and multipurpose microcavity amplifiers. Stemming from this recent work, numerous potential applications of VCSOAs have been proposed, including use as preamplifiers, modulators, and optical switches [1]. In addition to applications in fiber-optic communication systems, VCSOAs have been shown to be ideal as board to board amplifiers or repeaters for optical interconnect applications [2]. Before covering the advantages of vertical-cavity amplifiers, a brief history of these unique devices will be presented.

1.1.1 History of the VCSOA

In contrast with their more common in-plane counterparts, vertical-cavity SOAs represent a relatively recent class of devices. Although the first demonstration of optical amplification in a GaAs injection laser was presented in 1963 [3], it was not until 1991 that the first VCSOA was demonstrated by Koyama, Kubota, and Iga at the Tokyo Institute of Technology [4]. This device originated from the same lab that had previously developed the first VCSEL in 1979 [5]. The first VCSOA structure consisted of an electrically pumped GaAs/AlGaAs VCSEL, operated below threshold, in order to amplify an injected 885-nm signal. In this demonstration the favorable filtering properties of the high-finesse VCSEL cavity were recognized and the device was not explicitly presented as an amplifier, but rather as an "active filter". Two years later, in 1993, pulsed operation of an optically pumped reflection mode device, also at 850 nm, was presented by Raj et al. at France Telecom [6]. This

same group introduced resonant pumping in a following generation of 850-nm devices [7] and in 1996 they presented the first long-wavelength VCSOA [8]. Also in 1996, Wiedenmann et al. at the University of Ulm presented an electrically pumped reflection mode VCSOA operating at 980 nm [9]. In 1998, Wiedenmann et al. presented their second generation of highly advanced VCSOAs: electrically pumped transmission mode amplifiers with oxide apertures for current and mode confinement producing up to 16 dB of gain [10]. Progressing beyond short-wavelength VCSOAs, in 1998 Lewen et al. at KTH used a 1.55-μm VCSEL structure for what was the first electrically pumped long wavelength VCSOA [11]. This device exhibited 18 dB of gain at 218 K (not including coupling losses). More recently, researchers at the University of Strathclyde, UK, have demonstrated monolithic GaInNAs-based devices, lattice matched to GaAs, operating in the 1.3-μm wavelength range [12], [13].

The VCSOA project at UCSB began in 1999 and led to the demonstration of the first 1.3-μm VCSOA in 2000 [14]. These devices were fabricated using InP to GaAs wafer bonding, were optically pumped, and were designed to operate in reflection mode. During the course of this research, two generations of devices were fabricated, with the first generation used to fully characterize this still fairly new class of devices, develop improved theoretical models, and to explore possible applications for long-wavelength VCSOAs [15]-[19]. A second generation of carrier confined 1.3-μm devices with improved efficiency and higher gain—17 dB fiber to fiber gain—were presented in 2002 [1]. The knowledge gained from these devices was then extended to 1.55-μm VCSOAs, resulting in vertical-cavity amplifiers with

record-high saturation output power [20], as well as excellent preamplifier characteristics [21]. In parallel with the 1.55-μm VCSOAs, the push to make the first widely tunable VCSOA was initiated in the fall of 2002. These devices can be seen as a logical extension of fixed-wavelength vertical-cavity amplifiers. The addition of wavelength tunability allows for increased flexibility and makes MT-VCSOAs appealing as tunable amplifying-filters for use in multiwavelength and reconfigurable optical communications systems. Compared with existing optical amplifier technologies, VCSOAs—especially tunable VCSOAs—exhibit a number of advantages, as discussed in the following section.

1.1.2 Advantages Over Existing Amplifier Technologies

Long-wavelength VCSOAs are an attractive alternative to conventional in-plane SOAs for use in fiber optic communication systems such as metro-area networks and fiber to the home. In these applications, in-plane SOAs suffer from a poor coupling efficiency to optical fiber, are typically sensitive to polarization, and are not yet price competitive with existing fiber amplifiers. In contrast with in-plane devices, the surface normal operation of vertical-cavity SOAs gives rise to a number of advantages including a high coupling efficiency to optical fiber, polarization insensitive gain, the potential to fabricate two-dimensional arrays, and the ability to test devices on wafer. Moreover, by altering the composition of the active material, amplification can be achieved at nearly any desired wavelength, in contrast with the limited wavelength range of fiber amplifiers.

For in-plane traveling-wave SOAs and fiber amplifiers, the signal gain spectrum is determined solely by the gain medium of the device. Conversely, for Fabry-Pérot (FP) SOAs, including VCSOAs, the signal-gain spectrum is controlled by the overlap of the FP mode with the material gain spectrum. In these devices, the signal-gain bandwidth is constricted to the linewidth of the resonant cavity mode, which for VCSOAs is typically less than 1 nm. This narrow gain bandwidth eliminates the need for an optical filter after the amplifier due to the inherent spectral filtering of the high finesse FP structure [19]. The filtering properties of VCSOAs result in the elimination of out-of-band noise and allow for channel selective amplification; however, in low-cost systems, uncooled sources are typically used, and the signal wavelength can vary over a fairly wide range. If the signal wavelength deviates only slightly from the peak gain wavelength of the VCSOA, distortion of the signal may result. Furthermore, for multi-wavelength communications systems such as reconfigurable or wavelength division multiplexed (WDM) networks, a narrow-band amplifier with a fixed center wavelength becomes a limitation.

In these applications it is of great interest to develop tunable VCSOAs that can cover a wide wavelength range and be dynamically adjusted to match the signal wavelength. Previously, temperature tuning of long-wavelength VCSOAs has been investigated [22], [12]; however, temperature tuning is hampered by a high power consumption, a slow temporal response, and a limited total wavelength span. A more promising approach is micromechanical, or MEMS-based tuning. In this case, mechanical alteration of the effective FP mode gives rise to tuning ranges greater than those that can be achieved by refractive index modulation. Moreover, by using

an electrostatic actuator it is possible to achieve rapid response times—on the order of a few microseconds—with power consumption levels in the microwatt range.

1.2 MEMS-Tunable Vertical-Cavity Devices

The use of MEMS-based tuning has become a popular mechanism for wavelength selection in various vertical-cavity devices including VCSELs [23]-[25], resonant-cavity light-emitting diodes (RCLEDs) [26], asymmetric FP modulators [27], and vertical-cavity filters [28]; until this work no attempt has been made to develop a tunable vertical-cavity amplifier. Because of the similarity in the basic optical cavity design, previous work on these devices is readily applicable to the development of tunable VCSOAs; this is especially true in the case of tunable VCSELs. Much as the fixed-wavelength VCSOA has benefited from the extensive literature on surface emitting lasers, research into tunable VCSOAs benefits greatly from previous research into tunable VCSELs. With this in mind, a brief overview of historical background on MEMS-tunable VCSELs will be presented.

A common method of achieving wavelength tuning with in-plane lasers is via refractive index modulation of the mirrors and/or cavity by means of temperature variation or carrier injection [29]. However, given the short interaction length in vertical-cavity devices, refractive index modulation results in a relatively insignificant shift in the total optical thickness of the structure. In these devices the cavity length variation is typically limited to much less than 1%, and in the case of

temperature tuning, is hampered by a comparatively slow temporal response, on the order of milliseconds.

A more effective means of achieving wavelength tuning in vertical-cavity devices is through direct mechanical alteration of the optical cavity length. It is interesting to note that the first mechanically tunable VCSEL was demonstrated by the same group that presented both the first VCSEL in 1979 [5] and the first VCSOA in 1991 [4]. These initial devices showed that the wide axial mode spacing of vertical-cavity devices allowed for continuous single-mode wavelength tuning through direct alteration of the cavity length [30]. Although an interesting concept, this first demonstration of a mechanically tunable VCSEL relied on an external cavity for tuning and the total wavelength variation was limited to 4 nm.

Following this initial demonstration, groups at the University of California, Berkeley and Stanford University went one step further and developed the first micromechanically tunable VCSELs in 1995/1996 [23], [24]. These MEMS-tunable VCSELs incorporated an integrated micromechanical element into the device structure in order to vary the thickness of an air gap within the top mirror. By changing the thickness of the air gap, the effective cavity length of the device could be altered and the center wavelength would be tuned. Unlike bulky external-cavity structures, MEMS-tunable VCSELs could be fabricated monolithically using micromachining techniques and the small size of the moveable elements allowed for faster and more efficient wavelength tuning.

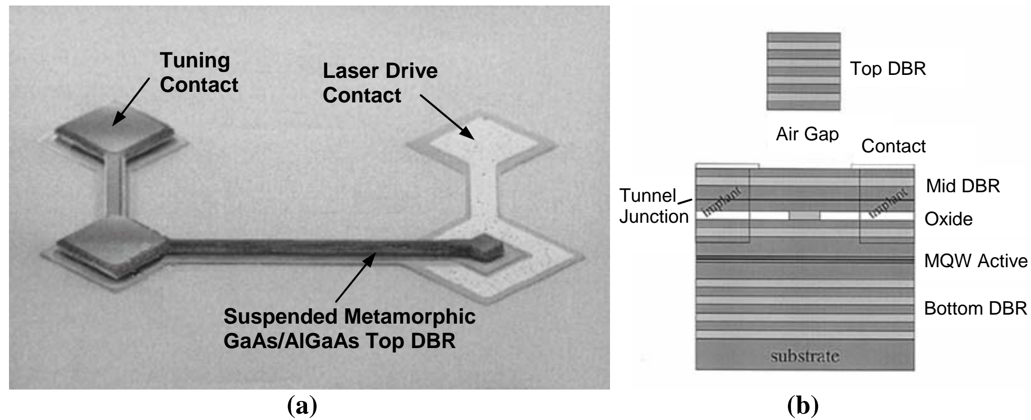

Fig. 1.1: (a) Scanning electron micrograph and (b) cross-sectional schematic of the cantilever-tunable VCSEL developed by the Chang-Hasnain group at University of California, Berkeley and commercially available through the now defunct Bandwidth9 [23], [31].

These initial tunable VCSELs were three-terminal electrically injected devices with InGaAs/GaAs active regions (resonant wavelengths between 850-950 nm). Here, the third contact was used to control the bias on an integrated electrostatic actuator; thus, controlling the lasing wavelength. The air gap functioned as a low index layer in the top distributed Bragg reflector (DBR) and tuning was realized through a phase shift in the top mirror structure. With a decrease in the air-gap thickness, the effective cavity length is reduced, resulting in a blue-shift of the resonance wavelength. Although these devices were very similar in concept, the mechanical design of the MEMS structures showed striking diversity. The tunable VCSEL demonstrated by Wu et al. of the Chang-Hasnain group [23] consisted of a suspended cantilever (Fig. 1.1), while the devices developed by Larson et al. of the Harris group [24] was a four-leg membrane design (Fig. 1.2). Using these devices, extensive optical and mechanical modeling, as well as investigations into potential

applications of tunable VCSELs was completed; thus, the groundwork was laid for future generations of tunable vertical-cavity devices.

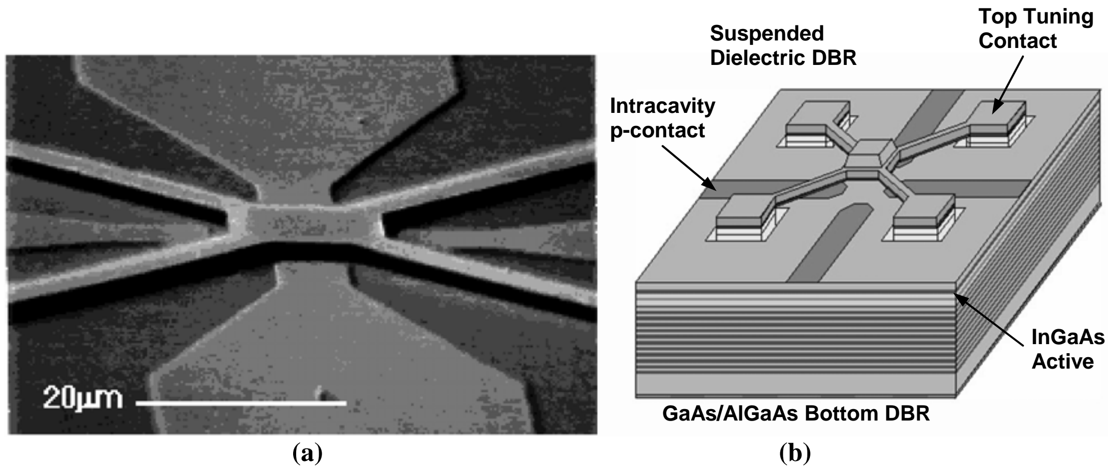

Fig. 1.2: (a) Scanning electron micrograph and (b) three-dimensional schematic of the deformable membrane tunable VCSEL developed by M. C. Larson of the Harris group at Stanford University [24].

Work on MEMS-tunable VCSELs continues after more than a decade of development. Noteworthy results include electrically pumped long-wavelength cantielever-tunable VCSELs produced commercially by Bandwidth9. These structures utilize an InP-based active region, a metamorphic GaAs/AlGaAs tunable top mirror, and a metamorphic GaAs-based tunnel junction for current and optical confinement [31]. Further milestones involve the realization of >30-nm continuous single-mode wavelength tuning in state-of-the-art long-wavelength MEMS-tunable VCSELs, including the optically pumped half-symmetric tunable VCSEL developed by Tayebati et al. [32]. Future generations of the half-symmetric devices have shown the best performance parameters for tunable VCSELs to date: fiber coupled output

powers in excess of 20 mW over a tuning range of 27 nm [33] and roughly 10 mW of output over an extended tuning range of 65 nm [34]. More recently Syrbu et al. has demonstrated a double-bonded structure combining an AlInGaAs/InP active region with GaAs/AlGaAs mirrors. These devices are also optically pumped with a 980-nm laser and have achieved continuous wavelength tuning over 32 nm (with a maximum tuning bias of 4 V) and a peak output power of 2 mW [35]. A European consortium under the TUNVIC program has demonstrated a “two-chip” tunable VCSEL by using an InP half-VCSEL, containing the bottom InP-based DBR, active region, and BTJ structure, with a GaAs-based electrothermally actuated MEMS tuning element. In this structure, the micromechanical tuning element is flip-chip bonded to a submount containing the half-VCSEL [36]. These devices have demonstrated tuning ranges of 40 nm with a peak output power of 100 μW [37].

The main focus of this dissertation is to build upon previous work focusing on fixed-wavelength VCSOAs and MEMS-tunable VCSELs in order to demonstrate not only the first, but also high performance widely tunable VCSOAs. In the same way that MEMS-tunable VCSELs have added wavelength flexibility to fixed-wavelength surface-emitting lasers, by incorporating wavelength tunability into a VCSOA it is possible to produce wavelength agile amplifying filters for use in reconfigurable and multi-channel optical networks. By integrating a micromechanical tuning element with a VCSOA (Fig. 1.3), similar to the tunable VCSELs described previously, it is possible to selectively amplify signals faster, more efficiently, and over a wider wavelength range when compared to temperature tuned fixed-wavelength devices.

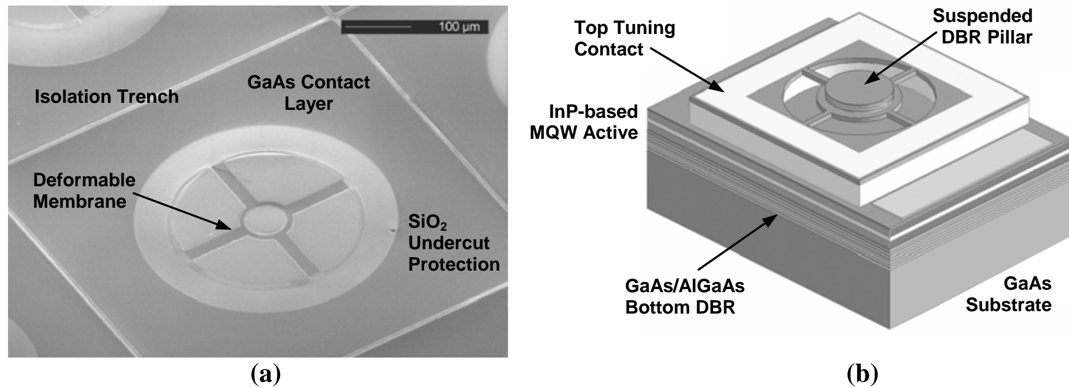

Fig. 1.3: (a) Micrograph (lacking top contact) and (b) three-dimensional schematic of the MT-VCSOA. The device utilizes an integrated electrostatic actuator to vary the effective cavity length.

As can be seen in the figure, the tunable VCSOA structure utilizes a four-leg suspension design similar to the widely tunable vertical-cavity devices developed previously [24]–[26], [28], [36]. This design was chosen for its inherent stability as compared to a cantilever structure, which has recently been shown to be susceptible to strain relaxation effects and external vibration, leading to an inherent lack of wavelength stability [38]. Furthermore, by separately defining the DBR pillar and suspensions in this structure, as shown in Fig. 1.3, it is possible to simultaneously optimize the effective reflectance of the tunable mirror structure and the compliance of the micromechanical actuator [39]. Although electrothermal actuation has been shown to be an effective means of achieving actuation in this structure [36], electrostatic operation is chosen for the MT-VCSOA due to its excellent temporal response and reduced power consumption.

1.3 Scope of this Dissertation

The research outlined in this dissertation represents the first demonstration of a micromechanically-tunable VCSOA. The development of MT-VCSOAs outlined in this dissertation is based largely upon research thrusts at outside institutions focused on the development of MEMS-tunable vertical-cavity devices including tunable filters, RCLEDs, detectors, modulators, and VCSELs as referenced previously. More importantly, however, this work can be seen as an extension of the rather rigorous investigation of fixed-wavelength VCSOAs completed by E. S. Björlin [40]. Due to the similarity between tunable VCSOAs and other MEMS-tunable vertical-cavity devices, the theoretical design and device fabrication presented in this dissertation can be transferred to future micromechanicall-tunable vertical-cavity device research.

The following chapters cover nearly all aspects of MT-VCSOAs, including the device design, fabrication, characterization and analysis. In total, three generations of devices have been demonstrated. Subsequent iterations of MT-VCSOAs were developed in order to refine the properties of previous devices; after identifying the major limitations in each design, the necessary changes were made in order to realize improved characteristics such as a lower required tuning voltage, improved reliability, and a wider effective tuning range. Subsequent revisions culminated in the final generation of devices exhibiting the best performance to date.

Chapter 2 introduces the design of MT-VCSOAs, including the general design principles, modes of operation, and the necessary theoretical framework behind both

the vertical-cavity amplifier and the MEMS electrostatic actuator. Here, a general FP model is used to analyze both the tuning and signal gain properties, while the saturation and noise characteristics are illustrated with the amplifier rate equations. Finally, the basic properties of the electrostatic actuator and the mechanical properties of the MEMS element are covered, including both the static and dynamic response of the system.

Chapter 3 illustrates the general fabrication process required for the three generations of MT-VCSOAs. The basic fabrication methods employed for these devices include a combination of GaAs to InP direct wafer bonding and GaAs/AlGaAs micromachining. The chapter begins with a brief review of MEMS in GaAs. Following this, compound semiconductor direct wafer bonding is described, including the motivation behind the use of this technique, as well as a brief review of the past work in this area. A specific description is given of the GaAs to InP direct wafer bonding procedure used in this dissertation. With the wafer bonding process established, the general fabrication procedure for the three generations of MT-VCSOAs is described. Specific details of the process changes made in succeeding generations of devices are clarified in the following chapters.

Chapter 4 outlines the first generation of MT-VCSOAs—notable as the initial demonstration of widely tunable VCSOAs. These devices are optically pumped gain-guided structures, operate in reflection mode, and incorporate a variable thickness air gap (as well as an integrated electrostatic actuator) for wavelength tuning. This chapter covers the materials structure and testing procedure for the top emitting devices, which is relevant for both Generations 1 and 2. The best peak gain

performance for the initial demonstration devices is a minimum of 10 dB on-chip gain (3 dB fiber-to-fiber) over 11 nm of tuning, with a peak amplifier gain of 17 dB at 1570 nm. Limitations of these devices include excessively high tuning voltage requirements (~60 V) and poor reliability arising from oxidation of the exposed sacrificial material. Regardless of the initial shortcomings, these structures represent the first demonstration of a tunable VCSOA and provide the groundwork for the following generations of devices.

Chapter 5 analyzes the second generation of MT-VCSOAs. The focus of these devices is to create a revised mechanical structure in order to overcome the limitations of the initial tunable VCSOAs. For the second generation, changes to the device design consist of improvements in the mechanical design of the actuator. Utilizing the revised mechanical structure, the total amplified spontaneous emission (ASE) wavelength tuning range is extended to greater than 50 nm, while the required tuning voltages are reduced to below 30 V. The revised design also exhibits improved stability, allowing for an in-depth examination of the dynamic properties of the electrostatic actuator. Results are presented for the actuation response both in vacuum and at atmosphere. Natural frequency values range from 117–209 kHz depending on the geometry of the structure. In air, the devices exhibit a nearly critically damped response with a settling time of less than 10 μs. Although these devices are capable of rather larger ASE wavelength shifts, the effective tuning range is limited to roughly 10 nm. In order to investigate potential improvements, a thorough investigation of alternative cavity designs is presented; this includes both experimental and theoretical investigations of the wavelength tuning response, peak

signal gain, saturation properties, and noise figure of MT-VCSOAs for various optical cavity designs and modes of operation.

Chapter 6 presents the characteristics of the final generation of tunable VCSOAs. Building upon the previous generations of devices, the third generation of MT-VCSOAs incorporates an improved optical cavity structure. These devices utilize a bottom-emitting configuration in which the optical cavity is inverted and the MEMS-tuning structure serves as the high-reflectivity back mirror. By suppressing the variation in mirror reflectance with tuning, this configuration exhibits a two-fold increase in the effective tuning range—with a minimum of 5 dB fiber-to-fiber gain (12 dB on-chip gain) over a wavelength span of 21 nm, from 1557.4 nm to 1536.4 nm. Additionally, these devices exhibit saturation, bandwidth, and noise figure properties similar to state-of-the-art fixed-wavelength VCSOAs, including a maximum fiber-coupled saturation output power of -1.4 dBm, an average gain bandwidth of 65.2 GHz, and an average fiber-coupled noise figure of 7.5 dB over the 21-nm tuning range. Through improvements to the electrostatic actuator, the maximum required tuning voltage has been reduced to 10.5 V, a five-fold reduction compared with the first generation of MT-VCSOAs.

Chapter 7 provides a summary and also presents potential future directions of this work. This final chapter reviews the progress made during the course of this dissertation and highlights the major contributions of this research. Future device possibilities aimed at continued device development are proposed, including the development of transmission mode devices, extended cavity tuning structures,

simplified processing procedures, and finally, electrically pumped long-wavelength VCSOAs, both fixed wavelength and tunable.

References

[1] E. S. Björlin, T. Kimura, J. E. Bowers, "Carrier-confined vertical-cavity semiconductor optical amplifiers for higher gain and efficiency," *IEEE J. Select. Topics Quantum Electron.*, vol. 9, pp. 1374–1385, Sep. 2003.

[2] N. Suzuki, M. Ohashi, M. Nakamura, "A proposed vertical-cavity optical repeater for optical inter-board connections," *IEEE Photon. Technol. Lett.*, vol. 9, pp. 1149–1151, Aug. 1997.

[3] M. J. Coupland, K. G. Hambleton, C. Hilsum, "Measurement of amplification in a GaAs injection laser," *Phys. Lett.*, vol. 7, pp. 231–232, Dec. 1963.

[4] F. Koyama, S. Kubota, K. Iga, "GaAlAs/GaAs active filter based on vertical-cavity surface emitting laser," *Electron. Lett.*, vol. 27, pp. 1093-1095, Jun. 1991.

[5] H. Soda, K. Iga, C. Kitahara, Y. Suematsu, "GaInAsP/InP surface emitting injection lasers," *Jpn. J. Appl. Phys.*, vol. 18, pp. 2329, Dec. 1979.

[6] R. Raj, J. A. Levenson, J. L. Oudar, M. Bensoussan, "Vertical microcavity optical amplifying switch," *Electron Lett.*, vol. 29, pp. 167–169, Jan. 1993.

[7] R. Raj, J. L. Oudar, M. Bensoussan, "Vertical cavity amplifying photonic switch," *Appl. Phys. Lett.*, vol. 65, pp. 2359–2361, Oct. 1994.

[8] N. Bouché, B. Corbett, R. Kuszelewicz, R. Raj, "Vertical-cavity Amplifying Photonic Switch at 1.5 µm", *IEEE Photon. Technol. Lett.*, vol. 8, pp. 1035–1037, Aug. 1996.

[9] D. Wiedenmann, B. Moeller, R. Michalzik, K. J. Ebeling, "Performance characteristics of vertical-cavity semiconductor optical amplifiers," *Electron. Lett.*, vol. 32, pp. 342–343, Feb. 1996.

[10] D. Wiedenmann, C. Jung, M. Grabherr, R. Jäger, U. Martin, R. Michalzik, K. J. Ebeling, "Oxide-confined vertical-cavity semiconductor optical amplifier for 980 nm wavelength", in *CLEO 98 Technical Digest*, Paper CThM5, pp. 378, 1998.

[11] R. Lewén, K. Streubel, A. Karlsson, S. Rapp, “Experimental demonstration of a multifunctional long-wavelength vertical-cavity laser amplifier-detector”, *IEEE Photon. Technol. Lett.*, vol. 10, pp. 1067–1069, Aug. 1998.

[12] S. Calvez, A. H. Clark, J.-M. Hopkins, R. Macaluso, P. Merlin, H. D. Sun, M. D. Dawson, T. Jouhti, M. Pessa, “1.3 µm GaInNAs optically-pumped vertical cavity semiconductor optical amplifier,” *Electron. Lett.*, vol. 39, pp. 100–102, Jan. 2003.

[13] N. Laurand, S. Calvez, M. D. Dawson, A. C. Bryce, T. Jouhti, J. Konttinen, M. Pessa, “Performance comparison of GaInNAs vertical-cavity semiconductor optical amplifiers,” *IEEE J. Quantum Electron.*, vol. 41, pp. 642–649, May 2005.

[14] E. S. Björlin, B. Riou, A. Keating, P. Abraham, Y.-J. Chiu, J. Piprek, J. E. Bowers, “1.3-µm vertical-cavity amplifier,” *IEEE Photon. Technol. Lett.*, vol. 12, pp. 951–953, Aug. 2000.

[15] E. S. Björlin, B. Riou, P. Abraham, J. Piprek, Y.-J. Chiu, K. A. Black, A. Keating, J. E. Bowers, “Long-wavelength vertical-cavity semiconductor optical amplifiers”, *IEEE J. Quantum Electron.*, vol. 37, pp. 274–281, Feb. 2001.

[16] E. S. Björlin, J. E. Bowers, “Noise figure of vertical-cavity semiconductor optical amplifiers,” *IEEE J. Quantum Electron.*, vol. 38, pp. 61–66, Jan. 2002.

[17] J. Piprek, S. Björlin, J. E. Bowers, “Design and analysis of vertical-cavity semiconductor optical amplifiers,” *IEEE J. Quantum Electron.*, vol. 37, 127–134, Jan. 2001.

[18] J. Piprek, E. S. Björlin, J. E. Bowers, “Optical gain-bandwidth product of vertical-cavity laser amplifiers,” *Electron. Lett.*, vol. 37, pp. 298–299, Mar. 2001.

[19] E. S. Björlin, J. Geske, J. E. Bowers, “Optically preamplified receiver at 10 Gbit/s using vertical-cavity SOA,” *Electron. Lett.*, vol. 37, pp. 1474–1475, Nov. 2001.

[20] E. S. Björlin, T. Kimura, Q. Chen, C. Wang, J. E. Bowers, “High output power 1540nm vertical cavity semiconductor optical amplifiers,” *Electron. Lett.*, vol. 40, pp. 121–123, Jan. 2004.

[21] T. Kimura, E. S. Björlin, H.-F. Chou, Q. Chen, S. Wu, J. E. Bowers, "Optically preamplified receiver at 10, 20, and 40 Gb/s using a 1550-nm vertical-cavity SOA," *IEEE Photon. Technol. Lett.*, vol. 17, pp. 456–458, Feb. 2005.

[22] T. Kimura, E. S. Björlin, J. Piprek, J. E. Bowers, "High-temperature characteristics and tunability of long-wavelength vertical-cavity semiconductor optical amplifiers," *IEEE Photon. Technol. Lett.*, vol. 15, pp. 1501–1503, Nov. 2003.

[23] M. S. Wu, E. C. Vail, G. S. Li, W. Yuen, C. J. Chang-Hasnain, "Tunable micromachined vertical cavity surface emitting laser," *Electron. Lett.*, vol. 31, pp. 1671–1672, Sep. 1995.

[24] M. C. Larson, A. R. Massengale, J. S. Harris Jr., "Continuously tunable micromachined vertical-cavity surface-emitting laser with 18 nm wavelength range," Electron. Lett., vol. 32, pp. 330–332, Feb. 1996.

[25] P. Tayebati, P. D. Wang, D. Vakhshoori, C. C. Lu, M. Azimi, R. N. Sacks, "Half symmetric cavity tunable microelectromechanical VCSEL with single spatial mode," *IEEE Photon. Technol. Lett.*, vol. 10, pp. 1679–1681, Dec. 1998.

[26] G. L. Christensen, A. T. T. D. Tran, Z. H. Zhu, Y. H. Lo, M. Hong, J. P. Mannaerts, R. Bhat, "Long-wavelength resonant vertical-cavity LED/photodetector with a 75-nm tuning range," *IEEE Photon. Technol. Lett.*, vol. 9, pp. 725–727, Jun. 1997.

[27] W. S. Rabinovich, T. H. Stievater, N. A. Papanicolaou, D. S. Katzer, P. G. Goetz, "Demonstration of a microelectromechanical tunable asymmetric Fabry–Pérot quantum well modulator," *Appl. Phys. Lett.*, vol. 83, pp. 1923–1925, Sep. 2003.

[28] J. Daleiden, N. Chitica, M. Strassner, A. Spisser, J. L. Leclercq, P. Viktorovitch, D. Rondi, E. Goutain, J. Peerlings, J. Pfeiffer, R. Reimenschneider, K. Hjort, "Tunable InP/air gap Fabry Perot filter for wavelength division multiplex fiber optical transmission," in *Proc. 11th Int. Conf. InP and Related Materials*, May 16–20, 1999, pp. 285–287.

[29] L. A. Coldren and S. W. Corzine, *Diode Lasers and Photonic Integrated Circuits*, New York, NY: Wiley, 1995.

[30] N. Yokouchi, T. Miyamoto, T. Uchida, Y. Inaba, F. Koyama, K. Iga, "40 Å continuous tuning of GaInAsP/InP vertical-cavity surface-emitting laser using an external cavity mirror," *IEEE Photon. Technol. Lett.*, vol. 4, pp. 701–703, Jul. 1992.

[31] P. Kner, T. Kageyama, J. Boucart, R. Stone, D. Sun, R. F. Nabiev, R. Pathack W. Yuen, "A long-wavelength MEMS tunable VCSEL incorporating a tunnel junction", *IEEE Photon. Tech. Lett.*, vol. 15, pp. 1183 – 1185, Sep. 2003.

[32] P. Tayebati, P. Wang, D. Vakhshoori, C.-C. Lu, M. Azimi, R. N. Sacks, "Half-symmetric cavity tunable microelectromechanical VCSEL with single spatial mode," *IEEE Photon. Tech. Lett.*, vol. 10, pp. 1679 – 1681, Dec. 1998.

[33] K. J. Knopp, D. Vakhshoori, P. D. Wang, M. Azimi, M. Jiang, P. Chen, Y. Matsui, K. McCallion, A. Baliga, F. Sakhitab, M. Letsch, B. Johnson, R. Huang, A. Jean, B. DeLargy, C. Pinzone, F. Fan, J. Liu, C. Lu, J. Zhou, H. Zhu, R. Gurjar, P. Tayebati, D. MacDaniel, R. Baorui, R. Waterson, G. VanderRhodes, "High power MEMs-tunable vertical-cavity surface-emitting lasers," in *Digest LEOS Summer Topical Meetings 2001, Advanced Semiconductor Lasers and Applications*, 30 Jul.–1 Aug. 2001 pp. 31–32.

[34] Y. Matsui, D. Vakhshoori, P. Wang; P. Chen, C.-C. Lu; M. Jiang, K. Knopp, S. Burroughs, P. Tayebati, "Complete polarization mode control of long-wavelength tunable vertical-cavity surface-emitting lasers over 65-nm tuning, up to 14-mW output power," *IEEE J. Quantum Electron.*, vol. 39, pp. 1037–1048, Sep. 2003.

[35] A. Syrbu, V. Iakovlev, G. Suruceanu, A. Caliman, A. Rudra, A. Mircea, A. Mereuta, S. Tadeoni, C.-A. Berseth, M. Achtenhagen, J. Boucart, E. Kapon, "1.55-μm optically pumped wafer-fused tunable VCSELs with 32-nm tuning range," *IEEE Photon. Technol. Lett.*, vol. 16, pp. 1991–1993, Sep. 2004.

[36] F. Riemenschneider, H. Halbritter, P. Meissner, M. Maute, M. C. Amann, M. Ortsiefer, R. Shau, R.; "A new concept for micro-mechanically tunable long wavelength VCSELs," in *Proc. 2004 Conf. on Lasers and Electro-Optics (CLEO)*, vol. 1, 16–21 May 2004.

[37] F. Riemenschneider, M. Maute, H. Halbritter, G. Bohm, M.-C. Amann, P. Meissner, "Continuously tunable long-wavelength MEMS-VCSEL with over 40-nm tuning range," *IEEE Photon. Technol. Lett.*, vol. 16, pp. 2212–2214, Oct. 2004.

[38] S. Decai, W. Fan, P. Kner, J. Boucart, T. Kageyama, Z. Dongxu, R. Pathak, R. F. Nabiev, W. Yuen, "Long wavelength-tunable VCSELs with optimized MEMS bridge tuning structure," *IEEE Photon. Tech. Lett.*, vol. 16, pp. 714–716, Mar. 2004.

[39] F. Sugihwo, M. Larson, J. S. Harris, Jr., "Simultaneous optimization of membrane reflectance and tuning voltage for tunable vertical cavity lasers," *Appl. Phys. Lett.*, vol 72, pp. 10–12, Jan. 1998.

[40] E. S. Björlin, "Long-wavelength vertical-cavity semiconductor optical amplifiers," Ph.D. dissertation, UCSB, Santa Barbara, CA, 2002.

CHAPTER 2

Device Design

The development of VCSOAs has benefited greatly from previous research on vertical-cavity lasers. Generally theoretical models, materials, and processing technologies developed for VCSELs can be directly applied to VCSOAs. Because VCSOAs are optimized to operate as resonant optical amplifiers, the theoretical framework of these devices also includes the extensive body of knowledge developed for in-plane FP-SOAs. Extending this theory to describe tunable VCSOAs requires the incorporation of the theoretical models developed for FP-based MEMS-tunable vertical-cavity devices.

The work presented in this chapter was fortunate to build upon a rather solid foundation of fixed-wavelength VCSOA research at UCSB, most notably the seminal work of E. S. Björlin [1]. Further contributions in this area include the theoretical analyses of P. Royo [2] and J. Piprek [3]. The models developed to describe the MEMS-based tuning mechanism leverage the pioneering work on deformable-membrane tunable vertical-cavity devices conducted by M. C. Larson of Stanford University [4]. The MT-VCSOAs developed at UCSB represent the first demonstration of widely tunable VCSOAs, and as such these devices allow further

exploration of the design space of micromechanically tunable vertical-cavity devices. Due to the unique requirements of VCSOAs (e.g. lower mirror reflectivities) these devices help to shed light on some of the fundamental limitations of coupled-cavity tuning structures.

In this chapter, I will review the theoretical underpinnings of both fixed-wavelength and tunable VCSOAs. The chapter begins with a brief description of the MT-VCSOA structure and principle of operation. In section 2.2 the basic design issues and theoretical models of fixed-wavelength VCSOAs are covered. Using a general FP model, the tuning response and the signal gain properties of MT-VCSOAs are analyzed. The saturation and noise characteristics of these unique devices may be illustrated with the amplifier rate equations. In Section 2.3 an overview of the various cavity designs available for MEMS-tunable vertical-cavity amplifiers is presented, along with the corresponding wavelength tuning response. These models are extended to incorporate the peak signal gain response of MT-VCSOAs in Section 2.4. Finally, a brief description of electrostatic actuation and the basic mechanical properties of the MEMS transducer are covered in Section 2.5, along with the response of the actuator to both static and dynamic forcing functions.

2.1 Tunable VCSOA Principle of Operation

A schematic of the basic structure of an MT-VCSOA is shown in Fig. 2.1. This device consists of a fixed bottom mirror, a semiconductor cavity containing the active material, an adjustable air gap for cavity length variation, and a suspended top

mirror. Here, the bottom mirror and active region are functionally identical to that of fixed-wavelength VCSOAs. The top DBR consists of a rigid central reflector suspended by four flexible legs, creating the deformable membrane structure. In these devices, the FP cavity length is controlled by an integrated electrostatic actuator. Using this design, a suitable applied bias results in a vertical displacement of the suspended DBR toward the substrate, reducing the effective cavity length and blue-shifting the resonant wavelength of the VCSOA. Similar to a standard fixed-wavelength VCSOA, light is coupled in and out of the device vertically, either through the top mirror or the substrate, depending on which mirror is made transmissive at the operating wavelength.

In an ideal wavelength-tunable VCSOA, the tuning mechanism should be transparent to the operation of the device, resulting in constant amplifier properties over the achievable wavelength span. This would include the peak gain, bandwidth, saturation, and noise figure of the VCSOA. In these devices, the peak gain envelope should ideally be as wide as possible—similar to traveling wave in-plane SOAs—where the gain bandwidth is limited by the gain spectrum of the material. With MT-VCSOAs, this requires wide bandwidth DBRs (with reflectivity and phase properties independent of the tuning mechanism), no additional loss with tuning (due to changes in gain enhancement, average cavity loss, etc.), a wide material gain spectrum, and a large free spectral range for continuous single-mode tuning. This dissertation strives to understand the limitations of the fabricated devices when compared with this idealized structure.

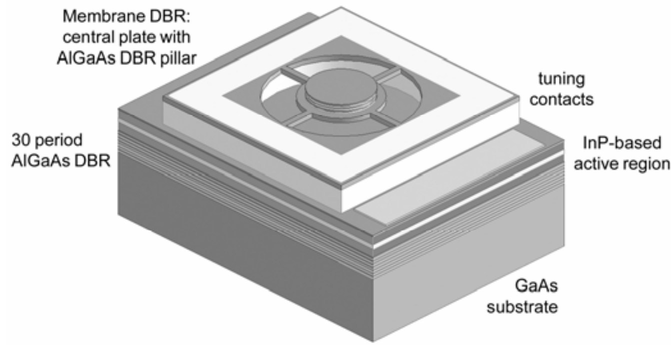

Fig. 2.1: Three-dimensional schematic of the MT-VCSOA, highlighting the four-leg design of the suspended DBR structure. With an applied voltage, the membrane DBR is attracted towards the substrate, reducing the air-gap thickness, and resulting in a blue shift of the VCSOA cavity mode.

2.2 Fixed-Wavelength VCSOA Theoretical Model

The first theoretical predictions of VCSOA performance were presented by Tombling et al. in 1994 [5]. The model presented in this article is largely based on in-plane FP-SOA work by Mukai et al. [6]. Following the initial predictions on device performance, a number of authors investigated both general FP and rate equation approaches to model VCSOAs [7], [8], [3]. In these early theoretical papers, the results obtained using the rate equation analysis and the FP approach did not agree. This disagreement was caused by the omission of interference between the fields that traverse the input mirror in both directions, resulting in an incorrect expression for the mirror loss in the photon rate equation. The discrepancy was resolved in 2002 by Royo et al. who showed that the mirror loss depends on the gain in the amplifier and derived a corrected mirror loss expression [9]. A further contribution to VCSOA theory, and a key contribution to this thesis, was the

extensive theoretical and experimental research into long-wavelength VCSOAs completed by E. S. Björlin [10]. The models presented in this chapter are largely based on the work discussed above.

2.2.1 General Design Principles

As with VCSELs and in-plane laser diodes, the vertical-cavity geometry of VCSOAs gives rise to major differences in amplifier properties when compared with in-plane FP-SOAs. The relatively short cavity length, which lies perpendicular to the plane of the wafer surface, results in a small mode volume and a circular symmetric mode. In addition, the optical field passes perpendicularly through the material layers, greatly reducing the active material length that the optical mode overlaps with, resulting in a large reduction in the achievable single-pass gain. For in-plane SOAs, the active material length may be on the order of hundreds of micrometers, whereas in a VCSOA, the combined thickness of the MQW layers may be on the order of tens or hundreds of nanometers. The corresponding reduction in single-pass gain requires an increase in feedback necessary to achieve a desired gain level. As with VCSELs, this feedback is achieved by incorporating highly reflective DBRs to create an FP optical cavity. The resulting feedback from the resonant cavity structure constricts the gain bandwidth to the linewidth of the FP mode, which is typically on the order of a nanometer or less.

The basic structure of a VCSOA consists of an active region enclosed by two mirrors. The device can be optimized for operation in either reflection mode or

transmission mode, as shown schematically in Fig. 2.2. In reflection mode, the VCSOA is designed to have one highly reflective mirror (~100%), and the signal enters and exits from the same side of the device through a slightly transmissive mirror. In transmission mode operation, both mirrors are slightly transmissive and the signal is injected on one side of the device and collected on the other.

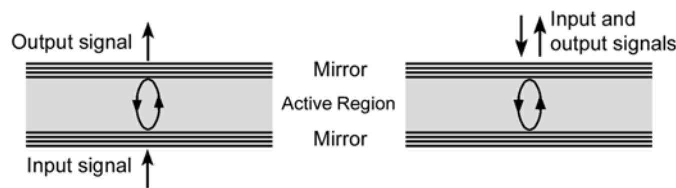

Fig. 2.2: Schematic of the operating modes of VCSOAs, including transmission mode (left) and reflection mode (right).

Using reflection mode operation, it is typically easier to achieve good amplifier characteristics. In this configuration, the combined mirror loss is generally lower when compared with transmission mode operation, so a high signal gain can be achieved for a lower single-pass gain. Furthermore, reflection mode operation may prove to be a more cost effective approach as the fiber alignment, which is a very difficult and costly step in manufacturing, is reduced from two fibers to one. However, the input and output signals must be separated in this mode of operation, requiring an additional component—either a coupler or circulator—which adds complexity, cost, and additional signal loss. Operation in transmission mode is more attractive in certain applications, e.g. integration with detectors for preamplification or array applications; it is, however, a more difficult approach as far as testing and

packaging is concerned. The choice of the mode of operation, either reflection mode or transmission mode, will ultimately depend on the intended application.

The most significant difference when comparing VCSOAs and VCSELs lies in the reduced mirror reflectivities used in the resonant cavity structure, as well as the increased number of quantum wells (QWs) necessary to achieve a high single-pass gain. In order to minimize the required threshold current in VCSELs, strong feedback is necessary. With VCSOAs, on the other hand, reduced feedback is advantageous in order to enable high gain without the onset of lasing. VCSOAs therefore require higher single-pass gain—more QWs—in order to make up for the increased mirror loss. Low mirror reflectance allows for operation at higher carrier density and thus higher single-pass gain, resulting in a wider gain bandwidth, higher saturation power, and a reduced noise figure [1], [3], [5]. It is important to recognize that there is a limit to the lowest mirror reflectance that may be used; if the reflectance is too low, the mirror losses will result in insufficient signal gain. With VCOSAs there exists an optimum design with an intermediate reflectance that allows for operation at high carrier density, while at the same time avoiding exceeding lasing threshold. Typical power reflectance values of the transmissive mirror used in reflection mode long-wavelength VCSOAs range from approximately 0.96 to 0.90 [10].

Another important difference between VCSELs and VCSOAs is the number of active material layers used in the device. The need for increased single-pass gain requires the incorporation of a large number of QWs in the FP resonant cavity. With VCSOAs a stacked multi-quantum well (MQW) active region is used to increase the

total active material length in the inherently short optical cavity. The large number of QWs typically used in VCSOAs—typically greater than 20 total wells [10]—makes it difficult to achieve uniform carrier distribution throughout the QWs using electrical injection. In order to generate a uniform carrier distribution in the active region, optical pumping is typically used. Compared with electrical injection, optical pumping is an attractive carrier generation technique for VCSOAs. Using this approach carriers may be generated directly in the QWs, without the need of transporting charge through the structure. This results in very uniform carrier distribution throughout a large number of QWs. Optical pumping also allows the entire structure to be undoped, which simplifies growth and processing, and minimizes optical losses. Furthermore, optical pumping allows for the generation of a uniform carrier distribution across a laterally large active region. Several high-performance long wavelength VCSELs have been presented that use optical pumping [11], [12]. To maintain a small footprint, the device and pump laser can be situated in the same package, or even integrated on the same wafer [11].

2.2.2 Signal Gain and Gain Bandwidth

A convenient approach for modeling VCSOAs is to replace the DBRs by hard mirrors of the same reflectance and use an effective cavity length, which includes the penetration of the optical field into the DBRs [13]. With this method it is possible to utilize the well-known FP relationships to describe both the amplifier and wavelength tuning characteristics of the MT-VCSOA. Because the FP equations

contain only a small number of unknowns, it is possible to generate a relatively general description of the device properties. The FP approach is carried out by considering an incoming optical field and summing all of the field components exiting the cavity. To obtain the power gain, the fields are squared and the total output power is divided by the input power. Using this technique, it is possible to model the gain spectrum of a VCSOA for both reflection mode (G_r) and transmission mode (G_t) operation [14]:

$$G_r = \frac{(\sqrt{R_t} - \sqrt{R_b} g_s)^2 + 4\sqrt{R_t R_b} g_s \sin^2 \phi_s}{(1 - \sqrt{R_t R_b} g_s)^2 + 4\sqrt{R_t R_b} g_s \sin^2 \phi_s} \qquad (2.1)$$

$$G_t = \frac{(1 - R_t)(1 - R_b) g_s}{(1 - \sqrt{R_t R_b} g_s)^2 + 4\sqrt{R_t R_b} g_s \sin^2 \phi_s} \qquad (2.2)$$

$$\phi_s = 2\pi\, n_c L_c \left(\frac{1}{\lambda} - \frac{1}{\lambda_R} \right) \qquad (2.3)$$

where R_t is the top mirror reflectance, R_b is the bottom mirror reflectance, g_s is the single-pass gain, and ϕ_s is the single-pass phase detuning. The phase in Eq. 2.3 gives the deviation of the signal wavelength λ from the resonant wavelength of the cavity λ_R, with the effective index of the optical cavity n_c and the total cavity length L_c. When the signal wavelength is identical to the FP resonance, $\phi_s = 0$ in Eq. 2.3, and Eqs. 2.1 and 2.2 can be used to calculate the peak gain. It is important to note that the amplifier must operate under the condition of $g_s^2 R_t R_b < 1$ to avoid reaching lasing threshold.

From Eqs. 2.1 and 2.2, expressions for calculating the gain bandwidth are readily obtained. The gain bandwidth, or full width at half maximum (FWHM) of the gain spectrum, for each mode of operation is given by:

$$\Delta f_r = \frac{c}{\pi n_c L_c} \cdot \arcsin\left[4\sqrt{R_t R_b} g_s \left(\frac{1}{(1-\sqrt{R_t R_b} g_s)^2} - \frac{2}{(\sqrt{R_t} - \sqrt{R_b})^2} \right) \right]^{-1/2} \quad (2.4)$$

$$\Delta f_t = \frac{c}{\pi n_c L_c} \cdot \arcsin\left[\frac{(1-\sqrt{R_t R_b} g_s)^2}{4\sqrt{R_t R_b} g_s} \right]^{1/2} \quad (2.5)$$

where c is the velocity of light in vacuum. Assuming uniform active material over the extent of the signal spot size, the single-pass gain of the VCSOA is calculated using:

$$g_s = \exp[\xi g L_a - \alpha_i L_c] \quad (2.6)$$

with the combined thickness of the QWs L_a, the average cavity loss α_i, the total cavity length L_c—including the penetration depth into the mirrors, and the gain enhancement factor ξ. With vertical-cavity devices, standing wave effects must be considered. In this case gain enhancement results from the placement of the active material layers at the peaks of the optical standing wave and ξ is given by [15]:

$$\xi = 1 + \cos 2\beta z_s \frac{\sin \beta L_{MQW}}{\beta L_{MQW}} \quad (2.7)$$

where L_{MQW} is the thickness of the each MQW stack, $\beta = 2\pi n_c/\lambda$, n_c is the effective index of the semiconductor cavity, and z_s is the spatial separation between the standing wave peak and the center of the MQW stack. This form of ξ is useful for

determining the change in gain enhancement that occurs with wavelength tuning. The gain enhancement factor can be 2 for very small values of L_{MQW} and quickly converges to a value of 1 for QWs distributed over a section longer than a wavelength. In practice ξ is usually less than 2 due to the finite thickness of the gain region. The quantum well material gain g, as a function of carrier density N, is approximated using a three-parameter model [16]:

$$g = g_o \ln\left[\frac{N + N_s}{N_{tr} + N_s}\right] \qquad (2.8)$$

with the transparency carrier density N_{tr}, and fitting parameters g_o and N_s. This model allows for an accurate description of the material gain at low carrier densities; however, for very high carrier densities, the logarithmic gain model may be limited, as it does not predict saturation of the material gain.

2.2.3 Saturation and Noise Figure

At high input signal powers, or at operation near threshold, the large photon density present in the resonant cavity will lead to carrier depletion and saturation of the gain medium. A common approach to modeling the saturation properties of VCSOAs involves the use of steady-state rate equations for carriers and photons [1], [3], [5]. Compared with the well-known relationships used to analyze lasers, the rate equations for FP amplifiers include an additional term for the input signal and a modified mirror loss term. The rate equations for carriers N, and photons S, then take the following form:

$$\frac{dN}{dt} = G_{gen} - \xi v_g g S - \left(AN + BN^2 + CN^3\right) \qquad (2.9)$$

$$\frac{dS}{dt} = \frac{\eta_s P_s}{h\upsilon_s A_s L_c} + \beta_{sp} \Gamma B N^2 + \xi \Gamma v_g g S - \left(\alpha_i + \alpha_m\right) v_g S \,. \qquad (2.10)$$

The first term on the right hand side of Eq. 2.9, G_{gen}, is a carrier generation term that depends on whether optical, or electrical pumping is used. For optically pumped devices such as those presented here, $G_{gen} = \eta_p P_p / h\upsilon_p V_p$ with the pump efficiency η_p, the pump power P_p, the energy of the pump photons $h\upsilon_p$, and the pumped volume $V_p = L_a A_p$ (A_p is the area of the pump spot). The second term describes stimulated emission and includes the group velocity v_g. The final term constitutes all recombination parameters that do not contribute to amplification of the input signal: AN describes defect recombination, BN^2 is spontaneous emission, and CN^3 is Auger recombination.

The second rate equation summarizes the physical mechanisms that affect the average photon density S. The first term on the right hand side of Eq. 2.10 describes the increase in photon density resulting from the injected signal of power P_s, and energy $h\upsilon_s$. The signal coupling efficiency η_s and the signal spot size A_s complete the first term. The next two terms represent the generation of photons through spontaneous and stimulated emission, respectively. The coefficient β_{sp} describes the fraction of spontaneously emitted photons coupled into the signal mode, with the fill factor $\Gamma = L_a/L_c$. The final term in Eq. 2.10 describes photon loss, due to both cavity

and mirror losses. For VCSOAs α_m is described by a modified mirror loss expression that is a function of the mirror reflectance and the amplifier gain [9]:

$$\alpha_m = \frac{1}{L_c}\left(\frac{G_r + G_t}{G_r + G_t - 1}\right)\ln g_s \,. \qquad (2.11)$$

Using the procedure outlined in [3], the steady-state forms of Eqs. 2.9 and 2.10 may be used to determine the saturation characteristics of the MT-VCSOA.

The noise figure (NF) of an optical amplifier describes the signal-to-noise ratio (SNR) degradation that occurs as a signal passes through the device. In general, the amplification of an optical signal adds undesired power fluctuations due to the inherent randomness of the optical processes involved. With a VCSOA, the dominant noise component at high signal powers is signal-spontaneous beat noise [1], [5]. The noise factor F, defined as the input SNR over output SNR, is given by:

$$F = 2n_{sp}\chi\left(\frac{G-1}{G}\right). \qquad (2.12)$$

In this expression n_{sp} is the population inversion parameter $n_{sp} = N / N\text{-}N_{tr}$, G is the signal gain, and χ is the excess noise coefficient—which describes signal-spontaneous beat noise enhancement due to finite mirror reflectivity (the noise figure is defined as NF = 10log(F), and is expressed in decibels). For reflection mode and transmission mode operation, χ becomes [17]:

$$\chi_r = \frac{(1 + R_b g_s)(g_s - 1)}{(R_b g_s^{\,2} - 1)} \qquad (2.13)$$

$$\chi_t = \frac{(1 + R_b g_s)(1 - R_t)(g_s - 1)}{(1 - R_b)(1 - R_t) - \left(1 - \sqrt{R_b R_t}\, g_s\right)^2} . \qquad (2.14)$$

For a reflection mode device, χ_r depends only on the bottom mirror reflectivity, and for values of R_b greater than 0.999, $\chi_r \approx 1$. In the case of transmission mode operation, the excess noise coefficient equals one for single-pass gain values of $g_s = R_b^{-1/2}$. The population inversion parameter n_{sp} equals unity for complete inversion and increases for incomplete inversion. From Eq. 2.12 it is desirable to operate at high carrier densities in order to minimize n_{sp}. Unfortunately, high carrier densities may lead to lasing; it is therefore important to reduce the mirror reflectance in order to allow for full inversion without reaching the point of self-sustaining oscillation, while still maintaining sufficient reflectance to achieve the desired level of signal gain. Note that the important parameter when regarding noise in any amplifier application is the fiber-to-fiber noise figure. In this instance the superior coupling efficiency of VCSOAs, as compared to in-plane SOAs, becomes a clear advantage.

2.3 Tunable Cavity Design Options

In addition to standing wave effects, the short cavity length of the VCSOA leads to an inherently large axial mode spacing. Because of this fact, continuous mode-hop-free tuning is achievable over a relatively wide wavelength span. To realize wavelength tuning of the device, the MT-VCSOA utilizes an optical cavity design similar to that used in tunable VCSELS, RCLEDs and photodetectors. These devices

contain a variable thickness air gap within the resonant cavity structure that allows for variation of the effective cavity length. With a MEMS tunable vertical-cavity device, there exist a number of distinct optical cavity structures. This section makes use of the terminology employed by Larson [18] to outline the relevant optical cavity designs for active devices—these include the semiconductor coupled cavity (SCC), and extended cavity (EC) designs.

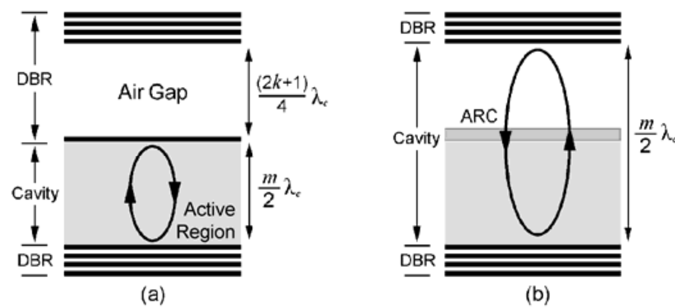

Fig. 2.3: Schematic of the (a) semiconductor coupled cavity and (b) extended cavity designs. For each configuration the mirror reference planes have been defined so that the DBR begins with a high index layer (black line). Additionally, the mirrors are designed to give a π phase shift at λ_c, and m and k are integers. In (a) the semiconductor active region is of a resonant thickness and the air gap serves as a low index layer of the top DBR. With the extended cavity structure shown in (b) the incorporation of an antireflection coating (ARC) creates a distributed cavity of a total length $m\lambda_c/2$. The circulating arrows indicate the position of maximum intensity of the optical standing wave.

Each cavity design incorporates an air gap within the optical cavity, as shown in Fig. 2.3. By modulating the thickness of the air gap, the resonant wavelength of the cavity may be tuned. For these structures the suspended mirror will be defined as the membrane DBR, while the combination of the membrane DBR and air gap will be referred to as the tunable mirror structure. The top and bottom mirrors are designed

to give a π phase shift at the center wavelength of the cavity λ_c, which is defined as the wavelength at which the air gap is of the ideal thickness and the DBRs meet the Bragg condition. For the following all lengths are given as optical thicknesses—physical thickness multiplied by the refractive index.

2.3.1 Semiconductor Coupled Cavity Design

The SCC-design utilizes a semiconductor cavity containing the active material of length a multiple of $\lambda_c/2$, along with an air gap of thickness near an odd multiple $\lambda_c/4$. Here the air gap acts as a low index layer of the top DBR, as seen in Fig. 2.3(a). The large index step afforded by the air gap allows for enhanced reflectance of the tunable mirror structure, as well as maximum overlap of the optical field with the active region. With the SCC-design, the increased optical overlap is achieved at the expense of a decreased wavelength tuning efficiency, resulting in a small wavelength shift for a given change in air-gap thickness. In a tunable vertical-cavity amplifier, the tradeoff of a decreased tuning range for an increased optical overlap may be preferred, as it is necessary to achieve the highest possible single-pass gain in these devices. In this design, the coupling between the air gap and semiconductor active region leads to complications in the tuning mechanism. These complications include changes in the top mirror reflectance and confinement factor with tuning, which may result in variations in the peak gain, bandwidth, saturation, and noise figure over the wavelength tuning range of the amplifier. Depending on the final application, the benefits of the SCC-design, including maximum overlap of the optical field with the

active material and enhanced top mirror reflectance, may outweigh the resulting tradeoff of a limited tuning response. Additionally, the SCC-design is simple to implement, as there is no need to access the optical cavity to create the antireflection coating (ARC) necessary in the EC-design.

2.3.2 Extended Cavity Design

By placing an ARC within the cavity, at the interface between the semiconductor active region and the variable air gap, the EC-design is produced. Here the combination of the active region and air gap produces an "extended cavity" of a total thickness of a multiple of $\lambda_c/2$ (in this case scaled by the effective index of the cavity, which is a combination of the air gap and semiconductor active region). In this design the ARC may be fabricated using a simple quarter-wave transformer, with a refractive index value equal to the square root of the active region refractive index. The EC-design allows for increased wavelength tuning ranges when compared to the SCC-design, and the tuning response of the EC-design is linear, as a function of air-gap thickness, over a relatively wide wavelength range (the DBR stop band as well as ARC bandwidth limits the linear tuning range). However, the larger achievable tuning range comes at the expense of a reduced optical overlap with the stacked MQW active region. Given a similar active region and mirror design, the EC-design will exhibit reduced peak gain for a given value of material gain, when compared to the SCC-design. Due to the presence of the ARC in the structure, coupled cavity effects are suppressed and more constant gain profiles will result over

the wavelength tuning range of the amplifier. Assuming an ideal ARC, the variations in device properties found with tuning will be caused by the wavelength shift of the cavity, as well as those changes brought about by the variation in the cavity length.

2.4 Tunable VCSOA Theoretical Model

With the theoretical models for fixed-wavelength VCSOAs outlined and the tunable cavity design options explored, the groundwork is now set for the development of tunable devices. In the following section, the analytical expressions describing the effective reflectance and phase of the coupled-cavity tuning structure are derived from the standard relationships for an FP interferometer. The phase coupling factor and wavelength tuning expressions for this structure are based on analytical expressions developed by Larson to describe MEMS-tunable coupled cavity filters, RCLEDs, detectors, and VCSELs [18].

2.4.1 Wavelength Tuning

In each of the optical cavity designs described above, the air gap allows for wavelength tuning through the variation in the effective cavity length of the device. Using the FP modeling approach outlined previously, the tunable mirror structure can be described using the standard relationships for a FP interferometer. The effective reflectance of the tunable mirror structure may then be written as [19]:

$$R_{eff} = \frac{R_c + R_m - 2\sqrt{R_c R_m}\cos(\phi_g)}{1 + R_c R_m - 2\sqrt{R_c R_m}\cos(\phi_g)} \qquad (2.15)$$

where R_m is the power reflectance of the membrane DBR, R_c is the reflectance of the interface between the semiconductor cavity and the air gap, ϕ_g is the round trip phase in the air gap = $2\beta_g L_g + 2(\beta_g - \beta_{go})L_m$, with $\beta_g = 2\pi/\lambda$, $\beta_{go} = 2\pi/\lambda_c$, L_m is the penetration depth into the membrane DBR, and L_g is the thickness of the air gap. Similarly, the reflected phase is given by the relation [18]:

$$\phi_{eff} = \tan^{-1} \frac{\sqrt{R_m}(R_c - 1)\sin(\phi_g)}{\sqrt{R_c}(1 + R_m) - \sqrt{R_m}(1 + R_c)\cos(\phi_g)} . \qquad (2.16)$$

From Eq. 2.15, the reflectance of the tunable mirror structure varies with the round trip phase in the air gap. Most notably, with the SCC-design the effective reflectance will be reduced with tuning due to phase interference from multiple reflections within the air-cavity structure. When the air gap is near a thickness of an odd multiple of $\lambda_c/4$, the multiple reflections add in phase and result in a maximum in R_{eff}. When the air gap reaches a thickness of a multiple of $\lambda_c/2$, destructive interference occurs and the reflectance reaches a minimum value. With the EC-design, the presence of the ARC removes the fixed phase reflection from the bottom of the air gap, and assuming an ideal ARC, $R_c \approx 0$, and $R_{eff} \rightarrow R_m$, resulting in a constant tunable mirror reflectance over the tuning range of the VCSOA, assuming this falls within the stop band of the DBR mirrors and the ARC bandwidth.

Continuing with the FP approach, it is possible to describe the wavelength tuning characteristics of the SCC-design by treating the air gap-DBR structure as a mirror

with a tunable phase shift. The resonant wavelength of the optical cavity occurs when the round trip phase of the semiconductor cavity and the DBRs (including the contribution of the air gap in the top mirror) is equal to an integer multiple of 2π. For small changes in L_g centered on the ideal air-gap thickness L_{go}, the shift in wavelength of the resonant cavity mode corresponding to a given change in air-gap thickness is given by [18]:

$$\frac{\Delta\lambda}{\lambda_o} = \frac{\gamma_\phi \Delta L_g}{L_b + L_{sc} + \gamma_\phi (L_g + L_m)} \qquad (2.17)$$

with the phase coupling factor $\gamma_\phi = d\phi_{eff} / d\phi_g$. The denominator in Eq. 2.17 describes the total cavity length of the device, including the penetration depth into the bottom DBR L_b, the length of the semiconductor cavity L_{sc}, and the effective length of the tunable mirror structure, which is the sum of the air-gap thickness L_g and the penetration depth into the membrane DBR L_m, scaled by γ_ϕ. In the design of tunable VCSELs, the expressions for the effective phase and phase coupling factor are simplified by assuming that the membrane reflectance is approximately equal to one [18]. However, given the low mirror reflectivities typically used in MT-VCSOAs (e.g. R_m = 0.9 for the first generation) it is important that the full relationships be utilized with these devices.

From Eq. 2.17, the wavelength shift of the SCC-design is directly proportional to the phase coupling factor; thus, for a given change in air-gap thickness, a device with a large γ_ϕ will exhibit a larger wavelength tuning rate. The response of R_{eff}, ϕ_{eff}, and γ_ϕ, as a function of the thickness of the air gap, is shown in Fig. 2.4. In this plot

it has been assumed that R_c = 0.32 and R_m = 0.95. With these values γ_ϕ exhibits a minimum value of about 0.28 when the air-gap thickness is equal to an odd multiple of $\lambda_c/4$. In this case, any change in the air-gap thickness will result in a change in the effective cavity length slightly less than one third of this amount. Within this linear tuning regime, the small value of the phase coupling factor reduces the effects of tilt or additional loss that may be caused by non-uniformity of the membrane DBR, by reducing the total penetration depth of the optical field into the tunable mirror structure. However, for large displacements, the phase coupling factor will increase dramatically, reaching a maximum value of 3.61 at integer multiples of $\lambda_c/2$.

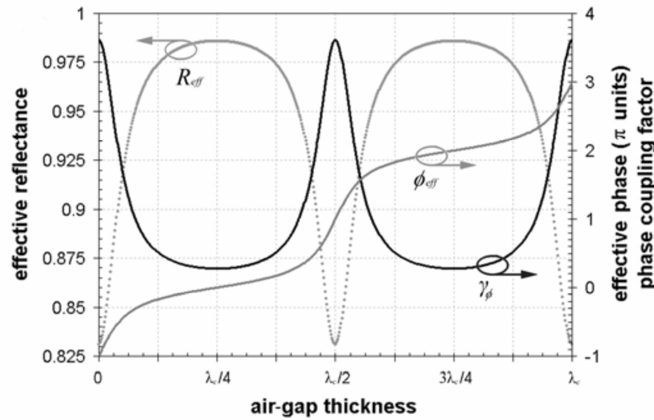

Fig. 2.4: Effective mirror reflectance, effective phase, and phase coupling factor of the SCC-design as a function of the thickness of the air gap, with R_c = 0.32 and R_m = 0.95.

For the EC-design, assuming that the active region-air interface contains an ideal ARC, γ_ϕ becomes unity in Eq. 2.17 and the tuning response is directly related to the change in air-gap thickness; noting that this linear tuning regime for the EC-design will be limited by the finite width of the DBR stop band, as well as the bandwidth of

the ARC. Because of the increase in γ_ϕ as compared to the SCC-design, the EC structure is more sensitive to imperfections in the membrane DBR due to the increased field penetration depth into the tunable mirror structure.

2.4.2 Peak Gain Response of MEMS-Tunable VCSOAs

From the relationships presented above it is possible to derive expressions to model the effects of the tunable mirror structure on the peak gain of the VCSOA. Combining Eq. 2.1 for the peak reflection gain (ϕ_s = 0) with the relationship describing the reflectance of the tunable mirror structure (Eq. 2.15), the peak signal gain of an SCC-design reflection mode tunable VCSOA is written:

$$G_r = \frac{\left(\sqrt{R_{eff}} - g_s\right)^2}{\left(1 - \sqrt{R_{eff}}\, g_s\right)^2}. \qquad (2.18)$$

In this expression it is assumed that the device contains a highly reflective fixed mirror (R_b = 1) and a slightly transmissive membrane DBR (R_m < 1). Furthermore, this expression shows that the peak gain is dependent on the effective reflectance of the tunable mirror structure, which is a function of the membrane reflectance, the cavity-air interface reflectance, and the round trip phase of the air gap.

Another option for the SCC-design reflection mode tunable VCSOA would be to use the tunable mirror structure as the highly reflective mirror. In the limit of R_m = 1 in Eq. 2.15, $R_{eff} \rightarrow 1$ regardless of the round trip phase of the air gap, and the expression for the peak gain is given by:

$$G_r = \frac{\left(\sqrt{R_t} - g_s\right)^2}{\left(1 - \sqrt{R_t}\, g_s\right)^2} \qquad (2.19)$$

with R_t defined as the reflectance of the transmissive mirror in this case. Thus, by using the MEMS tuning structure as the high reflectivity mirror in the reflection mode SCC-design tunable VCSOA, the peak gain relationship becomes independent of both the reflectance of the cavity-air interface and the round trip phase of the air gap. In this configuration the MEMS tuning element may be described as a Gires-Tournois interferometer, essentially a FP interferometer with a unity back reflector. This same expression can also be used to model the EC-design reflection mode tunable VCSOA. The incorporation of an ideal ARC results in $R_c \approx 0$ and the peak gain in reflection for both mirror positions reduces to that shown in Eq. 2.19 above, where R_t will be the reflectance of the transmissive mirror, regardless of position (again assuming the high reflectivity mirror has unity reflectance).

With a transmission mode tunable VCSOA the need for two transmissive mirrors requires that both R_m and $R_b < 1$. Combining Eq. 2.2 with 2.15, the peak gain for a transmission mode SCC-design tunable VCSOA becomes:

$$G_t = \frac{g_s\left(R_b - 1\right)\left(R_{eff} - 1\right)}{\left(1 - \sqrt{R_b R_{eff}}\, g_s\right)^2}. \quad (2.20)$$

In this configuration the peak transmission gain is dependent on the reflectance of the cavity-air interface and both DBRs, as well as the round trip phase in the air gap. The changing mirror reflectance with tuning described by Eq. 2.15 may be

suppressed by employing the EC-design in these devices. Again, assuming an ideal ARC ($R_c \approx 0$), the peak gain for a transmission mode VCSOA using the EC-design reduces to the standard expression of Eq. 2.2, with the membrane mirror reflectance R_m used for the reflectance of the tunable mirror structure.

2.5 MEMS Actuator Design

To achieve wide wavelength tuning of the VCSOA cavity mode it is necessary to construct a mechanical system to physically alter the thickness of the air gap. The most efficient realization of such a structure involves the use of an integrated micromechanical actuator. Depending on the configuration of the actuator, the air-gap thickness may be increased or decreased from its initial position. With an increase (decrease) in the air-gap thickness, the effective cavity length is increased (decreased) and the cavity resonance wavelength is red (blue) shifted, as can be seen in Eq. 2.17. Using a MEMS-based tuning element, various actuator designs are possible—the most commonly used being electrostatic and electrothermal actuators.

2.5.1 Electrostatic Actuation

For a low power, high speed tuning response the most effective actuator design is the integrated electrostatic actuator. In its simplest form the electrostatic actuator consists of a pair of parallel capacitor plates separated by an air gap of a specified thickness, in which one or more of the plates is capable of displacement. With an

applied bias, the Coulomb force is exerted on the plates due to charge separation. If one, or both, of the plates is free to move, then the electrostatic force results in a change in the air-gap thickness, leading to a variation in the effective cavity length of the VCSOA. Because the air gap is an integral part of the resonant cavity, the initial thickness will be constrained by the optical design of the device. Neglecting the effects of fringing fields, and assuming that the device consists of a rigid central plate suspended by four deflectable legs, with no intermediate insulating layers between the two electrodes, the resulting force, F_c may be calculated from [20]:

$$F_c = \frac{\varepsilon_o A_m V^2}{2(L_{g_o} - \delta_m)^2} + \frac{2\varepsilon_o b l V^2}{L_{g_o}(L_{g_o} - \delta_m)} \qquad (2.21)$$

where ε_o is the permittivity of free space, A_m is the total plate area, V is the applied bias, L_{go} is the initial separation between the plates of the actuator, δ_m is the vertical displacement of the rigid central plate, l is the length of the individual legs, and b is the leg width. In Eq. 2.21 the first term represents the force distributed across the central plate, while the second term represents the force generated along the length of the legs, assuming a linear deflection as a function of the lateral position. In this expression, the central plate is assumed to experience negligible deformation upon actuation due to the increased thickness of the DBR pillar (and correspondingly larger moment of inertia) as compared to the suspensions. The accuracy of this assumption has been verified by previous investigations into the optomechanical characteristics of deformable membrane structures [21], [22].

2.5.2 Static Response of the Deformable Membrane Structure

With the applied force known, the deflection of the MEMS structure may be described using Hooke's law, $F_c = F_{restore}$, with a simple single-degree-of-freedom model for the restoring force of the actuator, $F_{restore} = k_{mech}\,\delta_m$, where k_{mech} is the mechanical spring constant of the membrane structure. Because the electrostatic force itself is a function of the displacement, an iterative solution must be used to determine the equilibrium deflection of the actuator. More advanced modeling techniques used to describe the mechanical properties of the MEMS structure include the area-moment method [21], or full three-dimensional models using finite element analysis [22]. However, it has been found that by using analytical formulas such as those presented here, accurate predictions of the mechanical properties of the actuator can be made.

For the single-degree-of-freedom model, the restoring force may be described by utilizing the familiar relationships of the flexure of beams of uniform cross-section [23]. For small displacements the total restoring force of the mechanical system can be found by summing the forces resulting from bending of the beams, as well as the force present due to the intrinsic stress (F_{bend} and $F_{stretch}$), as shown in Eq. 5.22 below. However, for large displacements, the actuator may exhibit non-linear elastic effects, resulting in a displacement dependent stiffness. In a doubly-clamped structure, the increase in strain energy at large displacements results in a cubic nonlinearity in the restoring force. Assuming that the deflected shape may be

approximated by a cosine function, the non-linear component ($F_{stretch}$) of the restoring force of two crossed doubly-clamped center-loaded beams is given by [24]:

$$F_{bend} = \frac{\pi^4 E' h^3 b \delta_m}{24 l^3} \quad F_{stress} = \frac{\pi^2 h b \sigma \delta_m}{2l} \quad F_{stretch} = \frac{\pi^4 E' h b \delta_m^{\ 3}}{32 l^3}. \quad (2.22)$$

In this expression h is the thickness of the legs, E' is the biaxial modulus, with $E' = E/(1-\upsilon^2)$, E is the Young's modulus of the membrane material, υ is Poisson's ratio, and σ is the intrinsic film stress in the beam. With these expressions the mechanical spring constant k_{mech} may be found by dividing $F_{restore}$ by the membrane deflection δ_m. It should also be noted that the relationships above are valid only for uniform beams. For a composite actuator consisting of two distinct films, the modulus, thickness, and stress must be replaced by the effective values for a bilayer [25].

Given a very thin structure fabricated from materials with a high intrinsic film stress, the restoring force will be dominated by F_{stress}. In those structures in which the growth stresses have been minimized, or in structures with a relatively large cross-sectional area—such as a device with a full thickness DBR as the compliant structure—the restoring force will be dominated by the bending of the beams. As mentioned previously, $F_{stretch}$ becomes important at large displacements, although this term is usually insignificant for DC operation. Under dynamic conditions, including operation at resonance and in a low damping regime (e.g. dynamic testing in vacuum), the actuator may be capable of very large displacements and the non-linear component of the spring constant may become significant. A detailed explanation of the non-linear dynamics of this actuator is presented in Section 2.5.3.

As compared to a cantilever, the four-leg design is a more mechanically stable structure. In this configuration the sensitivity of the free-standing membrane to external mechanical vibrations and stress-induced bending in the structural films may be reduced [26]. In addition, the four-leg design helps to maintain a parallel alignment between the membrane DBR and fixed substrate DBR; thus, reducing the effects of beam walkoff loss upon actuation [20].

The displacement of the electrostatic actuator is highly non-linear, due to the changing force with displacement, as seen in Eq. 5.21. Due to this inherent non-linearity, the electrostatic actuator will only exhibit a limited range of valid solutions. As a rule of thumb, for displacements less than 1/3 of the initial air-gap thickness, there exists a stable equilibrium position for the actuator. Beyond this distance, the electrostatic force overwhelms the restoring force and leads to pull-in of the actuator. At this point the membrane will be forced into physical contact with the opposite electrode, resulting in a permanent fusing of the pair due to the effects of stiction, or damage due to capacitive discharge if there are no insulating materials separating the electrodes. A review of the intricacies of the electrostatic actuator may be found in [27]. Using this rule of thumb as a limit to the total travel of the actuator, it is possible to estimate the maximum voltage for the four-leg design. Combining Eq. 2.22 with the applied force in Eq. 2.21, and solving for the required voltage for a displacement of 1/3 L_{go} results in:

$$V_{stress}^{\max} = \frac{2\pi}{3}\left(\frac{hb\sigma L_{g_o}{}^{3}}{\varepsilon_o l(3A_m + 8bl)}\right)^{1/2} \quad V_{bend}^{\max} = \frac{\pi^2}{3}\left(\frac{h^3 bE' L_{g_o}{}^{3}}{3\varepsilon_o l^3 (3A_m + 8bl)}\right)^{1/2}. \qquad (2.23)$$

From Eq. 2.23, the voltage may be reduced by increasing the length of the legs and the area of the membrane, as well as decreasing the initial air-gap thickness. Specific to the stress dominated structure, the required tuning voltage may be minimized by decreasing the cross-sectional area of the legs (hb) and the film deposition stress. For the case where F_{bend} dominates, the required voltage is largely dependent on the thickness and length of the legs. Because the suspended structure serves as the top mirror for the device, the thickness of the legs will be predetermined by the optical design of the DBR, although additional processing steps may be used to decouple the mechanical and optical properties of the device, allowing increased freedom in design of the final structure [28].

In the push to demonstrate low voltage operation, MEMS-tunable vertical-cavity devices have been demonstrated with maximum tuning voltage below 4 V [29], [30]. In these structures the idea is to achieve the lowest possible spring constant (<1 N/m), and thus the lowest possible actuation voltage, by minimizing the intrinsic film stress and geometry of the suspensions. However, it is questionable to this author that the demonstration of such low voltage operation is truly an advantage. In this case, structures with unreasonably low spring constants may exhibit sensitivities to external vibrations or shock loads (due to their low resonant frequencies and high compliance) and may further be susceptible to collapse and stiction due to surface tension forces in moist/liquid environments. For a well designed electrostatic actuator, the current flow is typically so low (nanoamps) that the consumed power is negligible for reasonable operating voltages when compared with the power

requirements of the control electronics. Given the increased stability, increased resonant frequency, and relatively low power consumption of higher stiffness structures, there may be advantages to designing devices with spring constant values in the range of 10–50 N/m.

2.5.3 Dynamic Mechanical Response

Typically, the dynamic response of a micromechanical system is modeled using finite-element-based distributed field models in the electrical and mechanical domain. A simplified approach to simulate such a system involves the development of single-degree-of-freedom lumped element models, as discussed previously for the static response of the actuator. Although this approach neglects many of the details of the system, it is quite often sufficient in capturing the essence of the dynamics. In this dissertation the dynamic response of the membrane structure is modeled using an equivalent mass spring system driven by a time varying electrostatic force. Applying Newton's Second Law and including each of the components of the restoring force of the actuator, the motion of the membrane structure in response to a time varying voltage can be approximated by a forced Duffing equation [31]:

$$\ddot{x} + 2\delta\dot{x} + {\omega_0}^2 x + \mu x^3 = \frac{F_c(t)}{m_{eff}} \qquad (2.24)$$

with the effective actuator mass m_{eff}, linear damping term 2δ, natural frequency $\omega_0 = \sqrt{k_1 / m_{eff}}$, containing the linear spring constant k_1 (equal to the sum of the

bending and internal stress components, k_{bend} and k_{stress}), the coefficient of nonlinearity $\mu = k_{stretch} / m_{eff}$, including the non-linear spring constant k_{stretch} as described in Eq. 2.22, and finally the electrostatic force F_c from Eq. 2.21. In the differential equation presented above, complications arise from the position dependent force of the electrostatic actuator, as well as from the non-linear restoring force of the membrane structure for large displacements. Fortunately, it is possible to accurately model the devices presented in this dissertation by neglecting the position dependent force of the actuator—greatly simplifying the solutions to Eq. 2.24.

The frequency response of the micromechanical actuator can be divided into two regimes, including a simple harmonic response and a damped Duffing response. For small driving amplitudes in vacuum, or for operation at atmosphere, it is possible to neglect the nonlinear restoring force of the springs (assuming $\mu \approx 0$), given the relatively small displacements. In this regime the actuator exhibits a simple harmonic response, with the resulting displacement C, as a function of the driving frequency Ω, given by:

$$C = \frac{F_c}{m_{eff}} \left[\left(\omega_0^{\,2} - \Omega^2 \right)^2 + \left(2\delta\,\Omega \right)^2 \right]^{-\frac{1}{2}}. \qquad (2.25)$$

By fitting the frequency response of the actuator with this expression, it is possible to extract the damping coefficient and natural frequency. Combining this with the measured DC (or quasi-static) spring constant, the effective mass of the actuator can be determined. Due to the large ratio of lateral dimensions to air-gap thickness in MT-VCSOAs, damping of the actuator is dominated by squeeze film effects. An in-

depth discussion of the effects of viscous damping on resonating microstructures can be found in [32].

With the effective mass, damping coefficient, and linear restoring force of the actuator determined by curve fitting of the harmonic response, the damping factor ζ may be calculated using:

$$\zeta = \frac{\delta}{\omega_0^{\ 2}} . \quad (2.26)$$

For $\zeta < 1$, the system is considered to be underdamped and experiences a number of exponentially decaying oscillations before reaching equilibrium. A damping factor greater than unity ($\zeta > 1$) results in an overdamped system in which the time response is limited by the excessive damping in the system. Ideally, the actuator should exhibit a critically damped response ($\zeta = 1$) in order to minimize the time required to reach equilibrium. There is a simple relationship between the mechanical quality factor Q and damping factor: $Q^{-1} = 2\zeta$. With the damping factor known, the time response of an underdamped second order system can be approximated by:

$$\tau_{\pm 5\%} \approx \frac{2.5}{\zeta\, \omega_0} . \qquad (2.27)$$

This expression estimates the time necessary for the actuator to reach $\pm 5\%$ of its final displacement value. As can be seen from Eq. 2.27, the minimum time response is achieved for a critically damped system ($\zeta = 1$) with the highest possible natural frequency (achieved by reducing the suspended mass and increasing the stiffness).

For actuation near resonance and with low damping (e.g. in vacuum) the device enters the second operating regime, exhibiting a damped Duffing response. Due to the large displacements in this regime it is necessary to take into account the non-linear restoring force of the membrane structure as discussed previously. The Duffing response has been well characterized in a variety of micromechanical resonators [33]-[35]. Neglecting the displacement dependence of the electrostatic force, the displacement as a function of frequency can be calculated from:

$$\frac{F_c^{\,2}}{m_{eff}^{\,2}} = \left[\left(\omega_0^{\,2} - \Omega^2\right)C + \frac{3}{4}\mu C^3\right]^2 + 4\delta^2\Omega^2C^2, \qquad (2.28)$$

where the relevant terms have been defined above. Under these conditions the actuator exhibits a hysteretic response in the frequency domain arising from a significant cubic nonlinearity in the restoring force. By sweeping both up and down in the driving frequency, the bistable region of the response curve may be determined. For positive values of μ, the membrane stiffness increases with displacement (hardening spring), while for $\mu < 0$ the beam stiffness decreases with displacement and the nonlinear resonance shifts to shorter frequencies (softening spring). With the four-leg design of the MT-VCSOA, the suspensions are basically a pair of crossed fixed-fixed beams. This configuration typically exhibits a hardening spring response, with the nonlinear resonance being pushed to higher frequencies for increasing displacement. Although operation in this regime is not ideal, fitting of the Duffing response allows for an accurate determination of the actuator properties

including the natural frequency, damping coefficient, and cubic-nonlinearity of the restoring force, which may be difficult to pin down using simple static tests.

2.6 Summary

The balance between the reflectivity of the mirrors and the gain provided by the active region is the most important issue in VCSOA design. In these devices the reflectivity of the two mirrors has a large impact on all properties of the amplifier, and must be chosen carefully. Strong feedback, i.e. high mirror reflectivity, leads to high signal-gain for a given value of single-pass gain, but in this case the amplifier gain is limited by lasing threshold. High mirror reflectivity also leads to a poor noise figure and low saturation powers. Mirror reflectivity that is too low, on the other hand, simply does not provide sufficient feedback to reach high signal-gain. For optimum performance it is desirable that the mirror reflectivity be as high as possible without enabling lasing threshold to be reached. This condition allows for operation at full population inversion, which gives the highest possible amplifier gain, the highest saturation output power, and the lowest noise figure.

Two design options exist for the construction of the tunable optical cavity including the semiconductor coupled cavity and the extended cavity design. In order to maximize the achievable single-pass gain, as well as simplify the fabrication procedure for these devices, the semiconductor coupled cavity design is chosen. General Fabry-Pérot models are used to describe the effective reflectance, effective

phase, and wavelength tuning response of micromechanically-tunable VCSOAs. Combining the tuning expression with the standard relationship for a Fabry-Pérot cavity with gain, it is possible to construct analytical expressions describing the peak gain response as a function of the resonant wavelength of the MT-VCSOA.

Finally, the static and dynamic response of the electrostatic actuator is outlined. This actuator exhibits a rapid response time, a low power consumption, and a relatively large deflection range. However, the pull-in instability of this system limits the overall displacement to roughly 1/3 of the initial air-gap thickness. The spring constant, i.e. stiffness, of these structures is typically dominated by the intrinsic film stress of the structural material comprising the membrane, but can also be influenced by the overall geometry for devices with large cross-sectional areas, such as full thickness DBRs. Decreasing the spring height and film stress greatly lowers the total stiffness and allows for manageable tuning voltages. The dynamic response of the actuator, for small displacements, is described by the standard second order differential equation for a simple harmonic oscillator. However, for large displacements, nonlinearities in the restoring force result in a hysteretic response typical of a Duffing oscillator. The minimum time response is achieved by balancing the damping of the system in order to achieve near critical damping.

References

[1] E. S. Björlin, T. Kimura, J. E. Bowers, “Carrier-confined vertical-cavity semiconductor optical amplifiers for higher gain and efficiency,” *IEEE J. Select. Topics Quantum Electron.*, vol. 9, pp. 1374–1385, Sep./Oct. 2003.

[2] P. Royo, R. Koda, L. A. Coldren, “Rate equations of vertical-cavity semiconductor optical amplifiers,” *Appl. Phys. Lett.*, vol. 80, pp. 3057–3059, Apr. 2002.

[3] J. Piprek, E. S. Björlin, J. E. Bowers, “Design and analysis of vertical-cavity semiconductor optical amplifiers,” *IEEE J. Quantum Electron.*, vol. 37, pp. 127–134, Jan. 2001.

[4] M. C. Larson, B. Pezeshki, J. S. Harris, “Vertical coupled-cavity microinterferometer on GaAs with deformable-membrane top mirror,” *IEEE Photon. Technol. Lett.*, vol. 7, pp. 382–384, Apr. 1995.

[5] C. Tombling, T. Saitoh, T. Mukai, “Performance predictions for vertical-cavity semiconductor laser amplifiers,” *IEEE J. Quantum Electron.*, vol. 30, pp. 2491–2499, Nov. 1994.

[6] T. Mukai, Y. Yamamoto, T. Kimura, “Optical Amplification by Semiconductor Lasers,” in *Semiconductors and Semimetals*, vol. 22-E, R. K. Willardson and A. C. Beer (Eds.), pp. 265–319, New York: Academic, 1985.

[7] A. Karlsson, M. Höijer, “Analysis of a VCLAD: vertical-cavity laser amplifier detector,” IEEE *Photon. Tech. Lett.*, vol. 7, pp. 1336–1338, Nov. 1995.

[8] O. Kibar, “VCSEL-based digital free-space optoelectronic interconnections,” Ph.D. dissertation, UCSD, San Diego, CA, 1999.

[9] P. Royo, R. Koda, L. A. Coldren, “Vertical cavity semiconductor optical amplifiers: comparison of Fabry-Perot and rate equation approaches,” *IEEE J. Quantum Electron.*, vol. 38, pp. 279-284, Mar. 2002.

[10] E. S. Björlin, “Long-wavelength vertical-cavity semiconductor optical amplifiers,” Ph.D. dissertation, UCSB, Santa Barbara, CA, 2002.

[11] V. Jayaraman, T. J. Goodnough, T. L. Beam, F. M. Ahedo, R. A. Maurice, “Continuous-wave operation of single-transverse-mode 1310-nm VCSELs up to 115 ^{o}C,” *IEEE Photon. Technol. Lett.*, vol. 12, pp. 1595–1597, Dec. 2000.

[12] Y. Matsui, D. Vakhshoori, P. Wang; P. Chen, C.-C. Lu, M. Jiang; K. Knopp, S. Burroughs, P. Tayebati, “Complete polarization mode control of long-wavelength tunable vertical-cavity surface-emitting lasers over 65-nm tuning, up to 14-mW output power,” *IEEE J. Quantum Electron.*, vol. 39, pp. 1037–1048, Sep. 2003.

[13] D. I. Babić, S. W. Corzine, “Analytic expressions for the reflection delay, penetration depth, and absorptance of quarter-wave dielectric mirrors,” *IEEE J. Quantum Electron*, vol. 28, pp.514–524, Feb. 1992.

[14] H. Ghafouri-Shiraz, *Fundamentals of Laser Diode Amplifiers*, West Sussex, U.K.: Wiley, 1996.

[15] L. A. Coldren and E. R. Hegblom, “Fundamental Issues in VCSEL Design,” in *Vertical-Cavity Surface-Emitting Lasers*, vol. 1, C. W. Wilmsen, H. Temkin, and L. A. Coldren (Eds.), pp. 32–67, Cambridge, UK: Cambridge University Press, 1999.

[16] L. A. Coldren and S. W. Corzine, *Diode Lasers and Photonic Integrated Circuits*, New York, NY: Wiley, 1995.

[17] E. S. Björlin, J. E. Bowers, “Noise figure of vertical-cavity semiconductor optical amplifiers”, *IEEE J. Quantum Electron.*, vol. 38, pp. 61–66, Jan. 2002.

[18] M. C. Larson, “Microelectromechanical wavelength-tunable vertical-cavity light emitters and lasers,” Ph.D. dissertation, Stanford University, Stanford, CA, 1996.

[19] P. Hariharan, *Optical Interferometry*, Sydney, UK: Academic Press, 2003.

[20] F. Sugihwo, M. C. Larson, J. S. Harris, “Micromachined widely tunable vertical cavity laser diodes,” *J. Microelectromech. Syst.*, vol. 7, pp. 48–55, Mar. 1998.

[21] C.-C. Lin, W. A. Martin, J. S. Harris, “Optomechanical model of surface micromachined tunable optoelectronic devices,” *IEEE J. Select. Topics Quantum Electron.*, vol. 8, pp. 80–87, Jan./Feb. 2002.

[22] S. Greek, R. Gupta, K. Hjort, “Mechanical considerations in the design of a micromechanical tuneable InP-based WDM filter,” *J. Microelectromech. Syst.*, vol. 8, pp. 328–334, Sep. 1999.

[23] W. C. Young, *Roark’s Formulas for Stress and Strain*, New York, NY: McGraw-Hill, 1989.

[24] S. D. Senturia, *Microsystem Design*, Boston, MA: Kluwer Academic Publishers, 2001.

[25] L. Nicu, C. Bergaud, A. Martinez, P. Temple-Boyer, “Static and dynamic characterization of buckled composite SiO_2-Au microbridges,” in *Proc.*

Materials Science of Microelectromechanical Systems (MEMS) Devices II, Mater. Res. Soc. Symp., vol. 605, Nov. 29 – Dec. 1 1999, pp. 223–228.

[26] S. Decai, W. Fan, P. Kner, J. Boucart, T. Kageyama, Z. Dongxu, R. Pathak, R. F. Nabiev, W. Yuen, “Long wavelength-tunable VCSELs with optimized MEMS bridge tuning structure,” *IEEE Photon. Tech. Lett.*, vol. 16, pp. 714–716, Mar. 2004.

[27] J. A. Pelesko and D. H. Bernstein, *Modeling MEMS and NEMS*, Boca Raton, FL: Chapman and Hall/CRC, 2003.

[28] F. Sugihwo, M. Larson, J. S. Harris, Jr., “Simultaneous optimization of membrane reflectance and tuning voltage for tunable vertical cavity lasers,” *Appl. Phys. Lett.*, vol 72, pp. 10–12, Jan. 1998.

[29] A. Syrbu, V. Iakovlev, G. Suruceanu, A. Caliman, A. Rudra, A. Mircea, A. Mereuta, S. Tadeoni, C.-A. Berseth, M. Achtenhagen, J. Boucart, E. Kapon, “1.55-μm optically pumped wafer-fused tunable VCSELs with 32-nm tuning range,” *IEEE Photon. Technol. Lett.*, vol. 16, pp. 1991–1993, Sep. 2004.

[30] C. Prott, F. Romer, E. O. Ataro, J. Daleiden, S. Irmer, A. Tarraf, H. Hillmer, “Modeling of ultrawidely tunable vertical cavity air-gap filters and VCSELs”, *IEEE J. Select. Topics Quantum Electron.*, vol. 9, pp. 918–928, May/Jun. 2003.

[31] P. Hagedorn, *Non-Linear Oscillations*, New York, NY: Oxford University Press, 1988, pp. 1–59.

[32] G. M. Rebeiz, *RF MEMS: Theory, Design, and Technology*, New York, NY: Wiley, 2003.

[33] M. V. Andres, K. W. H. Foulds, M. J. Tudor, “Nonlinear vibrations and hysteresis of micromachined silicon resonators designed as frequency-out sensors,” *Electron. Lett.*, vol. 23, pp. 952–954 , Aug. 1987.

[34] S. Evoy, D.W. Carr, L. Sekaric, A. Olkhovets, J.M. Parpia, H.G. Craighead, “Nanofabrication and electrostatic operation of singlecrystal silicon paddle oscillators,” *J. Appl. Phys.*, vol. 86, pp. 6072–6077, Dec. 1999.

[35] M. Aikele, K. Bauer, W. Ficker, F. Neubauer, U. Prechtel, J. Schalk, H. Seidel, “Resonant accelerometer with self-test,” *Sensor Actuat A-Phys*, vol. A92, pp. 161–167, Aug. 2001.

CHAPTER 3

Tunable VCSOA Processing

As optomechanical devices, MT-VCSOAs require an eclectic mix of processing technologies—including a combination of VCSEL and MEMS fabrication techniques. This chapter focuses on the fabrication of MT-VCSOAs, which encompasses the formation of the optical cavity through InP to GaAs direct wafer bonding, as well as the creation of the deformable membrane structure through GaAs/AlGaAs micromachining.

Similar to the wafer fused long-wavelength VCSELs fabricated at UCSB, tunable VCSOAs utilize direct wafer bonding in order to combine the excellent thermal properties and high index contrast of GaAs/AlGaAs DBRs, with the high gain long-wavelength InP-based active material. The bonding procedure presented here is based on many years of wafer bonding development at UCSB, a review of which is presented in [1]. For the fabrication of MT-VCSOAs, bonding is completed on unpatterned wafers (neglecting bond channels) and no process steps are undertaken on the InP active material other than selective wet etching of the superlattice periods for fine tuning of the initial cavity length.

The micromachining process used to define the electrostatic actuator employs standard wet and dry etch chemistries used for patterning GaAs and AlGaAs. For the MT-VCSOAs a sacrificial AlGaAs etch layer is employed in order to create the variable air gap. The majority of the process steps necessary for fabricating the final structure are concentrated on defining the electrostatic actuator. In order to provide the relevant background for such a process, the following section highlights the previous work as well as the motivation behind AlGaAs-based MEMS.

3.1 MEMS in AlGaAs

Traditionally micromechanical devices have been based on the Si/SiO_2 materials system, and to this date only a minority of studies have involved MEMS devices fabricated from compound semiconductor materials such as AlGaAs [2]-[10]. Generally, the use of III-V materials such as AlGaAs for micromechanical devices is driven by the requirements of either integration, such as in RF switches and suspended spiral inductors on GaAs for monolithic microwave integrated circuits (MMICs), or by the need for optically active materials, as in the case of tunable optoelectronic devices [4]. The use of GaAs as a micromechanical material has been widely used in recent years for the fabrication of MEMS-tunable VCSELs [5]-[9]. Although this section focuses solely on MEMS in GaAs, the same merits are also true in other materials systems including InP/AlInGaAsP and GaN/InGaAlN.

Although a somewhat uncommon MEMS materials system, GaAs and its alloys exhibit many advantageous properties for such applications including a direct band gap transition (for Al compositions less than 40%), a high electron mobility, the piezoelectric effect, and a high piezoresistive constant [2]. Furthermore, these alloys may be epitaxially grown as monocrystalline heterostructures using deposition methods such as molecular beam epitaxy (MBE) and metal-organic chemical vapor deposition (MOCVD). The ability to control the lattice matching condition with ternary and quaternary alloys gives one the ability to "strain engineer" films, in order to create built in tensile or compressive stresses. This can be useful in creating unique three dimensional structures by utilizing controlled compressive stresses for out-of-plane deformation [10], or for pulling suspended doubly-clamped structures flat with a built in tensile strain. In addition to strain engineering, variations in the aluminum composition of AlGaAs allow for a wide range of selective etch chemistries over GaAs. Generally, these films display extremely high etch selectivites—in fact HF etching of AlAs versus GaAs exhibits a selectivity approaching 10^7:1 [11]. GaAs/AlGaAs heterostructures may thus be processed using standard micromachining techniques to yield atomically flat optical surfaces that are ideal for optoelectronic and photonic devices.

With AlGaAs MEMS fabrication, the most common micromachining technique is a subtractive process utilizing planar epitaxial layers. Via epitaxial growth methods, it is possible to initially build up a series of monocrystalline films on a suitably doped or undoped substrate to define the structural and sacrificial layers of

the device. Following the epitaxial growth procedure, a subtractive etching processes is then utilized to define the geometry of the device. Typically, wet chemical etching is used to selectively remove a sacrificial layer to create free-standing structures [2].

3.2 Tunable VCSOAs Fabricated in this Dissertation

Three distinct generations of MT-VCSOAs are developed in this dissertation. Each of these structures is optimized for operation in reflection mode; thus, each consists of a transmissive mirror for signal injection/extraction and a high reflectivity mirror that acts as the back reflector. Additionally, these devices are optimized for optical pumping at 980 nm, with an undoped active region and DBRs. All MT-VCSOAs presented in this work are gain-guided devices, incorporating a micromechanically-tunable top mirror structure, and consist of two GaAs-based DBRs enclosing an active region originally lattice-matched to InP. Wavelength tuning is achieved by utilizing an electrostatic actuator to physically alter the thickness of an air gap incorporated within the top DBR, resulting in a variation in the optical path length of the cavity. Fabrication begins with two direct wafer bonds using three separate wafers—two wafers for the DBRs and one containing the active region epitaxial structure. Beyond the definition of bonding channels for the wafer fusion procedure and the removal of superlattice periods for cavity length adjustment, no further processing is completed on the InP-based active region.

The first and second generation of MT-VCSOAs utilize the same active region design, as well as the same top and bottom DBR structures. In fact, all material for these two generations of devices was cleaved from the same wafers. These structures are top emitting, and as such, consist of a reduced reflectivity MEMS-tunable mirror structure and a high reflectivity fixed DBR. The general processing steps are also quite similar; though, the second generation MT-VCSOAs utilize an updated lithographic mask set (which carries over to Generation 3). The major differences between the first and second generations of MT-VCSOAs are in the form of extensive revisions to the mechanical design of the deformable membrane structure. These changes address the shortcomings of the initial demonstration devices, including uncontrollable out-of-plane deformation of the actuator and cracking of the mechanical support structure—resulting in excessively high tuning voltages and poor reliability. These issues will be covered in more detail in the following chapters (Generation 1 in Chapter 4, Generation 2 in Chapter 5).

The third generation of devices, which will be discussed in Chapter 6, utilize a revised optical cavity design and material structure, including a modified active region and DBRs. These devices were developed in order to overcome the limitations in the initial optical cavity design, specifically the limited effective tuning range. In this design the MT-VCSOA is configured as a bottom emitting structure, with the input and output signals passing through the undoped GaAs substrate and fixed bottom DBR, while the MEMS-tunable mirror structure functions as the high reflectivity back mirror.

The specific design and material structure for each generation of devices will be presented in the proceeding chapters. In the following sections, a description of the general fabrication process will be presented, beginning with the direct wafer bonding procedure in Section 3.3.

3.3 GaAs to InP Direct Wafer Bonding

The most common active materials for long-wavelength VCSELs and VCSOAs are InGaAsP and AlInGaAs lattice matched to InP. Unfortunately, lattice matched InP-based DBR materials suffer from poor index contrast and require very thick, and thus excessively long, mirror growths. The drawback of the increased thickness of these structures is further compounded by the low thermal conductivity of InP-based DBRs. In contrast, DBRs based on GaAs/AlGaAs exhibit excellent thermal and optical properties (high index contrast) resulting in superior device performance, as evidenced by the successful commercial implementation of short-wavelength VCSELs. Ideally, GaAs-based DBRs could be epitaxially grown on high gain long-wavelength InP-lattice-matched active material for the development of efficient long-wavelength VCSELs.

Unfortunately, conventional epitaxial growth techniques of GaAs on InP substrates are limited to a critical thickness much below that required for the formation of quarter-wave layers. Heteroepitaxial films beyond the critical thickness of approximately 1 nm exhibit an unacceptably high density of threading dislocations, due to the large lattice mismatch indicated in Fig. 3.1. Despite these

limitations, metamorphic growth of GaAs-based DBRs on InP has been successfully demonstrated for both fixed wavelength and MEMS-tunable VCSELs [12], [5]. However, the threading dislocations formed in the metamorphic mirror structure may compromise device reliability, as repeated thermal cycling may cause these defects to eventually propagate through the active material. A recent approach to combine optimized epitaxial films of lattice mismatched compound semiconductor materials is the process of "wafer fusion", or direct wafer bonding. Unlike conventional growth techniques, direct wafer bonding allows for the heterogeneous integration of materials with largely mismatched lattice constants. In this process a covalent bond is formed at the heterointerface between the bonded materials during a high temperature anneal. This process allows for the fabrication of devices using ideal materials for the active region and DBRs, removing the restriction imposed by a particular lattice constant.

The wafer bonding process for compound semiconductor based optoelectronic devices was initially proposed by Liau et al. [13] and was extended to GaAs to InP bonding at UCSB by Ram and Dudley et al. [14]. It is interesting to note that the first successful electrically injected *continuous-wave* long-wavelength VCSEL was fabricated using the wafer bonding procedure [15]. The fabrication process described in this section was initially developed at UCSB and applied to the fabrication of bonded long-wavelength VCSELs and VCSOAs, beginning with Dudley and continuing with Babić, Margalit, Black, Karim, Okuno, Geske, Björlin, and Mehta. Further details of the bonding process and analysis of the bonded junction can be

found in their publications and dissertations; a rather comprehensive description of the materials issues of this process is presented in [16].

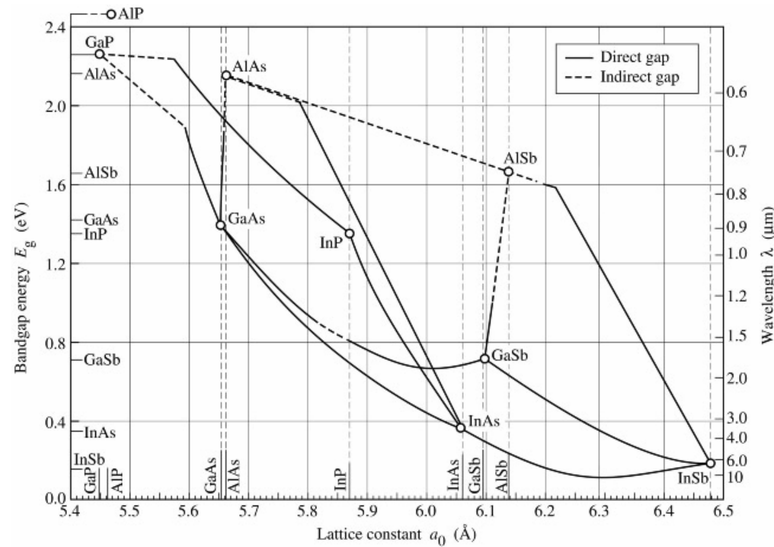

Fig. 3.1: The now infamous "map of the world", plotting the bandgap energy (and corresponding wavelength) of various III-V compounds as a function of the material lattice constant. Vertical alignment on this chart dictates the lattice matching condition. Binary materials are shown as points, ternary alloys are indicated by the connecting curves, and quaternary alloys fill the area enclosed by the ternary curves [17].

Wafer bonding enables a host of integration possibilities for the fabrication of optoelectronic devices including InGaAs:Si avalanche photodetectors [18], AlInGaP:GaP transparent substrate light emitting diodes (LEDs) [19], and wafer bonded GaAs/InP VCSELs [20]. In the following sections, the general wafer bonding process is discussed. It is important to note that this dissertation focuses solely on GaAs to InP bonding for the purpose of integrating GaAs/AlGaAs DBRs with AlInGaAs/InP active regions; as discussed previously, this combination is motivated by the favorable optical and thermal properties of GaAs-based DBRs.

Because the MT-VCSOAs presented in this dissertation are optically pumped, no consideration was given to the electrical characteristics of the fused junction.

Previous work has already demonstrated the optically transparent nature of the interface. Measurements by Liu et al. [21] indicate that the optical loss due to the bonded junction is no greater than 0.5 cm^{-1}. The optical cavity designs used in this work placed the bonded junctions at nulls in the standing wave pattern, further reducing the loss contribution from this interface. Finally, considering the short interaction length in a vertical-cavity device, the optical loss from the bonded junction can simply be neglected. Regarding degradation of the MQW active material, depth-resolved photoluminescence measurements by Black et al. [22] reveal that luminescence from both GaAs and InP quantum well structures are well-preserved or even improved through the bonding process with the incorporation of superlattice blocking layers. This surprising enhancement in PL intensity results from a complex combination of atomic interdiffusion, strain relaxation, and defect gettering from the superlattice layers [16]. Building on this previous work, the active material structures presented in this dissertation make use of superlattice barriers between the quantum wells and the bonded interface in order to reduce the negative impact of the thermal annealing process.

3.3.1 Pre-Bond Wafer Characterization

Prior to processing, it is essential that basic material characterization steps be completed. The characterization methods used in this dissertation include micro-

photoluminescence (micro-PL) measurements for estimation of the peak-gain wavelength and reflectivity spectrum measurements, recorded with a spectrophotometer, for an accurate determination of layer thicknesses. The procedure used in this dissertation is similar to that outlined in [23]. The spectrophotometer measurements are particularly important for vertical-cavity devices where small deviations in the as-grown thickness may lead to nanometer-scale shifts in the cavity resonance wavelength. Precise thickness measurements of the active region and mirror structure allow for accurate simulations of the initial cavity mode of the completed MT-VCSOA structure. This simulation may then be used to determine the proper number of superlattice layers to be removed from the active region prior to bonding in order to fine tune the optical length of the semiconductor cavity (each half period is 7.5 nm in thickness, see Appendix B for further details on the materials structure). More importantly, completion of the materials characterization procedure ensures that both the mirror and active material meet the desired design specifications.

Although at first glance it may seem as though this procedure is less critical in wavelength tunable devices—where the resonant cavity mode may be dynamically adjusted post processing—there still exists an optimum active region thickness for these structures. In this case, it is imperative that the optical standing wave peaks be positioned properly in the cavity in order to maximize the gain enhancement factor over the tuning range of the device (Section 5.4.1). Furthermore, with the electrostatic tuning element, it is crucial that the wavelength of the initial cavity

mode be longer than the peak gain of the active material. This requirement is dictated by the blue-shift-only limitation of the tuning mechanism.

While describing the pre-bond characterization process, the following section also underscores both the pros and cons of the wafer bonding procedure. On one hand, because the bonding process requires separately grown active material and DBR structures, it is possible to fine tune the cavity length and choose optimized top and bottom mirror material, allowing for increased freedom and flexibility in design when compared with single-growth processes. At the same time, the need for the production and assembly of three separate wafers to construct the optical cavity can also be seen as a potentially difficult and costly process. The debate still continues over the merits of the wafer bonding process.

The first step in the material characterization process involves measuring the photoluminescence (PL) of the multiquantum well active material. This procedure is completed on a custom built micro-PL measurement system, described in detail in [23]. As a basic description, the system uses a microscope to deliver 980-nm diode laser pump light to a wafer under test and then collects the generated photoemission. The pump light is delivered to the sample under test through one of three microscope objectives resulting in pump spot-sizes of 3, 5, and 15 µm. The position of the wafer relative to the objective is controlled by a motorized two-axis stage exhibiting a 1-µm accuracy. Both full wafer scans and single point measurements are possible with this system.

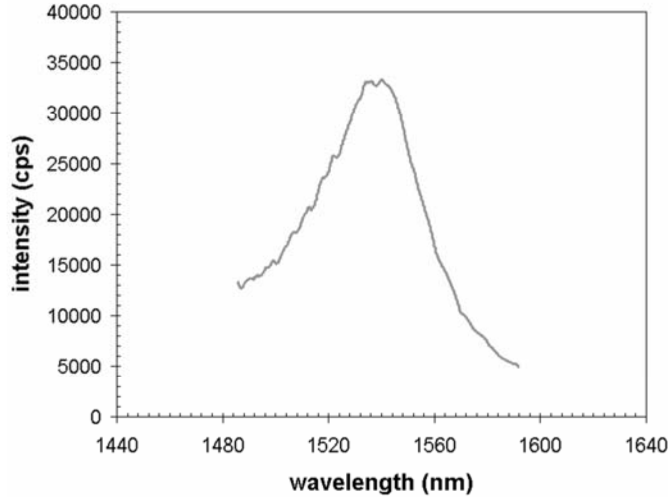

Fig. 3.2: PL spectrum of the 28 well active region. The FWHM of the curve is about 55 nm and compares well with typical VCSEL MQW structures given the relatively large number of QWs.

The critical wafer parameters to be measured with the micro-PL system are the FWHM and intensity of the PL spectrum, the peak wavelength of the PL, and the uniformity of the peak wavelength across the wafer surface. In this dissertation full wafer PL scans are only used to characterize the wafers as received from the manufacturer—in subsequent process runs single-point PL measurements are made in order to estimate the peak gain wavelength of the active material (Fig. 3.2). Sample sizes used in this work were approximately 8 mm by 8 mm; however, it is important to note that this sample size was dictated by the limited area of the graphite fixture used for wafer bonding and, furthermore, by a desire to conserve material. The wafer bonding procedure has been successfully demonstrated for compound semiconductor materials on full 2” wafers for the fabrication of commercial optoelectronic devices including transparent substrate LEDs [24] and double-bonded VCSELs [25], [26].

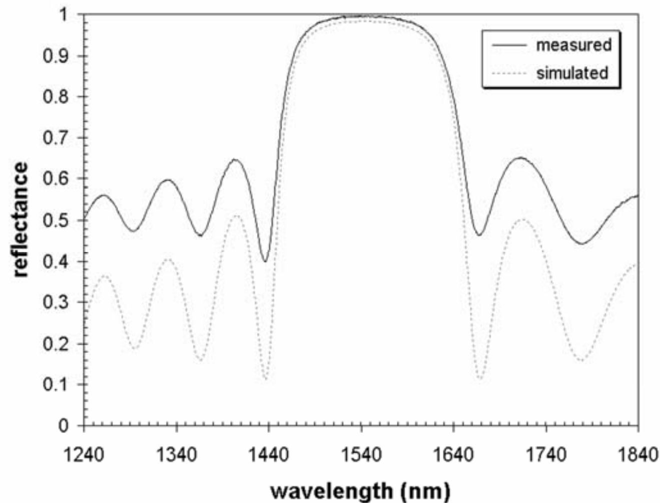

Fig. 3.3: Theoretical and experimental reflectance spectrum of a 14 period GaAa/$Al_{0.98}Ga_{0.02}As$ DBR. The simulated curve is generated using a transmission matrix solver (VERTICAL).

After recording the PL characteristics of the active region, the next step is to measure the precise thickness of both the InP-based active region and the GaAs-based mirror material using a spectrophotometer. Reflectivity measurements are conducted on the as-grown DBR material prior to bonding in order to determine the mirror stopband width and the wavelength of peak reflectance. The reflectivity data from the spectrophotometer is then fit using a transmission matrix software package (VERTICAL) to ascertain the precise thickness of the quarter wave layers, an example of this is included in Fig. 3.3. This data allows for an accurate determination of the growth error of the measured samples. It is important to note that when using the spectrophotometer it is not possible to directly measure the reflection spectrum of the MEMS-tunable DBR containing the air gap layer. However, by matching the VERTICAL simulations with the as grown mirror structure (with the unetched AlGaAs sacrificial layer) it is possible to estimate the

peak reflectance and stop band of the tunable mirror structure following release of the MEMS device, assuming the resulting air-gap thickness is equal to the as-grown thickness of the AlGaAs sacrificial layer.

Similar measurements and fitting procedures are also carried out on the InP-based active region in order to determine the as-grown cavity length. However, in this case, the InP substrate must be removed in order to achieve precise measurements of the active region thickness alone. This is realized by transferring the active material to a glass slide for both structural support and optical transparency. After cleaving a small sample from the center of the active wafer, the sample is mounted to a glass slide using high temperature wax. Following wax mounting, the substrate is removed in a 3:1 solution of $HCl:H_2O$, which requires about two hours to remove the roughly 400-μm thick substrate. The wet etch terminates on a 150-nm thick InGaAs etchstop layer. Following substrate removal, the InGaAs layer is removed using a 30-second etch in $H_2SO_4:H_2O_2:H_2O$ (1:1:10). With the active region transferred to the glass slide and the InP substrate removed, the reflectance spectrum of the cavity is measured.

After fitting the active material reflectance spectrum using VERTICAL, the simulated mirror material and active region can be combined to form a model optical cavity (Fig. 3.4). The design of the MT-VCSOA active region incorporates a number of superlattice periods that allow for accurate adjustment of the initial optical cavity length (individual superlattice layer thickness of 7.5 nm, with 3 periods sandwiching the MQW structure). By fitting the measured reflectivity spectrum, it is possible to calculate optimal thickness of the active region and determine the required number

of superlattice periods that should be removed. Here, the goal is to keep the electric-field standing wave centered on the QWs despite the growth-rate errors, and also to adjust the initial optical path length of the cavity.

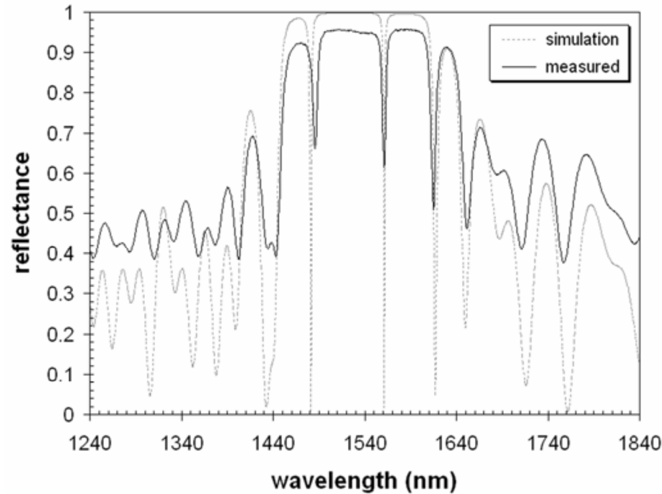

Fig. 3.4: Third generation MT-VCSOA reflectance spectrum following the second wafer bond, both simulated (VERTICAL) and measured values are included in the figure.

Due to the non-destructive nature of the mirror measurement process, the DBR thickness measurements are made for both the top and bottom mirrors during each process run. In contrast, the active region cavity thickness measurements are carried out only once after receiving the active material from the supplier, and this data is then used for each subsequent process run. Typical growth errors for the epitaxial material used in this dissertation were on the order of a few percent—well within the tolerance of the design specifications and only requiring the removal of one or two superlattice periods from the active region.

3.3.2 Wafer Bonding Process

In direct wafer bonding, the surfaces under consideration are bonded without the use of intermediate layers such as metals or adhesives. The ultimate goal of this process is to form a permanent covalently bonded junction between two dissimilar materials. Because of the need for an optically transparent interface, it is critically important to have surfaces free from particles, voids, oxides, and organic contaminants. Generally, cleanliness of the wafer surface is the paramount requirement for successful wafer bonding. In light of this fact, a thorough cleaning procedure was developed. This process is based upon a long line of GaAs to InP wafer bonding developed for long-wavelength VCSELs and VCSOAs at UCSB. This section presents a description of the general steps required to complete the bonding procedure, while a detailed process traveler is presented in Appendix C.

The wafer bonding procedure begins with the etching of a grid-like pattern of channels in the GaAs bottom mirror wafer using a solution of H_3PO_4:H_2O_2:H_2O (2:1:60) for 23 seconds. These channels allow for the escape of trapped gas and liquid during the thermal anneal step. A channel pitch of 250 μm in both directions, along with an etch depth of 1000 Å, have proven to be suitable [15]. The channel itself is roughly 5 μm in width. Surface morphology of the bonded wafers is also a relevant issue. Using smooth surfaces with low defect densities reduces the number of voids in bonded structures and leads to greater total bonding yield. However, it was found that the epi-wafers used in this work were suitable for bonding without the need for defect removal. After patterning the channels, the cleaning process

begins with a solvent soak in acetone and then isopropanol to achieve initial removal of organic contaminants from the surface of the samples. Next, coarse particulate removal is realized by physically scrubbing the sample surface with a cotton tipped swab in an acetone bath. After a spray rinse in isopropanol, the samples are scrubbed in a surfactant solution (5 drops of Tergitol dissolved in one liter of deionized water) using a nylon swab, in order to remove any fine particulates that remain on the sample surface. The surfactant nature of the Tergitol solution prevents generated particles from adhering to the sample surface. After cleaning, the sample is thoroughly rinsed in deionized water.

Following the solvent and surfactant cleaning process, great care is taken to ensure that the patterned surface of the GaAs bottom mirror wafer is free of photoresist residue. To achieve an organic free surface, an oxygen plasma is used to remove volatile hydrocarbons from the surface of the wafer. The resulting surface oxide is then etched with a buffered oxide etch solution. A similar process is carried out on the unpatterned InP sample in order to remove both organic contaminants, as well as the native oxide layer. Due to equipment limitations, it was necessary to transport the cleaned wafers to a separate facility for bonding. To remove the native oxide formed during the brisk walk across campus, a dilute NH_4OH solution was used. Next, the wafers are transferred to a non-oxidizing solvent (methanol) and pressed into physical contact to initiate bonding. For annealing, the samples are placed in a graphite fixture and loaded into an atmosphere controlled quartz tube-furnace. A detailed description of the graphite fixture, including schematic drawings, can be found in [23].

In this fixture, pressure is applied to the samples by controlling the applied torque on four graphite studs. Here, the applied torque determines the bonding pressure and a torque of 0.37 lb-in is used for all bonds. From previous measurements with a calibrated load cell [23], the approximate force, in units of N, is determined by multiplying the torque in lb-in by 343. Thus, for the bonding conditions used in this dissertation, the applied force is roughly 127 N and the resulting pressure for an 8 mm by 8 mm sample is about 2 MPa. Uniform pressure application is essential to a successful bonding process; thus, the fixture incorporates a hemispherical dome to achieve even load application. Bonding is completed in a quartz tube-furnace with a nitrogen ambient. The furnace temperature is elevated to 600 °C at a rate of 85 °C per minute (all samples fabricated in this dissertation used an anneal temperature of 600 °C). The wafers are held at the anneal temperature for 30 minutes and then cooled at 10 °C per minute to 300 °C to avoid excessive strain arising from the large difference in thermal expansion between the GaAs and InP samples.

Following the first bond—GaAs bottom mirror wafer to InP active region, the InP substrate is removed to facilitate further processing. To allow for reproducibility in the substrate removal process, an etch stop layer is included in the epitaxial structure, as discussed in Section 3.3.1. A detailed description of the material structure for the MT-VCSOA is included in Appendix B. The InP substrate is removed using a 3:1 HCl:H_2O solution. This solution has an etch rate of approximately 8 μm per minute and terminates on a 150-nm InGaAs etch stop layer.

The ternary etch stop material is then removed with a 30-second etch in $H_2SO_4:H_2O_2:H_2O$ (1:1:10).

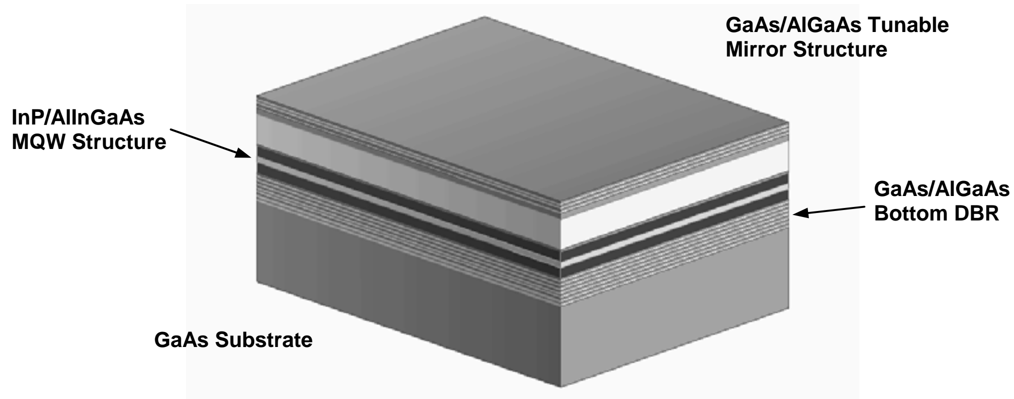

Fig. 3.5: Double wafer bonded structure. In this case, an InP-based MQW active region (black structure) is incorporated between two GaAs/AlGaAs DBRs and supported by a GaAs substrate. The thick layer above the active region is the AlGaAs sacrificial etch layer.

A second wafer bond is necessary to combine the previously bonded bottom mirror/active structure with the GaAs/AlGaAs top mirror. For the second bond the process is identical to that described above; it is interesting to note that the second bond process is typically more forgiving (i.e. yield at least equal to that of the first bond), due to the reduced thermal mismatch between the bonded samples. Following the second bond, the GaAs substrate of the top DBR is removed using a combination of mechanical lapping and wet chemical etching. Lapping is carried out by hand with a thickness adjustable fixture on sheets of 12 μm grit paper. Lapping was continued until the to-be-removed GaAs substrate thickness was reduced to less than 100 μm in thickness. Following lapping, a solution of 30:1 $H_2O_2:NH_4OH$ was used to

chemically etch the remainder of the GaAs substrate. This etch terminates on an $Al_{0.90}Ga_{0.10}As$ etch stop layer. To complete the bonding procedure, the etch stop layer is removed in a dilute HF solution (1:10 HF:H_2O). The double bonding process results in a transferred InP epitaxial film (the active region) sandwiched between two GaAs/AlGaAs DBRs and supported by a GaAs substrate, as shown in Fig. 3.5.

3.4 Basic Fabrication Sequence Following Bonding

The same general fabrication procedure holds for all of the MT-VCSOAs demonstrated in this dissertation. Key differences in subsequent generations of devices will be highlighted in the following sections. For the fabrication procedure presented here, all lithographic patterning is carried out using a suitable positive or negative photoresist on a standard contact alignment system; see Appendix D for the detailed process traveler for each generation of devices.

3.4.1 General Processing Procedure

Following wafer bonding, the fabrication procedure begins with the definition of the DBR pillar using a chlorine-based reactive ion etch (RIE). For the first two generations of devices, the DBR pillars (consisting of 4 or 5 periods of GaAs/$Al_{0.98}Ga_{0.02}As$) were etched using a $SiCl_4$ plasma. For the final generation of devices, the DBR pillar stack was increased to 15-periods and was etched using Cl_2/BCl_3. A schematic of the sample following the DBR pillar etch is shown in Fig.

3.6. In order to accurately and reproducibly control the etch depth, this process utilizes laser endpoint detection for in-situ etch depth monitoring.

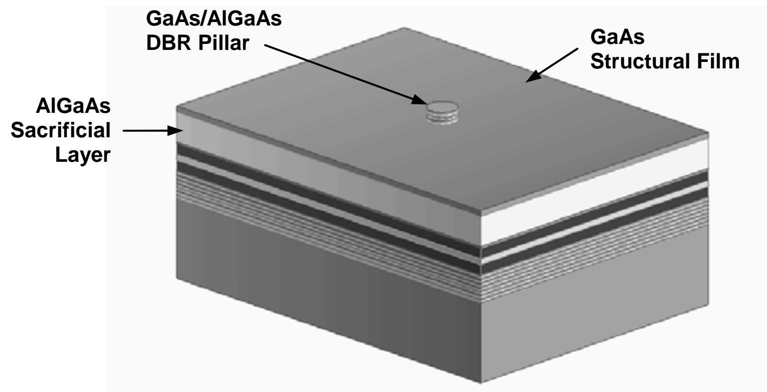

Fig. 3.6: Definition of DBR pillar using a chlorine-based plasma etch. In this process a photoresist mask is used to define the pillar and laser endpoint detection is used to control the etch depth.

With the initial devices, the DBR pillar was around 1 μm in thickness and it was trivial to reproducibly stop on the non-selective GaAs structural layer over the area of the sample. However, in the Generation 3 devices with a 15 period 92% Al content DBR, the total height of the DBR pillar was increased to approximately 5 μm. For the DBR etch, the $SiCl_4$ etch exhibited poor uniformity over the sample area—resulting in over-etching at the edges of the chip (here the plasma would punch through the structural film) and under-etching in the sample center (leaving unwanted DBR periods on the GaAs structural film). Previous process development on wafer bonded VCSELs had demonstrated that a Cl_2/BCl_3 plasma etch was capable of achieving the required uniformity over the sample surface. Additionally, this chemistry provided an increased etch rate.

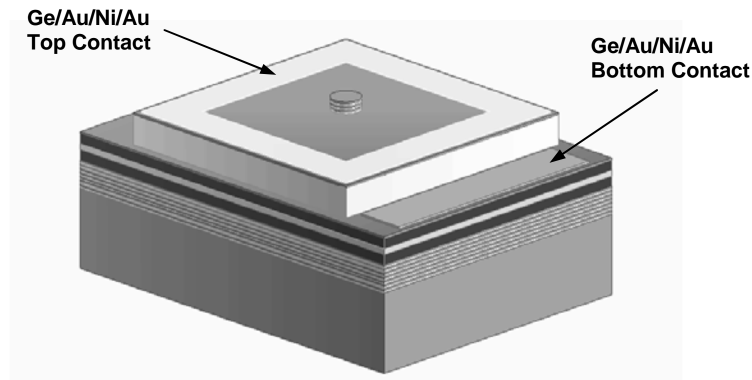

Fig. 3.7: Ohmic contacts are formed on n^+ GaAs using electron beam deposited Ge/Au/Ni/Au. After patterning by liftoff, the contact metal is alloyed under a forming gas ambient at 430 ºC.

After defining the DBR pillar, the common n^+ GaAs bottom contact layer is exposed with a series of alternating GaAs/AlGaAs selective wet etches. Next, Ge/Au/Ni/Au is deposited on the n^+ contact layers via electron beam evaporation. Following liftoff, the patterned contact metal is alloyed by annealing in forming gas at 430 ºC. In these devices the diode for the electrostatic actuator is reversed biased and ideally the current flow is negligible (measured to be in the nA range). Due to the extremely low current flow, no attempt was made to characterize the contact resistance of the films. A schematic of the patterned contacts is included as Fig. 3.7.

Following contact definition, the chip is blanket coated with SiN_x deposited by plasma enhanced chemical vapor deposition (PECVD). This film creates a slight tensile stress (260 MPa) in the structure to ensure the flatness of the free-standing membrane. Additionally, the SiN_x film acts as a hard mask for subsequent etch steps. Windows for access to the ohmic contacts and optical input/output are then dry

etched through the SiN_x film using a CF_4/O_2 plasma. Using the same etch chemistry, the actuator geometry is defined in the SiN_x hard mask. This pattern is then transferred through the GaAs structural layer and AlGaAs sacrificial material with a $SiCl_4$ RIE step (see Fig. 3.8) using in-situ laser monitoring to accurately stop on the approximately 115-nm thick n^+ GaAs bottom contact layer. In this case, $SiCl_4$ is used for all devices. For the second and third generation of devices, a low temperature dielectric liftoff step is performed prior to the membrane undercut etch in order to mask the sacrificial material beneath the support structure and physically constrain the outer edges of the support material. A detailed description of this procedure is presented in Section 5.1.2. For the bottom-emitting devices of Generation 3, additional processing steps are required including backside lapping/polishing, as well as the deposition of a SiO_x AR coating, as discussed in Section 6.1.2.

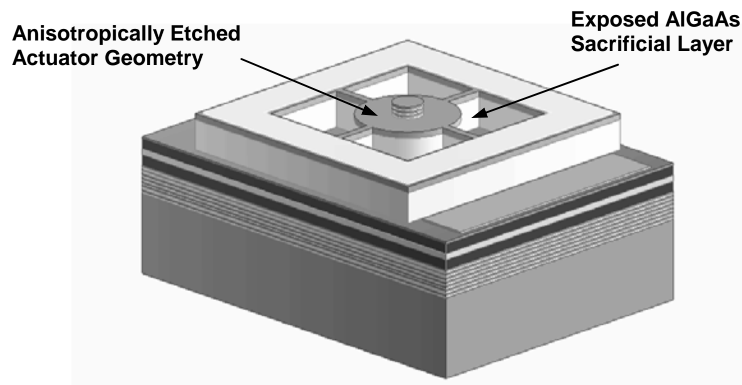

Fig. 3.8: Anisotropic etch of the actuator geometry through the GaAs structural layer and AlGaAs sacrificial material using a $SiCl_4$ plasma.

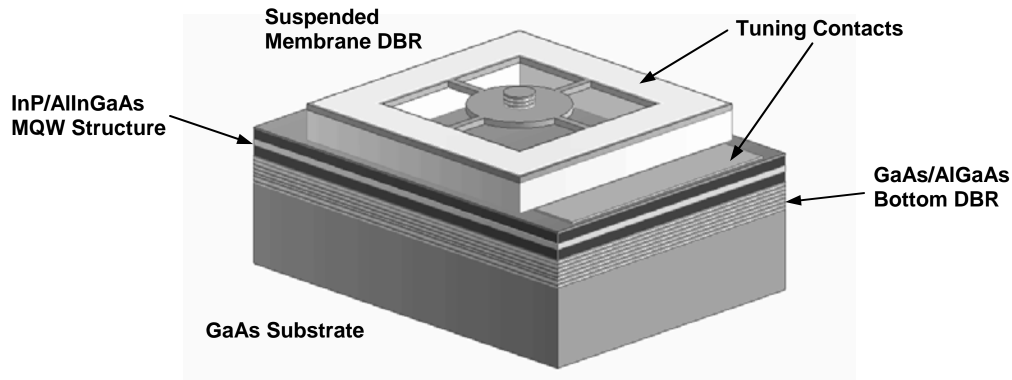

Fig. 3.9: Completed electrostatic actuator following the undercut of the membrane using dilute HCl. CO_2 critical point drying is utilized in order to avoid collapse of the free-standing structure.

Prior to the release etch, a photoresist mask is spin coated and defined with standard contact lithography in order to protect the AlGaAs in the DBR pillar and the sacrificial material between neighboring devices. To create the air-gap, the sacrificial AlGaAs layer is selectively wet-etched with a dilute HCl solution. For Generations 1 and 2, using $Al_{0.98}Ga_{0.02}As$ as a sacrificial material, the undercut etch solution consisted of 5:1 H_2O:HCl. Dropping the Al content to 85% in the third generation of devices required a much higher acid content, in this case 2:1 HCl:H_2O. In the undercut etch procedure, HCl is chosen over HF-based solutions in order to realize greater flexibility in fabrication. In this case, dielectric films including the SiN_x hard mask/tensile film, SiO_2 clamping layer, and dielectric-based AR coatings are impervious to HCl. As a result of the undercut etch, the p^+ AlGaAs layer directly below the GaAs membrane is removed from the optical cavity. This procedure eliminates the need for light to travel through highly p-doped material, thereby

minimizing absorption loss. In order to avoid collapse and resulting stiction of the membrane structure, due to surface tension forces in the wet etch, a CO_2 critical-point dryer is used. A solid model of a completed device is shown in Fig. 3.9.

3.5 Additional Processing Notes

By far the most time intensive portion of this dissertation involved the process development for these devices. Initially, simple "dummy" tunable filter structures, consisting of two sets of DBRs separated by an air gap, were constructed in order to refine the DBR pillar etch, membrane definition, and undercut etch. These process steps were then transferred to double-bonded structures in order to fabricate the first generation of active devices. The fabrication procedure for the first generation of MT-VCSOAs required a total of nine lithography steps, including two channel-etch steps to facilitate wafer bonding, using 6 total mask layers. Fortunately, the smallest linewidth for these devices was roughly 5-μm and the alignment tolerance between levels was only within a couple of micrometers. The total number of photolithography steps for all devices could have been reduced by two, by combining the SiN_x hard-mask etch steps, including the contact window definition and actuator etch. However, combining these levels constrains the order of the process, making it difficult to add or remove additional steps without ordering a revised mask set. For the MT-VCSOAs, a modular approach was utilized to allow for flexibility in the process flow. After a few trial runs with the tunable filter structures, a total of eight process runs were carried out on bonded material before

the first successful MT-VCSOA chip was fabricated. In this process, the undercut etch and the chlorine-based RIE etch of the actuator structure (including the GaAs membrane and AlGaAs sacrificial material) proved to be the most challenging steps.

For the revised mechanical design of Generation 2, an additional process step was required to create the mechanical clamping layer, resulting in a total of ten lithography steps. After a thorough investigation of the conformality of the inductively-coupled-PECVD (ICPECVD) SiO_2 mechanical constraint film, and an equally thorough investigation into the patterning of this film using liftoff, two process runs were carried out on bonded structures resulting in two successful device runs for Generation 2. This success was attributed to the large amount of preparation undertaken on the dummy samples before moving to the active material, and can also be attributed to the knowledge gained through the repetitive failures in the fabrication of the initial generation of devices.

The final generation of devices proved to be somewhat more difficult than first assumed. The basic fabrication procedure for the Generation 3 MT-VCSOAs was carried over from Generation 2, with variations being the longer DBR pillar etch (which ended up requiring a new etch chemistry) the need for backside polishing, SiO_x AR coating evaporation, clamping layer stress relief, and a revised wet etch chemistry for the $Al_{0.85}Ga_{0.15}As$ sacrificial layer. With two wafer bonds, eleven photolithography steps, five wet etches, six dry etches, one metal deposition and anneal, three CVD dielectric depositions, backside lapping and polishing, AR coating evaporation, membrane undercut etch and finally CO_2 critical point drying

the process was a relatively formidable task. Difficulties in this process included the inability to stop reproducibly on the non-selective 350-nm thick structural layer over the surface of the sample—due to etch rate variations across the chip with the 5-μm thick DBR—difficulties in a repeatable backside polish, and finally poor AR coating reproducibility. After a few months of process development on dummy tunable filter samples, the Generation 3 process was transferred to bonded material and required a total of three process runs before a successful chip was fabricated.

3.6 Summary

The general fabrication procedure for the three generations of MT-VCSOAs employs a combination of GaAs to InP direct wafer bonding and AlGaAs micromachining. Although not a common micromechanical material, GaAs and its related alloys exhibit a number of unique properties for MEMS applications. Previously demonstrated devices in GaAs include optical switches and microwave components such as suspended spiral inductors and RF switches. The fabrication procedure for tunable VCSOAs begins with the direct wafer bonding process. In these devices, wafer bonding is used to combine the high gain long-wavelength AlInGaAs/InP active material, with the excellent thermal and optical properties of GaAs/AlGaAs DBRs. Following wafer bonding, a series of dry and wet etch processes are used to define the DBR pillar, ohmic contacts for the electrostatic actuator, and finally the air gap and suspended membrane structure.

References

[1] A. Black, A. R. Hawkins, N. M. Margalit, D. I. Babić, A. L. Holmes, Jr., Y.-L. Chang, P. Abraham, J. E. Bowers, E. L. Hu, “Wafer fusion: materials issues and device results,” *IEEE J. Select. Topics Quantum Electron.*, vol. 3, pp. 943–951, Jun. 1997.

[2] K. Hjort, “Gallium arsenide micromechanics,” Ph.D. dissertation, Uppsala University, Uppsala, Sweden, 1993.

[3] Z. L. Zhang, N. C. MacDonald, "Fabrication of submicron high-aspect-ratio GaAs actuators," *J. Microelectromech. S.*, vol. 2, pp. 66–73, Jun. 1993.

[4] O. Blum Spahn, C. T. Sullivan, T. Bakke, A. Allerman, “Promise and Progress of GaAs MEMS and MOEMS,” in *Digest of the 2001 International Conference on Compound Semiconductor Manufacturing Technology (GaAs MANTECH)*, 21–24 May 2001, Las Vegas, NV.

[5] P. Kner, T. Kageyama, J. Boucart, R. Stone, D. Sun, R. F. Nabiev, R. Pathack W. Yuen, “A long-wavelength MEMS tunable VCSEL incorporating a tunnel junction”, *IEEE Photon. Tech. Lett.*, vol. 15, pp. 1183–1185, Sep. 2003.

[6] M. Maute, F. Riemenschneider, G. Bohm, H. Halbritter, M. Ortsiefer, R. Shau, P. Meissner, M.-C. Amann, “Micro-mechanically tunable long wavelength VCSEL with buried tunnel junction,” *Electron. Lett.*, vol. 40, pp. 430–431, Apr. 2004.

[7] A. Syrbu, V. Iakovlev, G. Suruceanu, A. Caliman, A. Rudra, A. Mircea, A. Mereuta, S. Tadeoni, C.-A. Berseth, M. Achtenhagen, J. Boucart, E. Kapon, “1.55-μm optically pumped wafer-fused tunable VCSELs with 32-nm tuning range”, *IEEE Photon. Technol. Lett.*, vol. 16, pp. 1991–1993, Sep. 2004.

[8] M. S. Wu, E. C. Vail, G. S. Li, W. Yuen, C. J. Chang-Hasnain, “Tunable micromachined vertical cavity surface emitting laser,” *Electron. Lett.*, vol. 31, pp. 1671–1672, Sep. 1995.

[9] M. C. Larson, A. R. Massengale, J. S. Harris, Jr., “Continuously tunable micromachined vertical-cavity surface-emitting laser with 18 nm wavelength range,” *Electron. Lett.*, vol. 32, pp. 330–332, Feb. 1996.

[10] F. Riemenschneider, M. Aziz, H. Halbritter, I. Sagnes, P. Meissner, “Low-cost electrothermally tunable optical microcavities based on GaAs,” *IEEE Photon. Technol. Lett.*, vol. 14, pp. 1566–1568, Nov. 2002.

[11] E. Yablonovitch, T. Gmitter, J. P. Harbison, R. Bhat, "Extreme selectivity in the lift-off of epitaxial GaAs films," *Appl. Phys. Lett.*, vol. 51, pp. 2222–2224, Dec. 1987.

[12] J. Boucart, C. Starck, F. Gaborit, A. Plais, N. Bouche, E. Derouin, J. C. Remy, J. Bonnet-Gamard, L. Goldstein, C. Fortin, D. Carpentier, P. Salet, F. Brillouet, J. Jacquet, "Metamorphic DBR and tunnel-junction injection. A CW RT monolithic long-wavelength VCSEL," *IEEE J. Select. Topics Quantum Electron.*, vol. 5, pp. 520–529, May/Jun. 1999.

[13] Z. L. Liau and D. E. Mull, "Wafer fusion: a novel technique for optoelectronic device fabrication and monolithic integration," *Appl. Phys. Lett.*, vol. 56, pp. 737–739, Feb. 1990.

[14] R. J. Ram, J. J. Dudley, J. E. Bowers, L. Yang, K. Carey, S. J. Rosner, K. Nauka, "GaAs to InP wafer fusion," *J. Appl. Phys.*, vol. 78, pp. 4227–4237, Sep. 1995.

[15] D. I. Babic, "Double-fused long-wavelength vertical-cavity lasers," Ph.D. dissertation, University of California, Santa Barbara, Santa Barbara, CA, 1995.

[16] K. A. Black, "Fused long-wavelength vertical-cavity lasers," Ph.D. dissertation, University of California, Santa Barbara, Santa Barbara, CA, 2000.

[17] E. F. Schubert, *Light-Emitting Diodes*, Cambridge, UK: Cambridge University Press, 2003.

[18] A. R. Hawkins, W. Weishu, P. Abraham, K. Streubel, J. E. Bowers, "High gain-bandwidth-product silicon heterointerface photodetector," *Appl. Phys. Lett.*, vol. 70, pp. 303–305, Jan. 1997.

[19] I. H. Tan, D. A. Vanderwater, J. W. Huang, G. E. Hofler, F. A. Kish, E. I. Chen, T. D. Ostentowski, "Wafer bonding of 75 mm diameter GaP to AlGaInP-GaP light-emitting diode wafers," *J. Electron. Mater.*, vol. 29, pp. 188–194, 2000.

[20] J. J. Dudley, "Wafer fused vertical cavity lasers," Ph.D. dissertation, University of California, Santa Barbara, Santa Barbara, CA, 1994.

[21] B. Liu, A. Shakouri, P. Abraham, K. Boo-Gyoun, A. W. Jackson, J. E. Bowers, "Fused vertical couplers," *Appl. Phys. Lett.*, vol. 72, pp. 2637–2638, May 1998.

[22] K. A. Black, P. Abraham, A. Karim, J. E. Bowers, E. L. Hu, "Improved luminescence from InGaAsP/InP MQW active regions using a wafer fused

superlattice barrier," in *Proc. 11th Int. Conf. InP and Related Materials (IPRM '99)*, May 16–20, 1999, pp. 357–360.

[23] J. Geske, "Ultra-wideband WDM VCSEL arrays by lateral heterogeneous integration," Ph.D. Dissertation, University of California, Santa Barbara, Santa Barbara, CA, 2004.

[24] Tan, D. A. Vanderwater, J. W. Huang, G. E. Hofler, F. A. Kish, E. I. Chen, T. D. Ostentowski, "Wafer bonding of 75 mm diameter GaP to AlGaInP-GaP light-emitting diode wafers," *J. Electron. Mater.*, vol. 29, pp. 188–194, 2000.

[25] V. Jayaraman, J. C. Geske, M. H. MacDougal, T. D. Lowes, F. H. Peters, D. VanDeusen, T. C. Goodnough, S. P. Kilcoyne, D. Welch, "High temperature 1300-nm VCSELs for single-mode fiber-optic communication," in *Digest of the LEOS Summer Topical Meetings 1999*, vol. 3, pp. 19–20, 1999.

[26] E. Kapon, "Wafer-fused VCSELs shape up for enterprise applications," *Compound Semiconductor*, Jan. 2005.

CHAPTER 4

Generation 1: Initial Device Demonstration

This chapter outlines the first ever demonstration of a micromechanically-tunable VCSOA. These devices build upon previous generations of fixed-wavelength VCSOAs, as well as the MEMS tunable vertical-cavity devices described in Section 1.2 [1]-[8]. As with subsequent generations of MT-VCSOAs, the initial demonstration devices are optically pumped gain-guided structures, operate in reflection mode, and incorporate a variable thickness air gap within the optical cavity. Electrostatic actuation of a suspended DBR structure results in 10 dB of on-chip gain over an 11-nm wavelength tuning range.

4.1 Top-Emitting MEMS-Tunable VCSOA

The initial generation of MT-VCSOAs was developed in parallel with the fixed wavelength 1550-nm VCSOAs demonstrated by Björlin and Kimura at UCSB [9], [10]. Similar to the fixed-wavelength devices, Generation 1 MT-VCSOAs are constructed using a double wafer bonding procedure, operate in reflection mode, are pumped with a 980-nm diode, and include a reduced reflectivity (transmissive) top mirror. In fact, these devices utilize the same bottom mirror and active region as the

non-tunable devices. The major difference in the structure of the tunable VCSOAs is the incorporation of a variable air gap in the top DBR, which is fabricated using the micromachining process described in the previous chapter. Wavelength tuning is achieved by altering the air-gap thickness with an integrated electrostatic actuator. The design of the deformable membrane structure is chosen to achieve a maximum required tuning voltage between 20–30 V (see Appendix A for details on the actuator geometry). Similar to previous generations of fixed-wavelength VCSOAs, the 980-nm optical pump is incident on the active region from the backside of the wafer, passing through the undoped GaAs substrate and bottom DBR. The long-wavelength signal enters/exits the device through the top mirror, which has a reduced reflectivity. By keeping the basic cavity structure similar to the top-emitting fixed-wavelength VCSOAs, development work on these devices could be readily transferred to the tunable structures and vice versa. Additional benefits of the top-emitting configuration include simplified fiber alignment and a reduced number of DBR pairs in the suspended portion of the top mirror—reducing the mass of the actuator and resulting in a decreased response time.

4.1.1 Material Structure

The first generation MT-VCSOAs utilize an InP/AlInGaAs active region that is bonded to two GaAs/AlGaAs DBRs via a direct wafer bonding procedure [11]. Utilizing wafer bonding, it is possible to combine the high gain, long-wavelength InP-based active material with the excellent thermal properties and high index

contrast of GaAs-based DBRs. The active region in these devices consists of a stacked MQW structure, containing five sets of five compressively strained AlInGaAs QWs placed at the peaks of the standing optical wave in a $5\lambda_c/2$ cavity, as seen in Fig. 4.1 (details of this structure are included in Appendix B). Each of the five sets of wells making up the individual MQW groups are arranged in a resonant periodic gain configuration in order to maximize the optical confinement [12]. When compared with the active region of a typical VCSEL, containing 3 to 7 quantum wells, this design incorporates a much larger number of wells (25 in total) in order to increase the per pass gain. The PL peak of this active region is designed to be at 1540 nm at room temperature.

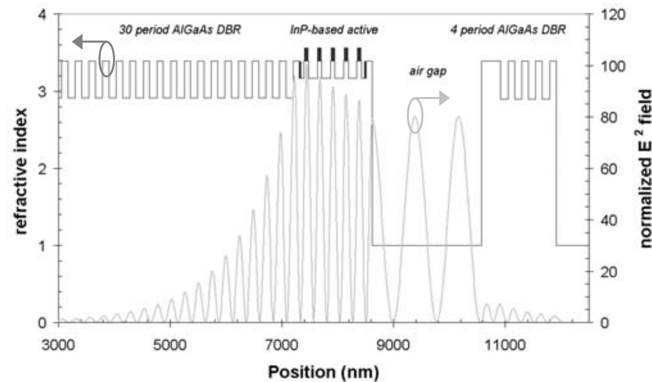

Fig. 4.1: Standing wave field distribution and refractive index profile of the 25-well active region.

The InP-based active material is grown by metal organic chemical vapor deposition (MOCVD). As the MT-VCSOA is designed for optical pumping, the DBRs and active region are undoped—though doping is required for the electrostatic

actuator. The only optically absorbing layers of the 980-nm pump in this design are the QWs, which allows for reduced heating and uniform pump absorption in the active region; however, this design also results in a low pump efficiency, as well as a reduced overall carrier density in the quantum wells for a given optical pump power.

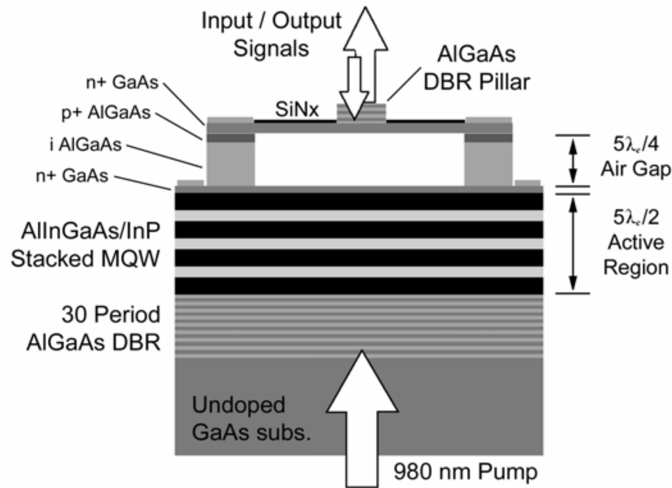

Fig. 4.2: Cross-sectional schematic of the Generation 1 MT-VCSOA material structure.

For the initial demonstration devices, the bottom mirror is a 30-period GaAs/$Al_{0.98}Ga_{0.02}As$ DBR with a calculated power reflectance of 0.999. Here, $Al_{0.98}Ga_{0.02}As$ is utilized for its high thermal conductivity, yet slightly slower oxidation rate, as compared with binary AlAs. The top DBR in these devices consists of 4 periods of GaAs/$Al_{0.98}Ga_{0.02}As$ on top of a $3\lambda_c/4$ n+ GaAs layer, a $5\lambda_c/4$ (optical thickness in air) $Al_{0.98}Ga_{0.02}As$ sacrificial etch layer, and a $\lambda_c/4$ n^+ GaAs layer directly above the active region that serves as the bottom electrode for the actuator. Both mirror structures are grown using molecular beam epitaxy (MBE).

The top mirror forms the SCC-design tunable DBR, including air gap as the first low index layer. The peak power reflectance of this structure is calculated to be 0.968 for 4 periods on top of the GaAs structural layer, including the contributions of the air gap. As grown, the AlGaAs top mirror wafer contains a 5 period DBR on the GaAs membrane layer; during the fabrication procedure one period is selectively removed to create the 4 period devices.

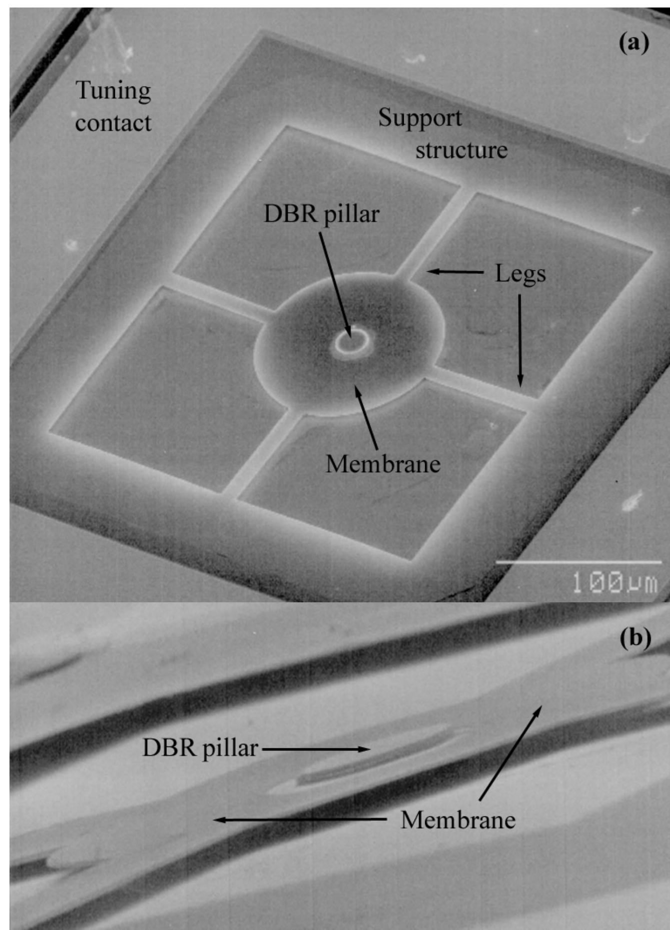

Fig. 4.3: SEM images of a completed Generation 1 MT-VCSOA showing (a) an overview of the device, and (b) angled close-up of the suspended membrane structure.

The electrostatic actuator incorporated in the top DBR is basically a parallel plate capacitor with one suspended electrode. As shown in Fig. 4.2, the GaAs membrane and the $\lambda_c/4$ GaAs layer closest to the active region are doped n^+. The sacrificial AlGaAs layer is comprised of 200 nm of p^+ $Al_{0.98}Ga_{0.02}As$, followed by 1750-nm of intrinsic $Al_{0.98}Ga_{0.02}As$. A reverse bias across the p-i-n portion of the diode creates an electrostatic force that results in the displacement of the membrane towards the substrate. With this actuator design, it is only possible to reduce the air gap; thus, it is only possible to blue shift the resonant wavelength of the VCSOA. The tuning diode is designed to have a reverse breakdown voltage of 60 V with the doping scheme described here. As discussed in the previous chapter, during the fabrication procedure a thin layer of tensile-stressed (260 MPa) SiN_x is deposited on top of the membrane and legs. This film creates a slight tensile stress in the structure to ensure the flatness of the free-standing membrane. Scanning electron micrographs of a completed device are included in Fig. 4.3.

4.2 Tunable VCSOA Characterization

Characterization of MT-VCSOAs requires precise measurements of both the optical and mechanical properties of the structure. This section outlines the variety of characterization tools utilized in this dissertation. To record the relevant properties of the amplifier, a custom built optical test setup is utilized. Mechanical characterization focuses on both the static and dynamic response of the MEMS actuator. Purely static (non-actuated) measurements of the membrane structure,

including characterization of the initial air-gap thickness and stress state of the actuator, were performed with a vertical scanning interferometer. Finally, quasi-static and dynamic measurements of the electrostatic actuator were made with the use of a custom microscope-coupled laser Doppler vibrometer.

4.2.1 Optical Test Setup

Optical characterization of the MT-VCSOA was completed with a semi-automated test system drawn schematically in Fig. 4.4. This system delivers the pump light to the bottom of the sample and has a top-side microscope capable of viewing the pump light leaking through the sample—allowing for rough alignment of the device-under-test with the pump beam. The entire measurement setup is controlled via a single LabVIEW program, which includes an automated 3-axis pump alignment routine, full stage motion and temperature control, data collection/storage, and pump laser power control. This system is described in further detail in [13].

For optical testing, an external cavity tunable laser diode operating near 1550 nm is used as the signal source, with the input signal power controlled by a variable optical attenuator. For peak gain measurements, the amplifier is operated below saturation with a typical input power level of -35 dBm. For saturation measurements the signal power is varied in increments of 5 dBm up to approximately 0 dBm. The input signal is coupled in through the top DBR using a long-wavelength fiber-focuser with a free-space beam waist of approximately 8 μm. As the device operates

in reflection mode, the amplified output is coupled back into the same focuser and a circulator (directional coupler) is necessary to separate the input and output signals. A 980 nm laser diode, which is coupled in through the bottom DBR by a second fiber focuser, serves as the optical pump. The use of optical pumping allows for the generation of a uniform carrier distribution given the large number of QWs. The pump focuser is optimized for operation at 980 nm and has a free-space spot size of approximately 12 μm. An optical spectrum analyzer (OSA) is used to record the characteristics of the VCSOA as a function of pump power, tuning bias, and wavelength.

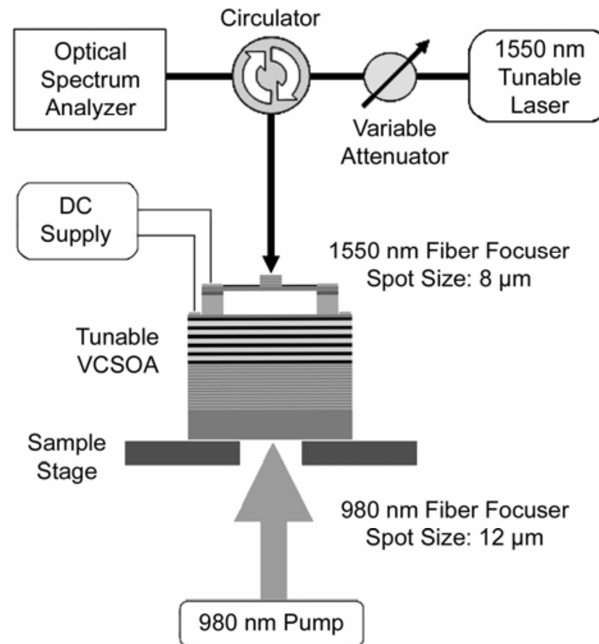

Fig. 4.4: Optical test setup for top-emitting devices. The spot sizes given for the two fiber focusers are the measured free-space values.

By recording the individual gain spectra as a function of wavelength, and fitting the data with Eq. 2.1, the variation in peak gain, top mirror reflectance, and single-pass gain may be determined over the wavelength span of the tunable VCSOA. In this case the tuning range is recorded by noting the wavelength of the amplified spontaneous emission (ASE) peak as a function of the applied bias to the electrostatic actuator. Saturation characteristics are measured by holding the tuning voltage and pump power constant and varying the injected signal power. The signal coupling loss for the optical test setup is measured to be about 7 dB. All testing is completed with the output signal coupled into single-mode fiber and sent to a calibrated OSA with a resolution bandwidth of 0.1 nm.

Analyzing an all-optical, active device such as an optically pumped VCSOA can be a daunting task. With these devices small adjustments in the alignment of the optical test setup results in significant changes in the coupling and pump efficiency. This naturally leads to difficulties in comparing data taken on different occasions. In order to minimize these problems, whenever possible, complete sets of data were taken without adjusting the alignment of the system.

4.2.2 Vertical Scanning Interferometer

In order to obtain quantitative information on the static air-gap thickness and stress state of the suspended portion of the electrostatic actuator, a white light interferometer is utilized. With MEMS devices, the use of stylus-based mechanical profilometry is a destructive technique. In contrast, optical profilometry is a non-

contact, and therefore non-destructive, means of generating quantitative surface geometry data with suspended micromechanical structures.

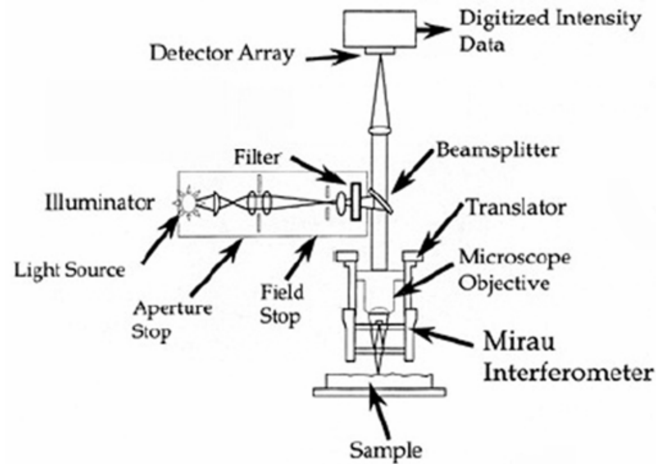

Fig. 4.5: Diagram of the Wyko NT1100 optical profiling system [14].

In this dissertation static surface profile measurements are made with a commercial optical profilometer; a schematic of this system may be seen Fig. 4.5. This profilometer consists of a fixed sample stage and a precision motorized optical assembly. The optical assembly is made up of a vertical translation system coupled to a Mirau interferometer. By monitoring the reflected phase from the sample surface as a function of the vertical position of the optics, the profiler is capable of producing high resolution three-dimensional surface measurements, including sub-nanometer vertical resolution, with lateral spot sizes ranging from a few square microns up to measurement areas of a few square millimeters when stitching is used. Using this system, direct measurements of the height of the suspended membrane structure, and information on the flatness (or tilt) of the membrane, can be found.

Furthermore, by measuring the deflection of simple bilayer cantilever test structures incorporated on the chip, it is possible to extract the stress state of the actuator.

4.2.3 Laser Doppler Vibrometer

Quasi-static and dynamic measurements of the response of the electrostatic actuator (including the displacement, velocity and frequency response) are carried out with a multidimensional MEMS-motion characterization system, as seen in Fig. 4.6 [15]. This characterization suite consists of a fiber-optic laser vibrometer coupled to an optical microscope incorporating long working distance objectives. With a 50x final lens, the minimum spot size is approximately 1 μm and can easily be focused on the center of the DBR pillar. Furthermore, the reference beam may be scanned across the surface of the actuator to map the position dependence of the actuator response. This setup also permits the integration of a small vacuum chamber with a topside viewport, which allows for testing over a wide range of pressures, from atmosphere to roughly 1.0 mTorr.

The optical-fiber vibrometer measures the pistoning motion of the suspended DBR through detection of the frequency and phase shift of a reference He-Ne laser signal. Utilizing a heterodyne configuration, the vibrometer is capable of determining the magnitude, as well as the sign, of the velocity and displacement. The vibrometer instrumentation is capable of resolving velocities to 0.1 μm/s and displacements to 4 nm, while operating with bandwidths up to 2.5 MHz. The real-time velocity and displacement information produced by the vibrometer is viewed using an oscilloscope, while frequency domain measurements are made with a vector

signal analyzer. Each of the instruments used in the test-setup are controlled via a custom LabView interface.

In order to characterize the static (or more accurately, quasi-static) response of the electrostatic actuator, the membrane displacement is measured as a function of applied voltage for a fixed driving frequency of 1 kHz. In this case the vibrometer output is sent to an oscilloscope for a direct measurement of the magnitude of displacement. In contrast, resonance curves are recorded for a fixed tuning bias and a varying driving frequency. Here, the velocity and displacement data are output from the vibrometer controller to a vector signal analyzer. Hysteresis in the resonance properties may be observed by sweeping the frequency in both directions.

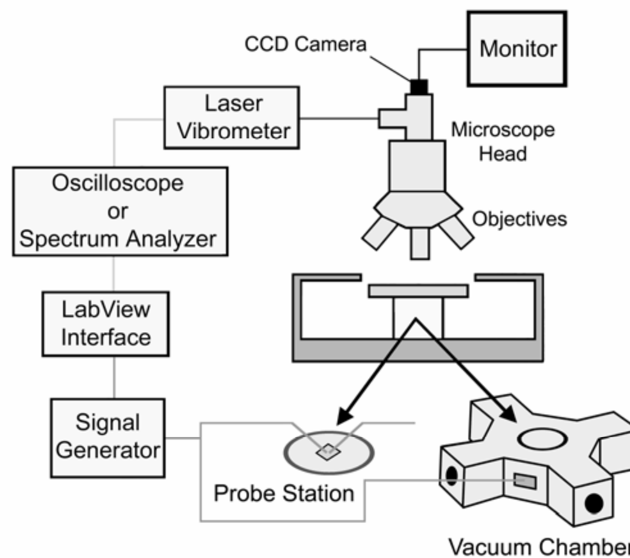

Fig. 4.6: Mechanical test setup: microscope coupled optical fiber vibrometer, from [15].

4.3 Generation 1 Results

As an initial demonstration, the first generation of tunable VCSOAs realized the goal of wide wavelength tuning of the resonant cavity mode and allowed for continuous tuning of the narrow gain bandwidth of the VCSOA. However, as described in this section, these devices were not without their limitations. Stress-related deformation of the actuator structure gave rise to high required tuning voltages, while oxidation of the unetched sacrificial AlGaAs led to cracking of the membrane and resulted in poor reliability. Finally, the changing properties of the resonant cavity with tuning reduced the effective tuning range of the amplifier.

4.3.1 Wavelength Tuning Response

The wavelength tuning response for a Generation 1 MT-VCSOA is shown in Fig. 4.7. In this device the membrane is displaced by approximately 340 nm with a reverse bias of 57 V. The quasi-static displacement of the released membrane is measured using a laser Doppler vibrometer. As expected, the deflection shows a parabolic dependence with the applied voltage and the experimental data matches well with the values generated by the one-dimensional electromechanical model described in Section 2.5.2. The 340-nm displacement results in a continuous blue-shift of the resonant cavity mode from 1590 nm to 1569 nm. With the membrane displacement known, the variation in wavelength of the resonant cavity mode as a

function of the air-gap thickness can be calculated using Eq. 2.17. Here, the tuning response follows the theoretical values extremely well—the points of largest error exhibit a red-shift in wavelength due to pump induced heating, which is not taken into account in the model.

The high required tuning voltages necessary with these devices result from a non-ideal initial air-gap thickness. Here, the increase in the air-gap thickness is due to stress related deformation of the mechanical support structure. Following processing, the air-gap thickness is measured using a vertical-scanning interferometer, revealing a much larger air gap than the ideal $5\lambda_c/4$ design of 1950 nm. The actual air-gap thickness measured for the device presented here is 3911 nm, due to stress related deformation of the undercut support structure. The large increase in the air-gap thickness—resulting from the support deformation—greatly diminishes the applied force and increases the required tuning voltage in this device.

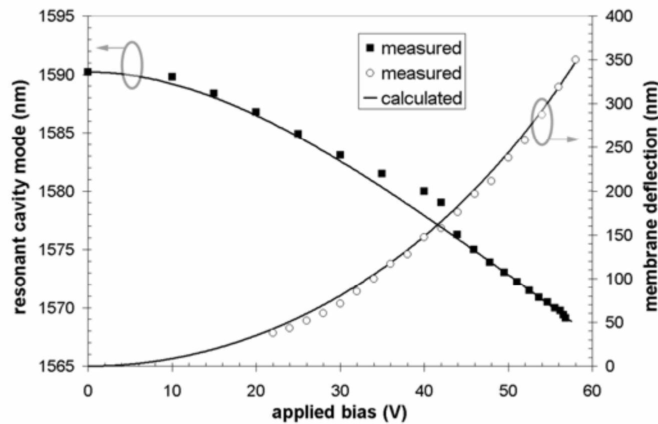

Fig. 4.7: Resonant wavelength and membrane deflection vs. tuning bias. The theoretical displacement curve is based on Eq. 2.15, while the calculated wavelength shift is generated using Eq. 2.17.

4.3.2 Signal Gain and Gain Bandwidth

Fig. 4.8 shows the MT-VCSOA gain spectra for various tuning voltages and pump powers, with an input signal power of -35 dBm. This result clearly demonstrates the first successful operation of a micromechanically tunable VCSOA and more importantly displays the key benefit of a tunable vertical-cavity amplifier—by varying the applied bias on the electrostatic actuator, the narrow gain spectrum of the VCSOA may be swept over the tuning range of the device. Thus, as shown in the figure, through the incorporation of wavelength tunability, the MT-VCSOA can be utilized as a channel selective amplifying filter.

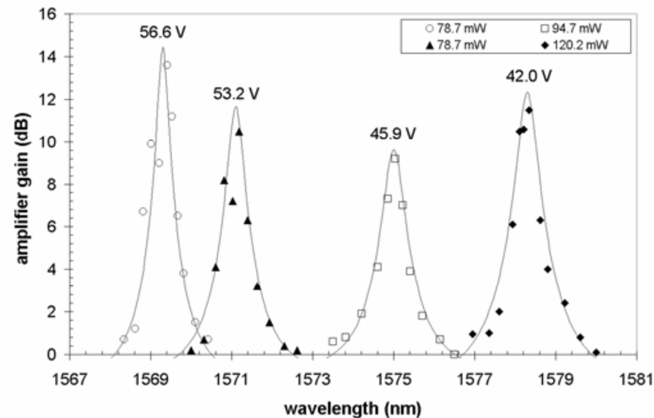

Fig. 4.8: Amplifier gain spectrum at multiple tuning bias values. The required pump power for each data set is included in the legend. Markers indicate measured values, while the solid lines are calculated curve fits based on the relationship for an FP cavity with gain, Eq. 2.1.

Upon examination of this data it is apparent that the device exhibits varying properties as a function of the resonant wavelength of the cavity. With increasing bias (tuning to shorter wavelengths) the MT-VCSOA displays a decrease in the gain

bandwidth and achieves an increase in the peak gain, even for the lower values of pump power shown. From fitting of the gain spectra in Fig. 4.8, the device exhibits a minimum gain bandwidth of 32.6 GHz and a peak amplifier gain of roughly 14 dB at 1569.3 nm. For longer operating wavelengths, the device displays a broadening of the amplifier gain spectrum and a decrease in the maximum achievable gain.

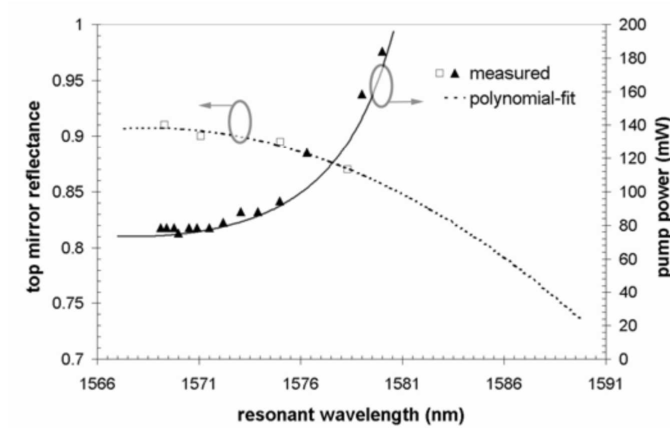

Fig. 4.9: Extracted top mirror reflectance and optical pump power required for 10 dB device gain as a function of the resonant wavelength of the optical cavity.

In order to characterize the MT-VCSOA two alternatives exist, including constant gain and constant pump power operation. An example of this first measurement technique is shown in Fig. 4.9; this plot presents the theoretical and experimental pump power required for 10 dB device gain (3 dB fiber-to-fiber), as well as the extracted mirror reflectance, as a function of the resonant wavelength of the optical cavity. The reflectance data is generated by fitting the individual gain spectrum at each tuning voltage using Eq. 2.1, while the theoretical required pump power curve is calculated by combining the carrier rate equation Eq. 2.9 with the

peak gain relationship given in Eq. 2.18. As shown in the plot, the MT-VCSOA must be tuned from 1590 nm to 1580 nm before 10 dB of device gain is observed (given a maximum pump power of 200 mW in the test setup). Device gain larger than 10 dB is measured for wavelengths between 1580 nm and 1569 nm, yielding an effective tuning range of 11 nm. A peak device gain of 17 dB is measured at 1570 nm.

Over the tuning range, the top mirror reflectance values increase from 85.7% at the initial cavity mode, to 90.7% near the breakdown voltage of the diode, which occurs at 57 V. The variation in mirror reflectance with tuning arises from the competing phases of the multiple reflections within the air cavity. Due to the non-ideal membrane deflection, the initial air gap results in an optical thickness near a multiple of $\lambda_c/2$. At this point, the reflection from the first air-semiconductor interface and the reflection from the bottom of the membrane are nearly out of phase. As the device is tuned, the decreasing air-gap thickness begins to approach an odd multiple of $\lambda_c/4$, and the reflected waves begin to add in phase, leading to a rapid increase in reflectance of the top mirror structure. Additionally, as the cavity mode is tuned closer to the active material gain peak, less pump power is needed to reach the same gain level.

In Fig. 4.10 the constant pump power (80 mW) characteristics of the MT-VCSOA are analyzed over the tuning range, including the peak gain performance and gain bandwidth. As the device is tuned to shorter wavelengths, the optical bandwidth decreases, reaching a minimum value near 1568 nm. The theoretical bandwidth curve is based on Eq. 2.4 and verifies the decrease in bandwidth as

recorded in Fig. 4.8. Also included in the figure is the peak gain of the amplifier as a function of the resonant wavelength of the optical cavity. In this case, the maximum on-chip gain is calculated to be 14.3 dB at 1568 nm with 80 mW of pump power. The theoretical peak gain curve is generated using Eq. 2.18. Here, the position of maximum gain and minimum bandwidth is dictated by the reflectance spectrum of the top mirror structure, and to a lesser extent, by the variation in the active material gain spectrum.

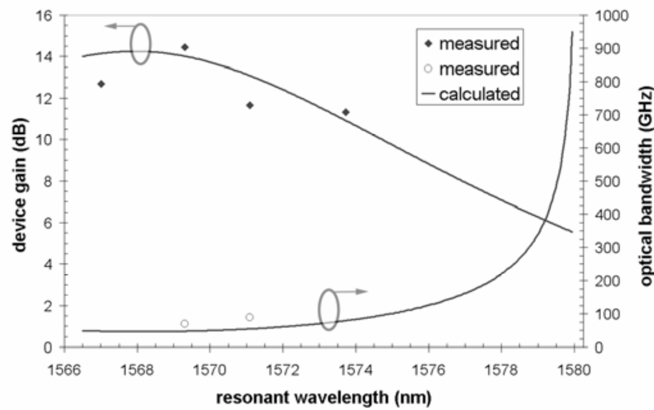

Fig. 4.10: Theoretical and experimental peak device gain and gain bandwidth of a first generation MT-VCSOA as a function of the resonant wavelength of the optical cavity.

Each of the measurement techniques described above, including constant gain and constant pump power measurements, allow for the determination of the properties of the MT-VCSOA when matched with the correct theoretical expressions outlined in Chapter 2. However, the constant pump power technique is simpler to implement, as the optical pump power can be directly controlled in the test setup.

Furthermore, by recording the amplifier characteristics (over the tuning range) for a variety of pump values, the constant gain characteristics can be backed out from the constant pump power data set. Thus, measurements for the following generations of MT-VCSOAs rely primarily on constant pump power operation.

4.3.3 Saturation Properties

The fiber-coupled amplifier gain as a function of the input signal power for a Generation 1 MT-VCSOA is presented in Fig. 4.11. For a tuning bias of 49.5 V (resonant wavelength of 1573.1 nm) and an optical pump power of 94.7 mW, the saturation input power, defined as the optical power at which the unsaturated gain drops by 3 dB, is found to be -12.8 dBm. Given a small signal fiber-to-fiber gain of 8.0 dB, the fiber-coupled saturation output power under these conditions is -7.8 dBm. With an increase in the tuning bias to 55.5 V and a decrease in the pump power to 81.9 mW (top curve in the figure), the resonant wavelength blue-shifts to 1570.0 nm and the saturation input power of the MT-VCSOA drops to -16 dBm, for an unsaturated fiber-coupled gain of 7.8 dB—resulting in a saturation output power of -11.2 dB. The theroretical curves (dashed lines) included in the figure are based on the following relationship [16]:

$$G = G_0\left(1+\frac{P}{P_{sat}}\right)^{-1} \qquad (4.1)$$

where G_0 is the unsaturated gain, P is the input signal power, and P_{sat} is the input power for which the gain drops by 3 dB. These saturation characteristics are typical

of the values measured for the initial generation of MT-VCSOAs and are comparable to the devices presented in [17], which exhibit an input saturation power of -17.6 dBm for an unsaturated on-chip gain of 11 dB (neglecting coupling loss). In comparison with state-of-the-art 1.5-μm fixed-wavelength VCSOAs, with a record high fiber-coupled output saturation power of +0.5 dBm [9], the saturation characteristics of the first generation MT-VCSOAs leave room for improvement.

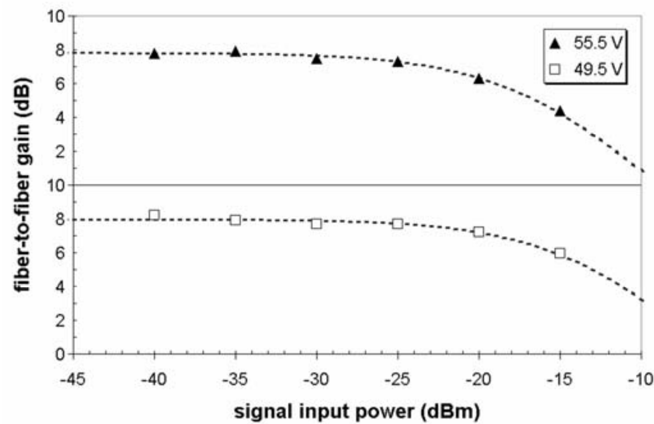

Fig. 4.11: Saturation properties of the first generation MT-VCSOA at two tuning bias values, corresponding to resonance wavelengths of 1573.1 nm (49.5 V) and 1570.0 nm (55.5 V). The dashed lines are theoretical fits based on Eq. 4.1.

Although no rigorous examination of the saturation properties were completed, it is possible to see that these devices follow similar trends as fixed wavelength VCSOAs. For increasing mirror reflectance (operation at shorter wavelengths, as in Fig. 4.9) the input saturation power is reduced, while the opposite is true for a reduced mirror reflectivity [9]. Unfortunately, in-depth measurements of the saturation characteristics were not made over the tuning range due to limitations in

the stability of the first generation of MT-VCSOAs. The main focus of the initial MT-VCSOAs was the demonstration and characterization of the peak gain response over the achievable wavelength span. The poor reliability of these initial devices proved to be a key limitation and will be discussed in the following section.

4.4 Limitations of the Initial Device Design

As touched upon briefly in the previous section, a number of deficiencies existed in the first generation of devices. This section highlights the two major limitations, including the high operating voltages and poor device stability. These limiting factors arise primarily from shortcomings in the mechanical design of the electrostatic actuator. Solutions to these problems will be addressed in the following chapter with the introduction of the second generation of MT-VCSOAs.

4.4.1 Control of Air-Gap Thickness

The most obvious issue with the initial demonstration devices is the excessively high operating voltages. Based on the mechanical design models presented in Chapter 2, these devices were predicted to have maximum tuning voltages between 25 and 35 V, depending on the geometry of the actuator (detailed actuator geometries may be found in Appendix A). Furthermore, the ultimate limit of the tuning range was expected to be controlled by the pull-in instability of the electrostatic actuator. However, as presented in Section 4.3.1, the required voltages of the Generation 1 devices tended to be on the order of 60 V and the tuning range

was limited by the reverse breakdown voltage of the intrinsic AlGaAs layer in the tuning diode. Measurements of the surface profile of the membrane structure reveal a lack of control over the initial air gap thickness. As seen in Fig. 4.12, the air gap is roughly twice the as-grown thickness of the AlGaAs sacrificial material, due to out-of-plane deformation of the actuator and mechanical support structure.

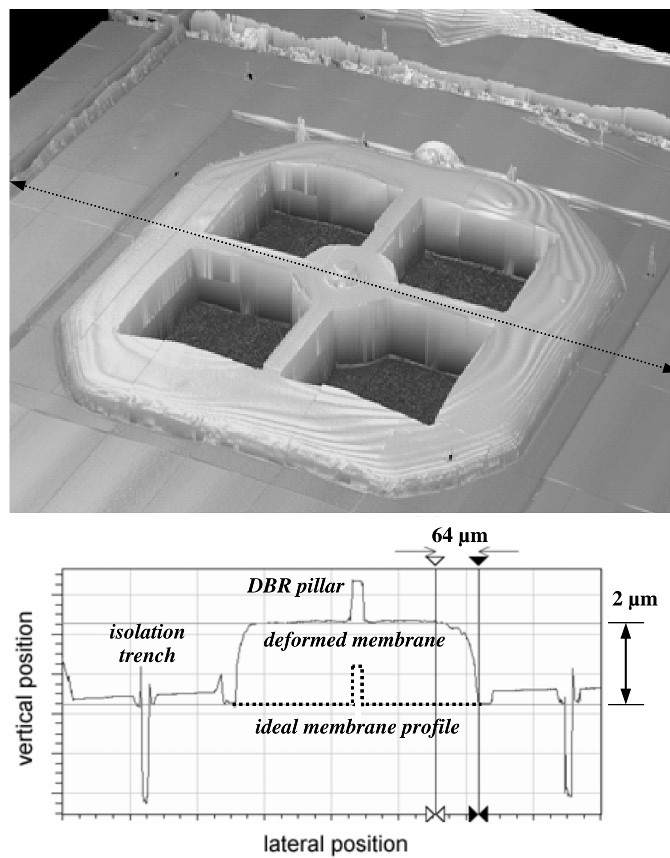

Fig. 4.12: Surface scan of a typical Generation 1 MT-VCSOA (top) and corresponding profile (bottom) recorded with the Wyko NT1100. The dashed line indicates the intersection of the sectioning plane with the MT-VCSOA surface. As indicated in the plot, the membrane is displaced nearly 2 µm out-of-plane as compared with the ideal membrane profile (dashed line). The ripples seen in the three-dimensional image are artifacts from the interferometric measurement technique.

The increase in the air-gap thickness is caused by a deformation of the undercut structure. This deformation results from a number of factors: excessive etching of the sacrificial material beneath the supports, the boundary conditions of the support structure, and strain relaxation of the free end of the support material. Because the sacrificial material is unmasked during the undercut etch, this film is removed from beneath the support structure by a minimum distance of half of the diameter of the central plate of the actuator. Additionally, during processing, a dual-purpose SiN_x film is deposited on the surface of the actuator to act as a hard mask for subsequent dry etch steps and also to act as a stressor to control the restoring force of the actuator. In concert with the oxidation induced cracking of the support material (as discussed in the following section), the free-standing membrane deflects out of plane in order to relieve the strain energy in the SiN_x film (Fig. 4.12). This deformation is similar in nature to that seen in the cantilever test structures included on the chip.

Due to the non-ideal boundary conditions of the support material, strain relaxation in the composite SiN_x/GaAs structure pulls the suspended portion of the membrane out of plane, resulting in a large increase in the initial air-gap thickness. Because the force on the electrostatic actuator is roughly proportional to the square of the initial air-gap thickness from Eq. 2.21 (assuming all else being equal) this results in a required tuning voltage, that is to the first order, approximately four-times higher than predicted. As can be seen in Eq. 2.17, the overall wavelength tuning range is inversely proportional to the total cavity length. Thus, the deformation of the membrane structure also limits the ASE tuning range of the

device. Finally, because the deformation is uncontrolled, the initial phase of the air gap—as well as the corresponding initial wavelength—is unpredictable.

4.4.2 Device Reliability

The second most pressing issue with the initial generation of MT-VCSOAs is the extremely poor reliability. Within one to two weeks following fabrication, cracks would begin to appear around the periphery of each device—at the interface between the etched and unetched sacrificial material. A micrograph containing cracked membrane structures can be seen in Fig. 4.13. Soon after their initial appearance, these cracks would encircle the device, removing the electrical and mechanical contact with the substrate and rendering the devices inoperable.

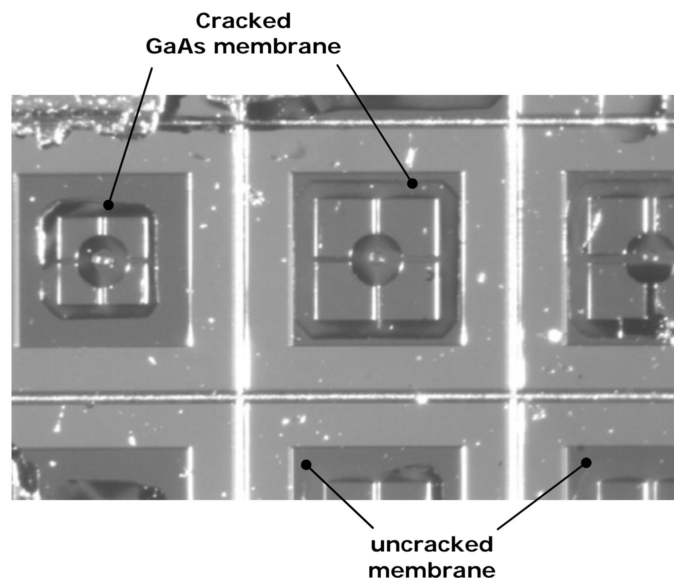

Fig. 4.13: Optical micrograph of a first-generation MT-VCSOA sample. The dark rings within the support structures of many of the devices are cracks in the GaAs membrane. Once the cracks encircle the device, mechanical and electrical contact to the substrate is lost.

Analysis using a combination of scanning electron microscopy and focused ion beam milling revealed that the exposed high Al-content sacrificial AlGaAs material had transformed to $AlGaO_x$. The resulting oxide is known to experience a large reduction in volume upon transformation, on the order of 10% [18]. This large volume shrinkage results in cracking of the GaAs/SiN_x due to the large tensile stresses present at the interface of the GaAs/$AlGaO_x$, and has been observed during rapid thermal annealing of oxidized VCSEL structures [19].

In contrast with the stable steam grown oxide demonstrated by Dallesasse et al. [20], oxidized AlGaAs formed under ambient conditions is a very unsatisfactory structural material. It is important to note that even with nitrogen purged dry-box storage, the initial devices exhibited rapid degradation. Additional cracking was found to occur at the corners of the mechanical support structure. With the initial mechanical design, the sharp angle (90 degree) features produce areas of large stress concentration in the mechanical supports and suspended membrane. This problem was exacerbated by the alignment of the orthogonal actuator features with the cleaved edges of the sample, resulting in cracking of the undercut support material along the <110> oriented cleavage planes of of GaAs.

Although the aforementioned issues somewhat limited the performance of the initial devices, these structures were, at the very least, successful in demonstrating the concept of a micromechanically-tunable VCSOA. Solutions to the shortcomings found in the initial demonstration devices are addressed and solved in subsequent generations of MT-VCSOAs, as discussed in the following chapters.

4.5 Summary

This chapter outlines the development and analysis of the first widely tunable VCSOAs. These devices are fabricated using a combination of GaAs to InP wafer bonding and AlGaAs-based micromachining and utilize an integrated electrostatic actuator for wavelength tuning. The best results measured with the initial structures were 10 dB on-chip gain (3 dB fiber-to-fiber gain) over 11 nm of tuning, as well as a peak amplifier gain of 17 dB (10 dB fiber-to-fiber gain) at 1570 nm. Additionally, typical input saturation powers for the first generation of MT-VCSOAs varied from -12.8 dBm to -16 dBm. As with any first demonstration, these devices exhibited a number of limitations. Stress-related deformation of the excessively undercut support structure resulted in a large out-of-plane deformation of the free-standing membrane. This deformation led to a doubling of the air gap thickness, and as a consequence, the required tuning voltages were on the order of 60 V. Furthermore, these devices exhibited poor stability due to oxidation of the high Al content sacrificial material.

Regardless of the limitations, the Generation 1 MT-VCSOAs represent the first micromechanically-tunable VCSOAs and the initial demonstration shows promising results. The ability to sweep the narrow gain bandwidth over the tuning range makes MT-VCSOAs attractive as tunable channel-selective preamplifiers. For multichannel optical networks, tunable VCSOAs can be precisely adjusted to match the wavelength of the desired input signal. Furthermore, because MT-VCSOAs are

capable of simultaneous amplification and spectral filtering, these devices can be seen as wavelength agile filters with the added benefit of optical gain.

References

[1] M. Maute, F. Riemenschneider, G. Bohm, H. Halbritter, M. Ortsiefer, R. Shau, P. Meissner, M.-C. Amann, "Micro-mechanically tunable long wavelength VCSEL with buried tunnel junction," *Electron. Lett.*, vol. 40, pp. 430–431, Apr. 2004.

[2] A. Syrbu, V. Iakovlev, G. Suruceanu, A. Caliman, A. Rudra, A. Mircea, A. Mereuta, S. Tadeoni, C.-A. Berseth, M. Achtenhagen, J. Boucart, E. Kapon, "1.55-µm optically pumped wafer-fused tunable VCSELs with 32-nm tuning range", *IEEE Photon. Technol. Lett.*, vol. 16, pp. 1991–1993, Sep. 2004.

[3] M. S. Wu, E. C. Vail, G. S. Li, W. Yuen, C. J. Chang-Hasnain, "Tunable micromachined vertical cavity surface emitting laser," *Electron. Lett.*, vol. 31, pp. 1671–1672, Sep. 1995.

[4] M. C. Larson, A. R. Massengale, J. S. Harris, Jr., "Continuously tunable micromachined vertical-cavity surface-emitting laser with 18 nm wavelength range," *Electron. Lett.*, vol. 32, pp. 330–332, Feb. 1996.

[5] P. Tayebati, P. D. Wang, D. Vakhshoori, C. C. Lu, M. Azimi, R. N. Sacks, "Half-symmetric cavity tunable microelectromechanical VCSEL with single spatial mode," *IEEE Photon. Technol. Lett.*, vol. 10, pp. 1679–1681, Dec. 1998.

[6] G. L. Christensen, A. T. T. D. Tran, Z. H. Zhu, Y. H. Lo, M. Hong, J. P. Mannaerts, R. Bhat, "Long-wavelength resonant vertical-cavity LED/ photodetector with a 75-nm tuning range," *IEEE Photon. Technol. Lett.*, vol. 9, pp. 725–727, Jun. 1997.

[7] W. S. Rabinovich, T. H. Stievater, N. A. Papanicolaou, D. S. Katzer, P. G. Goetz, "Demonstration of a microelectromechanical tunable asymmetric Fabry-Pérot quantum well modulator," *Appl. Phys. Lett.*, vol. 83, pp. 1923–1925, Sep. 2003.

[8] J. Daleiden, N. Chitica, M. Strassner, A. Spisser, J. L. Leclercq, P. Viktorovitch, D. Rondi, E. Goutain, J. Peerlings, J. Pfeiffer, R. Reimenschneider, K. Hjort, "Tunable InP/air gap Fabry Perot filter for

wavelength division multiplex fiber optical transmission," in *Proc. 11th Int. Conf. InP and Related Materials*, 16–20 May '99, Paper TuA3-4, pp. 285–287.

[9] E. S. Björlin, T. Kimura, Q. Chen, C. Wang, J. E. Bowers, "High output power 1540nm vertical cavity semiconductor optical amplifiers," *Electron. Lett.*, vol. 40, pp. 121–123, Jan. 2004.

[10] T. Kimura, E. S. Björlin, H.-F. Chou, Q. Chen, S. Wu, J. E. Bowers, "Optically preamplified receiver at 10, 20, and 40 Gb/s using a 1550-nm vertical-cavity SOA," *IEEE Photon. Technol. Lett.*, vol. 17, pp. 456–458, Feb. 2005.

[11] A. Black, A. R. Hawkins, N. M. Margalit, D. I. Babić, A. L. Holmes, Jr., Y.-L. Chang, P. Abraham, J. E. Bowers, E. L. Hu, "Wafer fusion: materials issues and device results," *IEEE J. Select. Topics Quantum Electron.*, vol. 3, pp. 943–951, Jun. 1997.

[12] S. W. Corzine, R. S. Geels, J. W. Scott, R.-H. Yan, L. A. Coldren, "Design of Fabry-Perot Surface-Emitting Lasers with a Periodic Gain Structure," *IEEE J. Quantum Electron.*, vol. 25, pp. 1513–1524, Jun. 1989.

[13] J. Geske, "Ultra-wideband WDM VCSEL arrays by lateral heterogeneous integration," Ph.D. Dissertation, University of California, Santa Barbara, Santa Barbara, CA, 2004.

[14] A. M. Pyzyna, "Thermal oxidation-induced strain in Silicon nanobeams," Ph.D. Dissertation, University of California, Santa Barbara, Santa Barbara, CA, 2005.

[15] K. L. Turner, P. G. Hartwell, N. C. Macdonald, "Multi-dimensional MEMS motion characterization using laser vibrometry," in *Digest of Technical Papers, Transducers '99 The 10th International conference on solid-state Sensors and Actuators*, Sendai, Japan, 7–10 Jun. 1999, pp. 1144–1147.

[16] T. Mukai, Y. Yamamoto, "Gain, frequency bandwidth, and saturation output power of AlGaAs DH laser amplifiers," *IEEE J. Quantum Electron.*, vol. 17, pp. 1028–1034, Jun. 1981.

[17] A. H. Clark, S. Calvez, N. Laurand, R. Macaluso, H. D. Sun, M. D. Dawson, T. Jouhti, J. Kontinnen, M. Pessa, "Long-wavelength monolithic GaInNAs vertical-cavity optical amplifiers," *IEEE J. Quantum Electron.*, vol. 40, pp. 878–883, Jul. 2004.

[18] M. H. MacDougal, H. Zhao, P. D. Dapkus, M. Ziari, W. H. Steier, "Wide-bandwidth distributed Bragg reflectors using oxide/GaAs multilayers," *Electron. Lett.*, vol. 30, pp. 1147–1149, Jul. 1994.

[19] K. D. Choquette, K. M. Geib, H. C. Chui, B. E. Hammons, H. Q. Hou, T. J. Drummond, R. Hull, "Selective oxidation of buried AlGaAs versus AlAs layers", *Appl. Phys. Lett.*, vol. 69, pp. 1385–1387, Sep. 1996.

[20] J. M. Dallesasse, N. Holonyak, Jr. A. R. Sugg, T. A. Richard, N. El-Zein, "Hydrolyzation oxidation of $Al_xGa_{1-x}As$-AlAs-GaAs quantum well heterostructures and superlattices," *Appl. Phys. Lett.*, vol. 57, pp. 2844–2846, Dec. 1990.

CHAPTER 5

Generation 2: Revised Mechanical Structure

The best performance parameters measured with the first generation of MT-VCSOAs was 10 dB of device gain (3 dB fiber-to-fiber) over a tuning range of 11 nm, as well as a peak signal gain of 17 dB (10 dB fiber-to-fiber). Although these devices were successful in demonstrating the concept of a micromechanically-tunable VCSOA, the electrostatic actuator exhibited a number of limitations, including excessively high tuning voltages and poor reliability. This chapter introduces a second generation of MT-VCSOAs, utilizing a revised mechanical structure that greatly reduces the required tuning voltage, increases the wavelength tuning range, and markedly improves the reliability of the devices. In addition to the standard static response, a detailed dynamic analysis of the electrostatic actuator is presented.

In order to further improve the effective tuning range of the MT-VCSOA, a detailed understanding of the optical cavity design options is developed. Here, an investigation of the signal gain, wavelength tuning characteristics, saturation properties, and noise figure (NF) of MT-VCSOAs utilizing various cavity designs is presented. These models rely on the theoretical framework outlined in Chapter 2. To

verify the accuracy of these models, the theoretical results are compared with data generated from a number of experimental devices.

5.1 Updated Lithographic Mask Set

As discussed in the previous chapter, the initial mechanical design of the MT-VCSOA was hampered by a number of limitations, including poor wavelength tuning efficiencies and short device lifetimes. In order to address these shortcomings, a second generation of MT-VCSOAs has been developed. The major changes in these devices come in the form of updates to both the lithographic mask set and fabrication procedure used to define the device geometry. Beyond these changes, the materials structure for the second generation of devices is identical to that used in Generation 1. Because of the similarity in materials used in these devices (which is actually cleaved from the same wafer) it is possible to make direct quantitative comparisons between these two generations of devices.

5.1.1 Modified Actuator Design

Fig. 5.1 shows a three-dimensional schematic of the Generation 1 devices highlighting the problematic areas of the structure. Design limitations in these devices include excessive undercutting of the sacrificial material beneath the membrane support structure, cracking of the support material—as a result of oxidation of the exposed AlGaAs and stress concentration at the sharp corners, the

reduced rigidity of the central plate of the membrane—due to the reduced diameter of the DBR pillar and bowing of the free-standing portion of the membrane—caused by stress-related deformation of the unconstrained free-edge of the support structure.

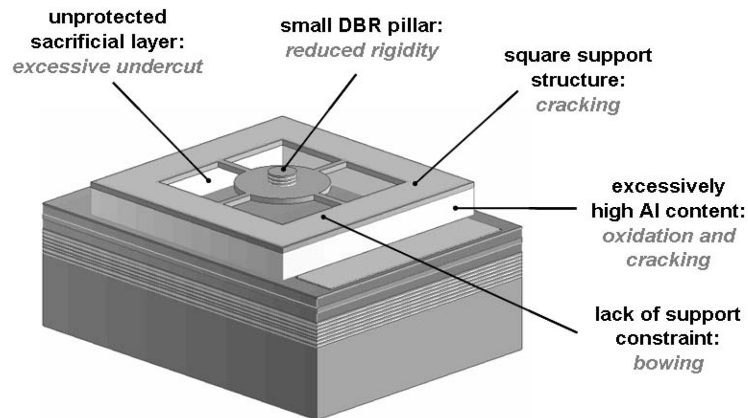

Fig. 5.1: Limitations in the mechanical design of the Generation 1 MT-VCSOAs.

In order to overcome these drawbacks, a revised mechanical design has been developed. A schematic of this structure is presented in Fig. 5.2. The major differences, when compared with the first generation of devices, include the addition of a radiused support structure—to reduce the effects of stress concentration at the sharp corners, an enlarged DBR pillar—to increase the rigidity of the central portion of the membrane, and finally undercut protection and support constraint brought about by deposition of a low temperature SiO_2 film—to negate the effects of unwanted deformation of the membrane structure. Because the epi-structure used in these devices is identical to that used in Generation 1, the high-Al content in the sacrificial layer remains unchanged. However, in the revised design, the addition of the low-temperature-deposited SiO_2 film markedly improves the MT-VCSOA

reliability, in spite of the oxidation of the AlGaAs. As a physical masking layer, the SiO_2 film reduces the undercutting of the sacrificial material beneath the supports and additionally serves as a mechanical constraint to prevent out of plane deformation of the support structure. Furthermore, due to the intrinsic compressive stress in this film, the propensity for the membrane structure to crack at the interface of the unetched sacrificial material is reduced.

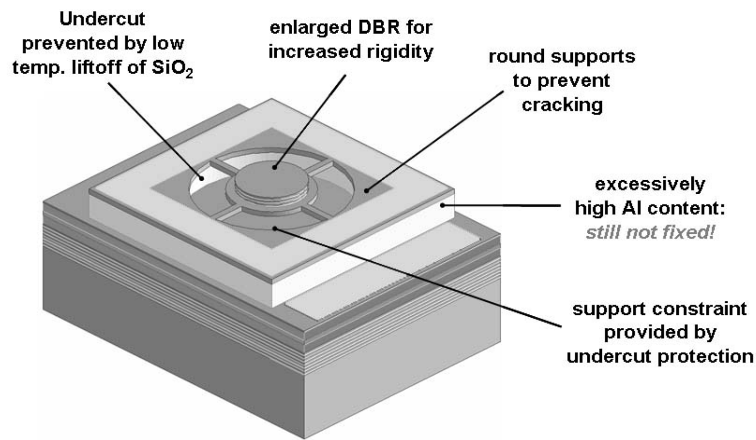

Fig. 5.2: Revised mechanical structure used for the second generation of devices.

5.1.2 Updated Process Flow

For the revised mechanical design, an additional liftoff step is added to the process flow in order to constrain the free edges of the supports and avoid excessive undercutting of the sacrificial AlGaAs below the support structure. The design of the mechanical constraint layer is similar to that described in [1]. Following the anisotropic etch of the actuator geometry through the GaAs structural film and AlGaAs sacrificial material, a liftoff pattern is defined using a bilayer resist process consisting of polymethylglutarimide (PMGI) and negative photoresist (Clariant

AZ5214). Next, a low temperature (100° C) SiO_2 layer is deposited using ICPECVD and is patterned by stripping the resist. As demonstrated in Fig. 5.3, the SiO_2 film serves as a physical constraint for the free edge of the support structure, inhibiting out-of-plane deformation and leading to improved control over the initial air-gap thickness. As a result, the revised MT-VCSOAs exhibit a largely reduced tuning voltage requirement, as well as a better controlled starting wavelength.

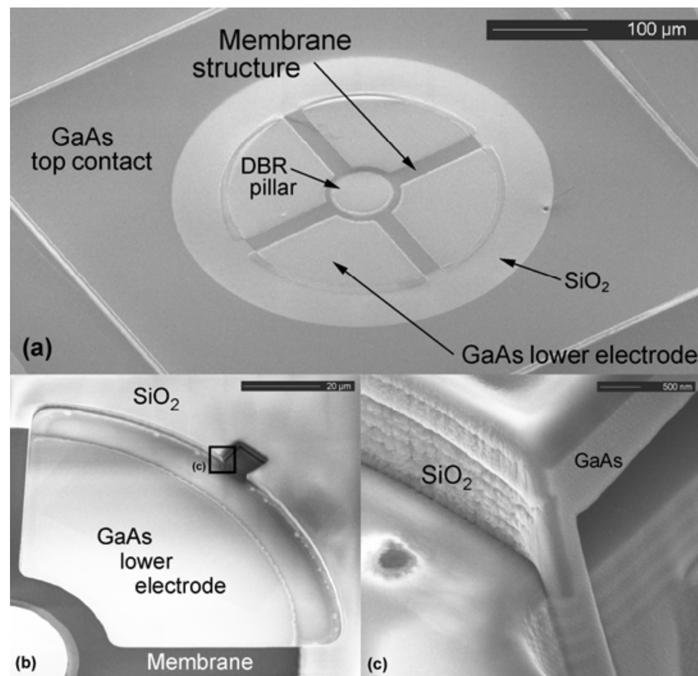

Fig. 5.3: Scanning electron micrographs of the updated tunable VCSOA mechanical design. (a) Here a low-temperature SiO_2 film has been patterned by liftoff to reduce excessive undercutting of the sacrificial material below the support structure. (b) A small via has been cut into the sidewall using a focused ion beam in order to examine the sidewall coverage of the SiO_2 film. (c) Close-up of the highlighted area in (b); note that the SiO_2 film exhibits conformal sidewall coverage.

5.2 Generation 2 Results

Characterization of the second generation of MT-VCSOAs utilizes identical optical and mechanical testing procedures as presented for the initial demonstration devices (and discussed in Section 4.2). The results in the following sections focus on the improvements in the overall wavelength tuning range and the reduction in the required tuning voltage realized through the use of the revised mechanical structure. Additionally, due to the increased stability of these devices, an in-depth analysis of the dynamic properties of the electrostatic actuator is presented. Finally, in order to explore both existing limitations, as well as potential improvements in these devices, experimental results from a number of Generation 2 MT-VCSOAs are compared to the analytical models developed in Chapter 2.

5.2.1 Improved Wavelength Tuning Response

With the MT-VCSOA, the decrease in air-gap thickness upon actuation leads to a reduction in the effective cavity length, and a blue shift in the peak gain wavelength. For the SCC-design, the competing phases from the multiple reflections present in the air-cavity structure lead to a varying phase coupling factor (as seen in Fig. 2.4) and a nonlinear wavelength shift with respect to the change in air-gap thickness, as seen in Fig. 5.4 below. In this plot the tuning response for a $\lambda_c/4$, $3\lambda_c/4$, and a $5\lambda_c/4$ air-gap structure are presented, as well as measured data from two second generation MT-VCSOAs. Using this plot it is possible to compare the maximum tuning range around the center wavelength of the cavity, λ_c, given the

limited travel of the electrostatic actuator [2]. Assuming that the displacement is limited to ~1/3 L_{go} (as discussed in Section 2.5.2) and centered at λ_c, the approximate wavelength shift for each structure is found to be 6.4 nm for the $\lambda_c/4$ air gap, 24.2 nm for the $3\lambda_c/4$ air gap, and 53.1 nm for the $5\lambda_c/4$ air gap. For the cavity designs presented here, the estimated tuning range is highlighted as the shaded area of the plot. By increasing the air-gap thickness the total wavelength tuning range may be extended. However, with an increasing air-gap thickness, the required tuning voltage will also increase due to a decrease in the applied force Eq. 2.19. Additionally, given a longer total cavity length, the FP mode spacing is reduced, decreasing the overall single-mode tuning range.

Using the revised mechanical design, the ASE wavelength tuning range is greatly extended when compared with the first generation of devices. In these devices the revised structure results in a slightly reduced initial air-gap thickness, and an initial cavity mode with a shorter wavelength than desired. Upon tuning, the phase coupling factor begins to increase dramatically, and the wavelength shift becomes very rapid with decreasing air-gap thickness. The results for the two most widely tunable devices are included in Fig. 5.4. As shown in the figure, the ASE wavelength shifts are 76.6 nm (1571.9 nm to 1495.3 nm) with the application of 30 volts to the tuning diode, and 53.8 nm (1553.8 nm to 1500.0 nm) at 25 volts. Due to the reduced initial air-gap thickness, the experimental tuning data is blue shifted with respect to the ideal design, resulting in measured data that extends beyond the

limit of the wavelength tuning range (bounded by the shaded region) as indicated in the figure.

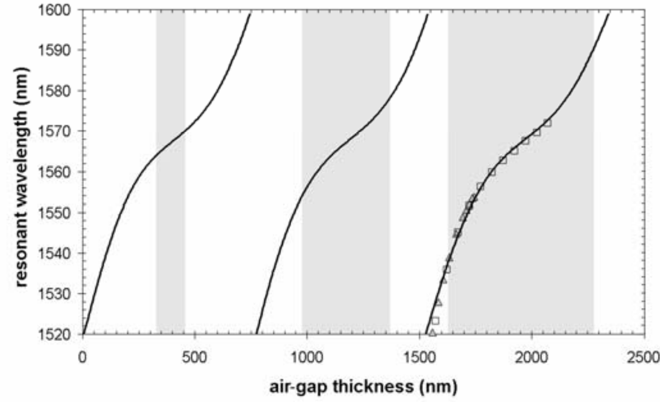

Fig. 5.4: Wavelength shift as a function of the air-gap thickness for L_g centered on $\lambda_c/4$, $3\lambda_c/4$, and $5\lambda_c/4$. The shaded regions indicate the estimated wavelength tuning range given the limited travel of the electrostatic actuator, while the open squares and triangles represent experimental data from devices with the widest tuning ranges.

Using the same procedure (as well as the same basic cavity structure) it is possible to predict the wavelength tuning response for the EC cavity design. In the limit of an ideal ARC, $R_c \approx 0$, and $\gamma_\phi \rightarrow 1$. With this design the resonant wavelength shift becomes linear as a function of the change in air-gap thickness (not taking into account dispersion effects in the DBRs or the ARC bandwidth). Again, using air-gap thicknesses centered around $\lambda_c/4$, $3\lambda_c/4$, and $5\lambda_c/4$, the limits to the wavelength shift are found to be 15.8 nm, 44.6 nm, and 70.5 nm respectively. Thus, by incorporating an ARC within the cavity, the wavelength tuning range of the VCSOA may be increased. However, the extended tuning range comes at the price of a reduced reflectivity of the tunable mirror structure (due to the incorporation of the ARC) and

also a reduced optical overlap with the stacked MQW active region, resulting in a reduced signal gain for a given pump power.

Apart from the physical limitations of the mechanical structure, the useful wavelength span of the MT-VCSOA will eventually be restricted by either the finite stop band of the DBR mirrors, or the gain spectrum of the active material. Wide mirror stop bands may be achieved through the use of air/semiconductor DBRs [3], [4], oxidized AlGaAs DBRs [5], or dielectric DBRs [6]. Additionally, the increased index contrast with these mirror systems leads to a smaller penetration depth and thus an increase in the wavelength tuning efficiency, due to a decrease in the overall cavity length. Given an infinite DBR stop band, and an actuator capable of an extended range of displacement, the wavelength range over which acceptable amplification may be achieved will be limited by the active material gain spectrum.

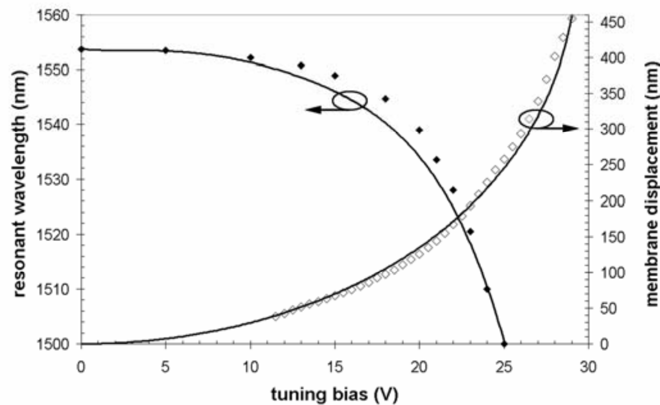

Fig. 5.5: Resonant cavity mode shift as a function of the applied tuning bias, as well as the corresponding membrane displacement. The solid lines indicate the theoretical device response, while the data points indicate experimental measurements.

With the updated mechanical structure, the total membrane displacement is improved, while at the same time, the required operating voltage is largely reduced, as compared with the previously reported devices [7]. With a plate diameter of 70 μm, a spring length and width of 95 μm and 20 μm respectively, a membrane thickness of 0.35 μm, and SiN_x thickness of 0.25 μm, the MT-VCSOA exhibits a total displacement of 455 nm with the application of 29 V to the tuning diode. With this actuator, the application of 25 V results in a membrane displacement of approximately 250 nm and a corresponding ASE wavelength shift of 53.8 nm, as shown in Fig. 5.5. The large decrease in the required tuning voltage is attributed to the better control over the initial air-gap thickness found with the revised mechanical design. With the first generation of devices, the deformation of the support structure caused the air gap to nearly double in thickness [7]. By constraining the support structure against out of plane deformation, the initial plate separation is now better controlled, leading to a large reduction in the required tuning voltage for the second generation of MT-VCSOAs.

Combining Eq. 2.19 with the sum of the components of the restoring force from Eq. 2.20, and using an iterative solution, it is possible to accurately predict the displacement of the membrane structure as a function of the applied bias. Fitting the theoretical curve to the measured values as shown in Fig. 5.5, the spring constant of the actuator is found to be 58.6 N/m. This value is relatively high due to the large tensile stress in the PECVD SiN_x layer. In this device the mechanical spring constant is dominated by the material stress term, k_{stress} = 56.1 N/m, while the bending and

stretching components contribute only slightly to the restoring force, with k_{bend} = 2.2 N/m and the cubic spring constant $k_{stretch}$ = 0.3 N/m at a displacement of 247 nm. To minimize the total restoring force of the actuator and further reduce the required tuning voltages, a low, or nearly zero, tensile stress actuator material should be used, similar to that demonstrated in [8]. Presently, a more thorough understanding of the stresses developed by the direct wafer bonding process is necessary in order to optimize the mechanical properties of the actuator.

5.2.2 Dynamic Characterization

Given the improved reliability of the Generation 2 MT-VCSOAs, it is possible to conduct an in-depth mechanical analysis of the electrostatic actuator. In this analysis, the dynamic response of the membrane structure is tested both in vacuum and at atmosphere using a multidimensional MEMS-motion characterization system [9], as described in Section 4.2.3. In order to record the spectral response of the actuator, a square-root sinusoidal signal $V = V_A\sqrt{1+\cos(\omega t)}$ is supplied by a function generator with a quasi-statically varying frequency. Because the force of the electrostatic actuator is proportional to V^2 (from Eq. 2.21), the use of the square-root sinusoidal signal results in a forcing function at the desired frequency, plus an additional DC offset. Out of plane motion is detected with a laser Doppler vibrometer (Fig. 5.6) and the resulting velocity and displacement output is captured and analyzed using a vector signal analyzer and oscilloscope. Fig. 5.6 shows a typical response of the MT-VCSOA for small excitation amplitude (2 V) in vacuum (6 mT). This particular

actuator exhibits a simple harmonic response with a resonant frequency f_0 of 168.32 kHz and a mechanical quality factor Q of 491, as determined from the width of the resonance peak. The small amplitude response of the actuator in vacuum allows for the extraction of the intrinsic damping as well as the natural frequency.

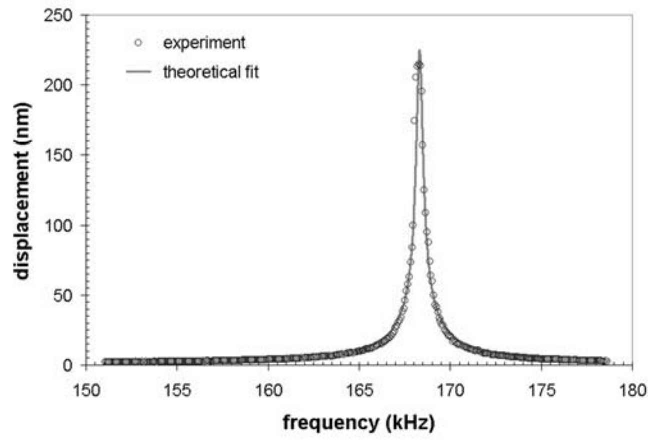

Fig. 5.6: Simple harmonic response at a pressure of 6 mT and driving amplitude of 2 V.

Typical natural frequencies for the MT-VCSOAs range from 117–209 kHz, depending on the geometry of the membrane structure (see Appendix A for a review of the lithographic mask set). For the actuator presented in Fig. 5.6, the spring length is 90 μm, the spring width is 20 μm, and the central plate diameter is 60 μm. In this design the central plate supports a 5-period GaAs/$Al_{0.98}Ga_{0.02}As$ DBR pillar (with a diameter of 50 μm). The thickness of the GaAs structural layer is approximately 350 nm and is coated with a nominally 200-nm thick tensile-strained SiN_x film (compared with a 250-nm thick SiN_x stressor film used in the device shown in Fig. 5.5). From DC displacement measurements, the linear spring constant of this

structure is 39.4 N/m, resulting in an effective mass of 3.5×10^{-11} kg. Calculations of the mass of this structure—using the appropriate density values—result in a theoretical total mass of 3.4×10^{-11} kg.

With increasing drive voltage the frequency response of the actuator becomes asymmetric and beyond a critical amplitude develops a hysteretic response typical of a hardening spring Duffing oscillator, arising from the nonlinear restoring force of the doubly-clamped springs. By sweeping up and down in the applied frequency, the bistable region of the response curve may be determined, as shown in Fig. 5.7. Utilizing the theoretical expressions in Section 2.5.3, it is possible to fit the experimental data in order to extract the relevant properties of the actuator. For the Duffing response, the boundary points of the bistable region occur where the resonance curve has a vertical tangent. By differentiating Eq. 2.28 with respect to the displacement C and equating $\frac{d\Omega}{dC}$ to zero, the resonant frequency of the nonlinear oscillator ω_{nl} as a function of displacement C may be expressed as [10]:

$$\omega_{nl} = \sqrt{\omega_0^{\,2} + \frac{3}{4}\mu C^2}\ . \quad (5.1)$$

In order to generate this relationship, small damping is assumed ($\delta \approx 0$). The definition of each variable remains the same as that presented in Section 2.5.3. Recording the frequency of the nonlinear resonance peak for different drive amplitudes and plotting $\omega_{nl}^{\,2}$ versus C^2 results in a linear function, with a y-intercept of $\omega_0^{\,2}$ and a slope of $3/4\mu$ as demonstrated in the inset of Fig. 5.7. This procedure allows for a rather accurate determination of μ and ω_0 without the need for fitting of

the individual response curves. For the device analyzed here, the linear fit results in a coefficient of nonlinearity $\mu = 3.35\times10^{22}$ m^{-2}s^{-2} ($k_{stretch} = 1.28$ µN/µm^{3}) and a natural frequency value that deviates by only 0.2% from the measured value. Combining these values with the damping coefficient calculated from the harmonic fit, it is possible to generate theoretical curves for the Duffing response, as in Fig. 5.8.

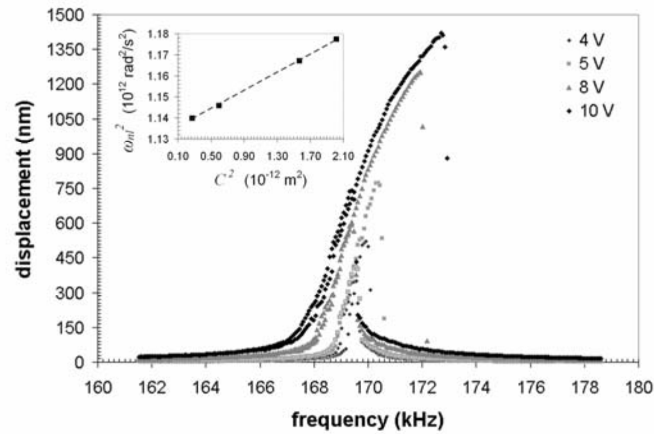

Fig. 5.7: Hardening spring Duffing response of the electrostatic actuator at 6 mT.

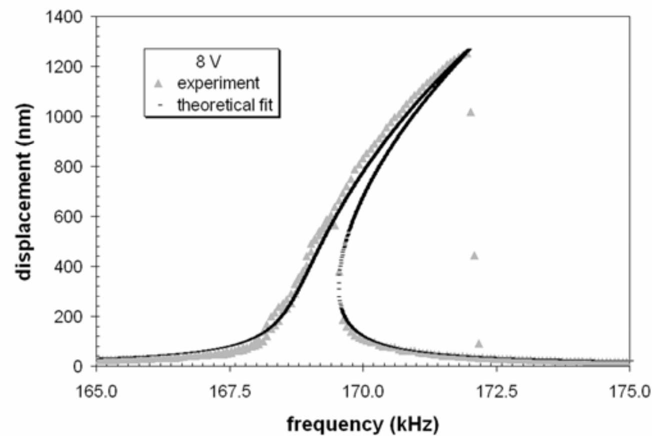

Fig. 5.8: Nonlinear resonance curve at 8 V drive amplitude. The theoretical fit is generated using values determined by a linear fit of Eq. 5.1, as shown in the inset of Fig. 5.7.

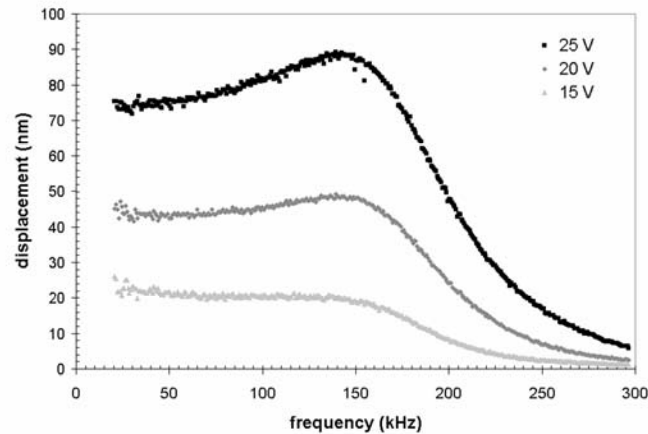

Fig. 5.9: Dynamic response of the MT-VCSOA at atmosphere. For each curve the measured quality factor is 1.2.

Operation of the MT-VCSOA in vacuum allows for the determination of the intrinsic damping, natural frequency, and nonlinear characteristics of the actuator. However, the lack of significant viscous damping in vacuum leads to excessive ringing and long settling times. For the intended application, it is desirable to increase the damping in order to minimize the response time—assuming the device remains underdamped. Because of the large ratio of lateral dimensions to air-gap thickness, squeeze film damping is significant at increased pressure. In comparison with testing in vacuum, at atmosphere Q is reduced considerably to 1.2, as seen in Fig. 5.9. This device is slightly underdamped with a damped resonant frequency f_d of roughly 150 kHz. Given these properties, the approximate settling time (as defined in Eq. 2.27) in ambient air for this actuator is 5.7 μs. Thus, the MT-VCSOA is capable of achieving a 10-nm wavelength shift—corresponding to a displacement of roughly 75 nm from Fig. 5.5—in less than 10 μs.

5.3 Limitations of the Current Optical Cavity Design

In the previous sections, the improvements in the properties of the electrostatic actuator were examined. Utilizing the revised mechanical structure, the second generation of MT-VCSOAs exhibit largely reduced tuning voltages, as well as an extended wavelength tuning range. However, optical characterization of these structures reveal that although the ASE tuning range had largely increased, the effective tuning range of the amplifier is limited to similar values recorded for the initial generation of devices. Even with ASE tuning ranges exceeding 50 nm, the effective tuning range (with at least 3 dB fiber-to-fiber gain) is limited to roughly 10 nm. In contrast, state-of-the-art optically-pumped tunable VCSELs have demonstrated over 30-nm single-mode tuning ranges [12], [13]. The following section utilizes the theoretical framework developed in Chapter 2 in order to better understand the limitations of the current cavity design and propose a viable solution.

5.3.1 Variation in Mirror Reflectance

Fig. 5.10 presents the gain spectrum, as a function of tuning bias, for a typical second generation MT-VCSOA given a constant optical pump power. From this figure it is apparent that the peak amplifier gain decreases significantly with tuning. As seen in Eq. 2.1, the signal gain of a reflection-mode VCSOA is determined by the single-pass gain, which is controlled by the material gain spectrum, as well as by the reflectivity of the top and bottom DBRs. Measurements on fixed-wavelength devices fabricated from the same active region wafer [14] reveal that sufficient gain is

available at these wavelengths; thus, the rapid decrease in the peak gain cannot be related to limitations in the material gain spectrum. Furthermore, measurements of the bottom mirror reflectance spectrum show the stop-band of this mirror to be nearly flat with a power reflectance near 0.999 over the wavelength span highlighted in the figure. Therefore, the remaining cause for the roll-off in signal gain is a variation in the effective reflectance of the tunable mirror structure over this wavelength span.

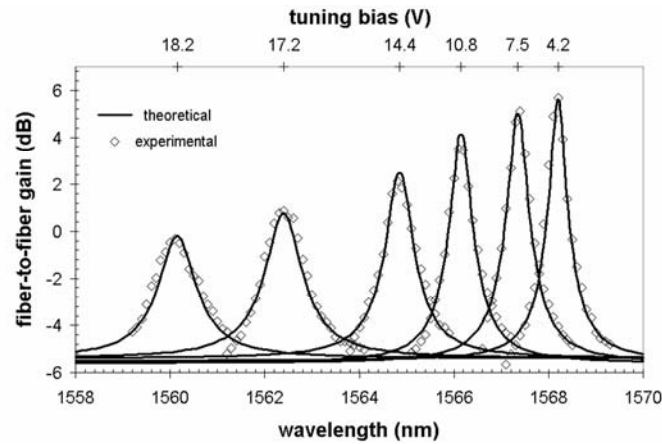

Fig. 5.10: Amplifier gain spectra recorded for a constant pump power and increasing bias. Measured data is indicated by open circles, while the theoretical curves (black lines) are generated using Eq. 2.1.

For VCSOAs the mirror reflectance is crucial in determining the characteristics of the amplifier, including the signal gain, gain bandwidth, saturation properties, and noise figure [15]-[17]. With fixed-wavelength devices, the mirror reflectance is simply dictated by the index contrast of the high and low index materials, the number of periods used in the DBR, and finally the intrinsic loss in the structure.

With tunable VCSOAs on the other hand, the addition of the air gap considerably complicates matters. From Eq. 2.15 the effective reflectance of the tunable mirror structure is controlled by the phase of the air gap ϕ_g, the reflectance of the suspended membrane R_m, and the reflectance of the interface between the air gap and active region R_c. Depending on the design of the tunable mirror structure, the use of MEMS-based wavelength tuning may result in varying mirror reflectance and a corresponding variation in the properties of the resonant cavity structure as a function of the air-gap thickness.

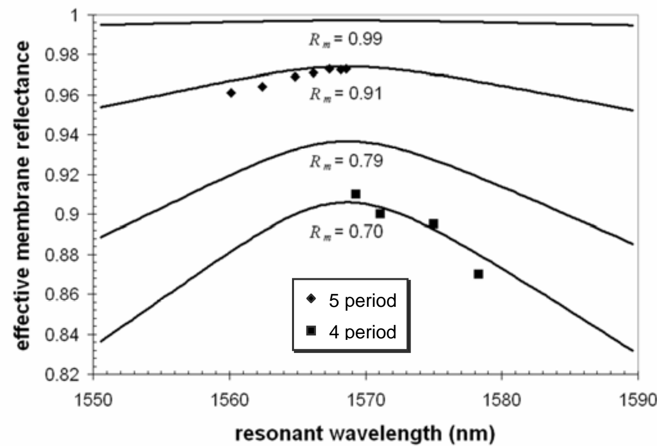

Fig. 5.11: Theoretical curves for the variation in reflectance of the tunable mirror structure for the SCC-design. Experimental data recorded for devices with 4 and 5 period DBR pillars are included.

Given an SCC-design MT-VCSOA, the varying reflectance is caused by the changing magnitude of interference from the multiple reflections within the passive air cavity. At the center of the tuning range, the air gap is near a point of anti-resonance and the multiple reflections add in phase, leading to a peak in the effective

reflectance. However, as L_g is varied, the air-gap thickness begins to approach a multiple of $\lambda_c/2$, eventually reaching a position where the reflection from the suspended DBR and semiconductor-air gap interface are 180° out of phase, resulting in a minimum in the effective mirror reflectance. From the perspective of the semiconductor cavity, the destructive interference leads to a reduced effective mirror reflectance as the air-gap thickness is deviated from its ideal value.

Combining Eqs. 2.15 and 2.17, it is possible to plot the effective reflectance of the SCC-design tunable mirror structure as a function of the resonant wavelength of the VCSOA cavity, as shown in Fig. 5.11. In this plot R_c = 0.32 (all reflectivity values are given as power reflectance for this work) and it is assumed that the center wavelength of the tunable mirror structure is the same for each of the measured devices. Because the experimental data was recorded for different samples, slight non-uniformities in the epitaxial growth procedure may shift the ideal value of λ_c for each device. Along with the theoretical curves, experimental data is included from a first generation MT-VCSOA with a 4 period DBR pillar and a second generation device with 5 periods. This data has been generated through curve fitting of individual gain spectra using Eq. 2.1. For the first generation device, the measured peak reflectance value is 0.91 at 1569.3 nm and drops to 0.87 at a wavelength of 1578.3 nm. In this case, the measured maximum reflectance is much lower than the theoretically calculated peak value of 0.968, and is attributed to additional mirror loss brought about by the wet chemical etching process used to remove one of the mirror periods [18]. For the second generation sample with the 5 period DBR pillar,

the peak R_{eff} of 0.974 matches well with predicted value of 0.976. Given a roughly 20 nm shift from the wavelength of peak reflectance, the theoretical reflectance of the tunable mirror structure is reduced to 0.953. Also included in Fig. 5.11 is the variation in mirror reflectance for a typical SCC-design MEMS-tunable VCSEL, with a peak effective reflectance of 0.997 for the tunable mirror structure [19]. Over the same wavelength range R_{eff} reduces only slightly to 0.995. Examining the limit of membrane reflectance, R_m equals 1.00, resulting in an effective reflectance of unity, independent of the phase of the air gap. Thus, for increasing values of the membrane reflectance, the roll-off in the effective reflectance upon tuning becomes less severe.

Over the wavelength tuning range of the MT-VCSOA, the variation in reflectance of the tunable mirror structure may be extremely large when using the SCC-design with a reduced reflectivity membrane DBR (low value of R_m). As compared with the mirror requirements of a tunable VCSEL, the lower reflectivity mirrors necessary for a tunable VCSOA lead to a much larger change in the effective reflectance as the air gap is varied from its ideal thickness. In these devices, the roll-off in reflectance will greatly diminish the wavelength span over which acceptable amplification may be achieved—resulting in a limited effective tuning range.

In order to minimize the roll-off in reflectance with tuning, two options exist. The first involves incorporating an ARC within the optical cavity to produce an EC-design MT-VCSOA. In this design the fixed phase reflection from the cavity-air interface is minimized ($R_c \approx 0$) and the effective reflectance of the tunable mirror structure remains roughly constant (and equal to the membrane reflectance)

regardless of the air-gap phase. The second option involves maximizing the reflectance of the membrane structure ($R_m \approx 1$), resulting in a roughly constant effective reflectance—near unity—over the tuning range. Due to the high reflectivity of the tunable mirror structure, this option is not compatible with a top-emitting device. However, by reducing the reflectance of the fixed DBR, a bottom-emitting MT-VCSOA can be realized with more consistent properties over the tuning range.

5.4 Investigation of Alternative Optical Cavity Designs

The preceding section revealed that the current optical cavity design, namely the SCC-design with a transmissive tunable mirror structure, exhibits inherent limitations when used for a tunable VCSOA. In this design the significant phase interference between reflections from the fixed air/active region interface and the reflection from the bottom of the suspended membrane structure result in large variations in the effective reflectance of the tunable mirror structure. To improve the effective tuning range of the MT-VCSOA, the following sections present the characteristics of alternative optical cavity designs for these devices.

5.4.1 Determination of the Materials Gain Spectrum

Using the relationships developed in Section 2.4.2 to describe the peak gain of the various tunable VCSOA configurations (Eqs. 2.18–2.20), it is possible to model the response of the MT-VCSOA as a function of the cavity resonance wavelength. In

order to complete these models, the wavelength dependence of the single-pass gain g_s must first be determined. As the cavity mode is tuned, the VCSOA will operate at different points along the material gain curve, leading to changes in g. Additionally, the wavelength shift will lead to a translation of the standing wave peaks within the active region. As a result, the position of the maximum field intensity will sweep across the MQW stack, leading to a varying gain enhancement factor with tuning. In terms of the cavity loss (product of $\alpha_i L_c$), the deflection of the membrane structure may lead to increased losses caused by tilting, or non-uniform deformation of the released structure; however, for the model presented here it is assumed that the product $\alpha_i L_c$ remains constant over the wavelength tuning range. For the following simulations, an average cavity loss of approximately 35 cm^{-1} is used. This value is relatively high compared to non-tunable vertical-cavity devices and is attributed to the doping levels used in the electrostatic actuator structure, the presence of multiple wet-etched semiconductor-air interfaces within the cavity, and increased diffraction loss associated with the longer cavity.

In order to estimate the change in ξ, a transmission matrix solver (VERTICAL) is used to determine the position of the standing wave peak as a function of the cavity resonance wavelength. For this calculation the QW structure consists of a given number of 5.5 nm thick wells separated by two 9 nm barriers (each MQW stack begins and ends with a layer of barrier material). In this simulation the optical cavity utilizes the SCC-design with a $5\lambda_c/4$ air gap—the same as the MT-VCSOAs presented in this dissertation. The calculation is completed for cavity lengths of

$3\lambda_c/2$, $4\lambda_c/2$, $5\lambda_c/2$, $6\lambda_c/2$, and $7\lambda_c/2$, containing, 8, 6, 5, 4, and 3 wells per MQW stack. With the transmission matrix solver, the shift in position of the standing wave peaks is recorded as a function of the cavity resonance wavelength. The peak shift is relatively linear as a function of wavelength, and the rate of the spatial shift increases with increasing cavity length. For the cavity lengths presented above, the average shift in position of the standing wave peaks are 0.98, 1.07, 1.16, 1.24, and 1.33 nm per nm of wavelength tuning respectively.

From the results in Fig. 5.12, it is possible to see that with the shorter cavity length designs, the larger required L_{MQW} results in a reduced initial value of ξ; however, the change in ξ becomes less pronounced as the device is tuned from λ_c. With an increased cavity length and a smaller number of wells per stack, the initial enhancement is increased, but the roll-off in ξ becomes more severe with tuning. Assuming a 50 nm wavelength tuning range centered on λ_c (approximately 1570 nm for this simulation), the largest variation in enhancement occurs for the $7\lambda_c/2$ cavity. In this structure ξ varies by approximately 20%, from a maximum value of 1.92 at λ_c, to a minimum of 1.56 after a blue shift of 25 nm. Within the approximately 50 nm achievable tuning range, a longer cavity with fewer wells per stack will result in a larger value of ξ. Nevertheless, if the tuning range is extended, or if the device operates off of the ideal center wavelength (λ_c), a larger L_{MQW} may be desired to ensure that ξ stays sufficiently high over the wavelength span of the device.

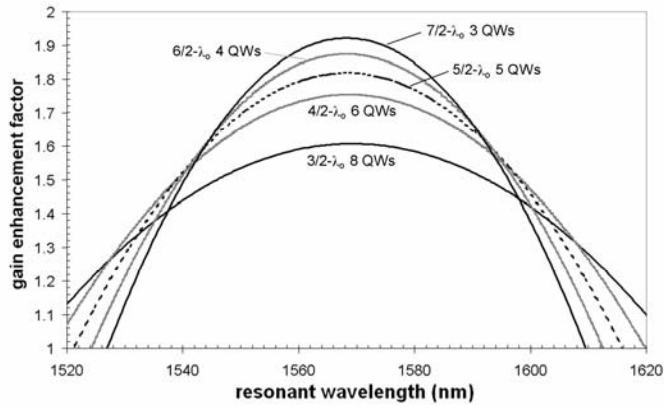

Fig. 5.12: Variation in gain enhancement of the SCC-design MT-VCSOA for various cavity lengths and MQW designs. After simulating the shift of the standing wave, ξ is calculated using Eq. 2.6.

With the variation in ξ established, the final parameter to be determined is the material gain spectrum. By recording the individual amplifier gain spectra for various tuning bias values (at a constant pump power), and fitting the data with theoretical curves generated from Eq. 2.1, it is possible to extract the changes in mirror reflectance and single-pass gain g_s with tuning. An example of this procedure may be seen in Fig. 5.10. After extracting the variation in g_s, the material gain as a function of wavelength can be calculated from Eq. 2.6 (Section 6.4.3 presents the extracted material gain spectrum for a third generation MT-VCSOA). In this model no wavelength dependent losses have been assumed [20]. With the wavelength dependence of g determined, the signal gain response of arbitrary tunable VCSOA designs can be modeled using the FP amplifier expressions.

5.4.2 Peak Gain Response: SCC-design MT-VCSOAs

In order to facilitate a more general comparison of the signal gain characteristics of the various tunable VCSOA configurations, it is desirable to decouple the properties of the MEMS actuator design. Rather than plotting the variation in gain with applied bias, a more general description involves the use of the peak gain expressions for MT-VCSOAs presented as Eqs. 2.18–2.20. Using these relationships, the variation in peak gain may be plotted as a function of the resonant wavelength of the optical cavity. The peak gain curves may be described as the envelope function of the individual gain spectra; an example of this can be seen as the dashed curve in Fig. 5.13. It is important to note that heating effects are not taken into account here.

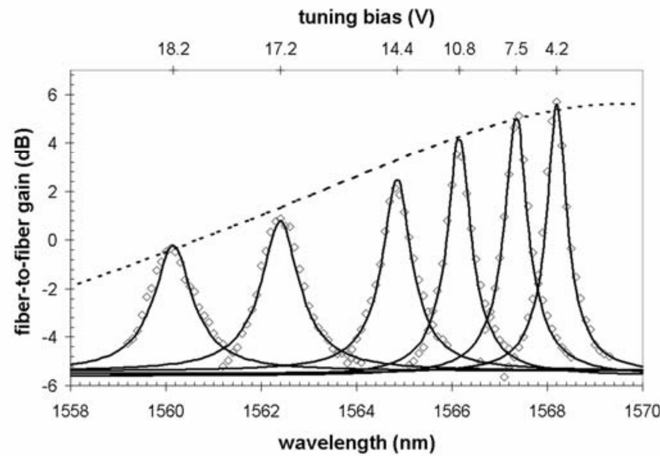

Fig. 5.13: Amplifier gain spectra recorded for a constant pump power and increasing tuning bias (open circles). Fitting the experimental gain spectra (solid lines) with Eq. 2.1, the variation in single-pass gain and mirror reflectance may be determined. Using these parameters, it is possible to generate curves describing the peak signal gain as a function of the cavity resonance wavelength (dashed line).

By recording the peak signal gain for a number of different pump powers—as a function of the resonant wavelength of the VCSOA—a family of gain-tuning curves may be generated. An example of this is shown in Fig. 5.14 for a second generation SCC-design MT-VCSOA. The theoretical peak signal gain curves assume a constant pump power over the device tuning range. For each pump power, the maximum value of material gain is labeled in order to facilitate a more general comparison of the device results, independent of the pumping method. The theoretical curves have been generated using the appropriate peak gain expression from Section 2.4.2; in this example Eq. 2.18 is used for the reflection mode SCC-design MT-VCSOA. This model includes all previously described parameters, including the wavelength response as a function of L_g, the variation in mirror reflectance, and the change in gain enhancement with tuning.

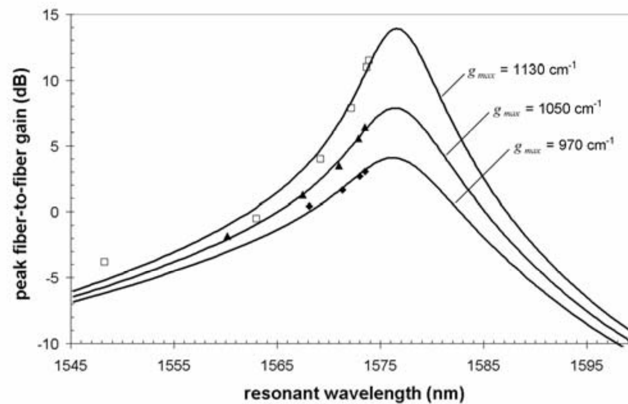

Fig. 5.14: Theoretical and experimentally measured peak fiber coupled gain as a function of the resonant cavity wavelength of the reflection mode SCC-design MT-VCSOA. The theoretical curves are generated from Eq. 2.18, after matching the wavelength tuning response in Eq. 2.17.

For the device presented in Fig. 5.14 the tunable mirror reflectance peaks near 1575 nm, while the best fit is achieved with the wavelength of maximum material gain at 1572 nm. The position of the maximum material gain agrees with the theoretically expected value for this active region. In this case the PL peak is designed to be at 1545 nm at room temperature, leading to a peak material gain near 1550 nm. Assuming the wavelength of maximum gain red-shifts at a rate of 0.5 nm/K [21], and given a temperature rise of roughly 40–50 K in the MQW structure with the pump powers used in testing, a red shift of the theoretical maximum material gain to wavelengths between 1570 nm and 1575 nm is expected. In this device the offset in the peak reflectance of the tunable mirror structure and the peak material gain wavelength leads to an asymmetric peak gain response. Additionally, the position of maximum signal gain is found to correspond with the wavelength of peak mirror reflectance, similar to that found for the first generation devices, as presented in Section 4.3.2.

From Fig. 5.14, the maximum-recorded fiber-to-fiber gain is 11.5 dB at a pump power of 100 mW (corresponding to a maximum material gain of 1130 cm^{-1}) and 3 dB on-chip gain, neglecting coupling losses, is recorded over a 25.6 nm wavelength range (from 1548.3 to 1573.9 nm). At 100 mW of pump power, at least 3 dB fiber-to-fiber gain (including 7 dB signal coupling loss) is recorded from roughly 1568 nm to 1574 nm. With increasing pump power, the device achieved lasing action at the initial (unbiased) resonant wavelength. Since it is only possible to blue shift the resonant wavelength of the VCSOA, signal gain values cannot be recorded for

wavelengths longer than about 1574 nm, which is the initial resonant wavelength of the cavity. Based on theses results, it is apparent that the theoretical model matches well with the recorded experimental data. With the accuracy of the model verified, it is now possible to simulate the peak gain response of the MT-VCSOA given arbitrary tunable cavity designs.

The first example focuses on a reflection mode SCC-design MT-VCSOA with a $5\lambda_c/2$ semiconductor cavity—containing the same stacked MQW active region used in the fabricated devices—a $5\lambda_c/4$ air gap, R_m = 0.91, R_c = 0.32, R_b = 0.999, and assuming a signal coupling loss of 7 dB. This model is similar to that shown previously; however, in this example, the peak reflectance of the tunable mirror structure occurs much closer to the wavelength of maximum material gain. The simulated peak fiber-to-fiber gain curves for this structure are shown in Fig. 5.15(a), in each plot the g_{max} indicates the maximum value of material gain for the given pump value. Also included with the theoretical curves is experimental data recorded for a second generation MT-VCSOA, exhibiting a peak mirror reflectance near 1570 nm (wavelength of maximum material gain is assumed to be at 1572 nm for all simulations). With the reflection mode SCC-design—using a transmissive tunable DBR—the theoretical wavelength span over which 10 dB of fiber-to-fiber gain may be achieved for a constant pump power of approximately 100 mW (1130 cm^{-1}) is 13.7 nm, between 1562.8 and 1576.5 nm. A further increase in the pump power results in lasing at the center wavelength of the cavity. To achieve the theoretical 10 dB fiber-to-fiber tuning range mentioned above, the initial air-gap thickness must

lead to a resonant wavelength ≥ 1576.5 nm, and the actuator must be capable of generating a wavelength shift ≥ 13.7 nm.

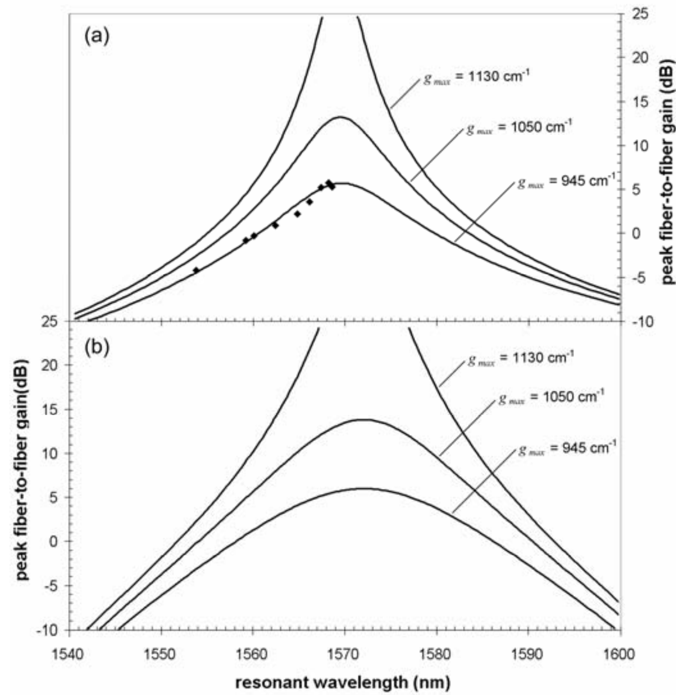

Fig. 5.15: Theoretical peak fiber-coupled gain as a function of the resonant cavity wavelength for a Generation 2 MT-VCSOA compared with experimental data (a), and for the bottom-emitting reflection mode SCC-design MT-VCSOA (b), with the membrane DBR used as the high reflectivity mirror (bottom-emitting). In both (a) and (b), the peak reflectance of the transmissive mirror is 0.974.

Fig. 5.15(b) presents a reflection mode SCC-design MT-VCSOA using the MEMS tuning element as the high reflectivity mirror (R_m = 0.999) and the fixed substrate DBR as the transmissive mirror (R_t = 0.974). This device will be referred to as a bottom-emitting MT-VCSOA. In this configuration, the 10 dB fiber-to-fiber tuning range is extended to 24.5 nm (1559.9 nm to 1584.4 nm). Due to the increased

membrane reflectance, the variation in R_{eff} with tuning is minimized, as discussed previously (Section 5.3.1). From this result it is possible to see that the limiting factor in the current optical cavity design is the significant reduction in the mirror reflectance that occurs with tuning.

With the bottom-emitting MT-VCSOA, the wavelength of the peak fiber-to-fiber gain is found to coincide with the position of the maximum material gain, in contrast with the top-emitting devices where the maximum gain is determined by the peak of the effective mirror reflectance. By comparing the theoretical gain curves in Fig. 5.15, it is possible to see that the width of the peak gain envelope is greatly increased with the bottom-emitting structure, due to the more constant mirror properties with tuning. In this configuration, the effective tuning range is no longer limited by the response of the resonant cavity; instead, this structure is limited by the available single-pass gain, which is dictated by the optical confinement, material gain spectrum, and the internal cavity loss.

Continuing on with the examination of alternative cavity designs, the next structure under consideration is a transmission mode SCC-design MT-VCSOA utilizing the same $5\lambda_c/2$ cavity and $5\lambda_c/4$ air gap, but with equal peak mirror reflectance values of $R_b = R_f = 0.974$. Applying Eq. 2.20, it is possible to plot the variation in peak gain with tuning—included in Figs. 5.16 and 5.17 below. In this design the peak gain response is similar to that seen in Fig. 5.15(a), however, given the increased mirror loss associated with transmission mode operation, higher material gain values are required in order to reach a similar level of signal gain. As

with the reflection mode devices of Generations 1 and 2, the use of the transmissive tunable mirror structure leads to a rapid roll-off in signal gain with tuning.

5.4.3 Peak Gain Response: EC-design MT-VCSOAs

In order to model EC-design tunable VCSOAs, the change in the enhancement factor with tuning must first be examined. Using the transmission matrix solver discussed previously, the lateral shift of the standing wave peaks in a $5\lambda_c/2$ cavity is found to be approximately 1 nm per nm of wavelength tuning, slightly less than the value of 1.16 for a similar cavity length SCC-design MT-VCSOA. With the EC-design, the incorporation of an ARC leads to $R_c \approx 0$, and $R_{eff} = R_m$ over the device tuning range. Assuming the top mirror consists of the same DBR pillar as the SCC-design, the effective reflectance of the tunable mirror structure is reduced to 0.91, due to the incorporation of the ARC. In addition to the increased mirror loss, the EC-design exhibits a longer total cavity length, arising from the increased field penetration depth into the tuning mirror (as discussed in Section 2.4.1). The corresponding increase in the overall cavity length results in a reduced fill factor (L_a/L_c) in these devices. The combination of a lower tunable mirror reflectance and decreased optical confinement leads to an increase in the required material gain in order to reach a similar level of signal gain in the EC-design MT-VCSOAs.

With transmission mode operation, the need for two reduced reflectivity mirrors leads to a further increase in the mirror loss, and in for a transmission mode EC-design MT-VCSOA the required single-pass gain for a fiber-to-fiber gain of 10 dB

becomes quite large (> 6%). In order to improve the achievable signal gain for these structures, the number of periods in the DBR pillar should be increased. For transmission mode MT-VCSOAs utilizing the EC-design, the peak gain response may be modeled using Eq. 2.19. It is interesting to note that this relationship can also be used to approximate the SCC-design MT-VCSOA with a high reflectivity tuning mirror. As with the bottom-emitting SCC-design, the peak signal gain curves for the EC-design peak at the wavelength of maximum material gain, due to the constant mirror properties with tuning. The gain-tuning curves for each of the simulated structures are included in Fig. 5.16 for a maximum material gain of 1100 cm^{-1}. In order to generate a more useful comparison of the EC-design MT-VCSOAs (given the increased mirror loss in this design), these structures have been modeled with a maximum material gain of 2200 cm^{-1} in Fig. 5.17.

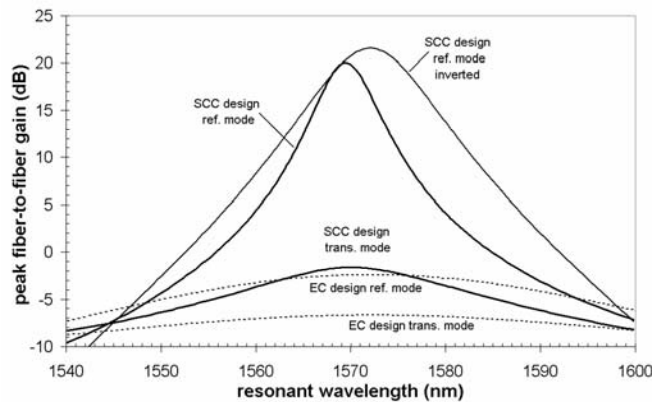

Fig. 5.16: Peak fiber coupled gain for each tunable VCSOA configuration, given a peak material gain value of 1100 cm^{-1} at 1572 nm. Dashed lines indicate devices utilizing the EC-design.

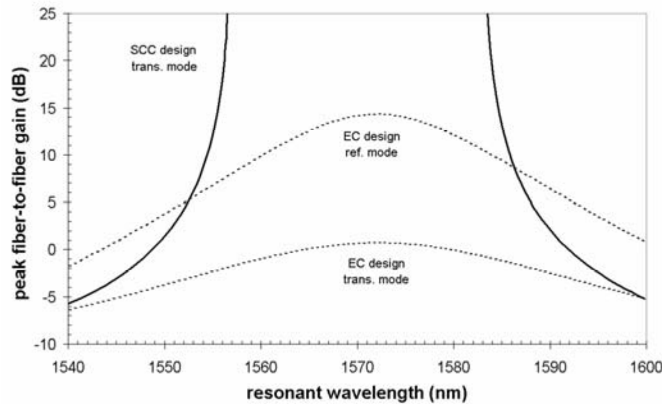

Fig. 5.17: Peak fiber coupled gain for the transmission mode SCC-design MT-VCSOA as well as the reflection and transmission mode EC-design tunable VCSOAs, given a peak material gain value of 2200 cm^{-1}. Note that the transmission mode SCC-design device has reached lasing threshold from roughly 1558 nm to 1586 nm.

5.4.4 Saturation Properties

Using the steady state amplifier rate equations—Eqs. 2.9 and 2.10—the saturation output power as a function of the cavity resonance wavelength may be determined. In this simulation the procedure outlined in [16] is employed to find the change in signal gain brought about by the increasing photon density in the resonant cavity. For any optical amplifier, the saturation output power is defined as the output signal power at which the amplifier gain is half of the small-signal value. At high input signal powers, the reduction in gain is controlled by the rate of stimulated emission in the cavity. With increasing stimulated recombination, the photon density grows rapidly at the expense of the carrier density in the gain medium. From the rate equations, the stimulated emission rate is proportional to the active material gain as well as the cavity photon lifetime. Over the wavelength-tuning span of the MT-

VCSOA these parameters will vary, leading to fluctuations in the saturation characteristics of the device. The theoretical saturation output power for a reflection mode SCC-design MT-VCSOA utilizing a transmissive tunable mirror structure (top-emitting device) is shown in Fig. 5.18.

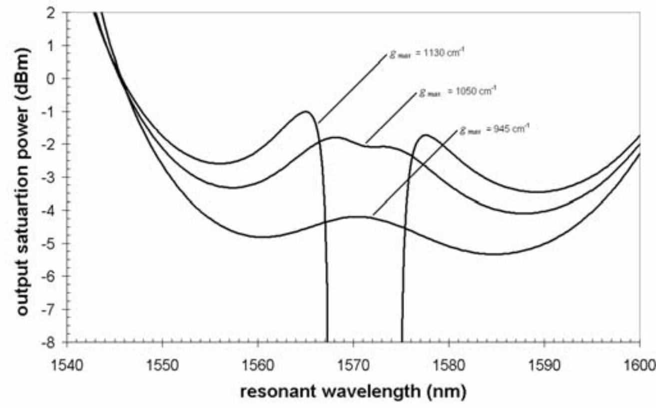

Fig. 5.18: Saturation output power of the reflection mode SCC-design MT-VCSOA for various pump powers. This design is the same as that used in the first two generations of tunable VCSOAs.

In this model, the roll-off in mirror reflectance with tuning leads to a decrease in the cavity photon lifetime, due to the increased mirror loss, and thus a large increase in the saturation output power at resonant wavelengths away from the position of maximum signal gain (for values of λ_R shorter than roughly 1550 nm and greater than about 1600 nm). Unfortunately, the amplifier gain in this regime is negligible. In the region of significant signal gain, from approximately 1555 nm to 1585 nm, and for low pump powers, the saturation output power reaches a local maximum at the wavelength corresponding to the peak gain of the VCSOA. To either side of this

maximum, the saturation output power drops, and two minima are found. In this region the mirror reflectance has increased, leading to a corresponding increase in the photon lifetime of the cavity; however, the signal gain is still low, thus limiting the output power of the MT-VCSOA. With pump powers approaching lasing threshold, the cavity photon density increases dramatically and the saturation output power drops sharply, as in the curve corresponding to a g_{max} value of 1130 cm^{-1}. In this regime the MT-VCSOA gain is significant (>20 dB); the large reduction in saturation output power results from a corresponding decrease in the input saturation power near threshold. This trend is identical to that observed in fixed-wavelength VCSOAs [16].

The saturation characteristics of the remaining cavity designs follow roughly the same trends as shown in Fig. 5.18 above. For the bottom-emitting reflection mode SCC-design MT-VCSOA the maximum saturation output power is similar, as the peak mirror reflectance is the same. However, the shape of the saturation output power curve is somewhat flatter around the wavelength of peak gain, due to the wider peak gain envelope in this device. From previous work on fixed-wavelength VCSOAs, increased saturation output power is found for devices with decreased mirror reflectance—at the expense of higher required pump powers [15], [16]. The same trend holds true for tunable VCSOAs. Assuming a peak fiber-to-fiber gain of 10 dB with the reflection mode SCC-design MT-VCSOA, the maximum saturation output power is roughly –2.5 dBm. For the transmission mode devices using the SCC-design, the saturation output power increases to –0.5 dBm, for a similar value

of peak gain, due to the increased mirror loss found in these devices. With MT-VCSOAs utilizing the EC-design, the peak saturation output power further increases, owing to the reduction in the reflectance of the tunable mirror structure brought about by the incorporation of the ARC. These values may be compared with the recently demonstrated record high saturation output power of 0.5 dBm [14].

5.4.5 Noise Characteristics

Similar to the saturation characteristics, the noise figure of MT-VCSOAs will fluctuate with tuning, due to changes in the mirror reflectance and single-pass gain. With VCSELs, once threshold is reached the gain clamps at a constant value resulting in relatively uniform properties with tuning. In contrast, the requirement of sub-threshold operation in VCSOAs leads to a varying value of material gain over the operating range of the device. Thus, with MT-VCSOAs, variations in pump power are required to maintain a constant signal gain, resulting in a corresponding variation in the carrier density. From Eq. 2.12 the changing carrier density in the active material results in a varying inversion parameter as a function of the resonant wavelength of the device. Using Eqs. 2.9–2.14, it is possible to make theoretical predictions of the noise figure of MT-VCSOAs. In this model it is assumed that the pump power is varied in order to achieve a constant fiber-to-fiber gain of 10 dB. The results of this simulation are presented in Fig. 5.19.

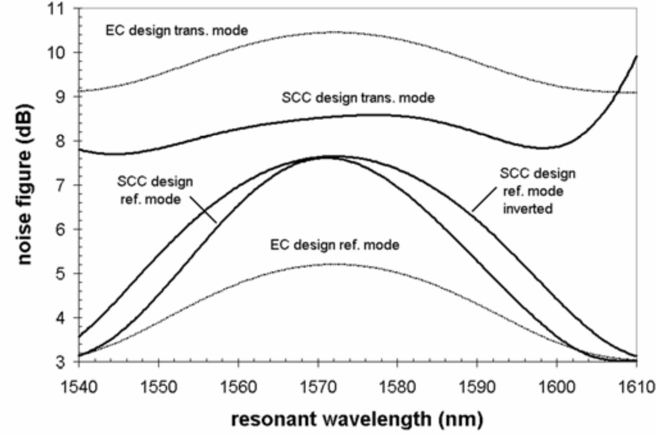

Fig. 5.19: Noise figure of each tunable VCSOA configuration given a constant peak fiber-to-fiber gain value of 10 dB over the wavelength tuning range.

The noise figure of the reflection mode tunable VCSOAs exhibits a peak at the wavelength of maximum effective mirror reflectance for the SCC-design with the transmissive tunable mirror structure, or at the point of maximum material gain for the EC-design and the bottom-emitting SCC-design MT-VCSOAs. With reflection mode operation, the bottom mirror reflectance near unity (0.999) leads to an excess noise coefficient $\chi_r \approx 1$. Additionally, for high signal gain, $NF \approx 2n_{sp}$, and the noise figure is solely a function of the inversion parameter, as discussed in Section 2.2.3. For these devices, the required pump power must be reduced near the maximum value of the active material gain, and also at the peak reflectance of the DBR mirrors, leading to an increase in n_{sp} and a corresponding increase in the overall noise figure. Due to the reduced variation in mirror reflectance for the bottom-emitting SCC-design, the required pump power is lower for a larger range of wavelengths; thus, the noise curve is somewhat broader, as compared with the top-

emitting devices. Note that the peak noise figure of 7.6 dB is the same for both designs, as the peak mirror reflectance values are equal.

For the reflection mode EC-design MT-VCSOA the maximum noise figure is reduced to 5.2 dB, as compared with reflection mode devices utilizing SCC-design. This can be explained by the reduced mirror reflectance and decreased optical overlap, which give rise to a higher required carrier density and a corresponding decrease in n_{sp}, for a given value of signal gain. The trend of decreased noise figure for lower transmissive mirror reflectance in the reflection mode MT-VCSOAs follows the trend observed in fixed-wavelength VCSOAs [22]. For the reflection mode devices, reducing the reflectance of the transmissive mirror to 0.91 in the SCC-design will result in noise figure values similar to that found for the EC-design.

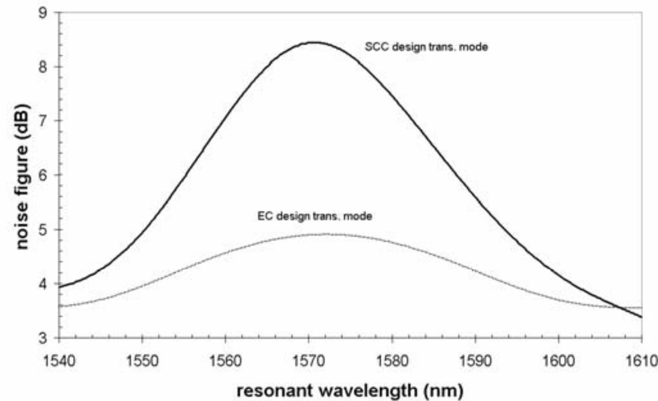

Fig. 5.20: Noise figure of transmission mode MT-VCSOAs for a constant peak fiber-to-fiber gain value of 10 dB over the wavelength tuning range. Here the input signal is injected through the opposite side of the device (as compared with Fig. 5.19).

With transmission mode tunable VCSOAs, the large mirror losses lead to the requirement of high pump powers for a given value of signal gain and thus a value of n_{sp} near unity. In these devices χ_t is minimized for $g_s = R_b^{-1/2}$. However, the varying single-pass gain with tuning makes it difficult to operate the MT-VCSOA under this condition. Following the results of fixed-wavelength VCSOAs, in order to optimize the noise figure of the transmission mode devices, the input DBR should be of a reduced reflectance, as compared to the output mirror. This may be seen by comparing the results of Fig. 5.19 with the theoretical noise figure of the transmission mode devices shown in Fig. 5.20. In this figure the structure of the transmission mode tunable VCSOA is unchanged; however, the signal now enters and exits the devices in the opposite direction. This leads to a reduced noise figure over the tuning range of the device for the transmission mode MT-VCSOA utilizing the EC-design. In this configuration the peak noise figure is reduced to 4.9 dB. With the transmission mode SCC-design tunable VCSOA, the peak value of the noise figure is the same as that shown in Fig. 5.19 (8.4 dB), as the peak mirror reflectance of the tunable mirror structure is equal to the reflectance of the fixed mirror (0.974). Here the roll-off in mirror reflectance with tuning leads to the condition of a reduced input mirror reflectance, decreasing the noise figure at the extremes of the device tuning range. Note that the signal gain and required pump power are unchanged for the transmission mode devices, regardless of the direction of signal input/output.

5.5 Summary

A second generation of MT-VCSOAs has been designed, fabricated, and analyzed. These devices utilize a revised mechanical structure in order to overcome the limitations of the initial MT-VCSOAs. Changes to the mechanical design of the actuator include a radiused support structure, an enlarged DBR pillar, as well as undercut protection and mechanical constraint brought about by a low temperature CVD-deposited SiO_2 film. For the measured data, the ASE wavelength tuning range is greatly extended as compared to the first generation of devices. Utilizing the updated design, the total ASE tuning range is extended to greater than 50 nm with the application of 30 V to the tuning diode. By constraining the mechanical support structure against out-of-plane deformation, these devices exhibit improved stability, allowing for an in-depth examination of the dynamic characteristics of the actuator.

The frequency response of the MT-VCSOA electrostatic actuator has been characterized in vacuum and at atmosphere using a laser Doppler vibrometer. At 6 mT and for small displacements, the actuator exhibits a simple harmonic response with a Q of 491, while for large displacements the device exhibits a hardening spring Duffing response. Typical natural frequency values of the MT-VCSOA actuator range from 117–209 kHz, depending on the device geometry. At atmosphere, the actuator exhibits significant viscous damping, reducing the Q to 1.2 and resulting in a nearly critically damped response with typical settling times below 10 μs.

Although the updated mechanical design allows for rather larger ASE wavelength shifts, the effective tuning range of the second generation of devices is

nonetheless limited to approximately 10 nm—similar to the first generation MT-VCSOAs. In order to improve the effective tuning range of these devices, a thorough investigation of alternative cavity designs is presented. This includes both a theoretical and experimental examination of the wavelength tuning response, peak signal gain, saturation properties, and noise figure of MT-VCSOAs for various optical cavity designs and modes of operation.

Making use of general FP relationships it is possible to predict the wavelength tuning characteristics and the signal gain of MT-VCSOAs. Additionally, using a steady state rate equation approach it is possible to describe the saturation output power and noise figure of these devices. With the MT-VCSOA the use of MEMS based wavelength-tuning leads to varying amplifier properties over the wavelength span of the device. The changing center wavelength of the cavity results in variations in the reflectance and penetration depth of the DBRs, changes in the confinement factor, and operation at different points on the material gain curve. In addition, the varying properties of the optical cavity—brought about by changes in the thickness of the air gap—serve to alter the device properties. For the SCC-design, the changing phase of reflection from the membrane DBR leads to largely varying mirror reflectance with tuning. With the EC-design the variation in amplifier properties is controlled by changes in the cavity length and material gain with tuning.

The major limitation to the wavelength span over which sufficient amplifier gain may be achieved in the top-emitting SCC-design reflection mode MT-VCSOA is the

roll-off in mirror reflectance that occurs as the air gap deviates from the ideal thickness. To overcome this limitation, it is proposed that the tunable mirror structure be used as the high reflectivity DBR, and the fixed bottom DBR be used as the transimissive mirror in reflection mode devices (resulting in a bottom-emitting structure). With this configuration the tuning range over which the MT-VCSOA can achieve 10 dB of fiber-to-fiber gain is increased by roughly 10 nm for a similar value of material gain. Unfortunately, a transmission mode MT-VCSOA requires the use of two reduced reflectivity mirrors, making the varying reflectance found with the SCC-design extremely difficult to avoid. With a transmission mode device, the EC-design may prove to be a better choice, as the presence of the ARC in the air cavity leads to a constant top mirror reflectance over the device tuning range. However, the EC-design requires larger material gain values, and corresponding optical pump powers, due to the reduction in top mirror reflectance and optical confinement brought about by the incorporation of the ARC in the top mirror.

Increased saturation output powers and decreased noise figures may be achieved in devices exhibiting reduced mirror reflectance values, following the same trend as fixed-wavelength VCSOAs. For the EC-design the incorporation of an ARC in the cavity results in a reduction in the effective reflectance of the tunable mirror structure and a decrease in the optical confinement factor—leading to an increase in the saturation output power, and a corresponding decrease in the signal-spontaneous beat noise. Nevertheless, the improvement in the saturation properties and noise figure come at the expense of increased required pump power values. For reflection

mode SCC-design MT-VCSOAs, further improvements may be found by reducing the reflectance of the transmissive DBR and ensuring that the reflectance of the high reflectivity mirror remains at or above 0.999 over the tuning range of the device.

References

[1] S. Irmer, J. Daleiden, V. Rangelov, C. Prott, F. Romer, M. Strassner, A. Tarraf, H. Hillmer, "Ultralow biased widely continuously tunable fabry-Perot filter," *IEEE Photon. Tech. Lett.*, vol. 15, pp. 434–436, Mar. 2003.

[2] F. Sugihwo, "Design and fabrication of wavelength tunable optoelectronic devices," Ph.D. dissertation, Stanford University, Stanford, CA, 1998.

[3] J. Daleiden, N. Chitica, M. Strassner, A. Spisser, J. L. Leclercq, P. Viktorovitch, D. Rondi, E. Goutain, J. Peerlings, J. Pfeiffer, R. Reimenschneider, K. Hjort, "Tunable InP/air gap Fabry Perot filter for wavelength division multiplex fiber optical transmission," in *Proc. 11th Int. Conf. InP and Related Materials*, May 16–20 1999, Paper TuA3-4, pp. 285–287.

[4] S. Irmer, J. Daleiden, V. Rangelov, C. Prott, F. Romer, M. Strassner, A. Tarraf, H. Hillmer, "Ultralow biased widely continuously tunable Fabry-Perot filter," *IEEE Photon. Tech. Lett.*, vol. 15, pp. 434–436, Mar. 2003.

[5] P. Tayebati, P. D. Wang, D. Vakhshoori, R. N. Sacks, "Widely tunable Fabry-Perot filter using Ga(Al)As-AlO_x deformable mirrors," *IEEE Photon. Technol. Lett.*, vol. 10, pp. 394–396, Mar. 1998.

[6] P. Tayebati, P. D. Wang, D. Vakhshoori, C. C. Lu, M. Azimi, R. N. Sacks, "Half-symmetric cavity tunable microelectromechanical VCSEL with single spatial mode," *IEEE Photon. Technol. Lett.*, vol. 10, pp. 1679–1681, Dec. 1998.

[7] Q. Chen, G. D. Cole, E. S. Björlin, T. Kimura, S. Wu, C. S. Wang, N. C. MacDonald, J. E. Bowers, "First demonstration of a MEMS tunable vertical-cavity SOA", *IEEE Photon. Technol. Lett.*, vol. 16, pp. 1438–1440, Jun. 2004.

[8] M. Strassner, N. Chitica, A. Tarraf, "Investigations of growth conditions for InP suited for micro opto electro mechanical systems for data communication,"

in *Proc. 14th Int. Conf. InP and Related Materials*, May 12–16 2002, Paper A4-5, pp. 351–354.

[9] K. L. Turner, P. G. Hartwell, N. C. Macdonald, "Multi-dimensional MEMS motion characterization using laser vibrometry," in *Digest of Technical Papers*, *Transducers '99: 10th International conference on solid-state Sensors and Actuators*, Sendai, Japan, 7–10 Jun. 1999, pp. 1144–1147.

[10] P. Hagedorn, *Non-Linear Oscillations*, New York, NY: Oxford University Press, 1988, pp. 1–59.

[11] G. D. Cole, E. S. Björlin, Q. Chen, C.-Y. Chan, S. Wu, C. S. Wang, N. C. MacDonald, J. E. Bowers, "MEMS-tunable vertical cavity SOAs," *IEEE J. Quantum Electron.*, vol. 41, pp. 390–407, Mar. 2005.

[12] Y. Matsui, D. Vakhshoori, P. Wang; P. Chen, C.-C. Lu, M. Jiang; K. Knopp, S. Burroughs, P. Tayebati, "Complete polarization mode control of long-wavelength tunable vertical-cavity surface-emitting lasers over 65-nm tuning, up to 14-mW output power," *IEEE J. Quantum Electron.*, vol. 39, pp. 1037–1048, Sep. 2003.

[13] A. Syrbu, V. Iakovlev, G. Suruceanu, A. Caliman, A. Rudra, A. Mircea, A. Mereuta, S. Tadeoni, C.-A. Berseth, M. Achtenhagen, J. Boucart, E. Kapon, "1.55-μm optically pumped wafer-fused tunable VCSELs with 32-nm tuning range", *IEEE Photon. Technol. Lett.*, vol. 16, pp. 1991–1993, Sep. 2004.

[14] E. S. Björlin, T. Kimura, Q. Chen, C. Wang, J. E. Bowers, "High output power 1540nm vertical cavity semiconductor optical amplifiers," *Electron. Lett.*, vol. 40, pp. 121–123, Jan. 2004.

[15] E. S. Björlin, T. Kimura, J. E. Bowers, "Carrier-confined vertical-cavity semiconductor optical amplifiers for higher gain and efficiency," *IEEE J. Select. Topics Quantum Electron.*, vol. 9, pp. 1374–1385, Sep./Oct. 2003.

[16] J. Piprek, E. S. Björlin, J. E. Bowers, "Design and analysis of vertical-cavity semiconductor optical amplifiers," *IEEE J. Quantum Electron.*, vol. 37, pp. 127–134, Jan. 2001.

[17] C. Tombling, T. Saitoh, T. Mukai, "Performance predictions for vertical-cavity semiconductor laser amplifiers," *IEEE J. Quantum Electron.*, vol. 30, pp. 2491–2499, Nov. 1994.

[18] E. S. Björlin, B. Riou, P. Abraham, J. Piprek, Y.-J. Chiu, K. A. Black, A. Keating, J. E. Bowers, "Long wavelength vertical-cavity semiconductor optical amplifiers," *IEEE J. Quantum Electron.*, vol. 37, pp. 274–281, Feb. 2001.

[19] F. Sugihwo, M. C. Larson, J. S. Harris, “Micromachined widely tunable vertical cavity laser diodes,” *J. Microelectromech. Syst.*, vol. 7, pp. 48–55, Mar. 1998.

[20] L. A. Coldren and S. W. Corzine, *Diode Lasers and Photonic Integrated Circuits*, New York, NY: Wiley, 1995.

[21] T. Kimura, E. S. Björlin, J. Piprek, J. E. Bowers, “High-temperature characteristics and tunability of long-wavelength vertical-cavity semiconductor optical amplifiers,” *IEEE Photon. Technol. Lett.*, vol. 15, pp. 1501–1503, Nov. 2003.

[22] E. S. Björlin, J. E. Bowers, “Noise figure of vertical-cavity semiconductor optical amplifiers”, *IEEE J. Quantum Electron.*, vol. 38, pp. 61–66, Jan. 2002.

CHAPTER 6

Generation 3: Revised Optical Cavity Design

The second generation of MT-VCSOAs was developed in order to overcome the limitations in the initial electrostatic actuator design. Utilizing a revised mechanical structure, the total ASE tuning range was extended to greater than 50 nm, while the required tuning bias was reduced below 30 V for the second generation of MT-VCSOAs. Additionally, the revised mechanical structure exhibited improved stability, allowing for an in-depth characterization of the dynamic response of the actuator. As discussed in the previous chapter, these results represent a significant improvement in the tuning response when compared with the initial generation of devices. Unfortunately, a thorough characterization of the peak gain response of the second generation MT-VCSOAs revealed that the optical cavity design was now the major limitation in realizing a wide effective wavelength tuning range.

With the top-emitting devices of Generations 1 and 2, the use of the MEMS-tunable DBR as the transmissive mirror resulted in a large variation in mirror reflectance with tuning, limiting the effective tuning range (wavelength span over which the amplifier can achieve at least 10 dB on-chip gain) to approximately 10 nm [1], [2]. Following an in-depth analysis of alternative optical cavity designs [2], it

was found that the rapid roll-off in mirror reflectance was exaggerated by the low power reflectance of the membrane, which was necessary for the top-emitting configuration. As discussed in Section 5.3, in order to realize more constant mirror properties with tuning, a bottom-emitting MT-VCSOA is preferred when using the SCC-design. The bottom-emitting configuration utilizes a high reflectivity MEMS-tunable mirror structure for the back reflector and a transmissive fixed substrate DBR for signal input/output. Accordingly, this chapter presents a third generation of MT-VCSOAs utilizing a revised optical cavity design that greatly increases the effective tuning range and results in more constant amplifier properties with tuning. Through modifications to the design of the electrostatic actuator, the required tuning voltages are again reduced and the device lifetime is further extended, as compared with previous generations of devices.

By suppressing the variation in mirror reflectance with tuning, the bottom-emitting MT-VCSOAs display a two-fold increase in the effective tuning range—with a minimum of 5 dB fiber-to-fiber gain (12 dB on-chip gain) over a wavelength span of 21 nm, from 1557.4 nm to 1536.4 nm. Additionally, these devices exhibit saturation, bandwidth, and noise properties similar to state-of-the-art fixed-wavelength VCSOAs, including a maximum fiber-coupled saturation output power of -1.4 dBm and an average gain bandwidth and noise figure of 65.2 GHz and 7.5 dB respectively. Finally, through improvements to the electrostatic actuator, the maximum required tuning voltage has been reduced to 10.5 V, a five-fold reduction compared with the first generation of MT-VCSOAs [1].

6.1 Bottom-Emitting Tunable VCSOAs

This chapter focuses on the development and analysis of bottom-emitting reflection-mode MT-VCSOAs. When compared with previous generations of tunable VCSOAs, these devices utilize a unique material structure, including a revised active region and DBRs. For the third generation MT-VCSOAs, the active region includes pump-absorbing barriers, an InP heat spreading layer, and a larger number of quantum wells. Modifications to the resonant cavity structure represent the most significant changes to these devices. This includes the use of a high reflectivity tunable mirror structure—to reduce the variation in reflectance with tuning, as well as a reduced Al-content sacrificial layer—in order to lower the oxidation rate of the unetched AlGaAs. In the bottom-emitting reflection mode MT-VCSOAs, the MEMS-tunable mirror structure acts as the high reflectivity back mirror, while the reduced reflectivity bottom DBR is used for signal injection and extraction. In addition to the more constant mirror properties with tuning, a further advantage of the bottom-emitting design is reduced signal loss, as the input and output signals no longer pass through multiple chemically etched air-semiconductor interfaces.

6.1.1 Material Structure

Fig. 6.1 shows a cross-sectional schematic of the bottom-emitting MT-VCSOA. Similar to previous generations of devices, the Generation 3 MT-VCSOAs consist of an InP-based active region wafer-bonded to two GaAs/AlGaAs DBRs, are designed

for optical pumping at 980 nm, and operate in reflection mode. The major difference in these devices, when compared with Generations 1 and 2, is the use of an improved optical cavity design—specifically a bottom-emitting configuration with a high reflectivity tunable DBR and a transmissive fixed DBR for signal input/output.

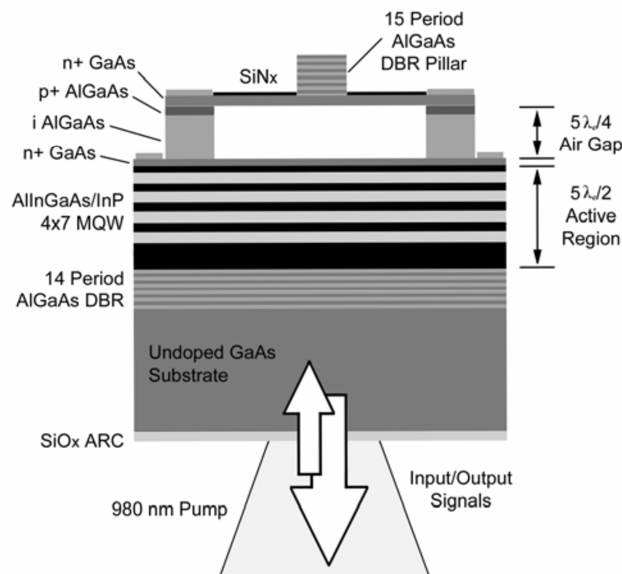

Fig. 6.1: Cross-sectional schematic of the bottom-emitting tunable VCSOA.

6.1.2 Active Region Design

The bottom-emitting MT-VCSOAs presented here utilize an updated active region that includes absorbing barriers and an InP-heat spreading layer. In previous VCSOA active region designs, the only optically absorbing layers of the 980 nm pump light were the QWs. Because pump absorption occurred only in the thin QW layers, these devices exhibited low pump absorption efficiency—on the order of 3% [3]. With the new active design, the band gap of the barriers has been reduced to allow for absorption of the pump, leading to an increase in the absorption efficiency

and higher carrier densities for a given pump power. In this iteration the stacked MQW structure contains four sets of seven 0.85% compressively strained AlInGaAs wells placed at the top four peaks of the standing optical wave in a $5\lambda_c/2$ cavity. Here, the last standing-wave peak overlaps with a 276-nm thick InP heat spreading layer, as seen in Fig. 6.2 (see Appendix B for a detailed description of this structure).

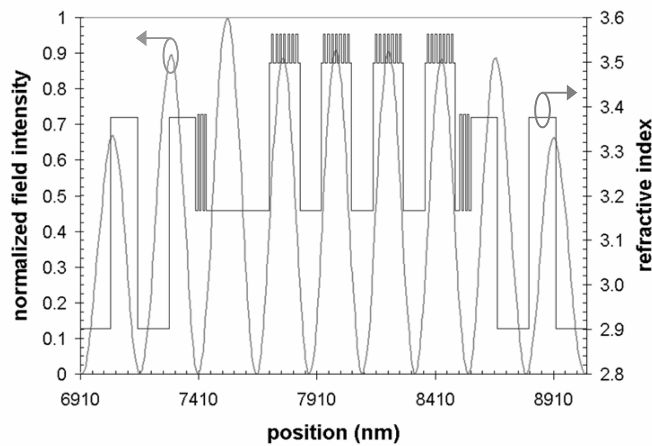

Fig. 6.2: Standing wave field distribution and refractive index profile of the 28-well active region.

The addition of the binary heat spreading layer is important as the active region incorporates absorbing -0.55% tensile strained AlInGaAs barriers. As a comparison, the thermal conductivity of the binary compound InP is 0.68 $Wcm^{-1}K^{-1}$, while the thermal conductivity of lattice matched quaternary alloys, such as InGaAsP and AlInGaAs, is an order of magnitude lower at 0.072 $Wcm^{-1}K^{-1}$ and 0.05 $Wcm^{-1}K^{-1}$ respectively [4]. As in previous generations of devices, the PL peak of the QWs is designed to be at 1540 nm at room temperature.

Similar to the previously used active material structure, the revised active region design is $5\lambda_c/2$ in length. From Eq. 2.17 it is apparent that the tuning efficiency of the MT-VCSOA is maximized with the shortest possible cavity length. In order to incorporate the heat spreading layer in this design and also keep the total cavity length similar, the QWs must be removed from the final $\lambda_c/2$-section of the cavity and incorporated in the existing stacks. To make up for the slight decrease in gain enhancement resulting from the wider MQW stack, while maintaining a similar value of single-pass gain in this structure, the total number of QWs has been increased from 25 to 28 total wells (see Eq. 2.6 and Fig. 5.11 for more information).

6.1.3 Resonant Cavity Design

The mirror design in these devices has been updated in order to realize an improved effective tuning range as discussed previously. For the bottom-emitting devices, the fixed substrate DBR is used as the trasnmissive mirror and consists of 14 periods of $GaAs/Al_{0.98}Ga_{0.02}As$, with a theoretical power reflectance of approximately 0.94. In order to reduce stray reflections from the substrate to air interface, these devices utilize a $\lambda_c/4$ SiOx ARC as shown in Fig. 6.1.

From the top down, the high reflectivity MEMS-tunable mirror structure consists of 15 periods of $GaAs/Al_{0.92}Ga_{0.08}As$, a $3\lambda_c/4$ n^+ GaAs membrane layer, an approximately $5\lambda_c/4$ (optical thickness in air) $Al_{0.85}Ga_{0.15}As$ sacrificial etch layer and a $\lambda_c/4$ n^+ GaAs layer directly above the active region. As in previous generations of devices, selective removal of the sacrificial AlGaAs layer forms the variable air gap,

which acts as the first low index layer in the MEMS-tunable DBR and forms the SCC-design MT-VCSOA [2]. The maximum power reflectance of the top mirror is calculated to be 0.996, including the contribution of the air gap and the loss from the doped layers that make up the electrostatic actuator.

The basic design of the electrostatic actuator structure remains unchanged from the previous devices. However, the patterned portions of this structure, including the DBR pillar and sacrificial layer, utilize a reduced Al content in order to slow the oxidation rate and further improve the reliability of the devices. In this case, the aluminum content of the $Al_xGa_{1-x}As$ sacrificial etch layer has been reduced from the original composition of x = 0.98, to x = 0.85. As discussed in Section 4.4.2, oxidation of the high Al content AlGaAs sacrificial material may lead to rapid degradation of the actuator due to due to cracking of the GaAs membrane layer. Here, substantial strains are generated in mechanical support structure, resulting from the large volume shrinkage of the sacrificial etch material, on the order of 10%, as the AlGaAs is converted to AlO_x [5]. Lowering the Al content from 98% to 85% reduces the oxidation rate of this material by over an order of magnitude [6]. For similar reasons, the DBR pillar is now composed of alternating layers of $GaAs/Al_{0.92}Ga_{0.08}As$, rather than the previously used $GaAs/Al_{0.98}Ga_{0.02}As$.

The operating principle of the electrostatic actuator used in the third generation devices is identical to that of previous generations of MT-VCSOAs. Again, a reverse bias across the $n^+/p^+/i/n^+$ diode creates a Coulomb force that displaces the membrane towards the substrate, reducing the air-gap thickness and blue-shifting the resonant

cavity mode. As in previous devices, it is only possible to reduce the air gap; thus, it is only possible to blue shift the resonant wavelength.

6.1.4 Process Modifications

As discussed briefly in Section 3.4.1, the major alterations to the fabrication procedure of the bottom-emitting devices include a revised chemistry for the DBR pillar etch, a modified wet etch for the selective removal of the $Al_{0.85}Ga_{0.15}As$ sacrificial layer, and the addition of an evaporated SiO_x quarter-wave transformer as an ARC. Initial process development for these devices focused on the establishment of a reproducible DBR pillar etch. In order to maximized the reflectance of the tunable mirror structure in the bottom-emitting devices, the number of periods in the DBR pillar is increased to 15. Combining this with the reduction in the Al content of the low index AlGaAs layer to 92% results in a DBR pillar height of approximately 5 μm. Because the DBR pillar etch terminates on a non-selective GaAs structural film of only 350-nm in thickness, achieving a uniform and reproducible RIE process proved to be somewhat difficult. Initial test runs revealed that non-uniformities in the DBR etch rate across the ~1 cm^2 sample resulted in overetching of the GaAs structural film near the edge of the chip and underetching of the final DBR periods in the center of the sample. In order to accommodate the increase in the DBR pillar height, the originally used etch chemistry, consisting solely of $SiCl_4$, was changed to a BCl_3/Cl_2 mixture that had demonstrated improved etch uniformity in the fabrication of wafer-bonded VCSELs (see Appendix D for detailed etch parameters).

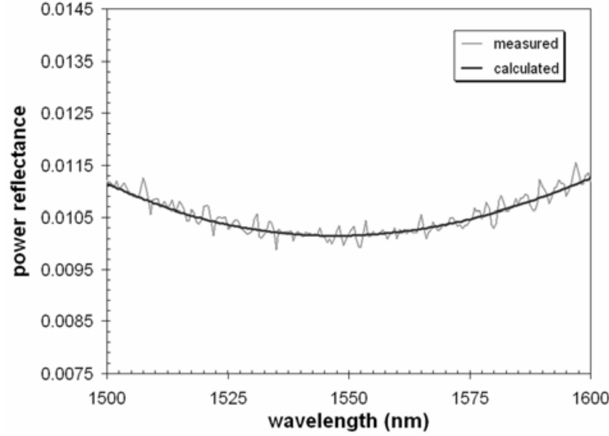

Fig. 6.3: Measured reflection spectrum for a typical SiO_x quarter-wave transformer (deposited on a Si dummy wafer). For this film the refractive index is found to be 1.67 and the film thickness is 231 nm.

Additional process modifications include lapping and polishing of the GaAs substrate, as well as the addition of an evaporated SiO_x ARC. Because the amplified output signal exits through the GaAs substrate in the bottom-emitting devices, backside polishing and deposition of an ARC are required to reduce signal losses as well as unwanted reflections from the substrate-air interface. In these devices an electron-beam evaporated SiO_x quarter-wave layer is employed. Reflection spectrum measurements of the ARC used in third generation of devices is included in Fig. 6.3. The reflectance spectrum of this film has been characterized using a spectrophotometer with a similar process described in Section 3.3.1. In order to determine the pertinent film properties, thicknesses were measured using a stylus profilometer, while fitting of the measured reflectance data with a simple transmission matrix model allowed for the extraction of the refractive index. To check the accuracy of the extracted index values an ellipsometer was used to directly

measure the refractive index of the SiO_x. Typical index values for this film were 1.6-1.8, with higher index films resulting from a slight increase in the deposition rate.

The final significant process modification was the development of a modified wet etch solution for the membrane release. In this case the decrease in the Al content of the sacrificial AlGaAs layer in the third generation of devices requires a corresponding increase in the HCl concentration for the undercut etch. With the previous generations of devices (utilizing an $Al_{0.98}Ga_{0.02}As$ sacrificial layer) a dilute HCl mixture consisting of 5:1 H_2O:HCl was capable of undercutting the membrane structure in approximately 25 minutes at room temperature. Given the reduced aluminum content ($Al_{0.85}Ga_{0.15}As$) sacrificial material, to achieve roughly the same etch rate, the wet etch chemistry was changed to a much higher HCl concentration, specifically 2:1 HCl:H_2O.

6.2 Revised Optical Test Setup

In order to avoid changes in pump efficiency due to the moving membrane structure, it is desirable to inject the 980-nm pump through the substrate and fixed mirror in MT-VCSOAs. However, the design of the third generation of devices also requires that signal input/output occur through the bottom mirror. In order to accommodate the bottom-emitting configuration, the third generation of MT-VCSOAs must be characterized in an updated optical test-setup. Modifications to the experimental setup include the addition of a WDM coupler in order to combine the 980 nm pump and 1550 nm input signal for injection through the substrate and

bottom mirror. Although this revised setup results in a slight decrease in the total available pump power (due to increased losses in the coupler), the use of a single fiber for both the pump and signal greatly simplifies alignment [7].

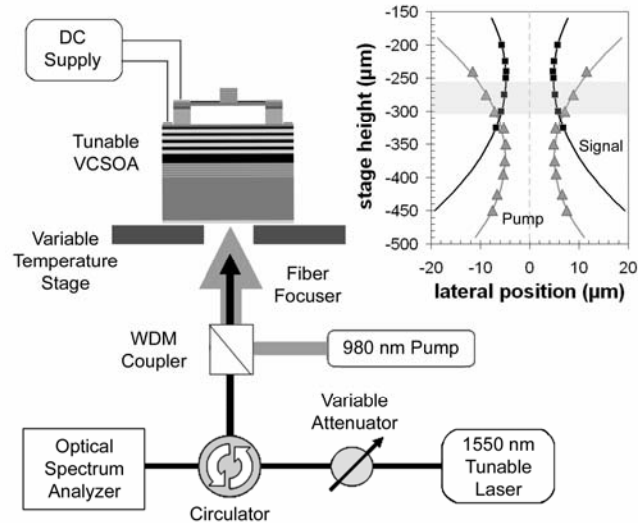

Fig. 6.4: Experimental setup used for the bottom-emitting MT-VCSOAs.

Fig. 6.4 shows a schematic of the optical test setup used for the bottom-emitting MT-VCSOAs. An external cavity tunable laser diode is used as the signal source and the input signal power is controlled by a variable optical attenuator to be -35 dBm. After multiplexing with a WDM coupler, both the 980-nm pump and long-wavelength signal are coupled through the bottom of the sample with a single 1550-nm fiber focuser. As seen in the inset of Fig. 6.4, due to the wavelength dependent focal length of the lens, there is a narrow range of stage positions where the pump spot size is slightly larger than that of the signal—the highlighted region is the approximate position used for testing. As the device operates in reflection, the

amplified output returns through the same fiber focuser and is separated from the input signal using a circulator. All measurements are made with the output signal coupled into single mode fiber on a calibrated optical spectrum analyzer at a resolution bandwidth of 0.1 nm. The coupling loss through the setup is measured to be approximately 7 dB, including back-coupling of the output into the focuser (5.8 dB) and the round trip through the WDM coupler and circulator (1.2 dB).

6.3 Generation 3 Results

Characterization of the final generation of MT-VCSOAs focuses on the variation in amplifier properties as a function of the resonant wavelength of the optical cavity. Properties of interest include the variation in peak gain, bandwidth, saturation, and noise figure of the optical amplifier. The calculated curves presented in the following sections rely on the theoretical models outlined in Chapter 2.

6.3.1 Enhanced Effective Tuning Range

Fig. 6.5 presents the gain spectra of a bottom-emitting MT-VCSOA for a pump power of 83 mW and a stage temperature of 15 ºC. As seen in the figure, the device is capable of at least 5 dB fiber-to-fiber gain (12 dB on-chip gain) over a 21 nm wavelength span, with a maximum applied voltage of 10.5 V. A maximum fiber-to-fiber gain value of 11.2 dB (18.2 dB on-chip gain) is recorded at 1548.0 nm. Investigations of the peak gain as a function of pump power reveal that 83 mW is the

optimal pump level for these devices—with increased pump powers the device could not be brought to lasing threshold.

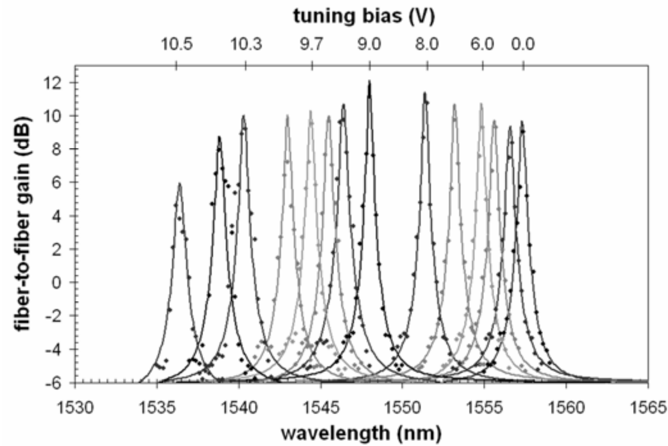

Fig. 6.5: Gain spectra over a >20 nm wavelength range at 15 ºC for a constant pump power of 83 mW and a maximum tuning bias of 10.5 V.

By fitting the individual gain spectra with the peak gain expression for a reflection-mode Fabry-Pérot amplifier (Eq. 2.1), it is possible to extract the mirror reflectance values, as well as the single-pass gain, as a function of the resonant wavelength of the cavity [2]. From theoretical fitting of the gain spectra, the device displays an average single-pass gain of 3.5% over the tuning range for a pump power of 83 mW. Combining this with the extracted mirror reflectance, the device is operating at an average of 97.8% of the single-pass gain required to reach threshold. In these devices the peak gain appears to be limited by device self heating. With decreasing temperature the gain continually increases, however low temperature operation is limited by the ambient dew point. The pull-in instability of the

electrostatic actuator is found to be the main failure mode and is also the limit of the overall wavelength tuning range in these devices

6.3.2 Improved Amplifier Properties

Fig. 6.6 presents the saturation output power and gain bandwidth of the bottom-emitting MT-VCSOA. From the figure, the average gain bandwidth of the device is 65.2 GHz over the 21-nm tuning range. Previous work on fixed-wavelength 1.5-μm VCSOAs has shown that a gain bandwidth of 32 GHz is sufficient to amplify a 10 Gb/s input signal [8].

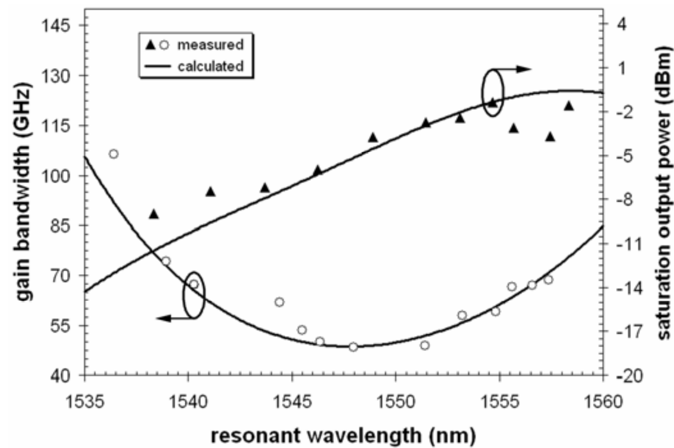

Fig. 6.6: Saturation output power and gain bandwidth as a function of resonant wavelength at 15 ºC for a pump power of 83 mW.

The best saturation output power measured for this devices is a maximum fiber-coupled saturation output power of -1.4 dBm at 1554.7 nm, with an unsaturated fiber-to-fiber gain of 9.2 dB (16.2 dB on-chip gain), as shown in Fig. 6.7. This value is comparable to the record high saturation output power of 0.5 dBm measured for a

fixed wavelength 1.5-μm device [9]. The excellent saturation properties recorded for the bottom-emitting MT-VCSOA is attributed to the low reflectivity of the transmissive mirror (with an average power reflectance of 0.92 over the tuning range) and the relatively large pump and signal spot sizes used in the test setup.

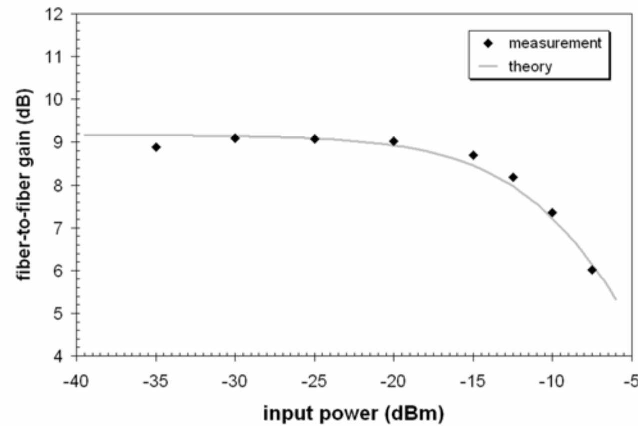

Fig. 6.7: Gain as a function of input signal power for a resonant wavelength of 1554.7 nm (tuning bias of 6.3 V, pump power of 83 mW at 15 ºC). In this plot the theoretical curve is based on Eq. 4.1. The measured input saturation power is -7.5 dBm and the saturation output power is -1.4 dBm.

In order to characterize the noise properties of the MT-VCSOA an all-optical noise measurement technique is employed [10]. This method has previously been shown to be comparable to more accurate electrical noise measurements for amplifiers operating below saturation [11] and is now commonly used to characterize the noise figure of VCSOAs [12]. It is important to stress that this method is only valid for unsaturated operation of the amplifier. The measurement procedure for the all-optical noise figure involves recording the ASE power at the signal wavelength and integrating this over the bandwidth of the optical spectrum

analyzer (for MT-VCSOA testing the resolution bandwidth of the OSA is always 0.1 nm). With the ASE spectral density determined, the noise factor F can then be calculated using:

$$F = \frac{2\rho_{ase}}{Gh\nu} + \frac{1}{G}. \qquad (6.1)$$

The first term in this expression represents signal-spontaneous beat noise and the second term represents shot noise. As defined previously, G is the amplifier gain, h is Planck's constant, ν is the frequency of the signal, and is ρ_{ase} is the ASE spectral density in the same polarization state as the signal (the noise figure is defined as NF = 10log(F), and is expressed in decibels, whereas the noise factor is given in linear units). As the optical spectrum analyzer measures the total optical power in both polarization states, the factor $2\rho_{ase}$ above is simply replaced by the measured value.

Optical measurements of the amplifier noise for the bottom-emitting MT-VCSOAs reveal a fiber-coupled noise figure of 7.5 dB for an average fiber-to-fiber gain of 9.0 dB. As seen in Fig. 6.8 the noise figure linearly decreases with increasing signal gain. Using Eq. 2.12 with a calculated excess noise coefficient (χ) of 1.16, the population inversion parameter (n_{sp}) for a pump power of 83 mW is approximately 2.7. The noise properties measured for the third generation MT-VCSOAs are comparable with the results of state-of-the-art fixed wavelength VCSOAs [10], [12]. In fact each of the results presented in the preceding section including the peak signal gain, gain bandwidth, and saturation output power are similar to, or exceed the performance of, 1.3–1.5 µm fixed-wavelength VCSOAs.

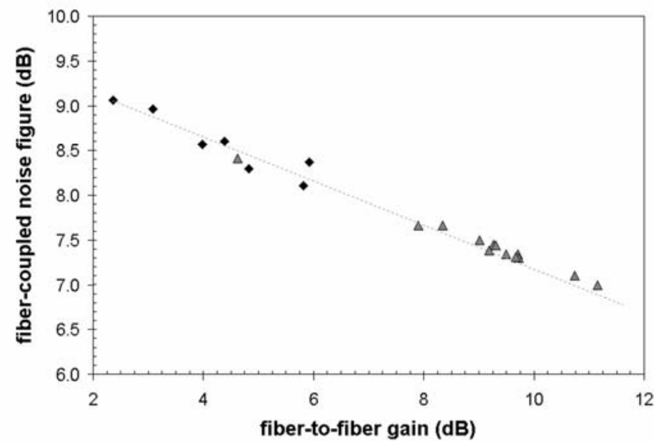

Fig. 6.8: Fiber-coupled noise figure as a function of resonant wavelength at 15º C for a pump power of 83 mW. The data set has been compiled from two third generation devices.

6.4 Variation in Amplifier Properties with Tuning

By fitting the measured response of the MT-VCSOA with the relevant theoretical models developed in Chapter 2, it is possible to extract the properties of the resonant cavity structure and gain medium over the wavelength span of the device. Important parameters to be determined include the variation in the effective reflectance of the tunable mirror structure and changes in the single-pass gain with tuning. In order to generate the fitting curves, a least-squares method is employed. By fitting the individual gain spectra with Eq. 2.1 (an example of which can be seen in in Fig. 6.5) the pertinent properties of the MT-VCSOA may be determined over the device tuning range, including the values of R_t, , R_b, and g_s. With the variation in these properties established, it is possible to compare the performance of the revised optical cavity design with results from previously fabricated structures.

6.4.1 Comparison with Initial Optical Cavity Design

The best peak gain performance measured for the first two generations of MT-VCSOAs was at least 3 dB fiber-to-fiber gain (10 dB on-chip gain) over 11 nm using a top-emitting configuration with a transmissive tunable DBR [1]. These devices required large variations in pump power in order to maintain a constant signal gain—as in Fig. 5.9—due to the significant variation in reflectance (>10%) of the MEMS-tunable DBR over the device tuning range [1], [2]. In contrast, the use of a high reflectivity tunable mirror structure, as in the bottom-emitting MT-VCSOAs, results in a significant increase in the width of the peak gain envelope, as shown in Fig. 6.9. It is interesting to note that the measured peak gain response of the bottom-emitting device is nearly identical to the theoretically predicted shape from Fig 5.16.

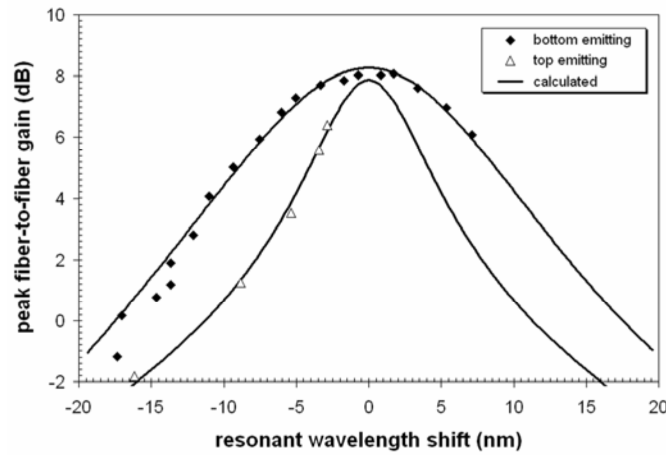

Fig. 6.9: Comparison of peak fiber-to-fiber gain at a constant pump power for two generations of MT-VCSOAs, including both top-emitting and bottom-emitting devices.

6.4.2 Effective Reflectance

For the bottom-emitting devices presented here, the tunable mirror reflectance varies from a maximum value of 0.993 to a minimum of 0.986, a difference of only 0.7% over the 21-nm tuning range. This is in contrast with the top-emitting devices of Generations 1 and 2, where typical reflectance variations were greater than 10% over a similar wavelength range. The consistent mirror properties displayed in Fig. 6.10 match the theoretically predicted variation presented in Section 5.3.1.

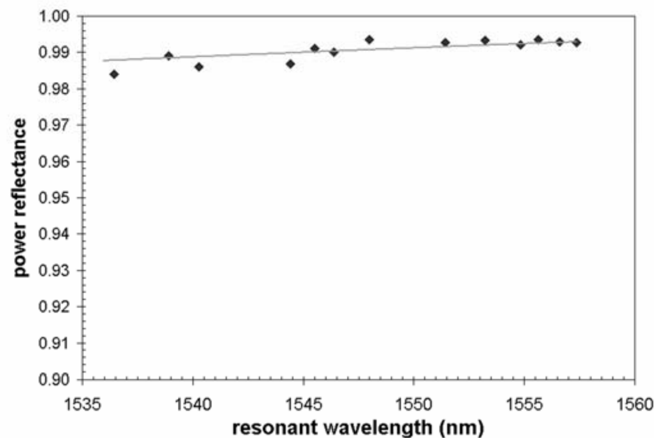

Fig. 6.10: Variation in reflectance of the high reflectivity back mirror used in the bottom-emitting devcies. In this design the total change in reflectance is less than 1% over the 21-nm tuning range.

6.4.3 Material Gain Spectrum

In addition to determining the properties of the resonant cavity, it is also possible to use fitting of the gain spectra to back out the single-pass gain of the MT-VCSOA over the tuning range. The variation single-pass gain for the device examined here is presented below in Fig. 6.11. For a pump power of 83 mW, the average single-pass

gain is approximately 3.5% over the wavelength tuning range, with a peak per-pass gain of 4.6% at 1540.28 nm. By combining the extracted mirror reflectance and single-pass gain values it is possible to determine the proximity to lasing threshold by calculating: $R_tR_bg_s^2$; when this product equals unity threshold is reached. The results of this calculation are also included in Fig. 6.11. At a pump power of 83 mW and a stage temperature of 15 ºC, the device is operating at an average of 97.8% of the single-pass gain required to reach threshold, and is closest to achieving lasing operation ($R_tR_bg_s^2$ = 98.3%) at a resonant wavelength of 1551.41 nm.

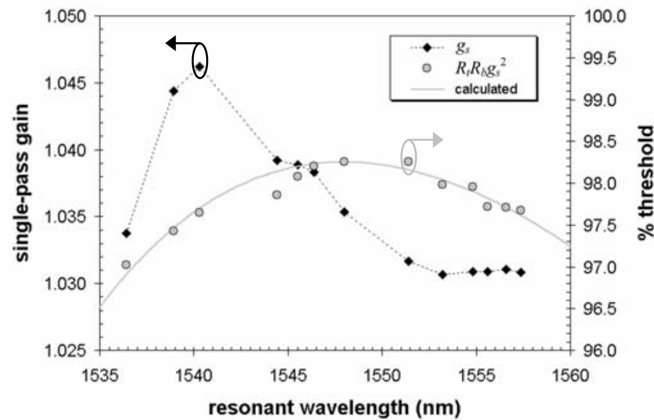

Fig. 6.11: Percent threshold and single-pass gain as a function of the cavity resonance wavelength.

Using the extracted values of single-pass gain and Eq. 2.6, it is possible to calculate the gain spectrum of the active medium. In order to solve for the material gain spectrum, a number of parameters are required including the variation in the enhancement factor with tuning ζ (as presented in Fig. 5.11), the active material

length L_a (combined thickness of the quantum wells), the average cavity loss α_i, and the total cavity length L_c (denominator of Eq. 2.17). The calculated material gain spectrum for the 28-QW AlInGaAs/InP active region used in the Generation 3 devices is presented below in Fig. 6.12 for a constant pump power of 83 mW (approximate carrier density of 3.9×10^{18} cm^{-3}). At this carrier density the active region exhibits a peak material gain value of 1664 cm^{-1} at 1540.3 nm.

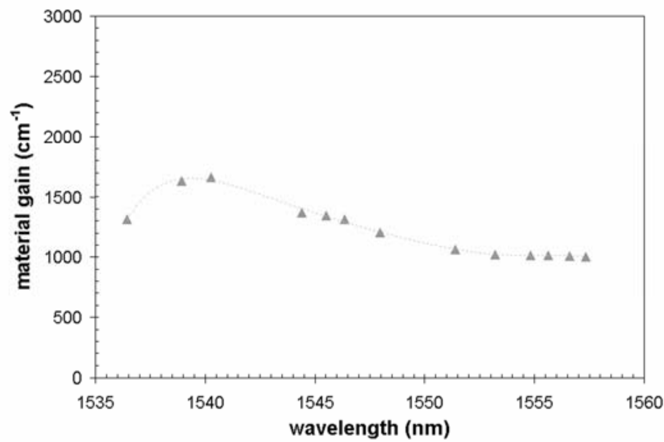

Fig. 6.12: Extracted material gain spectrum for a carrier density of 3.9×10^{18} cm^{-3} (pump power of 83 mW). The polynomial trend line is simply a guide for the eye.

Going one step further the characteristic material gain g_o can be determined with the three-parameter logarithmic gain model (Eq. 2.8). Calculated characteristic gain values for this active region have been found to be comparable with values determined by the Hakki-Paoli method for optically-pumped in-plane FP-lasers using the same basic MQW structure.

6.5 Summary

This chapter presents the design, fabrication, and characterization of bottom-emitting MT-VCSOAs with inherently superior properties when compared with top-emitting devices utilizing a transmissive tunable mirror. The bottom-emitting MT-VCSOAs incorporate a high reflectivity tunable DBR in order to suppress the variation in mirror reflectance found in the previous generations of devices. This configuration exhibits a minimum of 5 dB of fiber-to-fiber gain (12 dB on-chip gain) over 21 nm of tuning, with a constant pump power of 83 mW. Furthermore, the devices are capable of a peak fiber-to-fiber gain of 11.2 dB (18.2 dB on-chip gain), a maximum saturation output power of -1.4 dBm, and an average gain bandwidth and noise figure of 65.2 GHz and 7.5 dB over the attainable wavelength span. These properties are comparable with the current state of the art in fixed-wavelength VCSOAs, demonstrating that the addition of the high reflectivity MEMS-tuning element does not lead to degradation of the amplifier performance.

Using the analytical expressions presented in Chapter 2, accurate predictions of the performance of MT-VCSOAs can be made. Furthermore, through fitting of the amplifier gain spectra it is possible to determine the variation in properties of the resonant cavity structure and gain medium with tuning. In large part these calculations are made possible as the operation of these devices relies on the amplification of an external signal—thus, determination of the relevant properties of the MT-VCSOA can be directly determined through gain spectra measurements. With the added flexibility of wavelength tuning, it is now possible to extract these

properties over a wide wavelength range, in contrast with the rather limited single point measurements possible with fixed-wavelength devices.

References

[1] Q. Chen, G. D. Cole, E. S. Björlin, T. Kimura, S. Wu, C. S. Wang, N. C. MacDonald, J. E. Bowers, "First demonstration of a MEMS-tunable vertical-cavity SOA," *IEEE Photon. Technol. Lett.*, vol. 16, pp. 1438–1440, Jun. 2004.

[2] G. D. Cole, E. S. Björlin, Q. Chen, C.-Y. Chan, S. Wu, C. S. Wang, N. C. MacDonald, J. E. Bowers, "MEMS-tunable vertical-cavity SOAs," *IEEE J. Quantum Electron.*, vol. 41, pp. 390–407, Mar. 2005.

[3] E. S. Björlin, "Long-wavelength vertical-cavity semiconductor optical amplifiers," Ph.D. dissertation, University of California, Santa Barbara, Santa Barbara, CA, 2002.

[4] M. Guden, J. Piprek, "Materials parameters of quaternary III-V semiconductors for multilayer mirrors at 1.55-µm wavelength," *Modelling Simul. Mater. Sci. Eng.*, vol. 4, pp. 349–357, Jul. 1996.

[5] M. H. MacDougal, H. Zhao, P. D. Dapkus, M. Ziari, W. H. Steier, "Wide-bandwidth distributed Bragg reflectors using oxide/GaAs multilayers," *Electron. Lett.*, vol. 30, pp. 1147–1149, Jul. 1994.

[6] M. H. MacDougal "The development and analysis of vertical-cavity surface emitting laser employing oxide/semiconductor reflectors," Ph.D. dissertation, University of Southern California, Los Angeles, CA, 1997.

[7] S. Calvez, A. H. Clark, J.-M. Hopkins, R. Macaluso, P. Merlin, H. D. Sun, M. D. Dawson, T. Jouhti, M. Pessa, "1.3 µm GaInNAs optically-pumped vertical cavity semiconductor optical amplifier," *Electron. Lett.*, vol. 39, pp. 100–102, Jan. 2003.

[8] T. Kimura, E. S. Björlin, H.-F. Chou, Q. Chen, S. Wu, J. E. Bowers, "Optically preamplified receiver at 10, 20, and 40 Gb/s using a 1550-nm vertical-cavity SOA," *IEEE Photon. Technol. Lett.*, vol. 17, pp. 456–458, Feb. 2005.

[9] E. S. Björlin, T. Kimura, Q. Chen, C. Wang, J. E. Bowers, "High output power 1540nm vertical cavity semiconductor optical amplifiers," *Electron. Lett.*, vol. 40, pp. 121–123, Jan. 2004.

[10] D. M. Baney, P. Gallion, R. S. Tucker, "Theory and measurement techniques for the noise figure of optical amplifiers," *Opt. Fiber Technol.*, vol. 6, pp. 122–154, Apr. 2000.

[11] E. S. Björlin, J.E. Bowers, "Noise figure of vertical-cavity semiconductor optical amplifiers," *IEEE J. Quantum Electron.*, vol. 38, pp. 61–66, Jan. 2002.

[12] N. Laurand, S. Calvez, M. D. Dawson, A. C. Bryce, T. Jouhti, J. Konttinen, M. Pessa, "Performance comparison of GaInNAs vertical-cavity semiconductor optical amplifiers," *IEEE J. Quantum Electron.*, vol. 41, pp. 642–649, May 2005.

CHAPTER 7

Summary and Future Directions

The research presented in this dissertation was focused not only on demonstrating the first widely tunable VCSOA, but also on understanding the interplay between the wavelength tuning mechanism and the performance of the amplifier. The major achievements of this work include: 1) the first demonstration of a MEMS-tunable VCSOA; 2) the development of a second generation of devices with >50 nm total ASE wavelength tuning ranges and sub-10-μs response times; 3) an in-depth theoretical investigation of the relevant properties of various tunable VCSOA configurations; and 4) the demonstration of a third generation of devices, exhibiting state-of-the-art vertical-cavity amplifier performance with the added flexibility of wide wavelength tuning.

7.1 Summary

Similar to previously demonstrated fixed-wavelength VCSOAs, the initial tunable vertical-cavity amplifiers were optically pumped, gain-guided structures, operating in reflection mode and fabricated utilizing GaAs to InP wafer bonding. The major difference in the tunable device structure, when compared with fixed-

wavelength VCSOAs, is the incorporation of a variable thickness air gap within the optical cavity—formed using an AlGaAs-based micromachining process. The best peak gain performance measured for the first generation of MT-VCSOAs was a minimum of 10 dB on-chip gain (3 dB fiber-to-fiber) over 11 nm of tuning, with a peak on-chip gain of 17 dB at 1570 nm [1]-[3]. At high gain, typical gain-bandwidth values were roughly 30 GHz (~0.2 nm) [4] and the best recorded saturation output power was -7.8 dBm. Limitations of these devices included high tuning voltage requirements (on the order of 60 V), as well as poor stability. Looking beyond the initial shortcomings, these devices represent the first ever widely tunable VCSOAs, as well as the first MEMS-tunable vertical-cavity devices developed at UCSB.

Building upon the initial demonstration devices, a second generation of MT-VCSOAs was developed, utilizing a revised mechanical structure [5]. With the updated actuator structure the total ASE tuning range was extended beyond 50 nm, while the maximum tuning voltages were reduced to below 30 V. These devices also exhibited excellent dynamic properties, with a nearly critically damped frequency response and switching speeds below 10 μs [6]. Save for the mechanical updates, these devices utilized an identical optical design and materials structure as the first generation devices, and thus exhibited similar optical properties—including a limited effective tuning range.

In order to investigate potential improvements to the amplifier properties, a thorough investigation of alternative optical cavity structures was undertaken [4]. This included a theoretical investigation of the wavelength tuning response, peak signal gain, saturation properties, and noise figure of various optical cavity designs

and modes of operation. A general FP model was developed and used to analyze both the tuning and signal gain properties, while the saturation and noise characteristics were simulated using a rate equation approach. Due to their similarity with tunable VCSOAs, the results of these simulations are directly applicable to other MEMS-tunable vertical-cavity devices.

Utilizing the results of the theoretical investigations, a third generation of MT-VCSOAs was developed [7]. These devices employ a bottom-emitting configuration in which the MEMS-tuning element serves as the high reflectivity back mirror. By suppressing the variation in mirror reflectance with tuning [8], the bottom emitting devices exhibit a two-fold increase in the effective tuning range—with a minimum of 5 dB fiber-to-fiber gain (12 dB on-chip gain) over a wavelength span of 21 nm, given an applied bias of only 10.5 V to the electrostatic actuator. In addition to wide wavelength tuning, these devices exhibit state-of-the-art VCSOA performance, including a maximum fiber-coupled saturation output power of -1.4 dBm, and an average gain bandwidth and noise figure of 65.2 GHz and 7.5 dB respectively.

7.2 Future Directions

Continued research on VCSOAs should focus on the development of devices with increased versatility as well as enhanced efficiency. Potential goals include the demonstration of alternative device configurations, the design and analysis of electrically pumped devices, and the development of novel materials and fabrication approaches for MT-VCSOAs and tunable vertical-cavity devices in general.

7.2.1 Alternative Optical Cavity Designs

Thus far, all research on VCSOAs at UCSB, including this work, has focused on the development of reflection mode amplifiers. In order to increase the versatility of these devices, as well as verify theoretical predictions, transmission mode devices should be developed. For tunable VCSOAs, this may require the development of fabrication procedures that allow for the formation of an extended cavity tuning structure (EC-design), as seen in Fig. 7.1. Both transmission and reflection mode EC-design MT-VCSOAs will also serve to further validate the theoretical models presented in this dissertation.

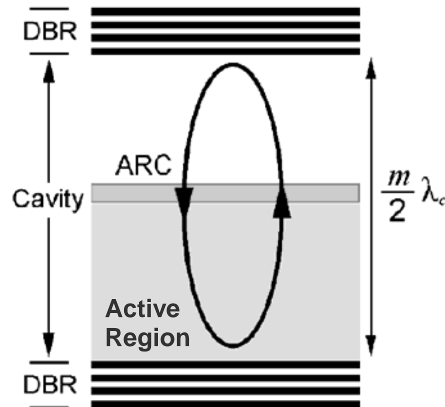

Fig. 7.1: Schematic of an EC-design MT-VCSOA. The incorporation of an antireflection coating (ARC) creates a distributed cavity of a total length $m\lambda_c/2$. The circulating arrow indicates the distributed nature of the electric field in this structure.

7.2.2 Electrically Pumped VCSOAs

To increase the versatility as well as the manufacturability of long-wavelength VCSOAs, electrically pumped devices must be developed. From the literature, the

majority of electrically pumped VCSOAs have been demonstrated at short wavelengths (850-980 nm), including the first documented vertical-cavity amplifier [9], [10]. Only a few examples of VCSOAs operating in the low loss transmission window for fiber optic communications (from roughly 1.3 μm–1.6 μm) have been demonstrated. Typically these devices are not optimized to operate amplifiers, but are simply VCSELs operated below threshold, as in [11]. The most pressing issue in electrically pumped VCSOAs is realizing satisfactory amplifier characteristics, requiring rather low mirror reflectivities [12]-[14], while still maintaining sufficient signal gain. As in the optically pumped devices, this most likely necessitates the use of a rather large number of quantum wells, with the best results found for devices with stacked MQW active regions containing 21–28 total wells. In order to generate a uniform distribution of carriers via electrical injection, novel active region designs must be investigated. One possibility is the use of a cascaded MQW design incorporating stacked multiple-active regions in series with tunnel junctions [15].

7.2.3 Novel Actuator Designs and Processing Procedures

An ideal doubly-clamped MEMS actuator exhibits a slight tensile strain to ensure that the suspended structure remains flat following release. In order to avoid the need for the SiN_x stressor film used in the MT-VCSOAs, high quality tensile strained films must be developed. An interesting way to realize a tensile-strained structure would be to integrate a strained epitaxial film into the growth sequence of the MEMS actuator structure. Possible materials choices for a tensile-strained GaAs-

based actuator include InGaP and GaAsP, dilute nitrides such as GaAsN, highly C-doped GaAs, or the use of a GaAs membrane on a highly In-doped GaAs substrate.

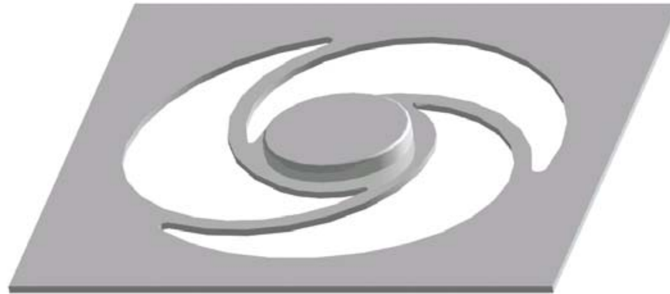

Fig. 7.2: Schematic of an alternative actuator geometry. Here, the suspensions intersect the central portion of the membrane tangentially, allowing in-plane strains to be converted to a rotation of the DBR pillar, alleviating undesired out of plane deformation, reducing the cubic nonlinearity of the structure, and reducing stresses that may be imparted on the central portion of the membrane.

Further possibilities to improve the current actuator design include the use of alternative membrane geometries, such as an actuator structure where the suspensions intersect the central portion of the membrane tangentially. An example of this configuration can be seen in Fig. 7.2. This geometry allows for a number of advantages: improved fill factor, arising from a reduction in the lateral expanse of the actuator; the alleviation of out-of-plane deformation due to a compressively stressed membrane (compressive strains in this geometry produce a simple in-plane rotation); a significant reduction in the coefficient of nonlinearity, again as the structure is capable of rotation to alleviate in-plane strain, and finally a reduction in potential inhomogeneous strain effects in the DBR pillar, by reducing the impressed stress on the central portion of the membrane upon actuation.

The current fabrication procedure for the MT-VCSOA requires a rather complex process flow, involving up to 11 photolithography steps. Future work should focus on the simplification of this procedure. One way to do this is to use pre-patterned bonding for the formation of the air cavity. Here, the air gap may be defined prior to wafer bonding in either the InP active material wafer, or GaAs top mirror wafer using RIE or wet chemical etching. Following wafer bonding the actuator geometry can be defined using an RIE process. In this way the membrane may be released using a dry etch, removing the need for a wet chemical undercut etch and avoiding the use of CO_2 critical point drying. Furthermore, definition of the air gap before bonding allows for access to the optical cavity, allowing for the addition of an ARC, or for the deposition of intracavity metal contacts (with low temperature bonding). The incorporation of an ARC within the MT-VCSOA optical cavity is especially useful for transmission mode devices, where the EC-design may be necessary for optimal performance (see Section 5.5 and Fig. 7.1 above). Direct wafer bonding on pre-patterned, or pre-processed wafers has been successfully demonstrated at UCSB, recent examples include both VCSOAs and VCSELs [12], [16].

7.2.4 Monolithic Integration

Long-wavelength VCSOAs are attractive for use as preamplifiers in high bit rate optical networks [17], [18]. Due to the surface normal operation of these devices, VCSOAs allow for vertical integration with various optoelectronic components. An interesting example of a vertically-integrated device would be a transmission mode

VCSOA stacked on top of a PIN structure—forming an integrated preamplifier-receiver [19]. In this case, optical preamplification using a VCSOA is an attractive means of increasing the sensitivity of the detector, especially at high bit-rates. A further extension of this structure would include a tunable VCSOA with the detector, as shown in Fig. 7.2 above. This structure combines an MT-VCSOA with a PIN detector to create a compact tunable receiver module, as shown schematically in Fig. 7.3. Although much work is needed to demonstrate this device, the development of tunable VCSOAs outlined in this dissertation brings us one step closer.

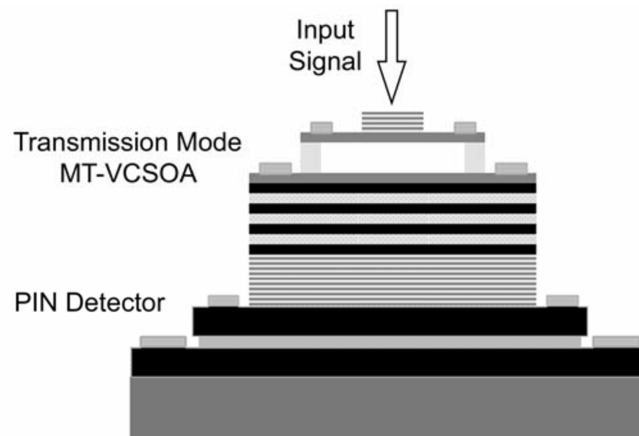

Fig. 7.3: Schematic of an integrated tunable receiver module. In this device a transmission mode tunable VCSOA is vertically integrated with a PIN detector in order to create a channel selective high speed receiver. The development of the tunable VCSOA as presented in this dissertation adds one more piece to the puzzle.

References

[1] Q. Chen, G. D. Cole, E. S. Björlin, T. Kimura, S. Wu, C. S. Wang, N. C. MacDonald, J. E. Bowers, "First demonstration of a MEMS tunable vertical-cavity SOA", *IEEE Photon. Technol. Lett.*, vol. 16, pp. 1438–1440, Jun. 2004.

[2] G. D. Cole, Q. Chen, E. S. Björlin, T. Kimura, S. Wu, C. S. Wang, J. E. Bowers, N. C. MacDonald, "Microelectromechanical tunable long-wavelength vertical-cavity semiconductor optical amplifiers," in *Proc. 16th Int. Conf. InP and Related Materials*, Kagoshima, Japan, Paper FA2-4, 31 May–4 Jun. 2004, pp. 708–711.

[3] T. Kimura, S. Bjorlin, G.D. Cole, H.F. Chou, J. Bowers, "1550-nm vertical-cavity SOAs for optically preamplified high bit rate receivers," *in Proc. 30th European Conf. on Optical Communications*, Stockholm, Sweden, 5–9 Sep. 2004, Paper We4.P.070.

[4] G. D. Cole, Q. Chen, E. S. Björlin, T. Kimura, S. Wu, C. S. Wang, J. E. Bowers, N. C. MacDonald, "Wavelength selection in MEMS tunable vertical-cavity SOAs," in *Tech. Dig. 15th Optical Amplifiers and Their Applications OSA Topical Meeting and Exhibit*, San Francisco, CA, Paper OMB3, 27 Jun.–2 Jul. 2004.

[5] G. D. Cole, E. S. Björlin, Q. Chen, C.-Y. Chan, S. Wu, C. S. Wang, N. C. MacDonald, J. E. Bowers, "MEMS-tunable vertical cavity SOAs," *IEEE J. Quantum Electron.*, vol. 41, pp. 390–407, Mar. 2005.

[6] G. D. Cole, J. E. Bowers, K. L. Turner, N. C. MacDonald, "Dynamic characterization of MEMS-tunable vertical-cavity SOAs," in *Conf. Dig. IEEE/LEOS Int. Conf. on Optical MEMS and Their Applications*, Oulu, Finland, Paper F4, pp. 99–100, 1–4 Aug. 2005.

[7] G. D. Cole, E. S. Bjorlin, C. S. Wang, N.C. MacDonald, J.E. Bowers, "Widely tunable bottom-emitting vertical-cavity SOAs," to be published in *IEEE Photon. Technol. Lett.*, vol. 17, Dec. 2005.

[8] G. D. Cole, E. S. Björlin, Q. Chen, C.-Y. Chan, S. Wu, C. S. Wang, N. C. MacDonald, J. E. Bowers, "Design and analysis of MEMS tunable vertical-cavity semiconductor optical amplifiers," in *Proc. 17th Int. Conf. InP and Related Materials*, Glasgow, Scotland, UK, Paper TuB-1-4, 8–12 May 2005.

[9] F. Koyama, S. Kubota, K. Iga, "GaAlAs/GaAs active filter based on vertical cavity surface emitting laser," *Electron. Lett.*, vol. 27, pp.1093–1095, Jun. 1991.

[10] D. Wiedenmann, C. Jung, M. Grabherr, R. Jäger, U. Martin, R. Michalzik, K. J. Ebeling, "Oxide-confined vertical-cavity semiconductor optical amplifier for 980 nm wavelength," in *CLEO 98 Tech. Dig.*, 1998, Paper CThM5, pp. 378.

[11] R. Lewén, K. Streubel, A. Karlsson, S. Rapp, "Experimental demonstration of a multifunctional long-wavelength vertical-cavity laser amplifier-detector," *IEEE Photon. Technol. Lett.*, vol. 10, pp. 1067–1069, Aug. 1998.

[12] E. S. Björlin, T. Kimura, J. E. Bowers, "Carrier-confined vertical-cavity semiconductor optical amplifiers for higher gain and efficiency," *IEEE J. Select. Topics Quantum Electron.*, vol. 9, pp. 1374–1385, Sep./Oct. 2003.

[13] J. Piprek, E. S. Björlin, J. E. Bowers, "Design and analysis of vertical-cavity semiconductor optical amplifiers," *IEEE J. Quantum Electron.*, vol. 37, pp. 127–134, Jan. 2001.

[14] C. Tombling, T. Saitoh, T. Mukai, "Performance predictions for vertical-cavity semiconductor laser amplifiers," *IEEE J. Quantum Electron.*, vol. 30, pp. 2491–2499, Nov. 1994.

[15] J. K. Kim, S. Nakagawa, E. Hall, L. A. Coldren, "Near-room-temperature continuous-wave operation of multiple-active-region 1.55 μm vertical-cavity lasers with high differential efficiency", *Appl. Phys. Lett.*, vol. 77, pp. 3137–3139, Nov. 2000.

[16] V. Jayaraman, M. Mehta, A. W. Jackson, Y. Okuno, J. Piprek, J. E. Bowers, "High-power 1320-nm wafer-bonded VCSELs with tunnel junctions," *IEEE Photon. Tech. Lett.*, vol. 15, pp. 1495–1497, Nov. 2003.

[17] E. S. Björlin, J. Geske, J. E. Bowers, "Optically preamplified receiver at 10 Gb/s using a vertical cavity SOA," *Electron. Lett.*, vol. 37, pp. 1474–1475, Nov. 2001.

[18] T. Kimura, E. S. Björlin, H.-F. Chou, Q. Chen, S. Wu, J. E. Bowers, "Optically preamplified receiver at 10, 20, and 40 Gb/s using a 1550-nm vertical-cavity SOA," *IEEE Photon. Technol. Lett.*, vol. 17, pp. 456–458, Feb. 2005.

[19] E. S. Björlin, "Long-wavelength vertical-cavity semiconductor optical amplifiers," Ph.D. dissertation, University of California, Santa Barbara, Santa Barbara, CA, 2002.

APPENDIX A

Mask Layout and Device Geometry

A.1 Generation 1 MT-VCSOAs

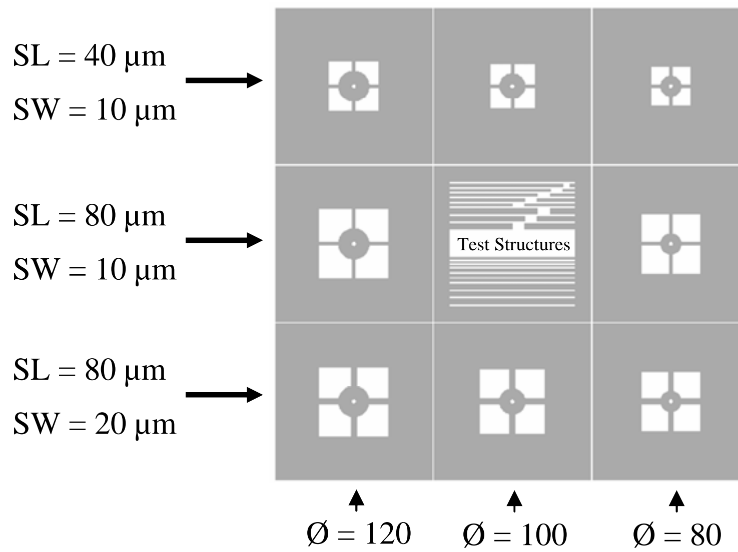

A.2 Generations 2 & 3 MT-VCSOAs

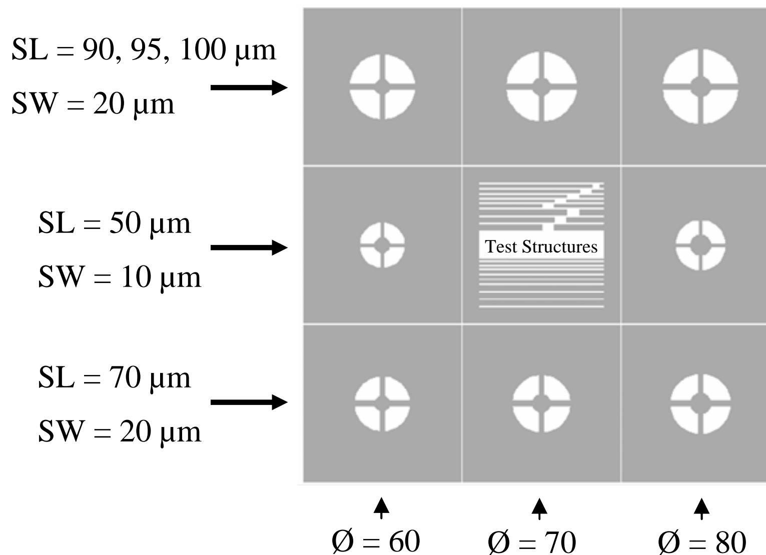

Legend: SL – spring length; SW – spring width; Ø – plate diameter; each unit cell shown above is arrayed over the surface of the sample.

APPENDIX B

Material Structures

B.1 Generations 1 & 2 Detailed Materials Structure

Gens. 1 & 2: Top DBR

Material	Thickness (nm)	
GaAs	115.53	n-doped 2×10^{19}
$Al_{0.98}Ga_{0.02}As$	1750.00	U.I.D
$Al_{0.98}Ga_{0.02}As$	200.00	p-doped 2×10^{19}
GaAs	346.58	n-doped 2×10^{19}
$Al_{0.98}Ga_{0.02}As$	134.38	UNDOPED
GaAs	115.53	Repeat x 5
$Al_{0.9}Ga_{0.1}As$	200.00	Stop etch
GaAs	undoped substrate	

abrupt interfaces
1 full wafer
target center wavelength = 1560 nm

Gens. 1 & 2: Bottom DBR

Material	Thickness (nm)	
GaAs	115.07	UNDOPED
$Al_{0.98}Ga_{0.02}As$	134.01	Repeat 30
GaAs	undoped substrate	

abrupt interfaces
1 full wafer
target center wavelength = 1560 nm

Gens. 1 & 2: Active Region Design

5 x 5 MQW stack - InP substrate

Layer #	Doping	Material	Thick (nm)	Composition	Strain	Comment
1	uid	InP	----------	InP	none	Growth Buffer Layer
2	uid	InGaAs	150	InGaAs	Lattice Matched	Etch Stop Layer
3	uid	InP	7.5	InP	Lattice Matched	Superlattice
4	uid	InGaAsP	7.5	Band Gap: 1.3 micron Q		Superlattice
5	uid	InP	7.5	InP	Lattice Matched	Superlattice
6	uid	InGaAsP	7.5	Band Gap: 1.3 micron Q		Superlattice
7	uid	InP	7.5	InP	Lattice Matched	Superlattice
8	uid	InGaAsP	7.5	Band Gap: 1.3 micron Q		Superlattice
9	uid	InP	53	InP	Lattice Matched	Cladding
10	uid	AlInGaAs	9	Band Gap: 1.3 eV	Tensile (-0.5-0.6%)	Barrier
11	uid	AlInGaAs	5.5	QW PL target: 1540nm	Compressive (+0.85%)	Quantum Well
12	uid	AlInGaAs	9	Band Gap: 1.3 eV	Tensile (-0.5-0.6%)	Barrier
13	uid	AlInGaAs	5.5	QW PL target: 1540nm	Compressive (+0.85%)	Quantum Well
14	uid	AlInGaAs	9	Band Gap: 1.3 eV	Tensile (-0.5-0.6%)	Barrier
15	uid	AlInGaAs	5.5	QW PL target: 1540nm	Compressive (+0.85%)	Quantum Well
16	uid	AlInGaAs	9	Band Gap: 1.3 eV	Tensile (-0.5-0.6%)	Barrier
17	uid	AlInGaAs	5.5	QW PL target: 1540nm	Compressive (+0.85%)	Quantum Well
18	uid	AlInGaAs	9	Band Gap: 1.3 eV	Tensile (-0.5-0.6%)	Barrier
19	uid	AlInGaAs	5.5	QW PL target: 1540nm	Compressive (+0.85%)	Quantum Well
20	uid	AlInGaAs	9	Band Gap: 1.3 eV	Tensile (-0.5-0.6%)	Barrier
21	uid	InP	152	InP	Lattice Matched	Cladding
22	uid	AlInGaAs	9	Band Gap: 1.3 eV	Tensile (-0.5-0.6%)	Barrier
23	uid	AlInGaAs	5.5	QW PL target: 1540nm	Compressive (+0.85%)	Quantum Well
24	uid	AlInGaAs	9	Band Gap: 1.3 eV	Tensile (-0.5-0.6%)	Barrier
25	uid	AlInGaAs	5.5	QW PL target: 1540nm	Compressive (+0.85%)	Quantum Well
26	uid	AlInGaAs	9	Band Gap: 1.3 eV	Tensile (-0.5-0.6%)	Barrier
27	uid	AlInGaAs	5.5	QW PL target: 1540nm	Compressive (+0.85%)	Quantum Well
28	uid	AlInGaAs	9	Band Gap: 1.3 eV	Tensile (-0.5-0.6%)	Barrier
29	uid	AlInGaAs	5.5	QW PL target: 1540nm	Compressive (+0.85%)	Quantum Well
30	uid	AlInGaAs	9	Band Gap: 1.3 eV	Tensile (-0.5-0.6%)	Barrier
31	uid	AlInGaAs	5.5	QW PL target: 1540nm	Compressive (+0.85%)	Quantum Well
32	uid	AlInGaAs	9	Band Gap: 1.3 eV	Tensile (-0.5-0.6%)	Barrier
33	uid	InP	152	InP	Lattice Matched	Cladding
34	uid	AlInGaAs	9	Band Gap: 1.3 eV	Tensile (-0.5-0.6%)	Barrier
35	uid	AlInGaAs	5.5	QW PL target: 1540nm	Compressive (+0.85%)	Quantum Well
36	uid	AlInGaAs	9	Band Gap: 1.3 eV	Tensile (-0.5-0.6%)	Barrier
37	uid	AlInGaAs	5.5	QW PL target: 1540nm	Compressive (+0.85%)	Quantum Well
38	uid	AlInGaAs	9	Band Gap: 1.3 eV	Tensile (-0.5-0.6%)	Barrier
39	uid	AlInGaAs	5.5	QW PL target: 1540nm	Compressive (+0.85%)	Quantum Well
40	uid	AlInGaAs	9	Band Gap: 1.3 eV	Tensile (-0.5-0.6%)	Barrier
41	uid	AlInGaAs	5.5	QW PL target: 1540nm	Compressive (+0.85%)	Quantum Well
42	uid	AlInGaAs	9	Band Gap: 1.3 eV	Tensile (-0.5-0.6%)	Barrier
43	uid	AlInGaAs	5.5	QW PL target: 1540nm	Compressive (+0.85%)	Quantum Well
44	uid	AlInGaAs	9	Band Gap: 1.3 eV	Tensile (-0.5-0.6%)	Barrier
45	uid	InP	152	InP	Lattice Matched	Cladding
46	uid	AlInGaAs	9	Band Gap: 1.3 eV	Tensile (-0.5-0.6%)	Barrier
47	uid	AlInGaAs	5.5	QW PL target: 1540nm	Compressive (+0.85%)	Quantum Well
48	uid	AlInGaAs	9	Band Gap: 1.3 eV	Tensile (-0.5-0.6%)	Barrier
49	uid	AlInGaAs	5.5	QW PL target: 1540nm	Compressive (+0.85%)	Quantum Well
50	uid	AlInGaAs	9	Band Gap: 1.3 eV	Tensile (-0.5-0.6%)	Barrier
51	uid	AlInGaAs	5.5	QW PL target: 1540nm	Compressive (+0.85%)	Quantum Well
52	uid	AlInGaAs	9	Band Gap: 1.3 eV	Tensile (-0.5-0.6%)	Barrier
53	uid	AlInGaAs	5.5	QW PL target: 1540nm	Compressive (+0.85%)	Quantum Well
54	uid	AlInGaAs	9	Band Gap: 1.3 eV	Tensile (-0.5-0.6%)	Barrier
55	uid	AlInGaAs	5.5	QW PL target: 1540nm	Compressive (+0.85%)	Quantum Well
56	uid	AlInGaAs	9	Band Gap: 1.3 eV	Tensile (-0.5-0.6%)	Barrier
57	uid	InP	152	InP	Lattice Matched	Cladding
58	uid	AlInGaAs	9	Band Gap: 1.3 eV	Tensile (-0.5-0.6%)	Barrier
59	uid	AlInGaAs	5.5	QW PL target: 1540nm	Compressive (+0.85%)	Quantum Well
60	uid	AlInGaAs	9	Band Gap: 1.3 eV	Tensile (-0.5-0.6%)	Barrier
61	uid	AlInGaAs	5.5	QW PL target: 1540nm	Compressive (+0.85%)	Quantum Well
62	uid	AlInGaAs	9	Band Gap: 1.3 eV	Tensile (-0.5-0.6%)	Barrier
63	uid	AlInGaAs	5.5	QW PL target: 1540nm	Compressive (+0.85%)	Quantum Well
64	uid	AlInGaAs	9	Band Gap: 1.3 eV	Tensile (-0.5-0.6%)	Barrier
65	uid	AlInGaAs	5.5	QW PL target: 1540nm	Compressive (+0.85%)	Quantum Well
66	uid	AlInGaAs	9	Band Gap: 1.3 eV	Tensile (-0.5-0.6%)	Barrier
67	uid	AlInGaAs	5.5	QW PL target: 1540nm	Compressive (+0.85%)	Quantum Well
68	uid	AlInGaAs	9	Band Gap: 1.3 eV	Tensile (-0.5-0.6%)	Barrier
69	uid	InP	53	InP	Lattice Matched	Cladding
70	uid	InGaAsP	7.5	Band Gap: 1.3 micron Q		Superlattice
71	uid	InP	7.5	InP	Lattice Matched	Superlattice
72	uid	InGaAsP	7.5	Band Gap: 1.3 micron Q		Superlattice
73	uid	InP	7.5	InP	Lattice Matched	Superlattice
74	uid	InGaAsP	7.5	Band Gap: 1.3 micron Q		Superlattice
75	uid	InP	7.5	InP	Lattice Matched	Superlattice

B.2 Generation 3 Detailed Materials Structure

Generation 3: Top DBR

Material	Thickness (nm)	
GaAs – 1/4-λ layer	115.07	n-doped 2×10^{19}
$Al_{0.85}Ga_{0.15}As$ – non digital!	1750	U.I.D
$Al_{0.85}Ga_{0.15}As$ – non digital!	200.00	p-doped 2×10^{19}
GaAs	345.22	n-doped 2×10^{19}
$Al_{0.92}Ga_{0.08}As$	132.76	UNDOPED
GaAs	115.07	Repeat 15
$Al_{0.9}Ga_{0.1}As$	250.00	Stop etch
GaAs	undoped substrate	

abrupt interfaces
1 full wafer
target center wavelength = 1560 nm

Generation 3: Bottom DBR

Material	Thickness (nm)	
GaAs	115.07	UNDOPED
$Al_{0.98}Ga_{0.02}As$	134.01	Repeat 14
GaAs	undoped substrate	

abrupt interfaces
1 full wafer
target center wavelength = 1560 nm

Generation 3: Active Region Design

4 x 7 MQW stack - InP substrate

Layer #	Doping	Material	Thick (nm)	Composition	Strain	Comment
1	uid	InP	----------	InP	none	Growth Buffer Layer
2	uid	InGaAs	150	InGaAs	Lattice Matched	Etch Stop Layer
3	n-5E18	InP	250	InP	none	Contact Layer
4	uid	InGaAsP	7.5	Band Gap: 1.3 micron Q		Superlattice
5	uid	InP	7.5	InP	Lattice Matched	Superlattice
6	uid	InGaAsP	7.5	Band Gap: 1.3 micron Q		Superlattice
7	uid	InP	7.5	InP	Lattice Matched	Superlattice
8	uid	InGaAsP	7.5	Band Gap: 1.3 micron Q		Superlattice
9	uid	InP	20	InP	Lattice Matched	Cladding
10	uid	AlInGaAs	10	Band Gap: 1.3 microns	Tensile (-0.5-0.6%)	Barrier
11	uid	AlInGaAs	7	QW PL target: 1530nm	Compressive (+0.85%)	Quantum Well
12	uid	AlInGaAs	10	Band Gap: 1.3 microns	Tensile (-0.5-0.6%)	Barrier
13	uid	AlInGaAs	7	QW PL target: 1530nm	Compressive (+0.85%)	Quantum Well
14	uid	AlInGaAs	10	Band Gap: 1.3 microns	Tensile (-0.5-0.6%)	Barrier
15	uid	AlInGaAs	7	QW PL target: 1530nm	Compressive (+0.85%)	Quantum Well
16	uid	AlInGaAs	10	Band Gap: 1.3 microns	Tensile (-0.5-0.6%)	Barrier
17	uid	AlInGaAs	7	QW PL target: 1530nm	Compressive (+0.85%)	Quantum Well
18	uid	AlInGaAs	10	Band Gap: 1.3 microns	Tensile (-0.5-0.6%)	Barrier
19	uid	AlInGaAs	7	QW PL target: 1530nm	Compressive (+0.85%)	Quantum Well
20	uid	AlInGaAs	10	Band Gap: 1.3 microns	Tensile (-0.5-0.6%)	Barrier
21	uid	AlInGaAs	7	QW PL target: 1530nm	Compressive (+0.85%)	Quantum Well
22	uid	AlInGaAs	10	Band Gap: 1.3 microns	Tensile (-0.5-0.6%)	Barrier
23	uid	AlInGaAs	7	QW PL target: 1530nm	Compressive (+0.85%)	Quantum Well
24	uid	AlInGaAs	10	Band Gap: 1.3 microns	Tensile (-0.5-0.6%)	Barrier
25	uid	InP	90	InP	Lattice Matched	Cladding
26	uid	AlInGaAs	10	Band Gap: 1.3 microns	Tensile (-0.5-0.6%)	Barrier
27	uid	AlInGaAs	7	QW PL target: 1530nm	Compressive (+0.85%)	Quantum Well
28	uid	AlInGaAs	10	Band Gap: 1.3 microns	Tensile (-0.5-0.6%)	Barrier
29	uid	AlInGaAs	7	QW PL target: 1530nm	Compressive (+0.85%)	Quantum Well
30	uid	AlInGaAs	10	Band Gap: 1.3 microns	Tensile (-0.5-0.6%)	Barrier
31	uid	AlInGaAs	7	QW PL target: 1530nm	Compressive (+0.85%)	Quantum Well
32	uid	AlInGaAs	10	Band Gap: 1.3 microns	Tensile (-0.5-0.6%)	Barrier
33	uid	AlInGaAs	7	QW PL target: 1530nm	Compressive (+0.85%)	Quantum Well
34	uid	AlInGaAs	10	Band Gap: 1.3 microns	Tensile (-0.5-0.6%)	Barrier
35	uid	AlInGaAs	7	QW PL target: 1530nm	Compressive (+0.85%)	Quantum Well
36	uid	AlInGaAs	10	Band Gap: 1.3 microns	Tensile (-0.5-0.6%)	Barrier
37	uid	AlInGaAs	7	QW PL target: 1530nm	Compressive (+0.85%)	Quantum Well
38	uid	AlInGaAs	10	Band Gap: 1.3 microns	Tensile (-0.5-0.6%)	Barrier
39	uid	AlInGaAs	7	QW PL target: 1530nm	Compressive (+0.85%)	Quantum Well
40	uid	AlInGaAs	10	Band Gap: 1.3 microns	Tensile (-0.5-0.6%)	Barrier
41	uid	InP	90	InP	Lattice Matched	Cladding
42	uid	AlInGaAs	10	Band Gap: 1.3 microns	Tensile (-0.5-0.6%)	Barrier
43	uid	AlInGaAs	7	QW PL target: 1530nm	Compressive (+0.85%)	Quantum Well
44	uid	AlInGaAs	10	Band Gap: 1.3 microns	Tensile (-0.5-0.6%)	Barrier
45	uid	AlInGaAs	7	QW PL target: 1530nm	Compressive (+0.85%)	Quantum Well
46	uid	AlInGaAs	10	Band Gap: 1.3 microns	Tensile (-0.5-0.6%)	Barrier
47	uid	AlInGaAs	7	QW PL target: 1530nm	Compressive (+0.85%)	Quantum Well
48	uid	AlInGaAs	10	Band Gap: 1.3 microns	Tensile (-0.5-0.6%)	Barrier
49	uid	AlInGaAs	7	QW PL target: 1530nm	Compressive (+0.85%)	Quantum Well
50	uid	AlInGaAs	10	Band Gap: 1.3 microns	Tensile (-0.5-0.6%)	Barrier
51	uid	AlInGaAs	7	QW PL target: 1530nm	Compressive (+0.85%)	Quantum Well
52	uid	AlInGaAs	10	Band Gap: 1.3 microns	Tensile (-0.5-0.6%)	Barrier
53	uid	AlInGaAs	7	QW PL target: 1530nm	Compressive (+0.85%)	Quantum Well
54	uid	AlInGaAs	10	Band Gap: 1.3 microns	Tensile (-0.5-0.6%)	Barrier
55	uid	AlInGaAs	7	QW PL target: 1530nm	Compressive (+0.85%)	Quantum Well
56	uid	AlInGaAs	10	Band Gap: 1.3 microns	Tensile (-0.5-0.6%)	Barrier
57	uid	InP	90	InP	Lattice Matched	Cladding
58	uid	AlInGaAs	10	Band Gap: 1.3 microns	Tensile (-0.5-0.6%)	Barrier
59	uid	AlInGaAs	7	QW PL target: 1530nm	Compressive (+0.85%)	Quantum Well
60	uid	AlInGaAs	10	Band Gap: 1.3 microns	Tensile (-0.5-0.6%)	Barrier
61	uid	AlInGaAs	7	QW PL target: 1530nm	Compressive (+0.85%)	Quantum Well
62	uid	AlInGaAs	10	Band Gap: 1.3 microns	Tensile (-0.5-0.6%)	Barrier
63	uid	AlInGaAs	7	QW PL target: 1530nm	Compressive (+0.85%)	Quantum Well
64	uid	AlInGaAs	10	Band Gap: 1.3 microns	Tensile (-0.5-0.6%)	Barrier
65	uid	AlInGaAs	7	QW PL target: 1530nm	Compressive (+0.85%)	Quantum Well
66	uid	AlInGaAs	10	Band Gap: 1.3 microns	Tensile (-0.5-0.6%)	Barrier
67	uid	AlInGaAs	7	QW PL target: 1530nm	Compressive (+0.85%)	Quantum Well
68	uid	AlInGaAs	10	Band Gap: 1.3 microns	Tensile (-0.5-0.6%)	Barrier
69	uid	AlInGaAs	7	QW PL target: 1530nm	Compressive (+0.85%)	Quantum Well
70	uid	AlInGaAs	10	Band Gap: 1.3 microns	Tensile (-0.5-0.6%)	Barrier
71	uid	AlInGaAs	7	QW PL target: 1530nm	Compressive (+0.85%)	Quantum Well
72	uid	AlInGaAs	10	Band Gap: 1.3 microns	Tensile (-0.5-0.6%)	Barrier
73	uid	InP	266	InP	Lattice Matched	Cladding
74	uid	InGaAsP	7.5	Band Gap: 1.3 micron Q		Superlattice
75	uid	InP	7.5	InP	Lattice Matched	Superlattice
76	uid	InGaAsP	7.5	Band Gap: 1.3 micron Q		Superlattice
77	uid	InP	7.5	InP	Lattice Matched	Superlattice
78	uid	InGaAsP	7.5	Band Gap: 1.3 micron Q		Superlattice
79	uid	InP	7.5	InP	Lattice Matched	Superlattice

APPENDIX C

Wafer Bonding Procedure

Step 1: scribe and break + channel etch in GaAs Date: ______________

Sample Prep: cleave InP active region and AlGaAs DBR material into 8 mm x 8 mm squares

Clean: both samples - acetone (2) ______ min iso (2)_______ min

Superlattice Etch: remove 1 superlattice period from InP active

wet etch InP; H3PO4:HCl 3:1 (20) ___________ sec; rinse DI (60) ______ sec; dry with N2

wet etch InGaAsP; H_2SO_4:H_2O_2:DI 1:1:10 (20) ___________ sec; rinse DI (60) ______ sec; dry with N2

Clean: acetone (2) ______ min iso (2)_______ min dehyd. bake GaAs sample at (110) ______ C for >3 min

Photolithography #1: channel etch on GaAs sample (mask: *VJ quick oxidation*)

resist (AZ4110) ____________ spin at (4) ______ krpm for (30) ______sec

prebake at (95) _______ C for (60) _________ sec cool (1) _______ min

expose image at (7.5) _______ mW for (30) _________ sec

develop in (1:4 AZ400k) _____________ developer for (65) _____________sec

rinse DI (60) ______ sec; dry with N2

Wet Etch: define bonding channels in GaAs

H_3PO_4:H_2O_2:H_2O 2:1:60 (23-27) ___________ sec

rinse DI (60) ______ sec; dry with N2

Step 2: pre-bond clean #1 Date: ______________

Strip Resist: GaAs sample - acetone (2) ______ min iso (2)_______ min; dry with N2

Coarse Particulate Removal: acetone spray over solvent dish

submerge in acetone, scrub with cotton swab 20x per edge (4)

iso spray to remove acetone residue; dry with N2

Fine Particulate Removal: tergitol and foam swab

submerge sample in tergitol/DI, wipe bonding surface with foam swab

iso spray to remove tergitol/DI; dry with N2

Polymer Strip: remove organics from both samples

O_2 Plasma Descum for (30) ______ sec at (100) ________ W

BHF Dip: remove surface oxide from both samples; (10) _______ s dip

rinse DI (30) ______ sec; dry with N2

Step 3: first wafer bond in teaching cleanroom Date: ______________

Native Oxide Strip: submerge samples in NH_4OH (2) _______ min

Methanol Soak: transfer samples to methanol

remove samples from methanol; butt adjancent sample edges on a cleanroom wipe

flip InP sample up onto GaAs chip; press together and return to methanol

align with tweezers in methanol; place stack in graphite bonding fixture

insert bonding dome and tighten pressure plate to (0.37) _______ inch-pounds

make sure to keep sample submerged in methanol!

Wafer Bonding in LPE Furnace: standard procedure

place bonding fixture in furnace tube; cover tube with seal and tighten seal screws

turn off the N2 flow and close the exhaust valve

turn on the venturi pump and open the vacuum valve

allow the tube pressure to drop below 1 psi on the digital vacuum guage

close the vacuum valve, turn off the venturi pump and turn on the N2 flow

allow the tube pressure to reach atmosphere (15-16) ________ psi

open the exhaust valve and adjust the N2 flow until it reaches (2) ________ sccm (~14.96 psi)

Bonding Program: automatic recipe

85 C/min ramp to bonding temperature of (600) _______ C

bonding time of (30) _______ min with 10 C/min ramp down to 300 C; step down to room temp

Step 4: InP substrate removal Date: ______________

InP substrate wet etch: HCl:DI 3:1 for (1.5-2)_________ hrs
replace etchant every (30-60) _______ min
rinse DI (60) ______ sec; dry with N2
Stop Etch Removal: remove InGaAsP etch stop; 1:1:10 H2SO4:H2O2:DI (15-30) _______ s
Superlattice Etch: remove 1 superlattice period from InP active
wet etch InP; H3PO4:HCl 3:1 (45)* ___________ sec; rinse DI (60) ______ sec; dry with N2
*for active version 2 InP contact layer is 250 nm thick - etch for 45-60 sec (bubbles stop)
wet etch InGaAsP; H_2SO_4:H_2O_2:DI 1:1:10 (20) ___________ sec; rinse DI (60) ______ sec; dry with N2

Step 5: channel etch in InP Date: ______________

Clean: acetone (2) ______ min iso (2)_______ min dehyd. bake at (110) ______ C for >3 min
Photolithography #2: channel etch in InP (mask: *VJ quick oxidation*)
resist (AZ4110) ____________ spin at (4) ______ krpm for (30) ______sec
prebake at (95) _______ C for (60) _________ sec cool (1) _______ min
expose image at (7.5) _______ mW for (30) _________ sec
develop in (1:4 AZ400k) _____________ developer for (60) _____________sec
rinse DI (60) ______ sec; dry with N2
Wet Etch: define bonding channels in InP
H_3PO_4:HCl 3:1 (7-10) ___________ sec
rinse DI (60) ______ sec; dry with N2

Step 6: pre-bond clean #2 Date: ______________

Strip Resist: acetone (2) ______ min iso (2)_______ min; dry with N2
Coarse Particulate Removal: acetone spray over solvent dish
submerge in acetone, scrub with cotton swab 20x per edge (4)
iso spray to remove acetone residue; dry with N2
Fine Particulate Removal: tergitol and foam swab
submerge sample in tergitol/DI, wipe bonding surface with foam swab
iso spray to remove tergitol/DI; dry with N2
Polymer Strip: remove organics from both samples
O_2 Plasma Descum for (30) ______ sec at (100) ________ W
BHF Dip: remove surface oxide from both samples; (10) _______ s dip
rinse DI (30) ______ sec; dry with N2

Step 7: second wafer bond in teaching cleanroom Date: ______________

Native Oxide Strip: submerge samples in NH_4OH (2) _______ min
Methanol Soak: transfer samples to methanol
remove samples from methanol; butt sample edges samples adjancent on a cleanroom wipe
flip MEMS GaAs sample up onto bonded GaAs/InP chip; press together and return to methanol
align with tweezers in methanol; place stack in graphite bonding fixture
insert bonding block and tighten pressure plate to (0.37) _______ inch-pounds
make sure to keep sample submerged in methanol!
Wafer Bonding in LPE Furnace: standard procedure
place bonding fixture in furnace tube; cover tube with seal and tighten seal screws
turn off the N2 flow and close the exhaust valve
turn on the venturi pump and open the vacuum valve
allow the tube pressure to drop below 1 psi on the digital vacuum guage
close the vacuum valve, turn off the venturi pump and turn on the N2 flow
allow the tube pressure to reach atmosphere (15-16) ________ psi
open the exhaust valve and adjust the N2 flow until it reaches (2) ________ sccm (~14.96 psi)
Bonding Program: automatic recipe
85 C/min ramp to bonding temperature of (600) _______ C
bonding time of (30) _______ min with 10 C/min ramp down to 300 C; step down to room temp

Step 8: GaAs substrate removal - lapping Date: ______________
Wax Bonding to Lapping Fixture: nanofab - get hot plate, MWH135 wax, vacuum chuck, filter paper, lapping block
heat bottom plate of vacuum chuck and lapping block to (180) ________ C
place two pieces of filter paper against the rubber diaphragm of vacuum fixture
carefully melt a small dab of MWH135 wax on lapping block; place sample on melted wax
cover with rubber diaphragm; pull under vacuum; allow sample and chuck to cool to room temp
turn on N2 to release diaphragm; remove lapping block with bonded sample
Lap Down GaAs substrate: teaching cleanroom - get glass lapping plate, lapping paper, lapping fixture
measure thickness of dummy MEMS DBR sample: ________ microns
measure thickness of bonded sample on lapping block: ________ microns
zero bonding fixture by placing on glass and tightening set screw; dial down scale on top
back scale off to remove (400) ________ microns (each tick is 25 microns)
loosen set screw, allow lapping block to drop; retighten set screw
lap in a figure "8" pattern (40) ________ times, repeat (8-10) ________ times
periodically check thickness of bonded sample to ensure that excessive lapping does not occur
measure final thickness of bonded sample (600-700) ________ microns
heat sample on hot plate to (180) ________ C; remove sample from lapping block
clean lapping block with ace/iso and return to nanofab

Step 9: GaAs substrate removal - etch Date: ______________
Clean: acetone (2) ______ min iso (2)_______ min
scrub with cotton swab to remove any residue; tergitol rinse
Wax Bonding to Glass Slide: xtal bond sample to a glass slide
heat glass slide to (120-140) ________ C
carefully melt a small dab of crystal bond on glass slide; place sample on slide
press sample into place with wooden stick from the cotton swab; swirl to distribute wax
GaAs Substrate Removal: H_2O_2:NH_4OH 30:1 (150:5 mL) for (30-60)_________ min
use small magnetic stir bar at (400-600) ________ RPM; place sample at angle over stir bar
do not remove sample from etchant during this process!
rinse DI (60) ______ sec; dry with N2
check to ensure all GaAs has been chemically removed before proceeding!
Stop Etch Removal: remove AlGaAs etch stop; 1:10 49% HF:DI (10-15) _______ s
rinse DI (60) ______ sec; dry with N2
Remove Sample: melt xtal bond to free sample from glass slide
heat on hot plate to (160) ________ C
Clean: acetone (2) ______ min iso (2)_______ min; scrub with cotton swab to remove xtal bond residue
Measure: reflectance spectrum in Cary 500 spectrophotometer

APPENDIX D

Process Travelers

D.1 Generation 1: Fabrication Procedure

Step 1: defining the center DBR stack Date: ______________

Clean: acetone (2) ______ min iso (2)_______ min dehyd. bake at (110) ______ C for >3 min
Photolithography #1: define upper DBR
HMDS: sit for (30) ______ sec spin at (4) ______ krpm for (30) ______ sec
resist (AZ4110) ____________ spin at (4) ______ krpm for (30) ______sec
prebake at (95) _______ C for (60) _________ sec cool (1) _______ min
edgebead: expose at (7.5) _______ mW for (60) _________ sec with edgebead mask (x2)
develop in (1:4 AZ400k) ___________ developer for (60) ______ sec
rinse DI (60) ______ sec; dry with N2
expose image at (7.5) _______ mW for (12) _________ sec
develop in (1:4 AZ400k) _____________ developer for (45) _____________sec
rinse DI (60) ______ sec; dry with N2
Dry Etch: RIE #5 with laser monitor @ 2V and 30 cm/hr
offsets: SiCl4 _____ sccm, Cl2 _____ sccm, BCl3 _____ sccm, He _____ sccm, Press _____ mTorr
recipe: SiCl4 (10) _______ sccm, Cl2 (0) _______ sccm, BCl3 (0) _______ sccm
He (10) ______ sccm, pressure (3) ______mTorr, power (100) ______ W
HF Dip: remove residual AlGaAs; 1:100 HF:DI (15) ______ sec
rinse DI (60) ______ sec; dry with N2
Clean: acetone (2) ________min, iso (2) _______ min, DekTak: __________nm

Step 2: n-GaAs contact metallization Date: ______________

Strip Resist: AZ 1165 (10) _______ min
Clean: acetone (2) ______ min iso (2)_______ min dehyd. bake at (110) ______ C for >3 min
Photolithography #2: lower n-GaAs contact
HMDS: sit for (30) ______ sec spin at (4) ______ krpm for (30) ______ sec
resist (AZ4110) ____________ spin at (4) ______ krpm for (30) ______sec
prebake at (95) _______ C for (60) _________ sec cool (1) _______ min
edgebead: expose at (7.5) _______ mW for (60) _________ sec with edgebead mask (x2)
develop in (1:4 AZ400k) ___________ developer for (60) ______ sec
rinse DI (60) ______ sec; dry with N2
GaAs/AlGaAs Wet Etch: expose lower n-GaAs contact
DI (20) ______ mL : Citric Acid (20) ______ mL : Hyd Peroxide (10) ______ mL
wet etch in above solution for (90) _____ sec (watch for color changes)
HF dip to remove AlGaAs sac. layer; 1:100 HF:DI (5.5) ______ min
Descum: O_2 plasma for (1.5) ______ min at (100) ________ W
Clean: AZ 400K 1:4 to rinse off residual AlGaAs particles and clean floor
rinse DI (60) ______ sec; dry with N2
Strip Resist: AZ 1165 (10) _______ min
Clean: acetone (2) ______ min iso (2)_______ min dehyd. bake at (110) ______ C for >3 min

Step 2: n-GaAs contact metallization continued Date: ______________

Photolithography #3: ohmic contact ring

HMDS: sit for (30) ______ sec, spin at (4) ______ krpm for (30) ______ sec
resist (AZ5214) ____________ spin at (4) ______ krpm for (30) ______sec
prebake at (95) _______ C for (60) _________ sec cool (1) _______ min
edgebead: expose at (7.5) _______ mW for (60) _________ sec with edgebead mask (x2)
develop in (1:4 AZ400k) ___________ developer for (45) ______ sec
rinse DI (60) ______ sec; dry with N2
expose image at (7.5) _______ mW for (12) _________ sec
contact separation: expose at (7.5) _______ mW for (12) _________ sec with edgebead mask (x2)
postbake at (110) ______ C for (1) ______ min
flood expose (image reversal) in aligner (1) ____________ min
develop in (1:4 AZ400k) _____________ developer for (35) _____________sec
rinse DI (60) ______ sec; dry with N2
O_2 Plasma Descum for (20) ______ sec at (100) ________ W

E-beam Evaporation: Ge _____ (260) A Au _____ (540) A Ni _____ (200) A Au _____ (2000) A

Liftoff: soak in acetone __________ for (5) ________ min, iso (5) _________ min

Strip Resist: AZ 1165 (10) _______ min at (80) _____ C

Descum: O_2 plasma for (30) ______ sec at (100) ________ W DekTak (300) _______ nm

Strip Annealer: Temp (430) _______ C, Time (30) _______ s

Step 3: SiNx deposition and etch Date: ______________

PECVD Deposition: film thickness (150) ___________nm

Clean: acetone (2) ______ min iso (2)_______ min dehyd. bake at (110) ______ C for >3 min

Photolithography #4: expose upper and lower contacts (windows in SiNx - negative resist)

HMDS: sit for (30) ______ sec, spin at (4) ______ krpm for (30) ______ sec
resist (AZ5214) ____________ spin at (4) ______ krpm for (30) ______sec
prebake at (95) _______ C for (60) _________ sec cool (1) _______ min
edgebead: expose at (7.5) _______ mW for (60) _________ sec with edgebead mask (x2)
develop in (1:4 AZ400k) ___________ developer for (60) ______ sec
rinse DI (60) ______ sec; dry with N2
expose image at (7.5) _______ mW for (12) _________ sec
contact separation: expose at (7.5) _______ mW for (12) _________ sec with edgebead mask (x2)
postbake at (110) ______ C for (1) ______ min
flood expose (image reversal) in aligner (1) ____________ min
develop in (1:4 AZ400k) _____________ developer for (35) _____________sec
rinse DI (60) ______ sec; dry with N2

Dry Etch SiNx #1: open contact windows in PEII-B asher

O_2 Plasma Descum for (20) ______ sec at (100) ________ W
CF4 etch: pressure (300) _______ mT power (100) ______ W etch time (4) ______ min

Strip Resist: AZ 1165 (10) _______ min

Clean: acetone (2) ______ min iso (2)_______ min dehyd. bake at (110) ______ C for >3 min

Photolithography #5: define GaAs actuator (no edgebead removal)

HMDS: sit for (30) ______ sec spin at (4) ______ krpm for (30) ______ sec
resist (AZ4110) ____________ spin at (4) ______ krpm for (30) ______sec
prebake at (95) _______ C for (60) _________ sec cool (1) _______ min
expose image at (7.5) _______ mW for (12) _________ sec
develop in (1:4 AZ400k) _____________ developer for (45) _____________sec

Dry Etch SiNx #2: define actuator etch mask in PEII-B asher

O_2 Plasma Descum for (20) ______ sec at (100) ________ W
CF4 etch: pressure (300) _______ mT power (100) ______ W etch time (4) ______ min

Step 4: GaAs structural layer Etch Date: ______________

Hard Bake Resist: place sample on hot plate (120) _______ C for (10) _______ min

Non-Solvent Clean: spin on chuck at 4kRPM and blow with N2

Photolithography #6: protect upper DBR (no HMDS and no edgebead removal)

resist (AZ4110) ____________ spin at (4) ______ krpm for (30) ______sec

prebake at (95) _______ C for (60) _________ sec cool (1) _______ min

expose image at (7.5) _______ mW for (12) _________ sec

develop in (1:4 AZ400k) _____________ developer for (35) _____________sec

rinse DI (60) ______ sec; dry with N2

Dry Etch: RIE #5 for (12) ______ min

offsets: SiCl4 _____ sccm, Cl2 _____ sccm, BCl3 _____ sccm He _____ sccm

recipe: SiCl4 (10) _______ sccm, Cl2 (0) _______ sccm, BCl3 (0) _______ sccm

He (10) ______ sccm, pressure (3) ______mTorr, power (100) ______ W

Step 5: release and CPD Date: ______________

Strip Resist: AZ 1165 (10-20) _______ min at (80) _______ C

Clean: acetone (2) ______ min iso (2)_______ min dehyd. bake at (110) ______ C for >3 min

Photolithography #7: DBR protection #2 and undercut protection (no edgebead removal)

HMDS: sit for (30) ______ sec spin at (4) ______ krpm for (30) ______ sec

resist (AZ4110) ____________ spin at (4) ______ krpm for (30) ______sec

prebake at (95) _______ C for (60) _________ sec cool (1) _______ min

expose image at (7.5) _______ mW for (12) _________ sec

develop in (1:4 AZ400k) _____________ developer for (45) _____________sec

rinse DI (60) ______ sec; dry with N2

Wet etch AlGaAs: remove sacrificial layer to release device

DI:HCl 5:1 (25-30) ___________ min, rinse DI (very gently!) 1 min

acetone (2) _______ min, iso (2) _______ min, Dehydrated Alcohol (Ethanol) for CPD

Critical Point Dry: standard procedure

place sample in boat filled with Ethanol

solution (Eth.) ________ temp. (36) ________ C pressure (1200) ________ psi

Post release polymer strip:

O_2 Plasma Descum for (2) ______ min at (300) ________ W

CF4 etch: pressure (300) _______ mT power (100) ______ W etch time (30-45) ______ sec

D.2 Generation 2: Fabrication Procedure

Step 1: defining the center DBR stack Date: ______________

Clean: acetone (2) ______ min iso (2)_______ min dehyd. bake at (110) ______ C for >3 min
Photolithography #1: define upper DBR - **5 PERIODS FOR THIS DEVICE!!!!!**
HMDS: sit for (30) ______ sec spin at (4) ______ krpm for (30) ______ sec
resist (AZ4110) ____________ spin at (4) ______ krpm for (30) ______sec
prebake at (95) _______ C for (75) _________ sec cool (1) _______ min
edgebead: expose at (7.5) _______ mW for (60) _________ sec with edgebead mask (x2)
develop in (1:4 AZ400k) ___________ developer for (60) ______ sec
rinse DI (60) ______ sec; dry with N2
expose image at (7.5) _______ mW for (12) _________ sec
develop in (1:4 AZ400k) _____________ developer for (45) _____________sec
rinse DI (60) ______ sec; dry with N2
Dry Etch: RIE #5 with laser monitor @ 2V and 30 cm/hr
offsets: SiCl4 _____ sccm, Cl2 _____ sccm, BCl3 _____ sccm, He _____ sccm, Press _____ mTorr
recipe: SiCl4 (10) _______ sccm, Cl2 (0) _______ sccm, BCl3 (0) _______ sccm
He (10) ______ sccm, pressure (3) ______mTorr, power (100) ______ W
HF Dip: remove residual AlGaAs; 1:100 HF:DI (15) ______ sec
rinse DI (60) ______ sec; dry with N2
Clean: acetone (2) ________min, iso (2) _______ min, DekTak: __________nm

Step 2: n-GaAs contact metallization Date: ______________

Strip Resist: acetone/iso dip, dry with N2; AZ 1165 (10) _______ min @ 85 C
rinse DI (2) ______ min; dry with N2
Post Strip Solvent Clean: iso (1-2) _______ min dehyd. bake at (110) ______ C for >3 min
Photolithography #2: lower n-GaAs contact
HMDS: sit for (30) ______ sec spin at (4) ______ krpm for (30) ______ sec
resist (AZ4110) ____________ spin at (4) ______ krpm for (30) ______sec
prebake at (95) _______ C for (75) _________ sec cool (1) _______ min
edgebead: expose at (7.5) _______ mW for (60) _________ sec with edgebead mask (x2)
develop in (1:4 AZ400k) ___________ developer for (60) ______ sec
rinse DI (60) ______ sec; dry with N2
GaAs/AlGaAs Wet Etch: expose lower n-GaAs contact
DI (20) ______ mL : Citric Acid (20) ______ mL : Hyd Peroxide (10) ______ mL
wet etch in above solution for (90) _____ sec (watch for color changes)
HF dip to remove AlGaAs sac. layer; 1:100 HF:DI (5.5) ______ min
Descum: O_2 plasma for (1.5) ______ min at (100) ________ W

Clean: AZ 400K 1:4 to rinse off residual AlGaAs particles and clean floor
rinse DI (60) ______ sec; dry with N2
Strip Resist: acetone/iso dip, dry with N2; AZ 1165 (10) _______ min @ 85 C
rinse DI (2) ______ min; dry with N2
Post Strip Solvent Clean: iso (1-2) _______ min dehyd. bake at (110) ______ C for >3 min
Photolithography #3: ohmic contact ring
HMDS: sit for (30) ______ sec, spin at (4) ______ krpm for (30) ______ sec
resist (AZ5214) ____________ spin at (4) ______ krpm for (30) ______sec
prebake at (95) _______ C for (75) _________ sec cool (1) _______ min
edgebead: expose at (7.5) _______ mW for (60) _________ sec with edgebead mask (x2)
develop in (1:4 AZ400k) ___________ developer for (45) ______ sec
rinse DI (60) ______ sec; dry with N2
expose image at (7.5) _______ mW for (12) _________ sec
contact separation: expose at (7.5) _______ mW for (12) _________ sec with edgebead mask (x2)
postbake at (110) ______ C for (1) ______ min
flood expose (image reversal) in aligner (1) ____________ min
develop in (1:4 AZ400k) _____________ developer for (35) _____________sec
rinse DI (60) ______ sec; dry with N2

Step 2: n-GaAs contact metallization continued Date: ______________
GaAs Oxide Strip: dip in HF for (20-30) _________ sec and NH4OH undiluted for (20-30) _________ sec rinse DI (1) ______ min; dry with N2 **E-beam Evaporation**: Ge _____ (260) A Au _____ (540) A Ni _____ (200) A Au _____ (2000) A **Liftoff**: soak in acetone __________ for (5) ________ min, iso (5) _________ min **Strip Resist**: AZ 1165 (10) _______ min at (80) _____ C **Descum**: O_2 plasma for (30) ______ sec at (100) ________ W DekTak (300) _______ nm **Strip Annealer**: Temp (430) _______ C, Time (30) _______ s

Step 3: SiNx deposition and etch Date: ______________
GaAs Oxide Strip: dip in HF for (20-30) _________ sec and NH4OH undiluted for (20-30) _________ sec rinse DI (1) ______ min; dry with N2 **Post Strip Solvent Clean**: iso (1-2) _______ min dehyd. bake at (110) ______ C for >3 min **PECVD Deposition**: film thickness (150) ___________nm **Clean**: acetone (2) ______ min iso (2)_______ min dehyd. bake at (110) ______ C for >3 min **Photolithography #4**: expose upper and lower contacts (windows in SiNx - negative resist) HMDS: sit for (30) ______ sec, spin at (4) ______ krpm for (30) ______ sec resist (AZ5214) ____________ spin at (4) ______ krpm for (30) ______sec prebake at (95) _______ C for (75) _________ sec cool (1) _______ min **edgebead:** expose at (7.5) _______ mW for (60) _________ sec with edgebead mask (x2) develop in (1:4 AZ400k) ___________ developer for (60) ______ sec rinse DI (60) ______ sec; dry with N2 expose image at (7.5) _______ mW for (12) _________ sec **contact separation**: expose at (7.5) _______ mW for (12) _________ sec with edgebead mask (x2) postbake at (110) ______ C for (1) ______ min flood expose (image reversal) in aligner (1) ____________ min develop in (1:4 AZ400k) _____________ developer for (35) _____________sec rinse DI (60) ______ sec; dry with N2 **Dry Etch SiNx #1**: open contact windows in PEII-B asher O_2 Plasma Descum for (20) ______ sec at (100) ________ W CF4 etch: pressure (300) _______ mT power (100) ______ W etch time (4) ______ min O_2 Plasma Descum for (20) ______ sec at (100) ________ W **Strip Resist**: acetone/iso dip, dry with N2; AZ 1165 (10) _______ min @ 85 C rinse DI (2) ______ min; dry with N2 **Post Strip Solvent Clean**: iso (1-2) _______ min dehyd. bake at (110) ______ C for >3 min **Photolithography #5**: open DBR window (no edgebead removal) HMDS: sit for (30) ______ sec spin at (4) ______ krpm for (30) ______ sec resist (AZ5214) ____________ spin at (4) ______ krpm for (30) ______sec prebake at (95) _______ C for (75) _________ sec cool (1) _______ min expose image at (7.5) _______ mW for (12) _________ sec postbake at (110) ______ C for (1) ______ min flood expose (image reversal) in aligner (1) ____________ min develop in (1:4 AZ400k) _____________ developer for (45) _____________sec **Dry Etch SiNx #2**: open DBR window in PEII-B asher O_2 Plasma Descum for (20) ______ sec at (100) ________ W CF4 etch: pressure (300) _______ mT power (100) ______ W etch time (4) ______ min O_2 Plasma Descum for (20) ______ sec at (100) ________ W **Strip Resist**: acetone/iso dip, dry with N2; AZ 1165 (10) _______ min @ 85 C rinse DI (2) ______ min; dry with N2 **Post Strip Solvent Clean**: iso (1-2) _______ min dehyd. bake at (110) ______ C for >3 min

Step 3: SiNx deposition and etch continued Date: ______________
Photolithography #6: define GaAs actuator (no edgebead removal)
HMDS: sit for (30) ______ sec spin at (4) ______ krpm for (30) ______ sec
resist (AZ4110) ____________ spin at (4) ______ krpm for (30) ______sec
prebake at (95) _______ C for (75) _________ sec cool (1) _______ min
expose image at (7.5) _______ mW for (12) _________ sec
develop in (1:4 AZ400k) _____________ developer for (45) _____________sec
Dry Etch SiNx #2: define actuator etch mask in PEII-B asher
O_2 Plasma Descum for (20) ______ sec at (100) ________ W
CF4 etch: pressure (300) _______ mT power (100) ______ W etch time (4) ______ min
O2 Plasma Descum for (20) ______ sec at (100) ________ W

Step 4: GaAs structural layer etch Date: ______________
Dry Etch: RIE #5 for (20-25) ______ min use dummy wafer as reference with laser monitor @ 2V and 10 cm/hr
offsets: SiCl4 _____ sccm, Cl2 _____ sccm, BCl3 _____ sccm He _____ sccm
recipe: SiCl4 (10) _______ sccm, Cl2 (0) _______ sccm, BCl3 (0) _______ sccm
He (10) ______ sccm, pressure (3) ______mTorr, power (100) ______ W
rinse DI (60) ______ sec immediately after etch; dry with N2
Record etch depth: DekTak (~2300) _______ nm
Strip Resist: acetone/iso dip, dry with N2; AZ 1165 (10) _______ min @ 85 C
rinse DI (2) ______ min; dry with N2

Step 5: mechanical clamping layer deposition Date: ______________
Post Strip Solvent Clean: iso (1-2) _______ min dehyd. bake at (110) ______ C for >3 min
Photolithography #7: clamping layer liftoff (no edgebead removal); double resist process
HMDS: sit for (30) ______ sec spin at (4) ______ krpm for (30) ______ sec
resist (AZ4110) ____________ spin at (4) ______ krpm for (30) ______sec
prebake at (95) _______ C for (75) _________ sec cool (1) _______ min
flood expose (for undercut profile) in aligner (15) ____________ sec
resist (AZ5214) ____________ spin at (4) ______ krpm for (30) ______sec
prebake at (95) _______ C for (75) _________ sec cool (1) _______ min
expose image at (7.5) _______ mW for (12) _________ sec
contact separation: expose at (7.5) _______ mW for (12) _________ sec with edgebead mask (x2)
postbake at (110) ______ C for (1) ______ min
flood expose (image reversal) in aligner (1) ____________ min
develop in (1:4 AZ400k) _____________ developer for (45) _____________sec
SiOx deposition: clamping layer deposition in Unaxis
season chamber, deposit (300-350) ________ (nm), clean chamber
Dielectric Liftoff: AZ 1165 (10) _______ min @ 85 C
soak in acetone, spray with pipette, iso dip with short (10-30) ___________ sec ultrasonic
Strip Resist: AZ 1165 (5) _______ min @ 85 C
rinse DI (2) ______ min; dry with N2
AlAs Oxide Strip: dip in undiluted AZ400k for (20-30) _________ sec
rinse DI (1) ______ min; dry with N2

Step 6: release and CPD Date: ______________

Post Strip Solvent Clean: iso (1-2) _______ min dehyd. bake at (110) ______ C for >3 min

Photolithography #8: DBR protection #2 and undercut protection (no edgebead removal)

HMDS: sit for (30) ______ sec spin at (4) ______ krpm for (30) ______ sec

resist (AZ4110) ____________ spin at (4) ______ krpm for (30) ______sec

prebake at (95) _______ C for (75) _________ sec cool (1) _______ min

expose image at (7.5) _______ mW for (12) _________ sec

develop in (1:4 AZ400k) _____________ developer for (45) _____________sec

rinse DI (60) ______ sec; dry with N2

Wet etch AlGaAs: remove sacrificial layer to release device

DI:HCl 5:1 (25-30) ___________ min, rinse DI (very gently!) 1 min

acetone (2) _______ min, iso (2) _______ min, Dehydrated Alcohol (Ethanol) for CPD

Critical Point Dry: standard procedure

place sample in boat filled with Ethanol

solution (Eth.) ________ temp. (36) ________ C pressure (1200) ________ psi

Post release polymer strip:

O_2 Plasma Descum for (10-15) ______ sec at (100) ________ W

CF4 etch: pressure (300) _______ mT power (100) ______ W etch time (5-10) ______ sec

O_2 Plasma Descum for (10-15) ______ sec at (300) ________ W

D.3 Generation 3: Fabrication Procedure

Step 1: AlGaAs etch - define the top DBR pillar Date: ______________

Clean: acetone (2) ______ min iso (2)_______ min dehyd. bake at (110) ______ C for >3 min
Photolithography #1: define upper DBR - **ALIGN PATTERN WITH BONDING CHANNELS**
HMDS: sit for (30) ______ sec spin at (4) ______ krpm for (30) ______ sec
resist (AZ4210) ____________ spin at (4) ______ krpm for (30) ______sec
prebake at (95) _______ C for (75) _________ sec cool (1) _______ min
edgebead: expose at (7.5) _______ mW for (75) _________ sec with edgebead mask (x2)
develop in (1:4 AZ400k) ___________ developer for (60) ______ sec
rinse DI (60) ______ sec; dry with N2
expose image at (7.5) _______ mW for (17) _________ sec
develop in (1:4 AZ400k) _____________ developer for (45-55) _____________sec
rinse DI (60) ______ sec; dry with N2
hard bake resist (110) ______ C for (75) _______ sec
Dry Etch: RIE #5 with laser monitor @ 2V and 30 cm/hr - **15 PERIODS**
offsets: SiCl4 _____ sccm, Cl2 _____ sccm, BCl3 _____ sccm, He _____ sccm, Press _____ mTorr
recipe: SiCl4 (0) _______ sccm, Cl2 (1.5) _______ sccm, BCl3 (19.5) _______ sccm
He (0) ______ sccm, pressure (5) ______mTorr, power (50) ______ W
HF Dip: remove residual AlGaAs; 1:100 HF:DI (15) ______ sec
rinse DI (60) ______ sec; dry with N2

Step 2: n-GaAs contact metallization Date: ______________

Strip Resist: acetone/iso dip, dry with N2; AZ 1165 (10) _______ min @ 85 C, O2 descum (1) ______ min
Post Strip Solvent Clean: ace/iso (1-2) _______ min dehyd. bake at (110) ______ C for >3 min
Photolithography #2: lower n-GaAs contact
HMDS: sit for (30) ______ sec spin at (4) ______ krpm for (30) ______ sec
resist (AZ4210) ____________ spin at (4) ______ krpm for (30) ______sec
prebake at (95) _______ C for (75) _________ sec cool (1) _______ min
edgebead: expose at (7.5) _______ mW for (75) _________ sec with edgebead mask (x2)
develop in (1:4 AZ400k) ___________ developer for (75) ______ sec
rinse DI (60) ______ sec; dry with N2
hard bake resist (110) ______ C for (75) _______ sec
GaAs/AlGaAs Wet Etch: expose lower n-GaAs contact
DI (20) ______ mL : Citric Acid (20) ______ mL : Hyd Peroxide (10) ______ mL
wet etch in above solution for (90) _____ sec (watch for color changes)
dilute HF etch to remove AlGaAs sac. layer; 1:50 HF:DI (10-20) ______ min
Descum: O_2 plasma for (1.5) ______ min at (100) ________ W
Oxide Clean: AZ 400K 1:4 to rinse off residual AlGaAs particles and clean floor
rinse DI (60) ______ sec; dry with N2
Strip Resist: acetone/iso dip, dry with N2; AZ 1165 (10) _______ min @ 85 C
Post Strip Solvent Clean: ace/iso (1-2) _______ min dehyd. bake at (110) ______ C for >3 min
Photolithography #3: ohmic contact ring
HMDS: sit for (30) ______ sec, spin at (4) ______ krpm for (30) ______ sec
resist (AZ5214) ____________ spin at (4) ______ krpm for (30) ______sec
prebake at (95) _______ C for (75) _________ sec cool (1) _______ min
edgebead: expose at (7.5) _______ mW for (60) _________ sec with edgebead mask (x2)
develop in (1:4 AZ400k) ___________ developer for (45) ______ sec
rinse DI (60) ______ sec; dry with N2
expose image at (7.5) _______ mW for (12) _________ sec
contact separation: expose at (7.5) _______ mW for (12) _________ sec with edgebead mask (x2)
postbake at (110) ______ C for (65) ______ sec
flood expose (image reversal) in aligner (1) ____________ min
develop in (1:4 AZ400k) _____________ developer for (35) _____________sec
rinse DI (60) ______ sec; dry with N2
O_2 Plasma Descum for (20) ______ sec at (100) ________ W

Step 2: n-GaAs contact metallization continued Date: ______________
GaAs Oxide Strip: 1:100 NH4OH:DI (10) _________ sec; 1:20 HCl:DI (10-20) ______ sec; rinse DI (1) ______ min; dry with N2 **E-beam Evaporation**: Ge _____ (260) A Au _____ (540) A Ni _____ (200) A Au _____ (2000) A *Process #40* **Liftoff**: soak in acetone, spray with pipette until cleared **Strip Resist**: AZ 1165 (10) _______ min at (80) _____ C, O2 descum (1) ______ min **Strip Annealer**: Temp (430) _______ C, Time (30) _______ s

Step 3: SiNx stress relief deposition Date: ______________
Clean: acetone (2) ______ min iso (2)_______ min, O2 descum (1) ______ min **GaAs Oxide Strip**: 1:20 NH4OH:DI (10) _________ sec; 1:20 HCl:DI (10) ______ sec rinse DI (1) ______ min; dry with N2 **PECVD Deposition**: film thickness (250) ___________nm **Clean**: acetone (2) ______ min iso (2)_______ min dehyd. bake at (110) ______ C for >3 min **Photolithography #4**: define SiNx clamping ring HMDS: sit for (30) ______ sec spin at (4) ______ krpm for (30) ______ sec resist (AZ4110) ____________ spin at (4) ______ krpm for (30) ______sec prebake at (95) _______ C for (75) _________ sec cool (1) _______ min **edgebead**: expose at (7.5) _______ mW for (60) _________ sec with edgebead mask (x2) develop in (1:4 AZ400k) ___________ developer for (60) ______ sec rinse DI (60) ______ sec; dry with N2 expose image at (7.5) _______ mW for (12) _________ sec develop in (1:4 AZ400k) _____________ developer for (50) _____________sec rinse DI (60) ______ sec; dry with N2 **Dry Etch SiNx #1**: define clamping ring CF4 etch: pressure (300) _______ mT power (100) ______ W etch time (3) ______ min O_2 Plasma Descum for (20) ______ sec at (100) ________ W

Step 4: SiNx structural layer deposition and backside polish Date: ______________
Strip Resist: acetone/iso dip, dry with N2; AZ 1165 (10) _______ min @ 85 C, O2 descum (1) ______ min **GaAs Oxide Strip**: 1:20 NH4OH:DI (10) _________ sec; 1:20 HCl:DI (10-20) ______ sec; rinse DI (1) ______ min; dry with N2 **PECVD Deposition**: film thickness (100) ___________nm **Clean**: acetone (2) ______ min iso (2)_______ min dehyd. bake at (110) ______ C for >3 min **PMGI Protection**: coat topside of chip for wax bonding HMDS: sit for (30) ______ sec spin at (4) ______ krpm for (30) ______ sec PMGI (SF-11) ____________ spin at (4) ______ krpm for (30) ______sec prebake at (200) _______ C for (2) _________ min cool (1) _______ min **Wax Bonding to Lapping Fixture**: nanofab - get hot plate, MWH135 wax, vacuum chuck, filter paper, lapping block heat bottom plate of vacuum chuck and lapping block to (180) ________ C place two pieces of filter paper against the rubber diaphragm of vacuum fixture carefully melt a small dab of MWH135 wax on lapping block; place sample on melted wax cover with rubber diaphragm; pull under vacuum; allow sample and chuck to cool to room temp turn on N2 to release diaphragm; remove lapping block with bonded sample **Polish GaAs Substrate**: teaching cleanroom - get silk covered glass lapping plate, lapping paper, lapping fixture lap in 25 um increments in lapping fixture with 3 um grit (pink cloth) until surface is uniform lap in 25 um increments with progressively finer grit - 1 um and finally 0.5 um remove from lapping fixture, clean lapping block with DI, swab to remove GaAs particles and grit polish in figure "8" pattern on silk cloth with bleach slurry (avoid DI on cloth) rinse in DI, blow dry with N2, check substrate surface condition in optical microscope, repeat heat sample on hot plate to (180) ________ C; remove sample from lapping block **Strip Wax**: acetone/iso dip, dry with N2; AZ 1165 (10) _______ min @ 85 C **Clean**: acetone (2) ______ min iso (2)_______ min dehyd. bake at (110) ______ C for >3 min **PMGI Protection**: coat backside of chip to reduce scratching HMDS: sit for (30) ______ sec spin at (4) ______ krpm for (30) ______ sec PMGI (SF-11) ____________ spin at (4) ______ krpm for (30) ______sec prebake at (200) _______ C for (2) _________ min cool (1) _______ min

Step 5: SiNx etch 1 - contact window Date: ______________
Clean: acetone (2) ______ min iso (2)_______ min dehyd. bake at (110) ______ C for >3 min
Photolithography #5: expose upper and lower contacts (windows in SiNx - negative resist)
HMDS: sit for (30) ______ sec, spin at (4) ______ krpm for (30) ______ sec
resist (AZ5214) ____________ spin at (4) ______ krpm for (30) ______sec
prebake at (95) _______ C for (75) _________ sec cool (1) _______ min
edgebead: expose at (7.5) _______ mW for (60) _________ sec with edgebead mask (x2)
develop in (1:4 AZ400k) ___________ developer for (45) ______ sec
rinse DI (60) ______ sec; dry with N2
expose image at (7.5) _______ mW for (12) _________ sec
contact separation: expose at (7.5) _______ mW for (12) _________ sec with edgebead mask (x2)
postbake at (110) ______ C for (1) ______ min
flood expose (image reversal) in aligner (1) ____________ min
develop in (1:4 AZ400k) _____________ developer for (35) _____________sec
rinse DI (60) ______ sec; dry with N2
Dry Etch SiNx #1: open contact windows in PEII-B asher
CF4 etch: pressure (300) _______ mT power (100) ______ W etch time (1) ______ min
O_2 Plasma Descum for (20) ______ sec at (100) ________ W

Step 6: SiNx etch 2 and AlGaAs structural layer etch - define actuator Date: ______________
Clean: acetone (2) ______ min iso (2)_______ min dehyd. bake at (110) ______ C for >3 min
Photolithography #6: define GaAs actuator (no edgebead removal)
HMDS: sit for (30) ______ sec spin at (4) ______ krpm for (30) ______ sec
resist (AZ4210) ____________ spin at (4) ______ krpm for (30) ______sec
prebake at (95) _______ C for (75) _________ sec cool (1) _______ min
expose image at (7.5) _______ mW for (17) _________ sec
develop in (1:4 AZ400k) _____________ developer for (45-55) _____________sec
rinse DI (60) ______ sec; dry with N2
hard bake resist (110) ______ C for (75) _______ sec
Dry Etch SiNx #2: define actuator etch mask in PEII-B asher
CF4 etch: pressure (300) _______ mT power (100) ______ W etch time (4) ______ min
O2 Plasma Descum for (20) ______ sec at (100) ________ W
GaAs Oxide Strip: 1:100 NH4OH:DI (10) _________ sec; 1:20 HCl:DI (10-20) ______ sec;
rinse DI (1) ______ min; dry with N2
Dry Etch: RIE #5 for (20-25) ______ min use dummy wafer as reference with laser monitor @ 2V and 10 cm/hr
offsets: SiCl4 _____ sccm, Cl2 _____ sccm, BCl3 _____ sccm He _____ sccm
recipe: SiCl4 (10) _______ sccm, Cl2 (0) _______ sccm, BCl3 (0) _______ sccm
He (10) ______ sccm, pressure (3) ______mTorr, power (100) ______ W
rinse DI (60) ______ sec immediately after etch; dry with N2

Step 7: SiNx etch 3 - DBR window Date: ______________
Clean: acetone (2) ______ min iso (2)_______ min dehyd. bake at (110) ______ C for >3 min
Record etch depth: DekTak (~2300) _______ nm
Photolithography #7: open DBR window (no edgebead removal)
HMDS: sit for (30) ______ sec spin at (4) ______ krpm for (30) ______ sec
resist (AZ5214) ____________ spin at (4) ______ krpm for (30) ______sec
prebake at (95) _______ C for (75) _________ sec cool (1) _______ min
expose image at (7.5) _______ mW for (12) _________ sec
postbake at (110) ______ C for (1) ______ min
flood expose (image reversal) in aligner (1) ____________ min
develop in (1:4 AZ400k) _____________ developer for (45) _____________sec
rinse DI (60) ______ sec; dry with N2
Dry Etch SiNx #3: open DBR window in PEII-B asher
CF4 etch: pressure (300) _______ mT power (100) ______ W etch time (1) ______ min
O_2 Plasma Descum for (20) ______ sec at (100) ________ W

Step 8: mechanical clamping layer deposition Date: ______________
Clean: acetone (2) ______ min iso (2)_______ min dehyd. bake at (110) ______ C for >3 min
Photolithography #8: PMGI/5214 bilayer liftoff
HMDS: sit for (30) ______ sec spin at (4) ______ krpm for (30) ______ sec
PMGI (SF-11) ____________ spin at (4) ______ krpm for (30) ______sec
prebake at (200) _______ C for (2) _________ min cool (1) _______ min
resist (AZ4110) ____________ spin at (4) ______ krpm for (30) ______sec
prebake at (95) _______ C for (75) _________ sec cool (1) _______ min
edgebead: expose at (7.5) _______ mW for (60) _________ sec with edgebead mask (x2)
develop in (1:4 AZ400k) ___________ developer for (45) ______ sec
rinse DI (60) ______ sec; dry with N2
DUV exposure (1000) _____ W for (600) _____ sec
develop in (SAL101) _____________ developer for (3) _____________ min
rinse DI (60) ______ sec; dry with N2 **(repeat exposure/develop process 2x)**
strip AZ4110 resist - acetone (2) ______ min iso (2)_______ min
resist (AZ5214) ____________ spin at (4) ______ krpm for (30) ______sec
prebake at (95) _______ C for (75) _________ sec cool (1) _______ min
expose image at (7.5) _______ mW for (12) _________ sec
contact separation: expose at (7.5) _______ mW for (12) _________ sec with edgebead mask (x2)
postbake at (110) ______ C for (1) ______ min
flood expose (image reversal) in aligner (1) ____________ min
develop in (1:4 AZ400k) _____________ developer for (45) _____________sec
DUV exposure (1000) _____ W for (300) _____ sec
develop in (SAL101) _____________ developer for (3) _____________ min
rinse DI (60) ______ sec; dry with N2 **(repeat exposure/develop process 2x)**
Descum: O2 plasma ash for (30) ______ sec at (100) ________ W
GaAs Oxide Strip: 1:100 NH4OH:DI (10) _________ sec; 1:20 HCl:DI (10) ______ sec
rinse DI (1) ______ min; dry with N2
SiO_2 film deposition: clamping layer deposition in Unaxis
season chamber, deposit (350) ________ (nm), clean chamber
Liftoff: AZ 1165 (10) _______ min @ 85 C; ultrasonic in stripper/acetone until excess SiO_2 is cleared

Step 9: SiOx antireflection coating deposition Date: ______________
Strip Resist: acetone/iso dip, dry with N2; AZ 1165 (10) _______ min @ 85 C, O2 descum (1) ______ min
Post Strip Solvent Clean: ace/iso (1-2) _______ min
PMGI Protection: coat patterned surface of chip to reduce scratching
HMDS: sit for (30) ______ sec spin at (4) ______ krpm for (30) ______ sec
PMGI (SF-11) ____________ spin at (4) ______ krpm for (30) ______sec
prebake at (200) _______ C for (2) _________ min cool (1) _______ min
Wax Bonding to silicon carrier: nanofab - get hot plate, MWH135 wax, vacuum chuck, filter paper, lapping block
heat bottom plate of vacuum chuck and Si carrier to (180) ________ C
place two pieces of filter paper against the rubber diaphragm of vacuum fixture
carefully melt a small dab of MWH135 wax on Si; place sample on melted wax
cover with rubber diaphragm; pull under vacuum; allow sample to cool to room temp
turn on N2 to release diaphragm; remove Si carrier with bonded sample
Backside AR Coating: e-beam#2 SiO deposition rate of ~2-5 A/s, final thickness approximately 200 nm
calibration run on dummy sample only - check film thickness and index with dektak, ellipsometer, Cary
adjust film thickness for given parameters, deposit on sample and Si carrier
evaporator settings: z-ratio (0.87) _______ tooling factor (130) _____ density (2.13) _____ g/cm^3
dektak SiOx thickness (215-225) _______ nm refractive index (1.6-1.8) ______
if necessary reduce film thickness in PEII-B, etch rate of 13.3 A/s
Cary measurement minimum reflectance of (1-2) _______ % at (1550) _______ nm

Step 10: release and CPD Date: ______________
Clean: acetone (2) ______ min iso (2)_______ min dehyd. bake at (110) ______ C for >3 min
AlAs Oxide Strip: dip in undiluted AZ400k for (20-30) _________ sec
rinse DI (1) ______ min; dry with N2
Photolithography #9: DBR protection #2 and undercut protection (no edgebead removal)
HMDS: sit for (30) ______ sec spin at (4) ______ krpm for (30) ______ sec
resist (AZ4110) ____________ spin at (4) ______ krpm for (30) ______sec
prebake at (95) _______ C for (75) _________ sec cool (1) _______ min
expose image at (7.5) _______ mW for (12) _________ sec
develop in (1:4 AZ400k) _____________ developer for (45) _____________sec
rinse DI (60) ______ sec; dry with N2
Wet etch AlGaAs: remove sacrificial layer to release device
DI:HCl 1:2 (20) ___________ min, rinse DI (very gently!) 1 min
strip oxide in undiluted AZ400k for (2) _________ min, rinse DI
acetone (2) _______ min, iso (2) _______ min, Dehydrated Alcohol (Ethanol) for CPD
Critical Point Dry: standard procedure
place sample in boat filled with Ethanol
solution (Eth.) ________ temp. (36) ________ C pressure (1200) ________ psi
Post release clean:
O_2 Plasma Descum for (20) ______ sec at (100) ________ W
CF4 etch: pressure (300) _______ mT power (100) ______ W etch time (10) ______ sec
O_2 Plasma Descum for (20) ______ sec at (300) ________ W